DESIGN & DEVELOPMENT OF PLANAR LIGHT CONCENTRATOR BASED SOLAR COLLECTORS

by

ANIMESH M R

Registration No: 20EE20A39003

A thesis submitted to the

Academy of Scientific and Innovative Research

for the award of the degree of

DOCTOR OF PHILOSOPHY

in

ENGINEERING

Under the supervision of

Dr. ADERSH ASOK

CSIR-National Institute for Interdisciplinary Science and Technology

(CSIR-NIIST), Thiruvananthapuram-695019, Kerala, India

Academy of Scientific and Innovative Research

AcSIR Headquarters, CSIR-HRDC campus, Sector 19, Kamla Nehru Nagar,

Ghaziabad, U.P.-201002, India.

December 2024

Dedicated to my family, teachers, and friends

राष्ट्रीय अंतर्विषयी विज्ञान तथा प्रौद्योगिकी संस्थान
वैज्ञानिक तथा औद्योगिक अनुसंधान परिषद् | विज्ञान तथा प्रौद्योगिकी मंत्रालय, भारत सरकार
इंडस्ट्रियल इस्टेट पी.ओ., पाप्पनंकोड, तिरुवनंतपुरम, भारत-695 019

CSIR-NATIONAL INSTITUTE FOR INTERDISCIPLINARY SCIENCE AND TECHNOLOGY (CSIR-NIIST)
Council of Scientific & Industrial Research | Ministry of Science and Technology, Govt. of India
Industrial Estate P.O., Pappanamcode, Thiruvananthapuram, India-695 019

Dr. Adersh Asok
Scientist, Centre for Sustainable Energy Technologies

Certificate

This is to certify that the work incorporated in this Ph.D. thesis entitled, **"Design & Development of Planar Light Concentrator based Solar Collectors"**, submitted by **Mr. Animesh M R** to the Academy of Scientific and Innovative Research (AcSIR) in fulfillment of the requirements for the award of the **Degree of Doctor of Philosophy in Engineering**, embodies original research work carried-out by the student. We, further certify that this work has not been submitted to any other University or Institution in part or full for the award of any degree or diploma. Research material(s) obtained from other source(s) and used in this research work have been duly acknowledged in the thesis. Image(s), illustrations(s), figures(s), tables(s) etc., used in the thesis from other source(s), have also been duly cited and acknowledged.

Animesh M R

6/12/2024
Thiruvananthapuram

Dr. Adersh Asok
(Thesis Supervisor)

6/12/2024
Thiruvananthapuram

STATEMENTS OF ACADEMIC INTEGRITY

I, **Animesh M R**, a Ph.D. student of the Academy of Scientific and Innovative Research (AcSIR) with Registration No. 20EE20A39003 hereby undertake that, the thesis entitled **"Design & Development of Planar Light Concentrator based Solar Collectors"** has been prepared by me and that the document reports original work carried out by me and is free of any plagiarism in compliance with the UGC Regulations on *"Promotion of Academic Integrity and Prevention of Plagiarism in Higher Educational Institutions (2018)"* and the CSIR Guidelines for *"Ethics in Research and in Governance (2020)"*.

Animesh M R

6/12/2024
Thiruvananthapuram

I hereby certify that the work done by the student, under my supervision, is plagiarism-free in accordance with the UGC Regulations on *"Promotion of Academic Integrity and Prevention of Plagiarism in Higher Educational Institutions (2018)"* and the CSIR Guidelines for *"Ethics in Research and in Governance (2020)"*.

Dr. Adersh Asok
(Thesis Supervisor)

6/12/2024
Thiruvananthapuram

ACKNOWLEDGEMENTS

First and foremost, I would like to express my deep sense of thanks and gratitude to my mentor and guide Dr. Adersh Asok for guiding me throughout my research work. His continuous encouragement, constant support, positive attitude, great patience, affection, and passion for translational research motivated and helped me complete the work on time.

I sincerely thank Dr. Narayanan Unni (head of the Centre for Sustainable Energy, CSIR-NIIST), Dr. Jubi John, and Dr. Subrata Das, my doctoral advisory committee members, for their valuable comments and fruitful discussions in my research work.

I am grateful to Dr. C. Anandharamakrishnan and Dr. A. Ajayaghosh the present and former directors of CSIR NIIST, for providing the necessary facilities and infrastructure to carry out my thesis work.

I wish to thank Dr. S. Savithri, the former head of the Materials Science and Technology Division & Dr. Saju Pillai during my tenure at the institute, for their valuable help in various academic and official matters, and also for their innumerable support. I am grateful to Mr. A. Peer Mohamed for his constant support and assistance in characterization facilities.

I would like to acknowledge the present and former AcSIR coordinators, Dr. Jayamurthy P, Dr. Karunakaran Venugopal, and Dr. C. H. Suresh and their office staff for the help and advice during my admission and all other academic procedures of AcSIR.

I thank all the scientists and technical staff of the Centre for Sustainable Energy Technologies, Chemical Sciences and Technology Division, and Materials Science and Technology Division for their help during my research work.

I would like to express my deep and sincere gratitude to Dr. Sumina N B and her family for their support through the years. I also acknowledge the collaborative research works and discussions we had throughout my research career.

I have had the pleasure of sharing the workspace and conducting collaborative research with some amazing people, Dr. Parvathy R Chandran, Dr. Reny Thankam Thomas, Dr. Nabeela Kallayi, Dr. Vipin V. V, Dr.Raji V Nair, and Mr. Deepu Mohanan. I adore their friendly attitude, care, and constant support throughout my research career. Thank you all from the bottom of my heart. I also thank my collaborators, Dr. Pierluigi Bonomo & Mr.

Paolo Corti, SUPSI, Switzerland, for the add-on research works and activities carried out. I also thank the industries that supported the thesis work.

I cherish the memorable days with my labmates Mr. Riyas, Mrs. Adithya, Mrs. Sangeetha, Mr. Manjit, Mr. Shaheer, Mrs. Reshma, Mrs. Neethu, Dr. Devika, Mr. Sankrish, Mrs. Maneesha, and all the post graduate project and internship students. I have my heartfelt acknowledgment for their support and research work conducted with them in the lab.

Words cannot express my gratitude to all my dear friends at the institute, Dr. Hari, Dr. Aswathy TR, Dr. Shaiju, Mr. Achu, Mrs. Silpa, Dr. Meghana, Dr. Hasna, Ms. Manasi, Ms. Gopika, Mrs. Adithya, Mr. Rahul, Dr. Aswathy, Mr. Heitor, Mr. Akhil, Ms. Ardra, Ms. Swetha, Ms. Dheekshitha, Mr. Sonu, Dr. Sudheesh, Mr. Gireesh. They have dealt with me in joy and stress and continue to care for and support me for that I am grateful.

I am incredibly grateful to all my teachers, and friends at school and colleges.

Finally, I would like to express my sincere love and gratitude to my father, mother, brother, and sister-in-law for their love, care, and support through times.

Animesh M R

TABLE OF CONTENTS

LIST OF ABBREVIATIONS

Abbreviations:

BIPV	Building Integrated Photovoltaics
D	Beam diameter
DDG	Decentralized Distributed Generation
DLP	Digital Light Processing
DOF	Depth of focus
DPW	Dynamic Power Window
DSSC	Dye-Sensitized Solar Cells
EC	Electrochromic
FC	Final Concentration
FCR	Final Concentration Ratio
FDM	Fused Deposition Modelling
GC	Geometric Concentration
GCR	Geometric Concentration Ratio
LED	Light emitting diode
LSC	Luminescent Solar Concentrator
Nd:YAG	neodymium: yttrium aluminium garnet
NIR	Near infrared
OE	Optical efficiency
P	Power
PC	Polycarbonate
PCE	Power conversion efficiency
PDLC	Polymer-Dispersed Liquid Crystal
PLA	Polylactic acid
PLC	Planar Light Concentrator
PMMA	Poly(methyl methacrylate)
PPI	Pulses per inch
RI	Refractive index
SLA	Stereolithography
SLS	Selective Laser Sintering
SPD	Suspended Particle Device
STC	Standard Testing Conditions
SV-PLC	Skewed V-groove based Planar Light Concentrator
TIR	Total internal reflection
UV	Ultraviolet

Greek letter symbols:

α	Refracting face angle
β	Angle made by ray with horizontal
β_{exit}	Exit angle
γ	Apex angle

θ	Reflecting face angle
λ	Wavelength
ϕ	Laser spot size

Symbols:

dh	Vertical displacement of ray
H	Height of PLC
h	Height of groove
i	Incident angle
L_{100}	Maximum length of the SV-PLC which can transport 100% of the light falling to the lateral face
L_{abs}	Absorption loss
$L_{fresnel}$	Fresnel loss
L_{leak}	Leakage loss
L_{max}	Maximum length of SV-PLC
M^2	Beam quality factor
n_a	Refractive index of air
N_{gmax}	Maximum number of grooves
n_m	Refractive index of material
r	Refraction angle
S	Inter-groove spacing
T_c	Cumulative Light Transmission
V_T	Visible transmittance
w	Width of groove
X^n	Horizontal length from the groove tip up to which a ray passes through n number of grooves

Units:

°	degree
°C	degree celsius
μm	micrometer or micron
cm	centimeter
kW	kilowatt
m	meter
mA	milliampere
mm	millimeter
MPa	megapascal
mW	milliwatt
nm	nanometer
V	volt
W	watt

LIST OF FIGURES

Chapter 1

Chapter 2

Chapter 3

Chapter 4

Chapter 5

LIST OF TABLES

Chapter 1

Chapter 2

Chapter 3

Chapter 4

PREFACE

Being the most abundant natural source of energy, solar energy is considered the future of the global renewable energy sector. However, unlike direct utilization of solar energy (for example, daylighting applications), energy-converted utilization of solar energy is limited to the low energy density of input solar radiation for the required conversion, which can be either thermal or electrical. The most straightforward approach that can be adopted to address this issue is concentrating solar radiation on a finite area using techniques of optical light concentration. Conventional light concentrators like parabolic mirrors rely on large-sized optics and produce a distant focal point. The systems thus suffer from bulkiness, low cost-effectiveness, and mounting costs. Optics size reduction and minimizing the overall bulkiness were always topics of research in the field of light concentrators.

To mitigate the limitations of conventional light concentrators, planar optics such as Fresnel lenses and mirrors emerged as compact light concentrator solutions. However, to address the issue of the focal gap, there was a need for innovative approaches rather than using imaging optics directly. In this regard, waveguide-based planar light concentrator (PLC) has evolved as the best solution, which enables a single point of energy collection, a zero focal length concept, dispersed light collection from the waveguide, and reduced sizing of the whole light concentrating system. Despite these advantages of waveguide-based PLCs, current designs face challenges including the need for precise microfabrication techniques, bulkier elements (larger width-to-length ratio), multiple optical elements with the need for precise alignments, or limited solar acceptance. Chapter 1 of the thesis will give a solid introduction to the waveguide-based PLCs, with emphasis on the geometric optics designs.

With the discussion on waveguide-based PLCs, a novel optical design featuring skewed V-groove patterns has been developed for use in low-concentration solar energy systems. The first-of-its-kind design approach differs from the existing methods in its light transport mechanism and has the following attributes: 1) Utilization of a non-sequential design (one optics element is not followed by any other) approach, employing a single optics element; this avoids the need for precise positioning of the optics 2) Low-concentration optics (less than 10X GC), eliminating the need for intricate thermal management systems; 3) A straightforward waveguide-based construction, allowing for production through a single manufacturing process; 4) Higher solar acceptance in an axis eliminating the need for 2-axis tracking; 5) A zero focal length configuration that negates the necessity for spacing

before the collectors; 6) Unidirectional light concentration design for higher concentration factor. The design and detailed mathematical model have been developed and discussed in Chapter 2. The mathematical model will be utilized as the base for the evaluation of the optics and for setting parameters and their optimization for the final simulation models.

Chapter 3 emphasized the fabrication possibilities of the SV-PLC optics with various manufacturing methods. Three different manufacturing processes are employed for the fabrication of SV-PLC optics. 1) Laser cutting, 2) Stereolithography 3D printing, 3) Injection molding. The chapter produces a thorough understanding of the different methods of fabrication, ranging from rapid prototyping to industrial-scale manufacturing. The advantages and limitations of each process have been discussed to carry the design solution from initial technological evaluation to mass production.

The SV-PLC optics evaluation has been conducted in Chapter 4. The different fabrication routes have been evaluated using optical microscopy and direct light transmittance measurement. The simulation models have been developed based on the mathematical modeling in the COMSOL Multiphysics Ray Optics platform. The optics simulation models were used to accurately predict the performance of SV-PLC. The optical efficiency and final light concentration were analyzed as performance indicators. Two-dimensional simulation is used to gauge the effectiveness of SV-PLC and expanded to 3D simulations for the analysis of angular acceptance along an axis. The SV-PLC optics fabricated with the best manufacturing route were experimentally evaluated using an amorphous silicon solar cell, under both standard conditions and direct solar radiation.

Chapter 5 discusses and demonstrates a novel Building Integrated Photovoltaic glazing concept using SV-PLC optics, which integrates active dynamicity and power generation in a single platform. The technology utilizes SV-PLC as the energy-generating component, which is integrated with optofluidics to attain active dynamism. The refractive index matching technique between SV-PLC optics and optofluid is used to create the dynamism in the window. The window solution works in two modes: 1) Power generating opaque mode with privacy and 50 % diffuse daylighting, and 2) Transparent mode without privacy and 90 % direct light transmittance for daylighting.

Finally, the thesis will be summarized and discussed in future research and development possibilities in Chapter 6.

Chapter 1

Introduction & Literature Review

1.1 Introduction

1.1.1 Light concentrators: From sun to stable light sources

Being the most abundant natural source of energy, solar energy is considered the future of the global renewable energy sector. However, unlike direct utilization of solar energy (for example, daylighting applications), energy-converted utilization of solar energy is limited to the low energy density of input solar radiation for the required conversion, which can be either thermal or electrical [1]. With the global expansion of urbanization, the area utilization of these solar power conversion systems and their environmental impacts are also becoming a major concern [2-4]. The most straightforward approach that can be adopted to address this issue is concentrating solar radiation on a finite area using techniques of optical light concentration [5-7]. The optical arrangement that carries out the process of increasing the energy density or intensity (W/m^2) of light to a smaller area is called a light concentrator.

The potential of concentrated solar power was marked in history around 214-212 BC when Archimedes used bronze mirrored shields to concentrate solar radiation on the invading ships [8]. The myth was later proved scientifically by Dr. Loannis Sakkas, with 60 bronze-coated mirrors to concentrate solar radiation on a ship approximately 200 ft away to catch fire [9]. Even though it all started with the myth of a defence application, the first documented utilization of concentrated solar power for energy application was marked in 1866, when Augustin Mouchout produced steam for engines with parabolic troughs [10]. He also built solar concentrator systems, such as solar pumps and solar ovens, during the same period of the 1860s and 1870s [11]. From there, light concentrators have shown immense potential for application in light energy control or management. Within the class of solar concentrators, various potential optical design solutions have been identified, including central receiver heliostats [12], Fresnel lenses and mirrors [13, 14], and others [15]. Modern optics demand more compact technologies, such as micro-optics-based [16] or waveguide-based systems [17], to reduce the size of optical elements and eliminate the need for focal gaps, making them adaptable to built environments like buildings [18-20], vehicles [21], and others.

Current era utilizes light concentrators for a wide domain such as for energy [22-24], agriculture [25, 26], instrumentations such as microscopes [27] and solar simulators [28],

architectural lighting [29], medical applications [30], UV treatment [31], cameras [32], displays [33]. Thus, the prospectus of light concentrators is not limited to outdoor solar energy applications. Solar concentrators differ from other artificial light concentrating systems in aspects of their incoming light spectral range and the angle of light incidence. Sun, as a light source, has parallel light rays (considering the major direct normal irradiance), but with varying light incidence throughout the day and seasons [34]. Due to this varying angle of light incidence, solar trackers are incorporated with many of the light concentrating systems, which have low solar angular acceptance (or solar acceptance) [35]. Artificial light, like LEDs, bulbs, and lamps, on the other hand, is static but spreads light rays, and needs to have other optical arrangements to make the light a parallel source. The solar irradiance constitutes 52%-55% of the near-infrared (NIR; >780 nm) region, 42%-43% of the visible light (380-780nm), and 3%-5% of the ultraviolet (UV; <380 nm) region [36]. The spectrum of artificial light depends on the application. For example, lighting application requires only the visible region of the spectrum; hence, LED sources are mostly used, whereas applications like solar simulators require a wide spectrum, hence, sources like Xenon lamps are used.

1.1.2 Light Concentrators: The system selection

Light concentrators essentially consist of an optical element (geometrical, luminescent, or diffraction-based) of an area (A_1) that can collect and confine the incoming light irradiation of a specific energy density ($E_{concentrator}$) to a much smaller area (A_2) of a light receiver, thereby increasing its energy density ($E_{receiver}$) with an energy loss (e_{loss}), as represented in Figure 1.1.

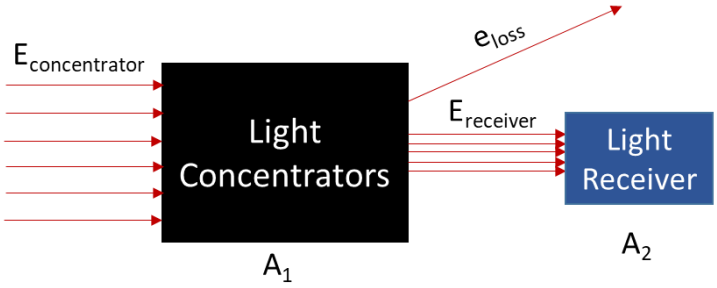

Figure 1.1. Schematic representation of light concentrators.

The selection of a light concentrator system for solar applications depends on the performance features and size constraints as follows:

Geometric Concentration Ratio (GCR)/ Geometric Concentration (GC): It is the ratio of the light concentrator area or inlet aperture area (input area) to the light receiver area (concentrated light output area). It gives the direct correlation of the final energy density, excluding the losses, providing the design merit.

$$GC = \frac{\text{Input area}}{\text{Output area}} \tag{1.1.1}$$

According to the GCR value, the light concentrators are classified into three [37]:

Low-concentration systems: Typically having a GCR of 1 to 10

Medium-concentration systems: Typically having a GCR of 10 to 100

High-concentration systems: Typically having a GCR > 100

Optical efficiency (OE): This is a merit value that determines how much light energy (for the concerned spectral range) is transported from the inlet aperture to the final output area. OE encompasses the merits of different optical elements, optical material efficiency, and system fabrication efficiency. It is the ratio of the power of radiation received at the receiver to that of the light concentrator. It incorporates the loss of energy in the system.

$$OE = \frac{\text{Output power}}{\text{Input power}} = \frac{E_{receiver}}{E_{concentrator}} = \frac{\int_{\lambda_{min}}^{\lambda_{max}} E_{out}(\lambda).d(\lambda)}{\int_{\lambda_{min}}^{\lambda_{max}} E_{in}(\lambda).d(\lambda)} \tag{1.1.2}$$

E_{out} (λ) measures the output energy of the photons that can be obtained from the output plane, and E_{in} (λ) measures the input energy of the system. λ_{max} and λ_{min} denote the maximum and minimum wavelengths of the concerned spectral coverage.

Final concentration ratio (FCR)/Final concentration (FC): This is the final performance factor of the whole concentrator system; i.e., the ratio of the intensity of the output radiation (at the receiver) to that at the light concentrator. It is the product of GC and OE.

$$FC = GC*OE \tag{1.1.3}$$

Acceptance angle: The acceptance angle of a system refers to the incident light angular range up to which the performance (OE) of the concentrator does not degrade to a required

percentage limit. The acceptance angle value is only used for dynamic light sources like solar rays or systems where the concentrator changes its position/ orientation with respect to the radiation direction.

Spectral selectivity: It refers to the spectral range in which the concentrator works reliably. For light concentrators that work on optical phenomena such as diffraction, fluorescence, or total internal reflection (TIR), spectral selection is voluntarily utilized or involuntarily happens.

Spatial distribution: This represents the uniformity (of both spectrum and intensity) of the final radiation received at the receiver end.

Physical features and constraints of the concentrator and the receiver: The selection of the concentrator design depends on the FC and projected area of the concentrated light. Upon application, the physical constraints such as the shape constraints of the receiver and concentrator, tracking possibilities, maximum focal length, and scope of receiver cooling need to be considered [38-40].

1.1.3 Light energy and optical phenomena

Light energy, being an electromagnetic radiation, possesses energy and delivers the fastest mode of energy transfer. The interaction and transfer of light energy through materials and medium interfaces depend on both the material's optical properties with the specific electromagnetic radiation, the material's surface properties, and the light incident conditions. The different light matter interactions that can occur are [41]:

1. Absorption: In absorption phenomena, a specific range of wavelengths will be absorbed by the material, which is near the energy levels of electrons in the matter. The absorbed electromagnetic energy will either heat the material or be re-emitted. The absorption coefficient (extent to which light of a particular wavelength is absorbed) of the material, along with the path length of the electromagnetic radiation in the material, determines the absorbed energy.
2. Reflection: Reflection is the phenomenon of bouncing back incident electromagnetic radiation to the same medium from a surface. Reflection can be of two types:

a. Specular reflection: Types of reflection that occur in polished surfaces, where parallel light beams sustain the continuity after reflection, as shown in Figure 1.2a. The governing

law (Law of reflection) states that the angle of reflection (θ_r, angle made by reflected light ray with the normal to the surface) will be equal to the incident angle (θ_r, angle made by incident light ray with the normal to the surface).

b. Diffuse reflection: Diffuse reflection occurs at irregular surfaces where light rays do not follow a regular direction, but scatter after reflection.

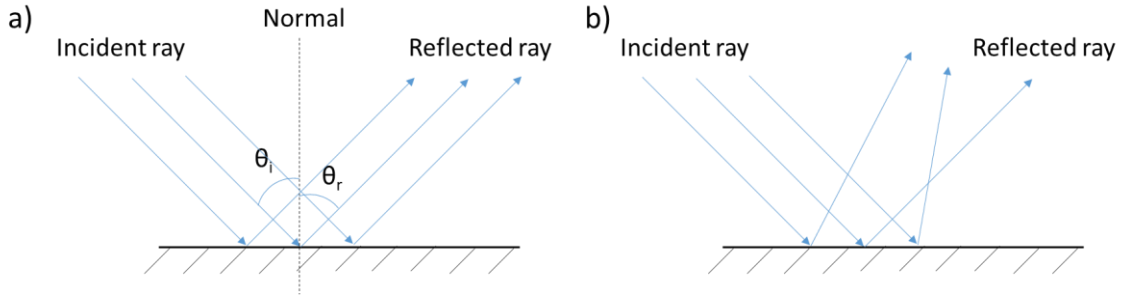

Figure 1.2. Schematic showing ray direction in a) Specular reflection and b) Diffuse reflection.

3. Refraction: In refraction phenomena, light tends to deviate from its original direction at the interface of two media with different refractive indices, as shown in Figure 1.3. Snell's law of refraction determines the directional change that occurs, and is as follows:

$$\frac{\sin\theta_i}{\sin\theta_t} = \frac{n_2}{n_1} \tag{1.1.4}$$

If $n_2 > n_1$, light is directed towards the normal to the interface, and if $n_2 < n_1$, light is directed away from the normal.

During refraction, i.e., when light travels from one medium to another, not all of the light energy will be transmitted; some part will be reflected, known as Fresnel reflection.

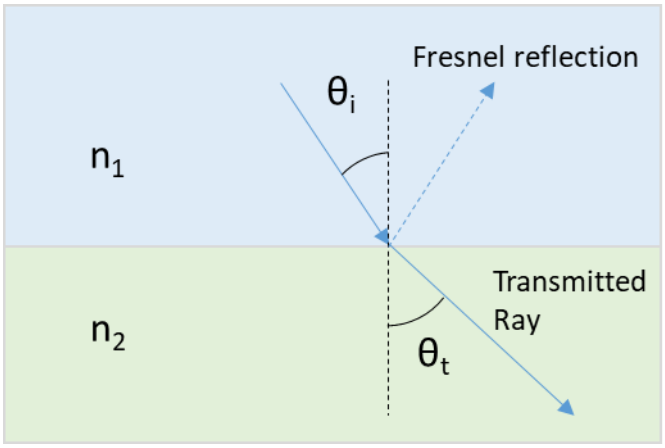

Figure 1.3. Schematic showing ray direction in refraction.

By Fresnel Law,

$$t_{\perp}=\frac{2n_1\cos\theta_i}{n_1\cos\theta_i+n_2\cos\theta_t} \tag{1.1.5}$$

$$t_{\parallel}=\frac{2n_1\cos\theta_i}{n_1\cos\theta_t+n_2\cos\theta_i} \tag{1.1.6}$$

where $t_{\perp}$ and $t_{\parallel}$ are Fresnel light transmission coefficients for s and p polarized light, respectively. From that, we have the final transmittance value for s ($T_{\perp}$) and p ($T_{\parallel}$) polarized light as:

$$T_{\perp}=\frac{n_2\cos\theta_t}{n_1\cos\theta_i}|t_s|^2$$

$$\Rightarrow \quad T_{\perp}=\frac{4n_1\cos\theta_i * n_2\cos\theta_t}{[n_1\cos\theta_i+n_2\cos\theta_t]^2} \tag{1.1.7}$$

$$T_{\parallel}=\frac{n_2\cos\theta_t}{n_1\cos\theta_i}|t_p|^2$$

$$\Rightarrow \quad T_{\parallel}=\frac{4n_1\cos\theta_i * n_2\cos\theta_t}{[n_1\cos\theta_t+n_2\cos\theta_i]^2} \tag{1.1.8}$$

Figure 1.4 shows a typical reflectance and transmittance graph for an air-glass interface (RI of glass is taken as 1.5). As shown, the s-polarized light will have reduced transmittance upon the increase in the angle of incidence. The decrease in transmittance is prominent after a certain value (in the graph, it is around 52°) of angle of incidence. However, the p-polarized light tends to behave differently. Upon an increase in angle of incidence, there will be an increase in transmittance, up to a point (Brewster's angle) where there will be 100% light transmittance, and after that, there will be a sharp reduction. In totality, the light transmittance will be reduced with the angle of incidence, which will be prominent with higher values of angle of incidence.

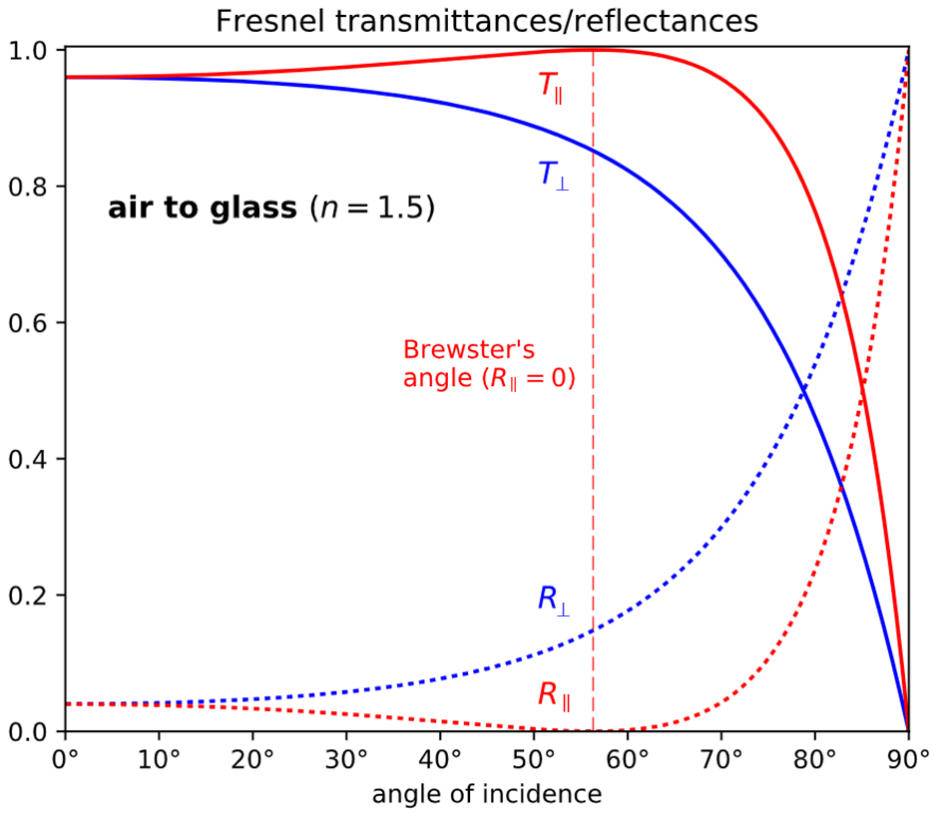

Figure 1.4. The typical reflectance and transmittance vs angle of incidence plot for an air-glass interface. Source: Original by Sbergjohansen (CC-BY-SA 4.0).

4. Total Internal Reflection (TIR): TIR is a light reflection phenomenon (Figure 1.5) that occurs when light travels from a higher to a lower RI material, where the incident light angle (θ_i) is higher than a critical angle (θ_c). TIR is considered to be a perfect reflection, where 100% of the light is reflected back to the denser medium at the interface.

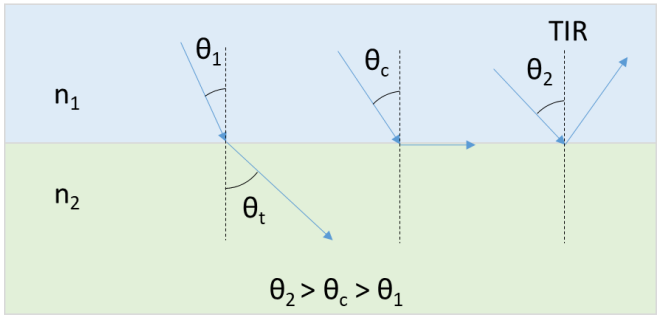

Figure 1.5. Schematic showing the principle of TIR.

Figure 1.6 shows a typical reflectance and transmittance graph for a glass-air interface (RI of glass is taken as 1.5). As shown, the graphs tend to show a similar profile up to a certain angle of incidence. After that, 100% of the light will be reflected, which marks the point of critical angle for TIR.

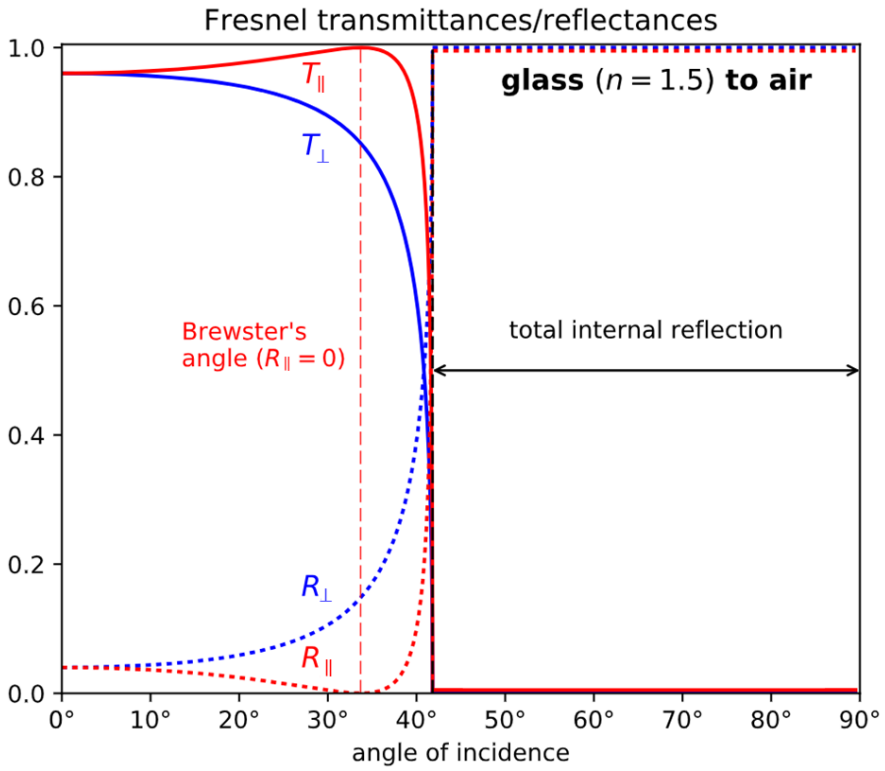

Figure 1.6. The typical reflectance and transmittance vs angle of incidence plot for a glass-air interface showing the point of TIR. Source: Original by Sbergjohansen (CC-BY-SA 4.0).

5. Diffraction: Diffraction occurs when electromagnetic waves are passed through an obstacle or aperture, where the line of propagation of the waves changes its direction

without any energy loss. Diffraction is wavelength-dependent, and the size of the obstacle or aperture should be smaller than the concerned wavelength.

6. Photoluminescence [42]: It is light emission caused by light irradiation on a material, where the material has the property to emit radiation at a different wavelength. Upon irradiation, the material will have the excitation of electrons into states with a higher energy, from where the radiative decay (i.e., attaining a lower energy state through radiation) will happen. When the decay time is up to milliseconds, it is called fluorescence; otherwise phosphorescence.

1.1.4 Optical methods for light concentration

Optical methods for light concentrators include any optical arrangement that utilizes the different optical phenomena to concentrate light rays to a smaller area, increasing the energy density. Based on the basic principle of light concentration, the methods are classified as:

1. Reflective imaging concentrators: These types of concentrators use the principle of imaging reflective optics, where reflective objects such as parabolic troughs [43], dishes [44], etc., concentrate light to a focal point, where it is collected.
2. Reflective non-imaging concentrators: These types of concentrators use non-imaging optics, where the direction of individual rays is dispersive, rather than focusing to a point. Optics such as Fresnel reflectors [45], hyperboloid [46], compound parabolic concentrators [47], etc., are utilized for this.
3. Refractive imaging concentrators: These types of concentrators use imaging optics based lens systems, such as convex lenses [48], Fresnel lenses [49], microlenses [50, etc., to concentrate light to a finite area.
4. Hybrid concentrators: Hybrid concentrators use multiple stages of optical arrangement for light concentration, where the primary aim is to reduce the bulkiness of the system. Some of such systems include the refractive (microlens)-reflective (imaging) type [51], reflective-waveguide [52], refractive-waveguide (TIR or mirror or dispersive) [53-56], diffractive optics-waveguide [57], etc.
5. Luminescent concentrators: These types of concentrators contain luminescent material dispersed in/ coated on a planar optical matrix. Light of a specific wavelength emitted from the luminescent material will be transported through TIR within the matrix and concentrated to the lateral side of the optical matrix [58, 59].

1.1.5 Planar Light Concentrators (PLC)

Conventional light concentrators like parabolic mirrors rely on large-sized optics and also outline the requirement of distance for the focal point [60]. The systems thus suffer from bulkiness, low cost-effectiveness, and mounting costs. Optics size reduction and minimizing the overall bulkiness were always the topics of research in the field of light concentrators [61]. The maturation of innovative design concepts in light concentrators (predominantly solar concentrators) for different end applications has been marked throughout their historical development [62, 63]. However, the system selection is always done according to the required output and receiver specificities [6]. Thermal energy conversion systems typically utilize a single receiver system from multiple or single optics elements, creating high energy concentration for applications like thermal power plants/ water heating [64, 65]. However, for applications such as Concentrated Photovoltaics (CPV) and daylighting, low (<10X) and medium (10X to 100X) concentration optics can also be beneficial, with multiple receivers [51, 66]. Apart from that, the utilization of such systems in built environments such as buildings [18, 19] and vehicles [21] requires compact optics and less overall bulkiness.

To mitigate the limitations of bulky imaging optics-based systems [65, 66] for light concentrators, planar optics such as Fresnel lenses and mirrors emerged as compact light concentrator solutions [13, 38, 67, 68]. However, to address the issue of the focal gap, there needs to be innovative approaches rather than using imaging optics directly. A similar approach of multiple collector systems has created designs such as the multiple lenses/microlenses, which still reduced the bulkiness [69-74]. However, the collection of energy from multiple points and aligning the optical elements became very crucial in these designs. Also, the system size is much larger than the optics size due to the focal length.

In this regard, waveguide-based PLC has evolved as the best solution, which enables a single point of energy collection, dispersed light collection from the waveguide, and reduced sizing of the whole light concentrating system [75, 52]. Recently, PLC technology has been well acknowledged globally, and many research efforts have been put forward to develop new designs and material solutions, indicating the prospect of CPV technology. Recognizing its importance, the US Department of Energy acknowledged the potential of waveguide-based PLC through the Advanced Research Projects Agency-Energy (ARPA-E) project in 2016 [76].

1.1.6 Waveguide-based PLC

The waveguide-based PLC has made a leap forward for light concentrator technologies with its innovative concept of zero focal length [77]. The current waveguide-based PLC essentially consists of a planar (shape can be extended from flat plate to circular, or other shaped, with regular or irregular cross-section) light-guiding element, enabling light transport through reflection at surfaces through TIR or mirror reflection. The condition of light transport is determined by the primary optics, which enable the amount and nature (spectral selection) of light output, which is collected from the lateral face. Figure 1.7 shows the schematic representation of typical conventional light concentrators and waveguide-based PLC, showing their distinction [77].

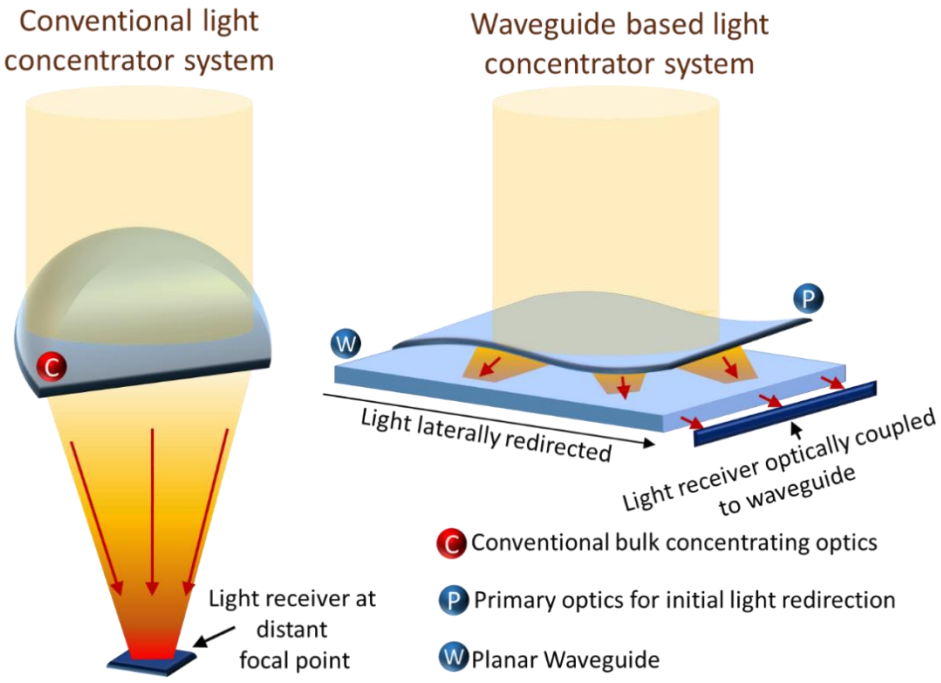

Figure 1.7. Schematic representation of typical conventional light concentrators and waveguide-based PLC. Source: Reproduced with permission from [77]. Copyright © 2022, Elsevier.

1.1.6.1 Classification of waveguide-based PLC

Within the last two decades, the field of waveguide-based PLC has evolved from geometric optics integration to optical material integration, such as luminescent solar concentrators (LSC) [78, 79], and nano-design solutions for diffraction-based PLC [80]. The utilization

of waveguide-based PLC for CPV has huge applicability due to its lower cost per energy. Figure 1.8 shows the classification of waveguide-based PLC technologies [77]. Depending on the primary optics, they are classified as geometric optics-based PLC (which utilizes reflective and refractive elements for light concentration and is coupled to the waveguide), LSC (which utilizes luminescent molecules for light concentration with spectral selectivity), and diffraction optics-based PLC (which use diffraction gratings for light redirection and spectral selection).

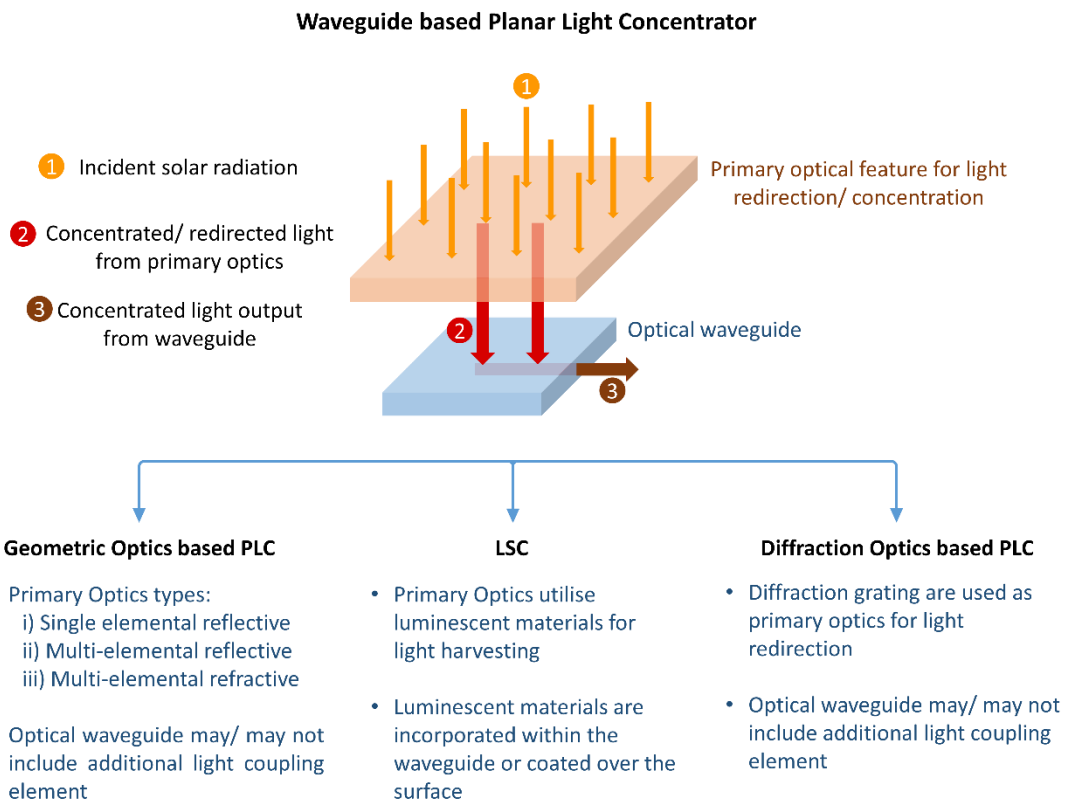

Figure 1.8. Representative scheme of waveguide-based PLC with its classification. Source: Reproduced with permission from [77]. Copyright © 2022, Elsevier.

In geometric optics-based PLC, the primary optics can redirect and concentrate light in planes of specific size and number using multi-modes of reflection, refraction, and TIR. The initially focused/directed light can be either directed directly to the waveguide or specific optical features inside/ outside the waveguide, for light redirection towards the plane of concentration. The planar light guiding element can be attached to the primary optics as a single unit or can be separated with additional optical features of light transport. Guiding the light within the element can be achieved mostly with TIR, except for reflecting surfaces. The definitive optical design vouches for the GC factor, OE, and acceptance

angle. Diverse approaches have been carried out for geometric optics-based PLC based on the mode of operation, such as microlens-dispersive element combination, and reflective surfaces (detailed in the Geometric Optics-based PLC section).

An LSC is a device that harvests light using a linear down-conversion/non-linear up-conversion process that uses luminophore materials that are either dispersed within or coated (with/without additional host material) over a transparent waveguide matrix. However, in practice, down-conversion-based LSC is primarily adopted to develop high-efficiency LSC-based CPV devices. The concept of utilizing down conversion for LSC was first put forward by Weber and Lambe in the 1970s, and within the last two decades, further developments have been encountered with the new classes of luminescent and transparent host matrix materials [81, 82]. In LSC, the transparent matrix serves as an optical waveguide for redirecting and concentrating solar radiation to the lateral face where a solar cell is attached. The approach of LSC-based PLC is mostly used for developing Building Integrated Photovoltaics (BIPV) glazing elements. Since fluorescence is the major optical down-conversion phenomenon utilized in LSC, in which highly emissive fluorophores are incorporated in the host matrix, it is also commonly termed a fluorescent concentrator. During the course, LSC has gained significant attention as a key driver in the research and development of photovoltaic systems, owing to its improved spectral response, economical approach, and potential to offer enhanced power conversion efficiency (PCE) of solar cells [81-84]. In comparison with the other concentrating PV systems, LSC eliminates the complexity of the adoption of efficiency-boosting techniques such as optics and tracker systems and the difficulties associated with the module assembly. This becomes possible due to the flexibility offered by the LSC, as it works under every solar angle and also collects diffuse light, thereby acting as an enabler for developing innovative technologies for building integrated applications. In recent years, LSC acquired a unique position in the BIPV sector as a viable, promising solar technology for glazing elements, due to its lower cost and improved aesthetic values compared with existing glazing solutions [85]. The relatively low-cost transparent plastic matrix materials (like Poly(methyl methacrylate) (PMMA)) can considerably reduce the area cost of the existing BIPV glazing solutions, offering a low cost per energy generation [82]. Hence, the LSCs are a revolutionary solar energy technology in the building architecture by facilitating semi-transparent, electrodeless PV glazing systems without diminishing the aesthetic value of the buildings and the standard of living of the indwellers. Large-scale applications, such as windows with

colored as well as transparent LSCs, can be easily accommodated to add visual comfort or daylight inside the buildings accordingly. Accounting for these benefits and the ease of 'invisible' integration of PV into urban structures to generate electricity and preserve the aesthetic and functional aspects, LSC can get wide public acceptance in the near future [58].

Diffraction is a phenomenon based on the wave theory of light, which splits the different wavelengths of light present in a polychromatic light source. While discussing the waveguide-based solar concentrators, several PLCs have been designed based on the diffraction and light interference principle. Diffraction-based concentrators are dominantly dependent upon the brightness theorem, which governs the order of diffraction and diffraction efficiency [86, 87]. The holographic technique is the most commonly used fabrication technique for diffraction gratings in bulk planar materials. Planar waveguide-based diffraction solar concentrators use holograms or diffraction gratings alone or in combination with Fresnel lenses or conventional lenses for redirecting and focusing the light to the waveguide, to concentrate light on the lateral face. One of the key selling points of the diffraction-based planar concentrator is its ability to concentrate the light with spectral selectiveness, utilizing the varied diffraction angle for different wavelengths. The basic working element of a diffraction-based PLC includes a diffraction grating that diffracts light with respect to the wavelength at an angle (diffraction angle), which can be altered by making a variation in the grating period and grating thickness. Unlike any other PLC, diffraction grating-based PLC can be developed as an ultra-thin element with less bulky systems, adding to its advantage of low weight and cost.

When analyzed, the lower solar acceptance angle poses a severe drawback for geometric optics-based and diffraction-based PLCs, limiting their adaptability in built environments with limited room for solar tracking. Hence, it is observed that LSC-based PLCs are more explored for Concentrated Photovoltaics (CPV) systems for BIPV applications (glazing solutions) due to their simple architecture, unconditional solar acceptance, ability to collect diffuse radiation, and the possibility of aesthetic improvements. However, the reported PCE and OE for LSC-based CPV systems seem to curb the enthusiasm. Hence, vigorous efforts on optical materials screening and development in conjunction with system design modulations are necessary for LSC-based CPV systems in the future. The involvement of multi-mode light collection approaches, for example, integrating LSC with geometrical/diffraction optics, is a promising approach to improve the system efficiency.

Further, it is observed that the current status of research is limited to lab-scale demonstrations, with very few successful on-field deployments. Hence, future research directions can be streamlined to cater to standard glazing size with required material stability, mechanical strength, and thermal characteristics to enable faster technology commercialization. When comparing the size of optics, diffraction-based systems offer very thin optics elements; however, the system is only beneficial if it is required to screen the incoming radiation, such as for connecting to Dye-Sensitized Solar Cells (DSSC). However, when comparing the implementation potential, geometric optics-based systems are more explored because of their higher GC, OE, broad spectral selectivity, low degradation factors, and economic viability. The general features of the different technologies are tabulated below in Table 1.1.

Table 1.1. General features of different waveguide-based PLC technologies.

Features	Geometric Optics	LSC	Diffraction Optics
GC	Low (<10X) to High (>100X)	Low (<10X) to High (>100X)	Low
OE	Depends on the system (>80% can be achieved)	Very low (<10%), since it is spectrally selective	Very low (<10%), since it is spectrally selective
Spectral Selection	Broad band	Narrow selection	Design depended on selection
Acceptance angle	Usually low (<10°); but acceptance can be achieved in a single axis (<60°), depending on the design	Very high (since it is not directionally dependent)	High (achieved 30° to 100°)
Diffuse light collection	Low (since it is directional)	Very high	High (since the acceptance angle is high)
System Degradation	Low (since it depends on the optical phenomena	High (since it depends on the	Low (since it depends on the optics

	such as refraction, reflection, etc.)	luminescent material stability)	arrangement rather than material property)
Cost	Depends on the design and material used. The conventional commercial systems uses expensive optical elements like mirrors and require heavy mounting structures.	Cost depends on material in use. One typical value is 5$/m^2 [88]. LSC is cost effective when implemented in built structures, such as buildings.	Consider cheaper, one typical value for CPV is 1$/W [89]. However, these types of solar concentrators are less explored .

Comprehending the advantages offered by Geometric Optics-based PLC systems, they can be considered a more straightforward approach to implementing PLC technologies for various applications in the future.

1.2 Literature Review

1.2.1 Geometric Optics-based PLC

To evaluate and select the method of designing a geometric optics-based PLC (with waveguide design), the following classification is made:

1.2.1.1 Refraction-based designs

Generally, refractive-type PLC systems consist of an array of convergent lenses (microlenses), and the output light rays from the lenses are connected optically with a light dispersive/coupling element (gratings, prisms, or scattering surfaces) in a light-guiding layer. The multiple light dispersive elements (usually air prisms) in the light-guiding layer, positioned in line with the incoming concentrated light, disperse the light and are guided by the guiding layer to the receiver at the lateral face. By using planar slab waveguides, the length of the concentrator can be extended unlimited, but the system suffers from decoupling losses that can occur at the subsequent coupling elements (as shown in Figure 1.9b) [16]. The decoupling loss is directly correlated to the coverage area of the coupling element. To eliminate the decoupling losses, the guiding layer can be converted to wedge-shaped, eliminating the process of multiple TIR within the guiding layer (Figure 1.9a) [16,

90]. However, the aspect ratio of the wedge-shaped guiding layer limits its usage for longer-length concentrators.

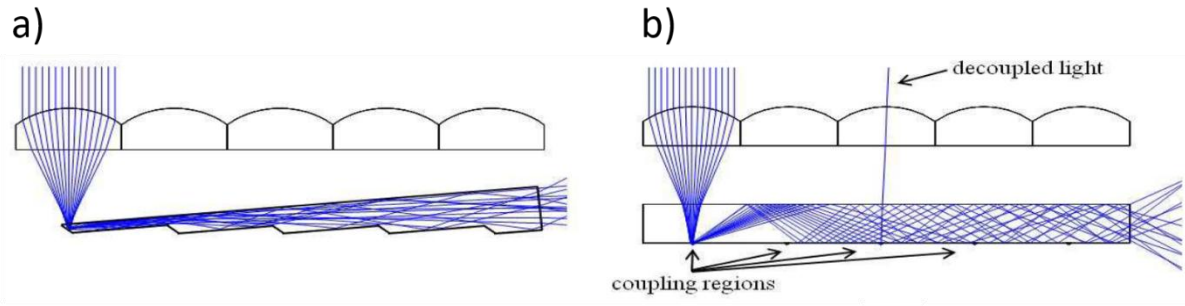

Figure 1.9. Ray tracing in a refractive type PLC with a) a wedge-shaped light guiding layer to avoid decoupling loss and (b) a uniform planar light guiding layer showing decoupling loss. Source: Reproduced with permission from [16]. Copyright © 2010, OSA.

Figure 1.10 shows the typical geometrical features of a micro lens-based PLC (with planar light waveguiding) system, where H and L are the width and length of the waveguide, P denotes the position of the lens, 2r is the lens diameter, and φ is the ray propagation angle.

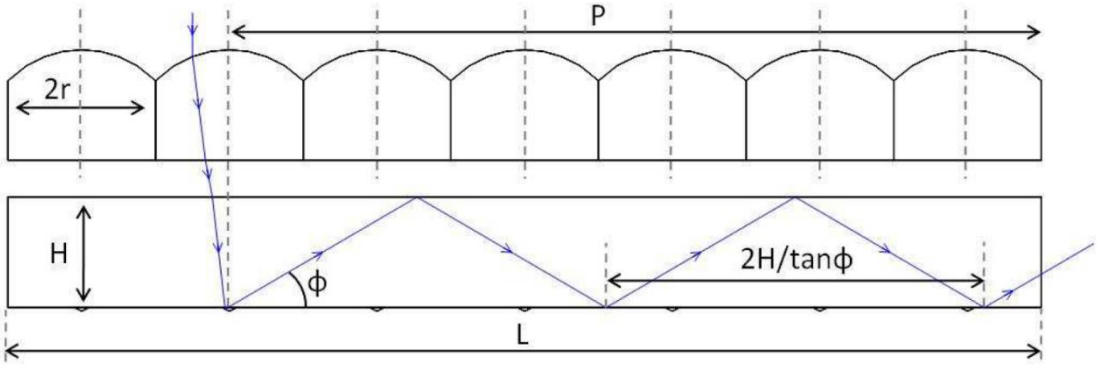

Figure 1.10. Geometric features in a lens-based refractive type PLC. Source: Reproduced with permission from [16]. Copyright © 2010, OSA.

To calculate the total efficiency, Equation 1.9 denotes the OE from input position P, which includes the back surface interactions, where C_{lens} is the concentration of the primary lens. Equation 1.10 includes the efficiency factor with Fresnel reflection loss (R) and material absorption, where α is the absorption coefficient of the matrix material. Equation 1.11 denotes the total efficiency, integrated over all coupled ray angles confined within the waveguide. The equation denotes that the efficiency has a direct correlation with the width

and length of the concentrator, i.e., a combination of higher length and width yields higher efficiencies.

$$\eta_{decouple}(P,\phi) = \left(1-\frac{1}{C_{lens}}\right)^{\frac{P\tan\phi}{2H}} \tag{1.1.9}$$

$$\eta_{position}(P,\phi) = (1-R)\,\eta_{decouple}(P,\phi)e^{(-\alpha P\cos\phi)} \tag{1.1.10}$$

$$\eta_{total} = \frac{\sum_P \int_\phi \eta_{position}(P,\phi)}{(L-r)/_{2r}},\ P = r,3r,5r,\ldots,(L-r)/2r \tag{1.1.11}$$

Tremblay et al. fabricated 120° apex symmetric prisms to collect the rays coming out at 60◦ to the horizontal, making no shadowing effect with adjacent prisms [16]. Also, certain parts of rays deviating more from the primary lens optics undergo TIR and travel to the lateral face (Figure 1.11a). For aligning the two optics, a self-aligned fabrication technique was used, which utilizes UV light that focuses light from the primary spherical lens to cure the polymer prism, which is already embossed with the pattern. Thus, the need for optical alignment is eliminated with the whole fabrication process. The fabricated prism is shown in Figure 1.11b. Optimized designs showed a theoretical light concentration of 300X with an OE of 81.9%. The major loss occurring for the optics system is the decoupling loss, and this is for a coupling region of size 78 μm. Upon increasing the size to 156 μm, there will be a reduction of 22% in the OE due to the increased decoupling loss.

Figure 1.11c shows the prototype demonstration of a whole concentrator system having a light concentration of 37.5X and 32.4% OE. The observed low OE can be attributed to manufacturing defects resulting in optical defects and faults in the lens array. Since the whole system relies on the positioning of the lens prism alignment (requires <20 μm lateral alignment and <0.01° rotational accuracy for the designed 300X concentration), the design tends to make a low acceptance angle and requires precise 2-axis tracking. The requirement of precise alignment for such systems limits their applicability in large-area optical concentrating systems and also for BIPV.

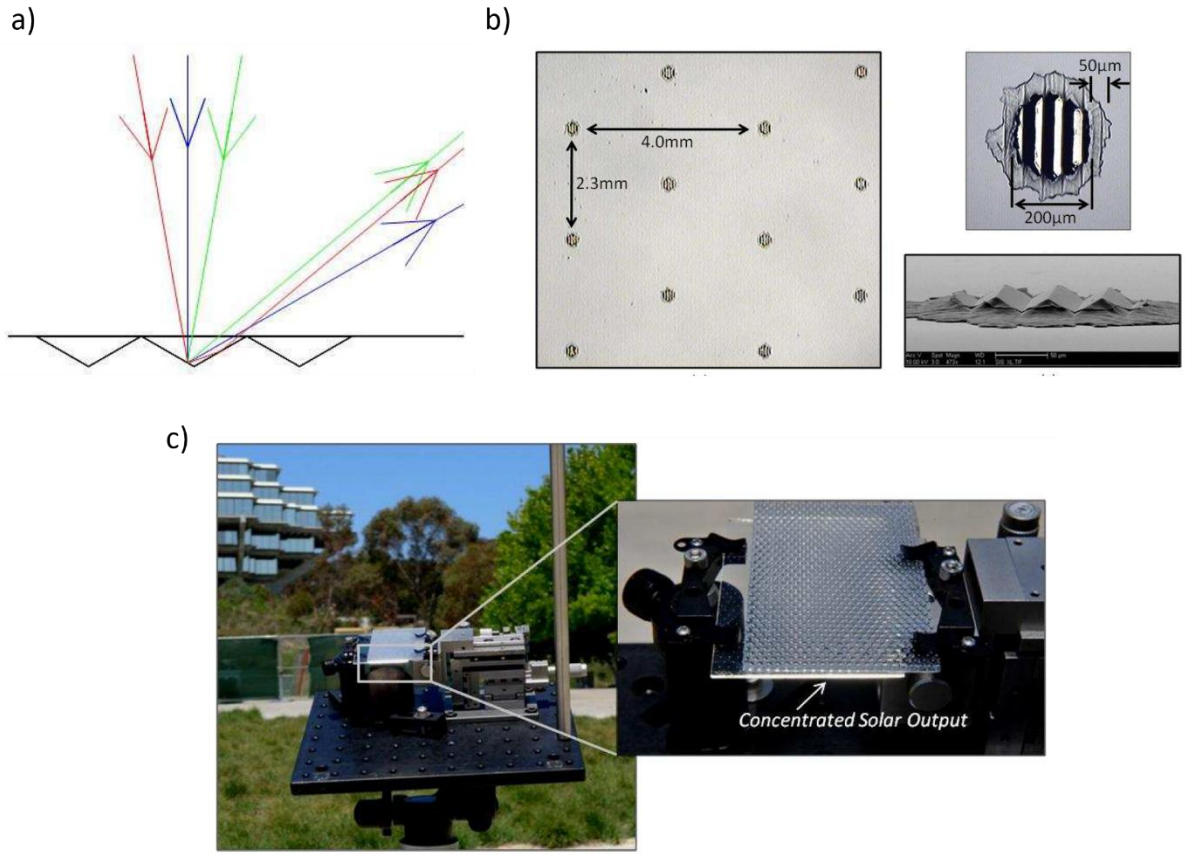

Figure 1.11. a) Possible ray pathways in a 120° apex symmetric prism showing maximum transport of light rays to the lateral side. b) Optical and SEM images of 120° apex symmetric prisms fabricated through a self-aligned fabrication technique (irregularities of 50µm are shown, causing the optical losses). c) Photographs of the prototyped refractive type PLC in outdoor settings showing light concentration when aligned properly at 90˚ to the sun. Source: Reproduced with permission from [16]. Copyright © 2010, OSA.

Bouchard et al. substituted the conventional spherical lens with a cylindrical lens, resulting in the reduction of the concentrator's cost of tracking by improving the acceptance angle in a single axis [91]. This also reduced the final geometrical concentration value. This design produces a compact, lightweight, and efficient concentrated photovoltaic system with a uniform distribution of flux and shows the possibility of low-cost roll-to-roll production. The model showed a peak concentration level of 8.1X with an OE of 80%, by conducting ray tracing using LightTools, during the daytime from 8:30 a.m. to 4:30 p.m. The proposed concentrator shows an acceptance angle of ±9◦ on the North-South axis and ±54◦ on the East-West axis.

Xie et al. also evaluated their cylindrical lens-based PLC design using the Zemax ray tracing tool [92]. The design of the concentrator is as shown in Figure 1.12, in which the light guiding layer is embedded with an air prism at the top surface as the light coupling element, and it is separated from the lens array with an air gap. At a geometrical concentration ratio of 50, the suggested concentrator system achieved 70% air prism optical couplers. Further, an acceptance of 7.5° was obtained with the utilisation of a cylindrical lens as the primary concentrator.

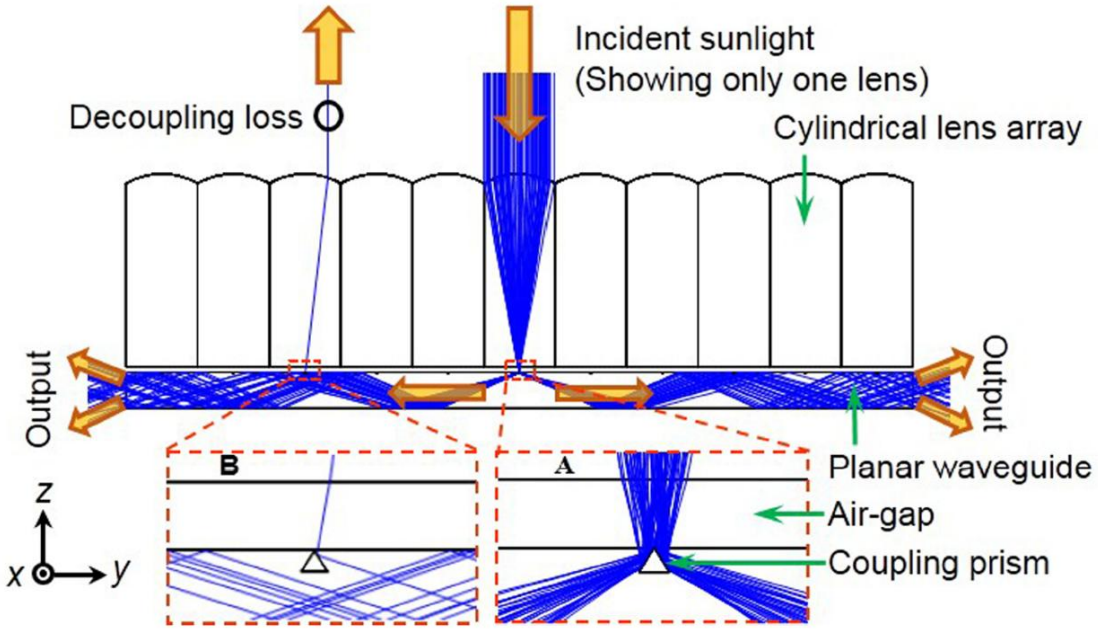

Figure 1.12. Cross-section view of the planar waveguide solar concentrator with the cylindrical microlens as primary concentrator and air prism as a coupling element, showing the ray tracing of incoming rays in a lenslet. Insets show the light coupling in the air prism (right) and the decoupling effect occurring due to TIR from the subsequent waveguide (left). Source: Reproduced with permission from [92]. Copyright © 2014, OSA.

Moore et al. presented a "stepped-shape" of injection facets (plane of couplers) based planar solar concentrator design with the major advantage of diminishing ray leakages from the waveguide, as shown in Figure 1.13 (shows two subsequent layers) [93]. The simulated design was able to transport 90% of light to reach the PV cells without undergoing any loss and achieved a geometrical concentration of 112.5X.

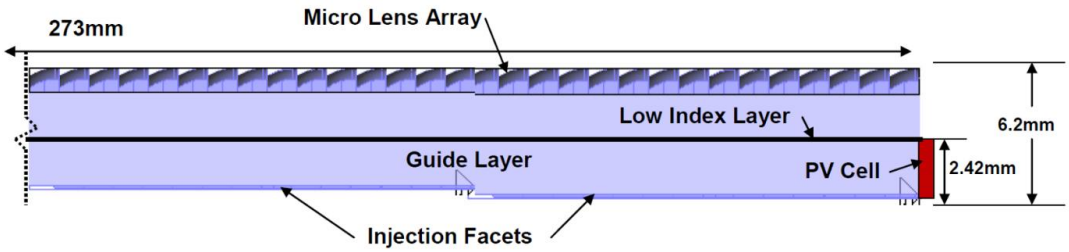

Figure 1.13. Subsequent layers of stepped planar light guides showing the offset of injection facets. Source: Reproduced with permission from [93]. Copyright © 2010, SPIE.

Apart from CPV application, the appropriateness of the usage of planar solar concentrators for the application in the natural daylighting system was investigated by Ong et al. [94]. The designed micro-optics solar concentrator is built up using a module of lens arrays and a waveguide of a planar slab structure with a uniform cross-section (Figure 1.14). The lens array concentrates light on the light couplers, which are embedded on the waveguide's bottom surface, and subsequently redirects it to the optical fibers. TIR is used to route the collected light into the planar waveguide, which is achieved by incorporating a layer between an array of lenses and a waveguide with a low index or air space. Roll-to-roll printing methods are compatible with the periodic array of lenses and constant waveguide cross-sections. The major consideration in the design of a uniform concentrator cross section is the injection of light that is focused, which should have high efficiency with minimal decoupling losses when it propagates through the length. Plain void structures are adopted in the proposed design to avoid decoupling losses caused by coupling features when redirecting light.

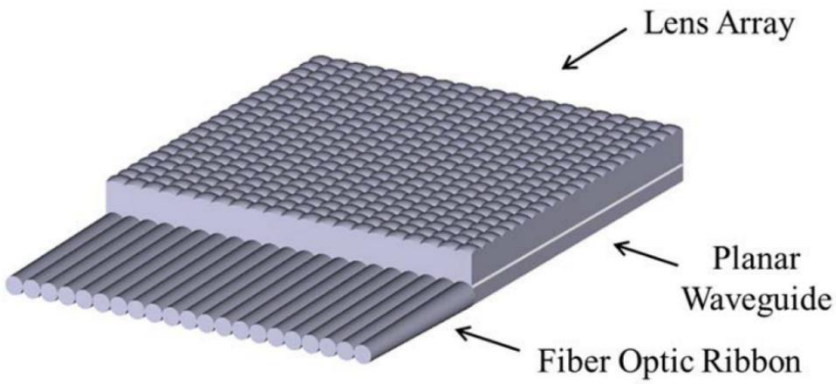

Figure 1.14. Schematic of refractive-type concentrator-based solar collector with lens array, planar waveguide, and fiber optic ribbon. Source: Reproduced with permission from [94]. Copyright © 2016, IEEE.

A simple concentrating photovoltaic system with a Fresnel lens array and double waveguide was proposed by Vu et al. [73]. The coupler prisms are coated with a dichroic mirror coating for the reflection of light with varied energy bands. The array of Fresnel lenses focuses the sunlight and redirects prisms through the upper waveguide, which has the property of reflecting the middle band of the solar spectrum, which then propagates within the first waveguide and is transported to the solar cell (GaInP/GaAs dual junction solar cell). Subsequently, the transmitting lower energy band enters the second waveguide and is reflected by the dichroic mirror-coated prism at the second waveguide to redirect to the solar cell (GaInAsP/GaInAs dual junction solar cell) of different absorption ranges. The simulation result shows that the system design has an OE of 84.02% for the middle energy band of the solar spectrum and 80.01% for the low energy band. The system has an acceptance angle of ± 0.5°.

Zagolla et al. further improved the concept of refractive-type PLC with the introduction of self-tracking within the system [95]. The design has a dichroic membrane layer that separates the solar spectrum (the visible region is reflected, and NIR (>750 nm) is transmitted). The active component of the concentrator is the actuator, which has a metal array of holes filled with black paraffin wax, the dichroic membrane layer. The paraffin wax absorbs the transmitted IR part and expands when a phase change occurs, which contributes to the actuation. Upon melting of the paraffin wax, its expansion in an upward direction occurs, thereby filling the air gap between the dichroic membrane and waveguide and converting it into a light coupler element. The direction of the expansion is constrained only in one direction by the metal holes. The formed light couplers redirect the light into the planar waveguide and propagate via TIR and reach PV cells attached to its edge. The scheme of the design and different stages of the mechanism are shown in Figure 1.15. The demonstrated system shows an effective light concentration of 3.5X over 80% of the desired acceptance angle of ±16°.

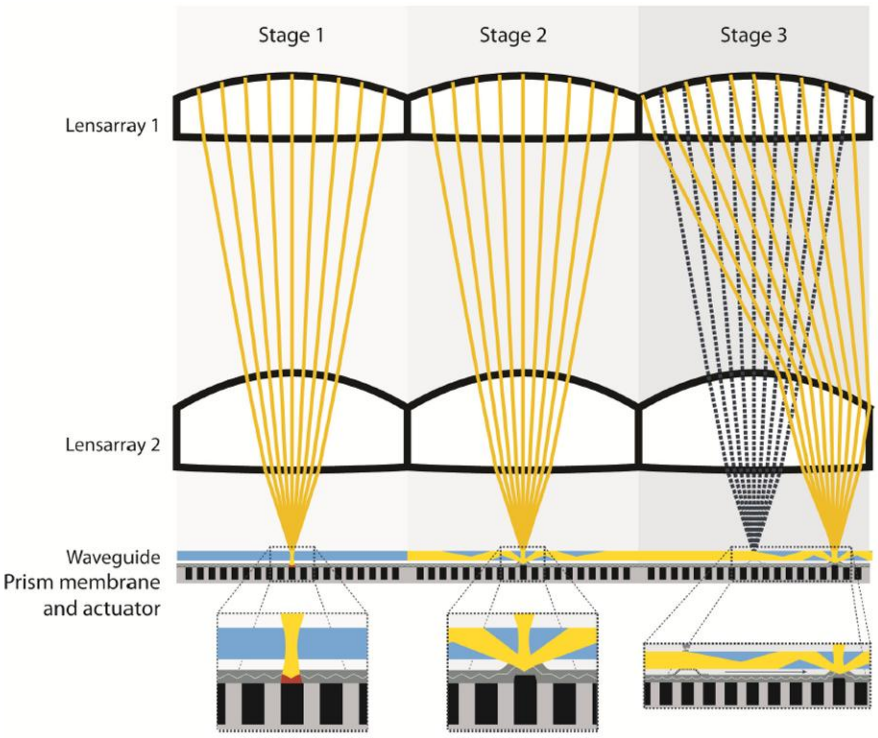

Figure 1.15. Representation of the stages in the self-tracking planar solar concentrator showing the mechanism. Stage 1: Splitting of rays by a dichroic mirror, paraffin wax absorbs transmitted light (> 750 nm), Stage 2: At the melting point of the wax, it melts and expands, converting it into a coupler to the incoming light, Stage 3: Actuation mechanism happening at the different position according to the sun's position. Source: Reproduced with permission from [95]. Copyright © 2014, OSA.

To eliminate the need for positioning the primary lens optics and coupler, Kim et al. proposed a curved light guiding layer connected optically with the multi-lens system through an optical funnel, as inspired by the ommatidium in the eye of insects [56]. The optimised design of the concentrator, as shown in Figure 1.16a, can achieve a light concentration factor up to 39 with an acceptance angle of ±15° (the concentrator design considered was about 20 cm in length and thickness under 1.1 cm). Figure 1.16b shows the light propagation with a normal and oblique angle of 40° in the designed concentrator. It has proven difficult to enhance both the angle of acceptance and the concentration factor in traditional flat concentrators. This challenge is overcome by this bio-inspired concentrator. The architecture and optical behavior of ommatidium, which is in the insect's compound eye, led to create a unique flat solar concentrator, where microlenses act as a light-gathering element. Ommatidium of insects has a transparent cornea which acts as a

lens, and a rod-like transparent cylindrical structure, which is the rhabdom. Collection of light along with focusing is done by the lens, and the rhabdom acts as a waveguide.

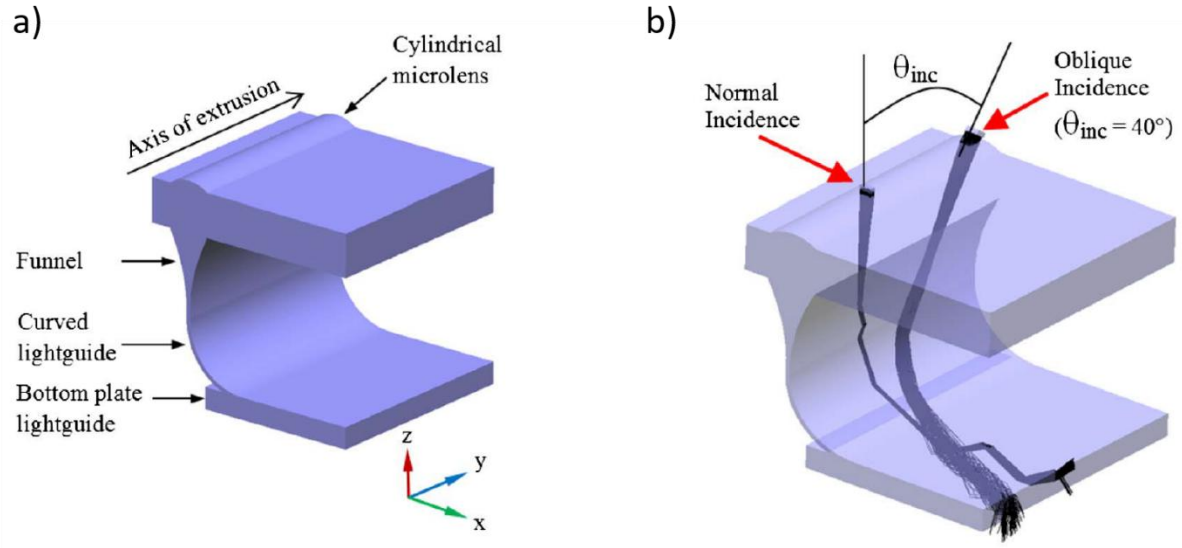

Figure 1.16. a) Schematic representation of cylindrical microlens and curved light waveguide-based refractive type solar concentrator. b) Ray tracing showing high angular tolerance of 40° in the y-z plane for light concentration. Source: Reproduced with permission from [56]. Copyright © 2014, Optical Society of America.

1.2.1.2 Reflection surface-based designs

Reflective type systems utilize either reflective mirrors/ surfaces or TIR to provide the light concentration in the optical designs. It can be designed for single-elemental or multi-elemental as follows:

1.2.1.2.1 Multi-elemental reflective type PLC

In this type, reflective surfaces are used for light redirection/concentration, which is optically distant from the waveguide, making a multi-elemental waveguide-based PLC. Much similar to the Sun Simba concentrator, a two-staged planar solar concentrator was presented by Kuo et al., which consists of transparent waveguide sheets stacked with an array of arc-segment structures (i.e., a sheet collector with arc-segment structures), as shown in Figure 1.17a [52]. An appreciable coupling efficiency with high concentration ratios and wide angular tolerance is obtained by the arc segment structures, which are carried by the stacked waveguide sheets as TIR collectors in the first stage. When light enters arc segment structures, it undergoes reflection and concentrates the light in the sheet waveguide below, where the light undergoes more of a skewed propagation. The second

stage (movable) of the system is to collect the concentrated light through light guiding channels and subsequently focus it on the solar cell placed at the end using a compound parabolic collector (shown in Figure 1.17b).

Additionally, embedded prisms of higher refractive index (taken as 1.77) are also used to reduce the skewness of the incoming light for better OE and reduced losses. The whole design is structured as a concentric circle towards the center. The incident angle has been varied from 0° to 12° to attain the angle distribution of light within ±15° for uniform light distribution to the solar cells. An average OE of 0.87 and a 738X concentration ratio were obtained from the simulation results of the designed system.

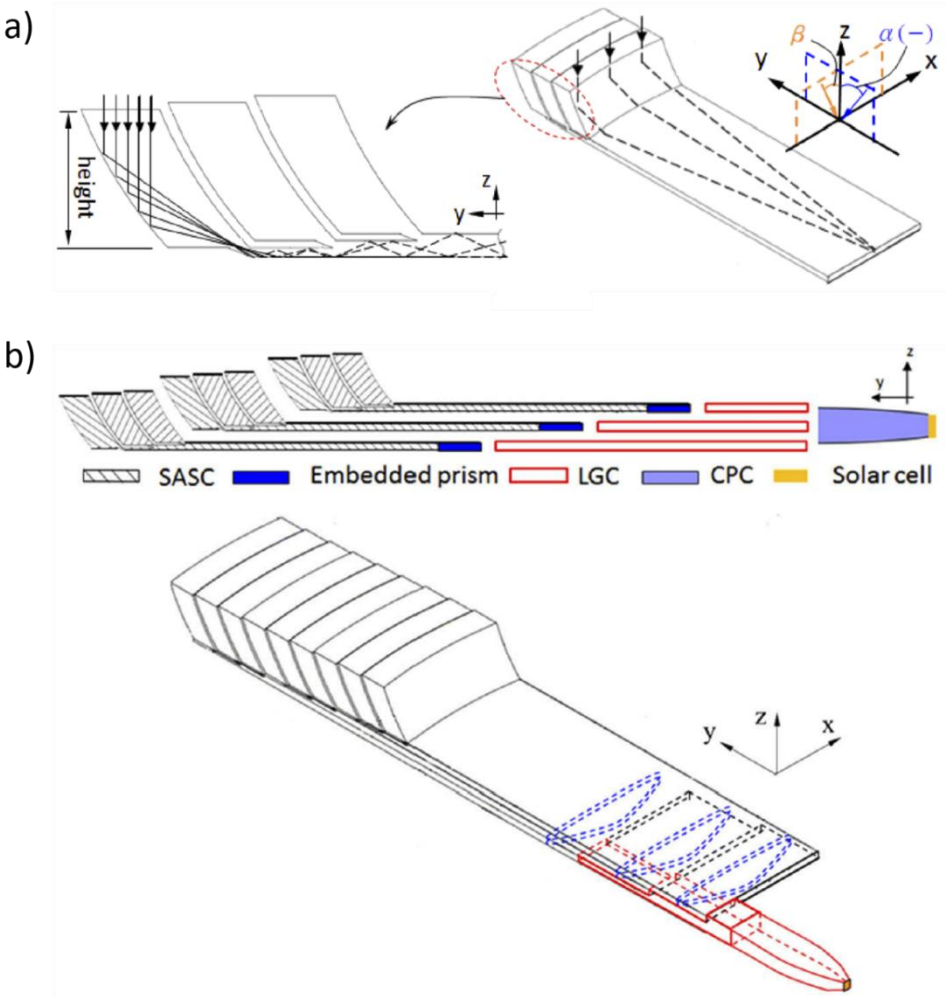

Figure 1.17. a) 2D and 3D representative ray tracing in the PLC of the sheet collector with arc-segment structures. b) Side view and perspective view of the complete stacked-up assembly of PLC with arc-segment structures (SASC), embedded prisms, light guide channels, compound parabolic collector, assembled with a solar cell. Source: Reproduced with permission from [52]. Copyright © 2020, Optical Society of America.

1.2.1.2.2 Single-elemental reflective type PLC

Here, reflective optics are incorporated within or outside the waveguide for light concentration/redirection to the waveguide. A reflective array of V-shaped grooves on a planar optical waveguide can be considered one of the most straightforward approaches for redirecting light to lateral directions. The reflection from the grooves can be either through reflective coatings or by TIR. Wei et al. proposed a planar solar concentrator with reflective arrays of V-grooves placed at the bottom of an optical slab, and in which solar cells are positioned at the edges, making a single-element compact configuration [96]. The system (scheme as shown in Figure 1.18a) essentially consists of an optically transparent material with a planar surface at the top and metal-coated (Aluminium coating with SiO_2 passivation layer, with average reflectance of 83.9% in 400-1000 nm wavelength range) reflective v-grooves at the bottom. Incident light falling on the system is reflected by the grooves and directed to the solar cells placed at the top portion of the lateral side of the concentrator, as shown in Figure 1.18b.

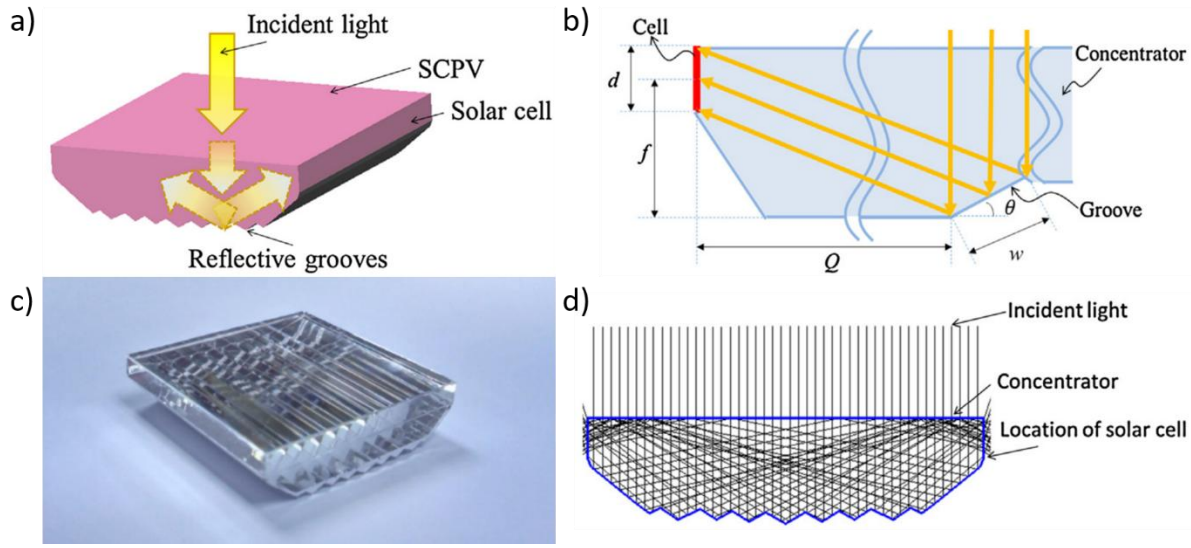

Figure 1.18. a) Schematic of the V-groove PLC. b) Schematic of the ray trajectories of light rays incident on the V-groove surface. c) Photograph of fabricated V-groove. d) Ray tracing conducted on the designed V-groove PLC using LightTools ray tracing tool. Source: Reproduced with permission from [96]. Copyright © 2016, Elsevier.

A complete geometrical design for the specific PLC can be described based on the equations described below;

$$\theta_i = \frac{1}{2}\tan^{-1}\left(\frac{Q_i}{f - d/2}\right) \tag{1.1.12}$$

$$w_1 = 2d\sin\theta_i \tag{1.1.13}$$

$$s_{i+1} = \frac{(Q_i + w_i\cos\theta_i)w_i\sin\theta_i}{f - d/2 - w_i\sin\theta_i} \tag{1.1.14}$$

Where, the major design parameters are shown in Figure 1.18c, and the design parameters concerned with the design for i_{th} groove are groove angle (θ_i), groove width (w_i), the vertical distance between the concentrator bottom and center of the solar cell (f), the distance between the solar cell and the groove ridge (Q_i), and inter-groove distance between i_{th} and $(i+1)_{th}$ groove (s_i+1) for eliminating the subsequent refection of light from adjacent grooves. The concentrator is designed and fabricated (as shown in Figure 1.18c) with PMMA (refractive index 1.507 ~ 1.483 in the range of wavelength 400 nm–1000 nm) as the transparent matrix and Aluminium and Silicon dioxide as reflective coatings with a theoretical reflectance of 83.9%. The simulated ray tracing conducted for the fabricated design is as shown in Figure 1.18d, using LightTools ray tracing software. The major design parametric limitation of V-groove PLC is the concentrator's aspect ratio, as there are no multiple reflections for guiding the light rays through the optical slab. Subsequently, this may yield a very high optical material requirement due to the higher width compared to the length of the system. The fabricated design shown in Figure 1.18c has an incident aperture size of 30 mm × 30 mm and a solar cell size of 30 mm × 5 mm, yielding a GCR of 5. The OE was expected to be 67.7% from the ray-tracing simulation, considering the reflection efficiency of the coating and Fresnel losses. However, the fabricated system showed a 50% OE when experimentally measured. This optical loss was attributed to fabrication inaccuracies like distorted valleys of grooves, the surface roughness of the optical materials used for the optics matrix, other discrepancies such as light collimation of the solar simulator, etc., as discussed in the article. Also, the acceptance angle is low (2°), indicating the limitation of V-groove designs. The major advantage of these types of design is that the whole system is single elemental, eliminating the need for elemental inter-alignment.

Another approach to fabricate a single elemental reflecting waveguide-based PLC is by creating a light-trapping layer embedded with solar cells. Dijka et al. utilised a concentrator array as an external light-trapping unit with solar cells [97]. The concentrator is a regular-shaped reflecting surface with a metallic coating (silver coating with reflectance of 95%) that concentrates and directs light to the solar cells. The rays that are reflected from the solar cells are reflected back to it from the bottom of the concentrator, making a cage for light trapping. A schematic of the design with a parabolic reflector as the concentrating element is shown in Figure 1.19a. The analysis was carried out with different concentrator geometries of square, hexagonal, circular, and parabolic, with the same GC of 6X (photographs of the prototype are shown in Figure 1.19b), which was fabricated through 3D printing. The printed parts are chemically polished and coated with silver to yield the reflecting surface. The theoretical analysis shows that circular concentrators in the hexagonal array have better optical performance, i.e., light transmissivity towards the solar cell, especially at higher concentration ratios.

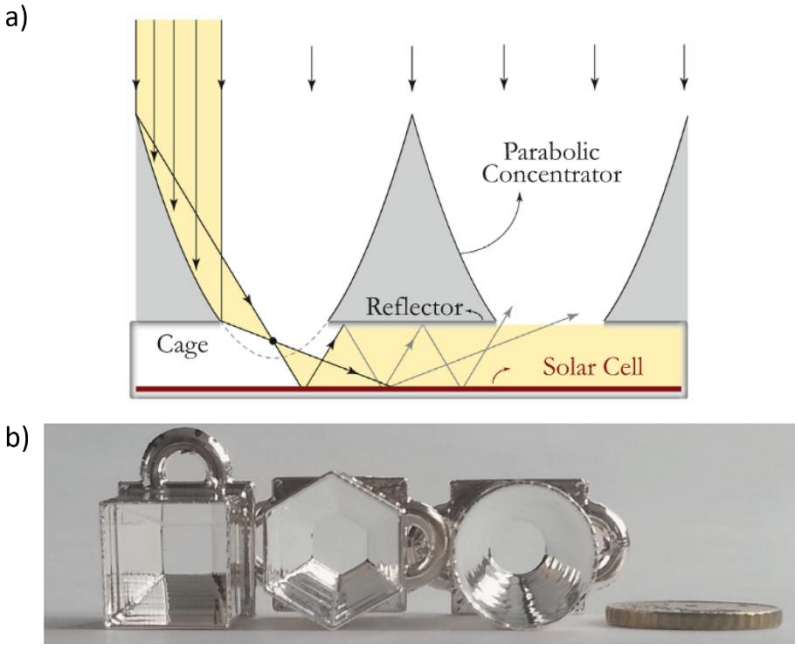

Figure 1.19. a) Schematic of the reflective and cage type PLC with a parabolic surface as the reflector. b) Fabricated square, hexagonal, and circular reflectors, with a silver coating (10 euro cent coin placed at right for size comparison). Source: Reproduced with permission from [97]. Copyright © 2015, The authors, Published by Elsevier.

The critical parameters for external light trapping are the transmittance of the concentrator, the number of reflections that can occur, the reflectivity of a solar cell, and the reflectivity

of the cage surface. The performance of the optical light trap is represented as the absorptance of the solar cell (AT),

$$A_T = T_C \cdot \frac{A_{SC}}{1-R_{SC}\left(1-C^{-1}\right)R_{cage}} \quad (1.1.15)$$

where T_C is the concentrator transmittance, ASC is the absorbance of the solar cell, R_{SC} and R_{cage} are the reflectance of the solar cell and cage, respectively.

The design, optical finish, and reflectivity of the concentrator surface determine the concentrator's OE, i.e., the transmissivity towards the solar cell. Figure 1.20 represents the number of reflections that occurred by rays that are transmitted through a hexagonal concentrator of 15X concentration, where the hue of the color code representation ranges from 0 to 13 times of reflection.

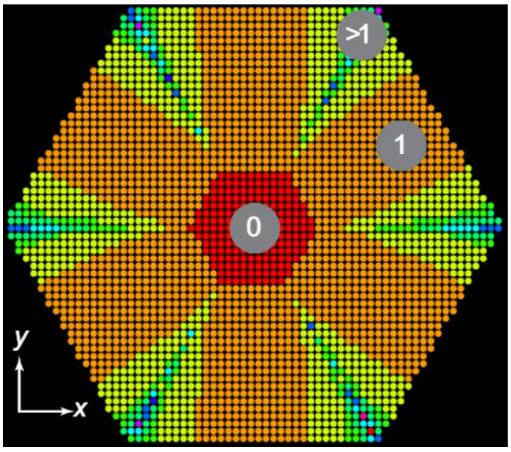

Figure 1.20. The number of reflections occurred per ray for 3000 rays in a hexagonal light concentrator. The position of rays is considered before the ray release; the range of reflections is 0 to 13, represented as the hue of the dots. Source: Reproduced with permission from [97]. Copyright © 2015, The authors, Elsevier.

Experimentally, the utilization of the external light trapping mechanism showed a path length enhancement of more than twice, yielding an improvement of up to 69% for the external quantum efficiency in an organic solar cell, with an increase of 13% in short circuit current. Sun Simba concentrator of Morgan Solar, is one of the commercially extended single-element reflective PLCs [98]. This light concentrating and guiding system is made with an optically transparent material like acrylic, consisting of two layers, as shown in Figure 1.21 (Figure 1.21a shows the photographs of the Sun Simba concentrator, and Figure

1.21b shows the typical design structure of the concept and the ray tracing of it) [98, 99]. However, the system can be considered as a single reflecting PLC entity, as the layers are embedded together. The first layer is a light-insertion layer, where light is reflected and concentrated as an output to the second stage of the light-guiding layer. The light output aperture from the first layer can be modified with different geometric features of the reflecting layer, like parabolic, cubic, hyperbolic, flat, etc. The light guiding layer can be flat or wedge-shaped to collect the light rays and transport them to the centre of the system, where the solar cell is attached. In wedge-shaped guiding layers, the thickness of the light guide increases near the center, which allows light to more efficiently couple towards the center without interacting with injection faces closer to the center. The whole design is structured as concentric circles towards the center. As it is a single elemental reflective PLC design with centre point light concentration, it faces a low solar acceptance angle, and hence requires a precise 2-axis tracking system. However, this limitation can be compensated for with a very high light concentration ratio and cheaper manufacturing techniques employed. Morgan Solar claims an acceptance angle of ±0.9° and a concentration of 1000 suns with a combined acrylic and glass optical structure [100].

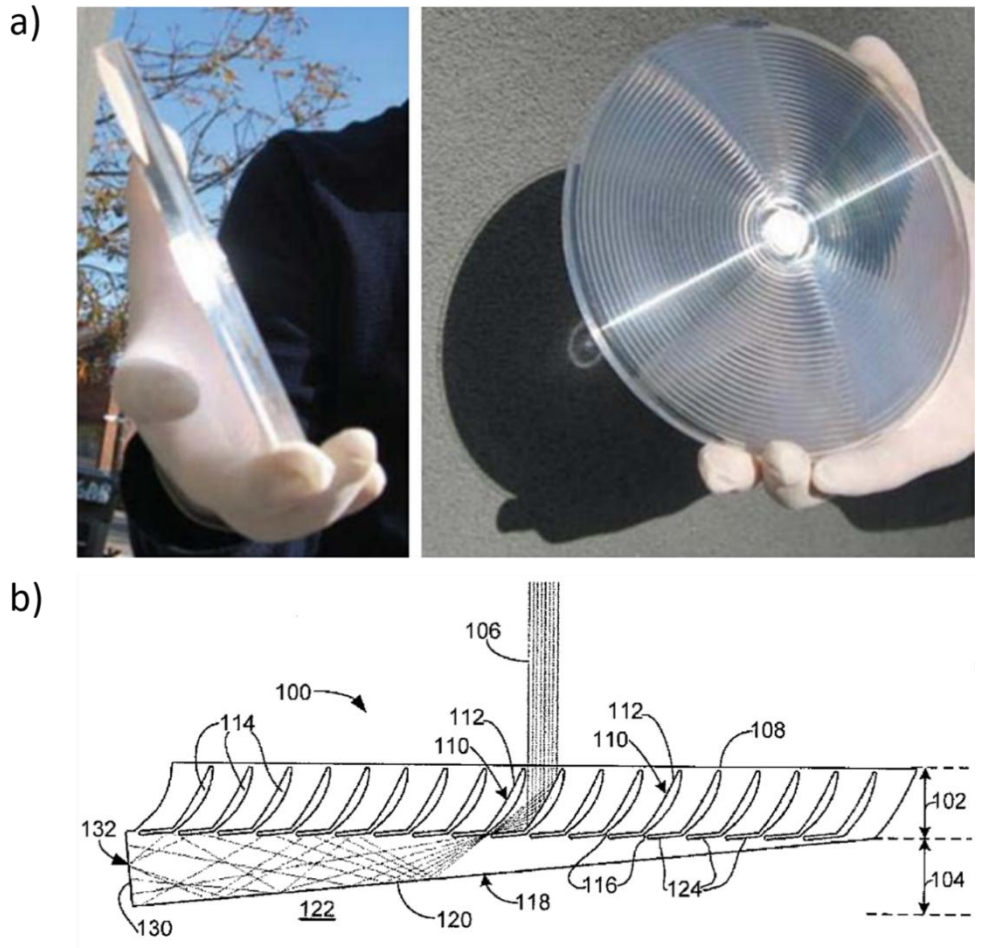

Figure 1.21. a) Photographs showing solar concentration in the Sun Simba concentrator of Morgan Solar. Source: Reproduced with permission from [99]. Copyright © 2014, © The Authors. Published by SPIE. b) Ray tracing in a typical single-element reflective type PLC design by Morgan Solar, showing the concentration of light in the lateral direction. Source: [98].

The waveguide-based PLCs are designed either longitudinally [93, 94] or radially [52, 101]. Longitudinal approaches are mainly used for creating designs with better solar angular acceptance [56, 91]. However, radial designs (that concentrate light on the center), even though they lack angular acceptance, can produce very high GC. Additionally, radial designs that concentrate light on the center have more application possibilities, such as for daylighting systems. However, creating a single elemental radial design seems to be the most challenging in waveguide-based PLCs, as the design freedom is very limited. The PLC developed by Morgan Solar is one such system [98, 99]. Even though it requires 2-axis solar tracking, any such innovative approach will be a boon considering their final light concentration value, and ease of fabrication and operation.

1.3 Statement of the problem, research gap, and solution hypothesis

To mitigate the limitations of bulky imaging optics-based systems for light concentrators, planar optics such as Fresnel lenses and mirrors emerged as compact light concentrator solutions. However, to address the issue of the focal gap, there was a need for innovative approaches rather than using imaging optics directly. In this regard, waveguide-based PLC has evolved as the best solution, which enables a single point of energy collection, a zero focal length concept, dispersed light collection from the waveguide, and reduced sizing of the whole light concentrating system. Despite these advantages of waveguide-based PLCs, current designs face challenges including the need for precise microfabrication techniques, bulkier elements (larger width-to-length ratio), multiple optical elements with the need for precise alignments, or limited solar acceptance angles.

As of now, the existing design innovations conducted on planar waveguide-based CPVs have more prominence for geometric optics-based designs. However, the primary design challenge is to achieve a scalable design solution without compromising on geometrical concentration, OE, and solar acceptance. More importantly, it is observed that very few design solutions are reported for larger optics areas (i.e., effective size greater than 10 cm). Even though designs with very high theoretical geometrical concentration (~1000X) ratios are reported, the translation to fabrication and assembly of flawless optics systems seems to be a major challenge, especially for designs with intricate shapes and multiple elements. Considering the product orientation, the applicability of geometric optics-based PLC systems is always under question when translating it to applications in built environments such as buildings, where integration and compactness should go hand in hand with the seasonal performance. Although products with optimized design and orientation are considered, a smaller number of systems only utilize tracking in buildings, which should be emphasized. Optics design adaptable for both longitudinal and radial concentration will be beneficial in the wider development of products for multi-applications.

Apart from the performance factors, the technical validation of the systems seems challenging on the laboratory scale. From a research and development point of view, the initial design validations can be either carried out with computer simulation models, or cheaper and rapid prototyping methods such as laser machining, 3D printing, etc. Even though simulation models satisfy the validation, optics manufacturing cannot be considered foolproof, especially in the prototyping stages. Carrying out the prototyping in major

manufacturing processes like injection molding seems to be costlier. Hence, the process development should be made better with a wider material library for prototyping methods such as 3D printing, for parameters such as dimensional accuracy, surface finish, and better surface profiles.

In line with the general introduction and literature survey conducted, the general hypothesis for a design solution for geometric optics-based waveguide PLC can be stated as follows:

1) A single elemental system that provides the provision for a single-step manufacturing route.
2) A non-sequential system to eliminate the need for precise optical positioning during the process of manufacturing or assembly.
3) Provision of solar acceptance, at least in a direction.
4) Flexibility to longitudinal and radial design, upon the application or required concentration.
5) Scalable with an industrial manufacturing route.

Herein, a novel optical design featuring skewed V-groove patterns has been developed for use in low-concentration solar energy systems. The first-of-its-kind design approach differs from the existing methods in its light transport mechanism and has the following attributes: 1) Utilization of a non-sequential design (one optics element is not followed by any other) approach, employing a single optics element; this avoids the need for precise positioning of the optics 2) Low-concentration optics (less than 10X GC), eliminating the need for intricate thermal management systems; 3) A straightforward waveguide-based construction, allowing for production through a single manufacturing process; 4) Higher solar acceptance in an axis eliminating the need for 2-axis tracking; 5) A zero focal length configuration that negates the necessity for spacing before the collectors; 6) Unidirectional light concentration design for higher concentration factor; 7) Design flexibility from longitudinal to radial design for higher concentration in expense of solar acceptance.

The objectives of the thesis are as follows:

- Introduction of the design concept of SV-PLC optics
- Mathematical modeling of SV-PLC for parameter optimizations in different materials

- Design validation, parametrization, and theoretical evaluation of SV-PLC optics through ray tracing simulation
- Evaluation of different fabrication routes of SV-PLC
- Experimental validation of SV-PLC showing its application potential
- Introduction to a novel concept of Dynamic Power Window using SV-PLC optics and its demonstration

1.4 Thesis Outlook

The thesis is designed in six chapters. With the comprehensive introduction and literature review carried out on geometric optics-based waveguide PLCs in the **first chapter**, the **second chapter** comprises developing a novel single-element optics design system that can accommodate the rectification of existing design limitations. The detailed mathematical model of the system is carried out for parametric dependent studies and efficiency evaluation. The **third chapter** pertains to the elaboration of the possible fabrication methods and corresponding design protocols of the PLC design. The **fourth chapter** corresponds to the characterization methods for the practical evaluation of the fabricated PLC optics. The performance study of the SV-PLC optics is carried out both in standard and outdoor conditions. A novel technology concept of Dynamic Power Windows (a window technology concept that combines both active transparency switching and power generation in a single platform) has been introduced and demonstrated in the **fifth chapter**. The thesis will be summarised and inferred in the **sixth chapter**, along with the discussion on future possibilities in design and product development.

Chapter 2

Skewed V-groove based Planar Light Concentrator (SV-PLC) and its Mathematical Modeling

2 Skewed V-groove based Planar Light Concentrator (SV-PLC) and its Mathematical Modeling

2.1 Abstract

Waveguide-based Planar Light Concentrator (PLC) technologies have embarked on its presence as an innovative light concentrator technology due to their compactness and application potential. A novel waveguide-based low-concentration PLC design, based on a skewed V-groove, has been introduced, which is single-elemental and non-sequential. The Skewed V-groove planar optics is a new leaf for PLC technologies with its uniqueness of single-element and non-sequential design approach. The introduced geometric optics-based design consists of a planar waveguide of a higher refractive index (RI) with a linear array of skewed V-grooves of void. The design and light transport mechanism in the SV-PLC have been discussed. A detailed mathematical model is developed based on the ray travel (single ray model) with corresponding design parameters for establishing the path of light rays (direction and position) and predicting the effectiveness of the PLC. The efficiency of the PLC has been discussed based on the mathematical model of a single typical groove. The workflow methodology of the chapter is illustrated in the flow chart below.

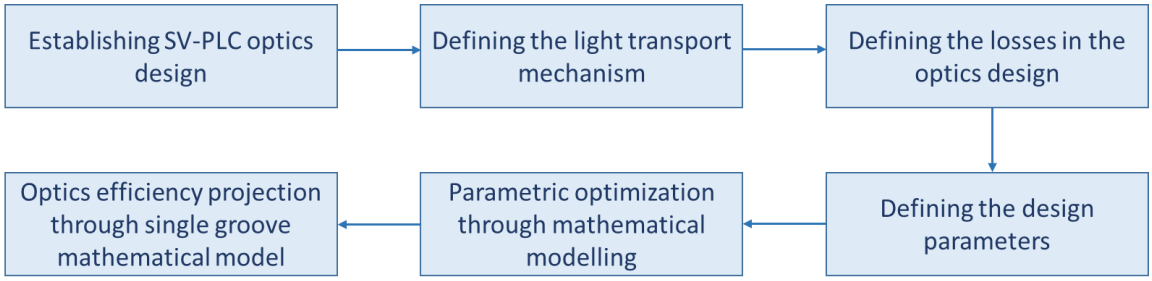

2.2 Introduction

Mathematical modeling is one of the elementary design optimization tools and performance predictors for optics systems [102, 103] such as light concentrators [104, 105]. Basic mathematical models are always carried out along with computer simulations to create a proper understanding of the theoretical mechanism and light transport pattern for predicting the Optical efficiency (OE), focal length, and light intensity distribution [106, 107]. The interdependency of different parameters can also be studied using mathematical models and utilized to reduce the steps of simulation studies. This can save time and cost when iterative studies need to be done for design parameters and optical materials to create

effective light concentrator solutions. This is most effective with unconventional optics systems where manufacturing cost limits experimental optimization. In summary, mathematical modeling of light concentrators is essential for design innovations, material selection, and performance improvements in optical systems.

Light concentrator technologies generally adopt reflection, refraction, dispersive reflection, diffraction, emission, and total internal reflection (TIR) as light transport mechanisms [61, 108-110]. Modern optics solutions utilize a combination of these phenomena to create design compactness and flexibility, and improve the application potential. Waveguide-based PLC technologies are set to have a foot in the arena as an innovative solution following their compactness and application potential [77]. From the status of the current waveguide-based PLCs, it is evident that the existing design innovations conducted on planar waveguide-based PLCs have more prominence for geometric optics-based designs. The design freedom provided by geometric optics-based PLCs makes it adaptable for low (<10X), medium (10X to 100X), and high (>100X) concentration optics. The review of the studies suggests that the prediction of the effectiveness of the newer designs is carried out predominantly with simulations, rather than directly with prototypes. The design approaches employed for geometric optics-based PLCs are:

1. Single-elemental reflective: The method uses reflective elements or faces to transport the light within the waveguide. The models use specular reflection as the basic tool for light transport. V-groove reflective surfaces [96] and cage-like structures [97] are utilized for this. The PLC developed by Morgan Solar is one of the superior single-elemental reflective designs when considering the GC it can provide [98, 99]. The mathematical models are developed based on the Law of Reflection and trigonometric considerations.
2. Multi-elemental reflective: Unlike single-elemental reflective mode, these waveguide-based PLCs have waveguides separated or distanced from the reflective surfaces [52]. The specular reflective surface often uses a profiled geometry to transport the light rays to the entry points of the waveguide. The mathematical models are developed based on the Law of Reflection, geometric profiles of the reflective surface, and trigonometric considerations.
3. Multi-elemental refractive: This method generally uses refractive optics (convergent lens) that converge the light rays to light dispersive elements for transporting the light rays to the waveguide [16, 56, 91, 94]. The dispersive elements are reflective

surfaces, which are mirrored surfaces or air prisms (producing TIR) placed in the waveguide itself [92, 93]. The mathematical models are developed based on the Law of Refraction, Law of Reflection, Fresnel equations for light transfer between media, and trigonometric considerations.

The optics design (skewed V-groove) discussed in this chapter encompasses a single elemental and non-sequential design in an optical slab (waveguide) that creates lateral light transport within the waveguide. A detailed mathematical model has been developed to establish the path of light rays, optimize the multiple design parameters involved, and preliminarily validate the effectiveness of the PLC.

2.3 Design & Methodology

The proposed design is a non-sequential single-element optics system that essentially consists of an array of skewed V-groove voids in an optically transparent slab. In order to establish the ray travel pattern for lateral light concentration in the skewed V-groove based Planar Light Concentrator (SV-PLC), a simulated model of a single ray (normal incident) carried out in COMSOL Multiphysics 6.1 is shown in Figure 2.1a. As illustrated, when a light ray hits the V-groove's reflecting face (as shown in Figure 2.1a), it will undergo TIR. This process steers the light horizontally through the SV-PLC, with multiple refractions at adjacent grooves causing an upward shift in the light rays within the SV-PLC, thereby enabling efficient light transport. Ultimately, the rays redirected from the array of grooves lead to intensified light collection at the lateral edge of the SV-PLC.

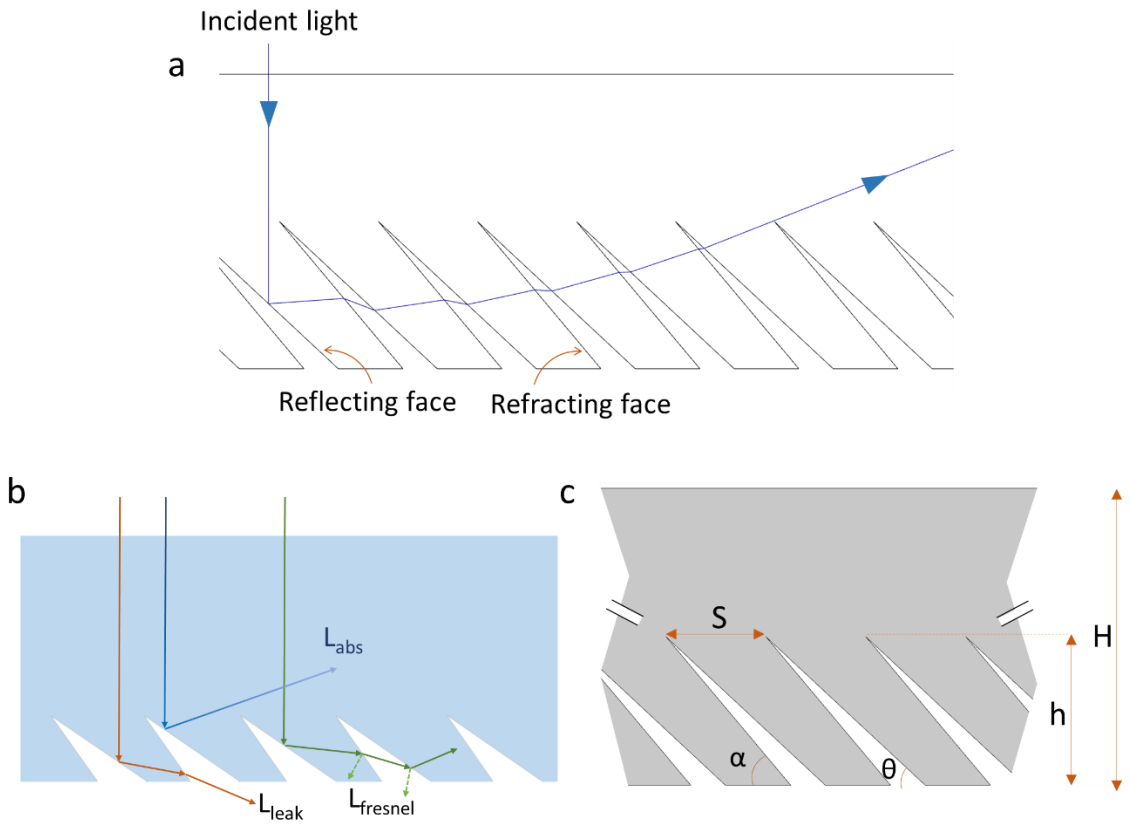

Figure 2.1. a) Typical ray transport mechanism within an SV-PLC, illustrated using a ray-tracing simulation model; b) Principal loss mechanisms in an SV-PLC optics; c) Key design parameters for SV-PLC optics.

To conduct the mathematical modeling or simulation studies in the SV-PLC, the parametric optimization and fixation should be carried out initially, contemplating the different loss mechanisms that can occur.

The different losses that occur in an SV-PLC are depicted in Figure 2.1b. The angle of incidence at the different faces determines the Fresnel loss ($L_{fresnel}$, represented as dotted lines), i.e., which is the light reflection loss during transmission. Additionally, material absorption loss (L_{abs}) significantly affects SV-PLC efficiency as light travels through the material. Beyond Fresnel and material absorption losses, there can also be leakage loss (L_{leak}) at the SV-PLC's base, as depicted in Figure 2.1b. $L_{fresnel}$ and L_{leak} are influenced by the design parameters of SV-PLC. Therefore, optimizing the design according to the material characteristics can enhance its efficiency and improve the final light concentration.

The key parameters of the SV-PLC optics (shown in Figure 2.1c) and the methodology for their optimization are given below.

Reflecting face angle (θ): The angle θ must be fixed such that the incident angle at the reflecting face should exceed the critical angle necessary for TIR to occur. To ensure maximum light transmission with the fewest refractions possible, it should be maintained a minimal θ value (increasing θ creates a more downward path of rays in the SV-PLC, making more $L_{fresnel}$ loss).

Refracting face angle (α): The reflective face angle, α, is the most critical factor in the SV-PLC optics to achieve the desired OE and FC, which is parameterized for the mathematical modelling and simulation studies.

Difference of Height of the slab & Height of the optical element (H-h): Reducing the size of the optical elements (groove height, h) or increasing the height of the PLC (H) offers significant benefits by increasing the (H-h) factor, thereby extending the rays' path length. Consequently, this results in an increase in the length of the SV-PLC; hence, the final concentration (FC) of light (this will be discussed).

Inter-groove spacing (S): The inter-groove spacing is always set to a maximum value without any L_{leak} loss in the SV-PLC.

To create a mathematical model for the study of SV-PLC, the pattern of possible ray travel should be analyzed first. Subsequently, the design parameters should be introduced along with their dependence on the overall optical system performance.

The typical SV-PLC optics and a random ray travel pattern are shown in Figure 2.2. Herein, the grooves a ray is passing through are numbered as “ab”, where a represents the groove number (from the ray's point of view), and b represents the face number (reflecting faces are taken as 2, and refracting faces are taken as 1). This annotation is used throughout with every parameter in this chapter, like h_{11} shown in Figure 2.2. The incident face is annotated with the letter “i”, like h_i shown in Figure 2.2.

The number of grooves a ray passes is determined by the design parameters θ and α, along with the position of the ray impinging in a groove (i.e., h_i). Accordingly, different rays pass through a different number of grooves (depending on the h_i), resulting in varied final intensity due to the $L_{fresnel}$ loss. This fact should be incorporated into the mathematical modeling to get a realistic picture of the light concentration in SV-PLC.

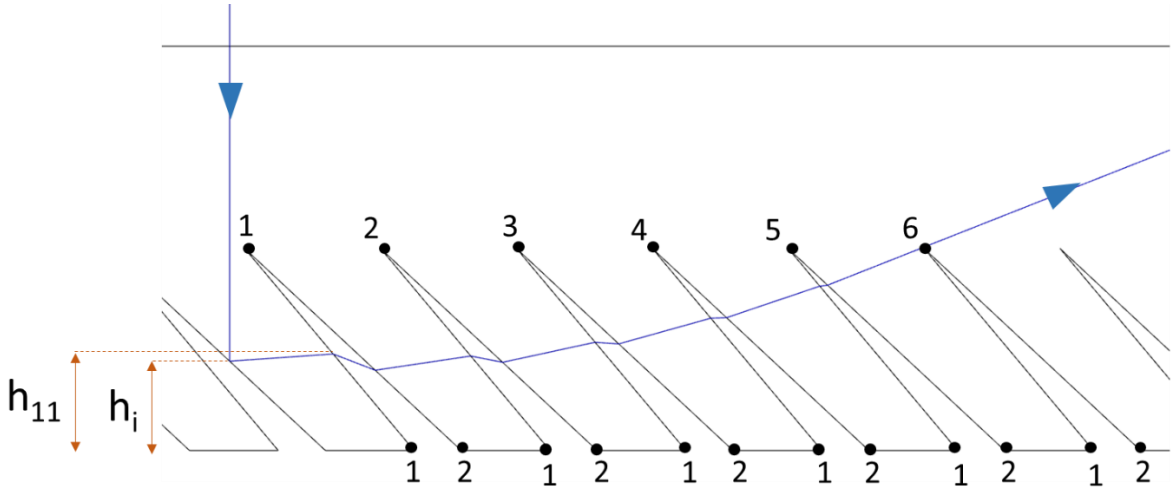

Figure 2.2. Typical ray path in SV-PLC optics, showing the annotation method for the grooves and parameters (examples shown as h_i and h_{11}).

Thus, to understand and simulate the models for the ray travel across the designed SV-PLC, the realization of a mathematical model predicting the ray position and ray power at the different interfaces is required. Since the design is dependent on the RI of the material, the mathematical models developed (for normal incidence of light rays) are used to compare the effectiveness of light concentration of common optical materials like PMMA, Glass, and Polycarbonate (PC) with RI taken approximately to single values, 1.49, 1.52, and 1.58 respectively.

2.4 Results and Discussion

The section is subdivided into individual parameters as below to gain a better understanding.

2.4.1 Optimisation of θ

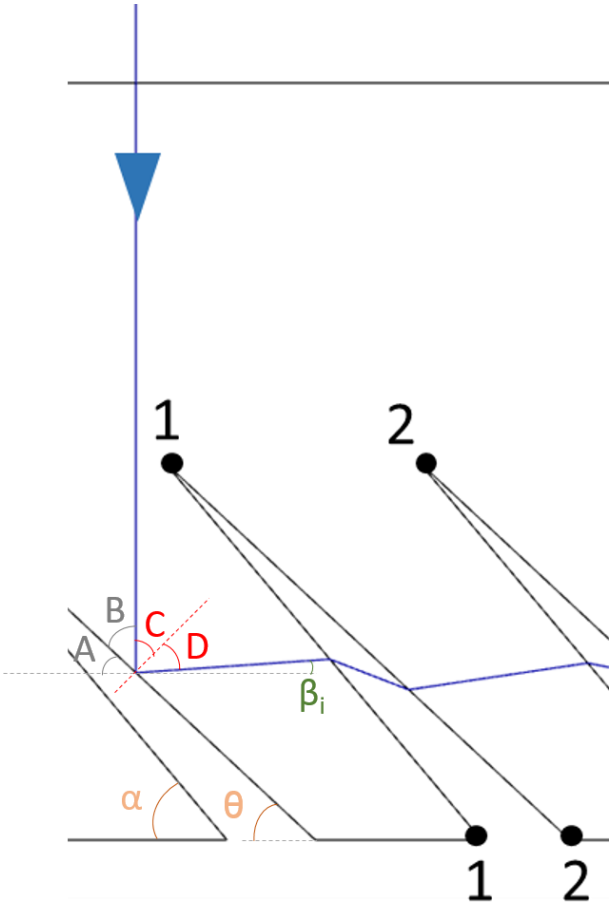

Figure 2.3. Schematic representation of ray travel (in blue color) in an SV-PLC optics showing the angular parameters and variables at the incident face, where the light ray is internally reflected at the reflecting face.

$$
\begin{aligned}
&A = \theta \text{ (Corresponding angles)} \\
&A+B = 90° \text{ (Considered ray at an angle of 90° with the PLC face)} \\
&\Rightarrow \quad B = 90°-\theta \\
&B+C = 90° \text{ (Angle made by normal to the groove face)} \\
&\Rightarrow \quad \theta = C
\end{aligned}
\tag{2.1}
$$

As defined by Snell's law, the critical angle for TIR to occur is given by,

$$\theta_c = \sin^{-1}\left(\frac{n_a}{n_m}\right) = \sin^{-1}\left(\frac{1}{n_m}\right) \tag{2.2}$$

where n_a and n_m are the RI of air and the optical material, respectively.

Angle C (i.e., θ (from Equation 2.1)) should be greater than θ_c, for TIR to occur. As mentioned in Section 2.3, θ should be kept to a minimum to ensure maximum light transmission with fewer refractions; θ is kept just over θ_c. Hence, for standard optic materials like PMMA (RI: 1.49), Glass (RI: 1.52), and PC (RI: 1.58), the θ is set to 43˚, 42˚, and 40˚, respectively.

2.4.2 Derivation of cumulative light transmission (T_c)

T_c value is the final light intensity of a ray propagating out of the groove area in an SV-PLC. Neglecting the L_{abs} loss, T_c shows a direct correlation with $L_{fresnel}$ happening at the different interfaces of the SV-PLC. Hence, it can be considered as a design-dependent variable. The dependent parameter of T_c is the RI of the material, and the dependent variable is the incident angle at the different interfaces of light refraction. The incident angles (i_{ab}, where ab represents the face number (refer to the Design & Methodology section of this chapter for annotation representation information) at the different faces determine the $L_{fresnel}$ occurring through the light transport. The derivation of the incident angle is as below:

2.4.2.1 Derivation of incident angle (i_{ab})

From Figure 2.3,

$$C = D \text{ (Law of reflection of light)}$$

$$C+D+\beta_i = 90° \text{ (Considered ray at an angle of 90° with the PLC face)}$$

$$\Rightarrow \quad \beta_i = 90°-2\theta \tag{2.3}$$

where β represents the angle made by a light ray with the horizontal.

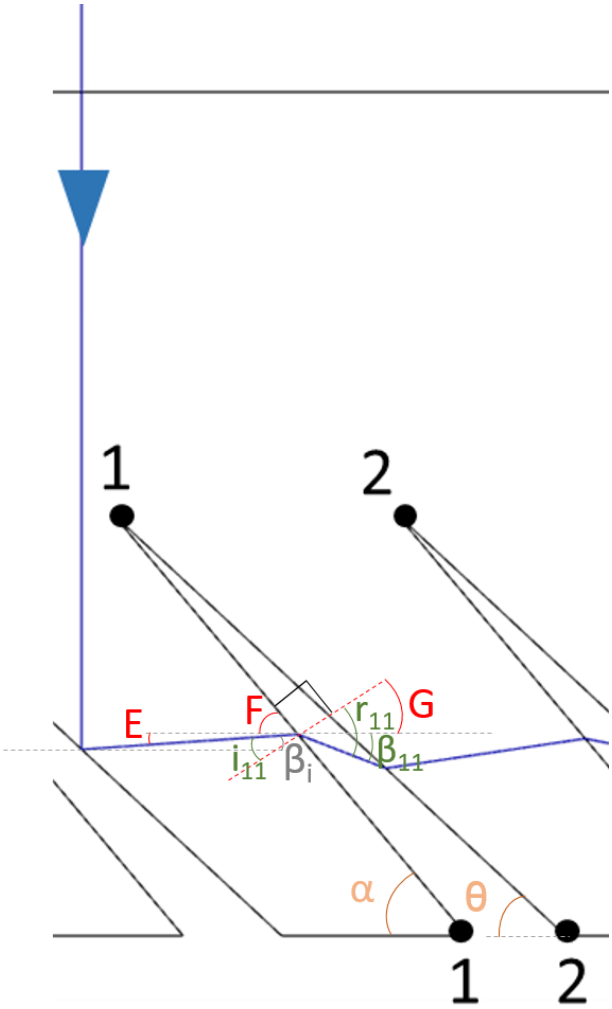

Figure 2.4. Schematic representation of ray travel (in blue color) in an SV-PLC optics showing the angular parameters and variables at the first groove interface, where the light ray undergoes refraction.

$F = \alpha$ (Corresponding angles)

$E = \beta_i$ (Alternate interior angles)

$E+F+i_{11} = 90°$ (Angle made by normal to the groove face)

$\Rightarrow \quad i_{11} = 90°-\alpha-\beta_i$

$\Rightarrow \quad i_{11} = 2\theta-\alpha$ (using Equation 2.3)

(2.4)

At the (11) interface,

$$r_{11} = \sin^{-1}\left[\sin(i_{11}) * \left(\frac{n_m}{n_a}\right)\right] \text{ (Snells' Law)}$$

(2.5)

$F+90°+ G = 180°$ (Straight line)

$\Rightarrow \quad G = 90°-\alpha$

$G+\beta_{11} = r_{11}$ (from Figure 2.4)

$\Rightarrow \quad \beta_{11} = r_{11}-90°+\alpha$

(2.6)

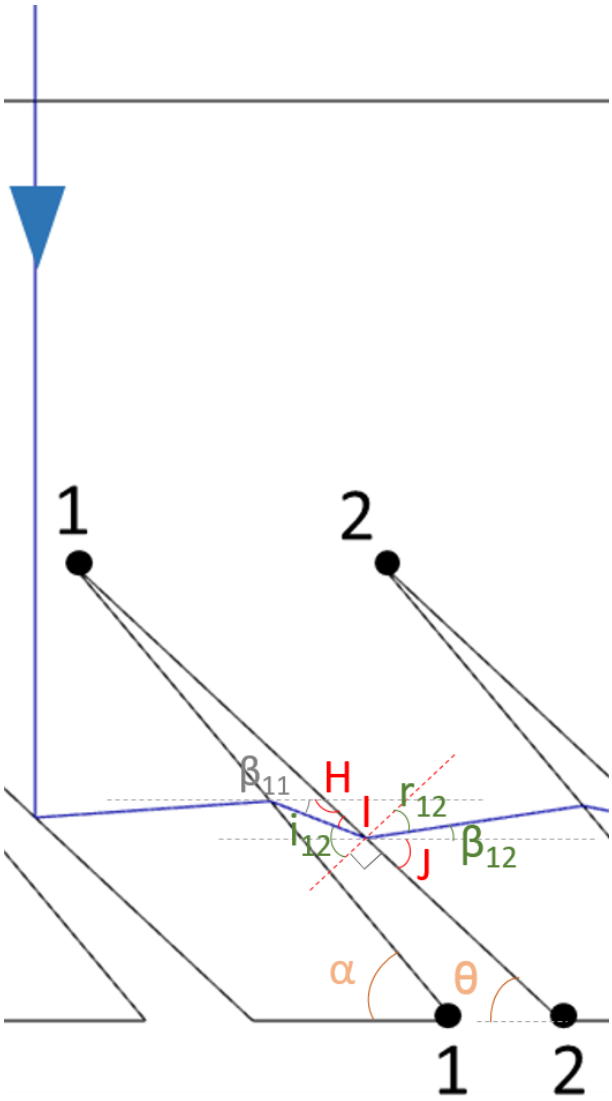

Figure 2.5. Schematic representation of ray travel (in blue color) in an SV-PLC optics showing the angular parameters and variables at the second groove interface, where the light ray undergoes refraction.

$\beta_{11}+H+I = 180°$ (Interior angles of a triangle)

$H+\theta = 180°$ (Consecutive interior angles)

$\Rightarrow \quad I = \theta-\beta_{11}$

$I+i_{12}+90° = 180°$ (Straight line)

$\Rightarrow \quad i_{12} = r_{11}+\alpha-\theta$

(2.7)

At the (12) interface,

$$r_{12} = \sin^{-1}\left[\sin(i_{12}) * \left(\frac{n_a}{n_m}\right)\right] \text{ (Snell'sLaw)}$$

$r_{12}+\beta_{12}+J = 90°$ (Angle made by normal to the groove face)

$J = \theta$ (Alternate interior angles)

$\Rightarrow \quad \beta_{12} = 90°-\theta-r_{12}$

(2.8)

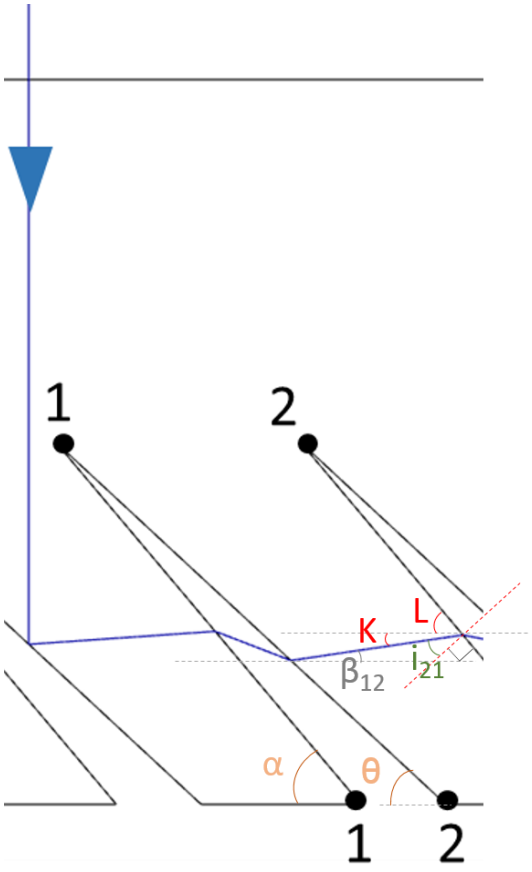

Figure 2.6. Schematic representation of ray travel (in blue color) in an SV-PLC optics showing the angular parameters and variables at the third groove interface, where the light ray undergoes refraction.

$L+K+i_{21}+90° = 180°$ (Straight line)

$L = \alpha$ (Corresponding angles)

$K = \beta_{12}$ (Alternate interiror angles)

$\Rightarrow \quad i_{21} = 90°-\alpha-\beta_{12}$

$\Rightarrow \quad i_{21} = \theta+r_{12}-\alpha$

(2.9)

Similarly,

$\beta_i = 90°-2\theta$ (Equation 2.3)

$\beta_{a1} = \alpha+r_{a1}-90°$

(2.10)

$\beta_{a2} = 90°-\theta-r_{a2}$

(2.11)

In general,

$i_{ab} = 2\theta-\alpha$, where a=b=1

(2.12)

$i_{ab} = r_{[a+b-2][b-(-1)^b]}+(-1)^b(\alpha-\theta)$, where (a or b)>1

(2.13)

$$r_{ab} = \sin^{-1}\left[\sin(i_{ab}) * \left(\frac{n_m}{n_a}\right)\right], \text{where } b=1$$

(2.14)

$$r_{ab} = \sin^{-1}\left[\sin(i_{ab}) * \left(\frac{n_a}{n_m}\right)\right], \text{where } b=2$$

(2.15)

Hence, the dependent parameters for i_{ab} are the RI of the material, θ, and α values. Since θ has been fixed (refer to the Design & Methodology section) for the selected materials (RI 1.49, 1.52 & 1.58) for evaluation, the α parameter has been varied to conduct the mathematical model-based study. The α value for the respective materials is taken above their corresponding θ angle up to 75°, above which the length of the SV-PLC is much smaller (will be discussed in this chapter).

The incident angles at different interfaces are calculated for the different refraction face angles (using Equations 2.12 and 2.13) and tabulated in Tables 2.1, 2.2, and 2.3, for materials with RI 1.49, 1.52, and 1.58, respectively. The tabulated values are used for the determination of transmitted ray power from each interface using Fresnel equations (equations 2.16 to 2.19). The grey region marked represents the region for back reflection loss (L_{br}), where the ray will be completely lost because of the TIR occurring at the bottom region of the refracting faces.

Table 2.1. Incident angles at the different faces of the SV-PLC with varying α angles for material of RI 1.49.

Material Refractive Index: 1.49 | Reflective face angle, θ: 43˚														
α	i_{11}	i_{12}	i_{21}	i_{22}	i_{31}	i_{32}	i_{41}	i_{42}	i_{51}	i_{52}	i_{61}	i_{62}	i_{71}	i_{72}
44.0000	42.0000	86.7786	41.0581	79.2035	40.2323	75.2706	39.4632	72.2939	38.7350	69.8220	38.0391	67.6737	37.3701	65.7546
45.0000	41.0000	79.8874	39.3428	72.8658	37.8844	68.2184	36.5453	64.5404	35.2928	61.4227	34.1081	58.6788	32.9790	56.2055
46.0000	40.0000	76.3208	37.6905	68.6580	35.6839	63.3692	33.8605	59.1256	32.1681	55.4992	30.5766	52.2880	29.0660	49.3781
47.0000	39.0000	73.6911	36.0920	65.3822	33.5937	59.5367	31.3404	54.8082	29.2592	50.7439	27.3084	47.1268	25.4605	43.8337
48.0000	38.0000	71.5580	34.5363	62.6509	31.5877	56.3085	28.9427	51.1456	26.5074	46.6851	24.2283	42.6964	22.0706	39.0476
49.0000	37.0000	69.7426	33.0154	60.2835	29.6488	53.4868	26.6405	47.9231	23.8758	43.0927	21.2896	38.7522	18.8401	34.7620
50.0000	36.0000	68.1514	31.5239	58.1790	27.7650	50.9592	24.4153	45.0180	21.3393	39.8343	18.4609	35.1530	15.7310	30.8271
51.0000	35.0000	66.7282	30.0575	56.2744	25.9274	48.6549	22.2533	42.3524	18.8798	36.8258	15.7194	31.8088	12.7163	27.1466
52.0000	34.0000	65.4365	28.6128	54.5271	24.1289	46.5259	20.1442	39.8735	16.4833	34.0097	13.0479	28.6573	9.7750	23.6535
53.0000	33.0000	64.2505	27.1872	52.9072	22.3643	44.5380	18.0799	37.5433	14.1390	31.3445	10.4327	25.6531	6.8907	20.2978
54.0000	32.0000	63.1518	25.7785	51.3924	20.6290	42.6657	16.0536	35.3334	11.8383	28.7988	7.8630	22.7615	4.0498	17.0404
55.0000	31.0000	62.1263	24.3849	49.9657	18.9193	40.8895	14.0600	33.2219	9.5736	26.3480	5.3292	19.9547	1.2407	13.8488
56.0000	30.0000	61.1631	23.0047	48.6139	17.2322	39.1940	12.0943	31.1913	7.3390	23.9721	2.8236	17.2092	-1.5470	10.6946
57.0000	29.0000	60.2536	21.6366	47.3262	15.5650	37.5668	10.1527	29.2273	5.1289	21.6546	0.3388	14.5049	-4.3230	7.5513
58.0000	28.0000	59.3908	20.2794	46.0941	13.9153	35.9976	8.2318	27.3179	2.9387	19.3810	-2.1314	11.8233	-7.0961	4.3933
59.0000	27.0000	58.5690	18.9322	44.9102	12.2812	34.4779	6.3284	25.4530	0.7641	17.1385	-4.5933	9.1470	-9.8755	1.1940
60.0000	26.0000	57.7834	17.5939	43.7686	10.6608	33.0004	4.4398	23.6234	-1.3989	14.9154	-7.0525	6.4589	-12.6702	-2.0757
61.0000	25.0000	57.0299	16.2638	42.6640	9.0527	31.5587	2.5636	21.8214	-3.5539	12.7006	-9.5148	3.7412	-15.4901	-5.4496
62.0000	24.0000	56.3051	14.9411	41.5920	7.4552	30.1472	0.6975	20.0394	-5.7044	10.4831	-11.9861	0.9748	-18.3458	-8.9687
63.0000	23.0000	55.6060	13.6252	40.5487	5.8672	28.7609	-1.1606	18.2706	-7.8539	8.2521	-14.4723	-1.8620	-21.2495	-12.6860
64.0000	22.0000	54.9300	12.3155	39.5306	4.2873	27.3955	-3.0127	16.5085	-10.0058	5.9960	-16.9799	-4.7942	-24.2155	-16.6746
65.0000	21.0000	54.2749	11.0114	38.5348	2.7146	26.0466	-4.8608	14.7468	-12.1636	3.7026	-19.5160	-7.8529	-27.2613	-21.0414
66.0000	20.0000	53.6386	9.7124	37.5585	1.1479	24.7105	-6.7066	12.9789	-14.3306	1.3581	-22.0886	-11.0776	-30.4090	-25.9591
67.0000	19.0000	53.0194	8.4180	36.5991	-0.4138	23.3835	-8.5521	11.1983	-16.5108	-1.0532	-24.7068	-14.5214	-33.6879	-31.7439
68.0000	18.0000	52.4157	7.1278	35.6544	-1.9713	22.0621	-10.3991	9.3981	-18.7082	-3.5499	-27.3816	-18.2597	-37.1390	-39.1188
69.0000	17.0000	51.8261	5.8414	34.7224	-3.5256	20.7428	-12.2493	7.5710	-20.9269	-6.1547	-30.1263	-22.4079	-40.8230	-50.9699
70.0000	16.0000	51.2492	4.5585	33.8009	-5.0775	19.4223	-14.1046	5.7088	-23.1721	-8.8966	-32.9576	-27.1599	-44.8396	
71.0000	15.0000	50.6838	3.2785	32.8883	-6.6280	18.0971	-15.9671	3.8025	-25.4490	-11.8134	-35.8974	-32.8957	-49.3765	
72.0000	14.0000	50.1289	2.0013	31.9827	-8.1778	16.7636	-17.8387	1.8416	-27.7641	-14.9576	-38.9753	-40.6087	-54.9011	
73.0000	13.0000	49.5835	0.7265	31.0825	-9.7277	15.4184	-19.7216	-0.1861	-30.1249	-18.4052	-42.2338	Total internal reflection occurs at the interface, causing loss L_{br}		
74.0000	12.0000	49.0466	-0.5463	30.1860	-11.2785	14.0574	-21.6181	-2.2955	-32.5404	-22.2760	-45.7384			
75.0000	11.0000	48.5174	-1.8173	29.2916	-12.8312	12.6765	-23.5307	-4.5047	-35.0216	-26.7791	-49.6005			

Table 2.2. Incident angles at the different faces of the SV-PLC with varying α angles for material of RI 1.52.

Material Refractive Index: 1.52 | Reflective face angle, θ: 42˚														
α	i_{11}	i_{12}	i_{21}	i_{22}	i_{31}	i_{32}	i_{41}	i_{42}	i_{51}	i_{52}	i_{61}	i_{62}	i_{71}	i_{72}
43.0000	41.0000	86.9458	40.0535	79.0528	39.2239	75.0199	38.4506	71.9712	37.7177	69.4401	37.0168	67.2403	36.3426	65.2750
44.0000	40.0000	79.7547	38.3349	72.5525	36.8670	67.7920	35.5172	64.0241	34.2534	60.8290	33.0568	58.0158	31.9153	55.4788
45.0000	39.0000	76.0858	36.6771	68.2338	34.6544	62.8147	32.8134	58.4640	31.1024	54.7434	29.4914	51.4463	27.9608	48.4565
46.0000	38.0000	73.3828	35.0725	64.8689	32.5510	58.8759	30.2727	54.0237	28.1653	49.8489	26.1871	46.1298	24.3110	42.7403
47.0000	37.0000	71.1896	33.5100	62.0606	30.5311	55.5540	27.8533	50.2510	25.3837	45.6639	23.0690	41.5565	20.8744	37.7942
48.0000	36.0000	69.3221	31.9822	59.6240	28.5776	52.6466	25.5286	46.9266	22.7213	41.9527	20.0907	37.4762	17.5950	33.3539
49.0000	35.0000	67.6841	30.4834	57.4558	26.6787	50.0389	23.2801	43.9248	20.1529	38.5804	17.2209	33.7445	14.4349	29.2662
50.0000	34.0000	66.2181	29.0094	55.4913	24.8256	47.6584	21.0942	41.1661	17.6604	35.4605	14.4366	30.2688	11.3665	25.4318
51.0000	33.0000	64.8863	27.5571	53.6874	23.0113	45.4562	18.9606	38.5963	15.2299	32.5343	11.7205	26.9852	8.3688	21.7812
52.0000	32.0000	63.6628	26.1237	52.0132	21.2305	43.3971	16.8711	36.1767	12.8504	29.7588	9.0589	23.8466	5.4250	18.2623
53.0000	31.0000	62.5284	24.7070	50.4460	19.4787	41.4552	14.8190	33.8779	10.5133	27.1018	6.4404	20.8168	2.5210	14.8335
54.0000	30.0000	61.4687	23.3052	48.9685	17.7522	39.6104	12.7988	31.6775	8.2109	24.5377	3.8557	17.8664	-0.3554	11.4597
55.0000	29.0000	60.4728	21.9167	47.5670	16.0479	37.8470	10.8059	29.5573	5.9370	22.0457	1.2962	14.9705	-3.2152	8.1095
56.0000	28.0000	59.5316	20.5402	46.2306	14.3631	36.1521	8.8363	27.5026	3.6862	19.6081	-1.2453	12.1069	-6.0688	4.7526
57.0000	27.0000	58.6381	19.1746	44.9505	12.6956	34.5152	6.8864	25.5009	1.4534	17.2095	-3.7759	9.2552	-8.9261	1.3585
58.0000	26.0000	57.7863	17.8187	43.7192	11.0433	32.9274	4.9533	23.5413	-0.7657	14.8361	-6.3019	6.3954	-11.7975	-2.1057
59.0000	25.0000	56.9715	16.4718	42.5305	9.4044	31.3812	3.0340	21.6145	-2.9754	12.4747	-8.8300	3.5071	-14.6935	-5.6780
60.0000	24.0000	56.1894	15.1328	41.3791	7.7773	29.8700	1.1260	19.7116	-5.1795	10.1129	-11.3665	0.5683	-17.6261	-9.4046
61.0000	23.0000	55.4365	13.8013	40.2604	6.1605	28.3878	-0.7731	17.8249	-7.3820	7.7380	-13.9180	-2.4454	-20.6086	-13.3457
62.0000	22.0000	54.7097	12.4763	39.1703	4.5526	26.9295	-2.6654	15.9467	-9.5865	5.3368	-16.4918	-5.5630	-23.6566	-17.5843
63.0000	21.0000	54.0065	11.1574	38.1054	2.9524	25.4903	-4.5531	14.0696	-11.7969	2.8952	-19.0958	-8.8199	-26.7895	-22.2450
64.0000	20.0000	53.3244	9.8440	37.0624	1.3589	24.0657	-6.4383	12.1864	-14.0172	0.3973	-21.7386	-12.2623	-30.0321	-27.5339
65.0000	19.0000	52.6615	8.5356	36.0385	-0.2292	22.6516	-8.3230	10.2894	-16.2514	-2.1749	-24.4306	-15.9531	-33.4176	-33.8456
66.0000	18.0000	52.0158	7.2317	35.0311	-1.8128	21.2439	-10.2092	8.3708	-18.5040	-4.8432	-27.1842	-19.9835	-36.9930	-42.1687
67.0000	17.0000	51.3858	5.9318	34.0377	-3.3930	19.8387	-12.0988	6.4222	-20.7799	-7.6346	-30.0143	-24.4977	-40.8307	-58.7639
68.0000	16.0000	50.7699	4.6356	33.0563	-4.9706	18.4322	-13.9941	4.4340	-23.0845	-10.5836	-32.9403	-29.7509	-45.0540	
69.0000	15.0000	50.1668	3.3427	32.0847	-6.5466	17.0205	-15.8970	2.3958	-25.4241	-13.7370	-35.9879	-36.2890	-49.9152	
70.0000	14.0000	49.5754	2.0526	31.1208	-8.1218	15.5995	-17.8099	0.2952	-27.8058	-17.1603	-39.1926	-45.8865	-56.1848	
71.0000	13.0000	48.9944	0.7651	30.1629	-9.6973	14.1651	-19.7352	-1.8823	-30.2383	-20.9533	-42.6073	Total internal reflection occurs at the interface, causing loss L_{br}		
72.0000	12.0000	48.4229	-0.5203	29.2091	-11.2739	12.7129	-21.6755	-4.1546	-32.7319	-25.2805	-46.3169			
73.0000	11.0000	47.8598	-1.8038	28.2577	-12.8524	11.2381	-23.6336	-6.5439	-35.2999	-30.4550	-50.4785			
74.0000	10.0000	47.3044	-3.0857	27.3068	-14.4339	9.7355	-25.6126	-9.0792	-37.9589	-37.2433	-55.4622			
75.0000	9.0000	46.7556	-4.3664	26.3547	-16.0192	8.1993	-27.6162	-11.7996	-40.7316	-49.7846	-63.1555			

Table 2.3. Incident angles at the different faces of the SV-PLC with varying α angles for material of RI 1.58.

Material Refractive Index: 1.58 | Reflective face angle, θ: 40°														
α	i_{11}	i_{12}	i_{21}	i_{22}	i_{31}	i_{32}	i_{41}	i_{42}	i_{51}	i_{52}	i_{61}	i_{62}	i_{71}	i_{72}
41.0000	39.0000	85.0438	38.0770	78.0662	37.2499	74.0467	36.4751	70.9553	35.7386	68.3685	35.0326	66.1093	34.3521	64.0842
42.0000	38.0000	78.6439	36.3437	71.4729	34.8702	66.6138	33.5091	62.7354	32.2305	59.4308	31.0169	56.5116	29.8566	53.8722
43.0000	37.0000	74.9968	34.6773	67.0356	32.6381	61.4555	30.7736	56.9469	29.0346	53.0754	27.3927	49.6340	25.8289	46.5050
44.0000	36.0000	72.2557	33.0629	63.5509	30.5128	57.3487	28.1974	52.2983	26.0478	47.9355	24.0237	44.0360	22.0987	40.4715
45.0000	35.0000	70.0093	31.4896	60.6272	28.4689	53.8692	25.7399	48.3306	23.2129	43.5194	20.8362	39.1956	18.5759	35.2211
46.0000	34.0000	68.0838	29.9501	58.0801	26.4899	50.8121	23.3747	44.8202	20.4940	39.5861	17.7845	34.8554	15.2047	30.4810
47.0000	33.0000	66.3868	28.4388	55.8056	24.5642	48.0606	21.0837	41.6383	17.8663	35.9961	14.8371	30.8660	11.9471	26.0915
48.0000	32.0000	64.8619	26.9518	53.7386	22.6831	45.5407	18.8536	38.7033	15.3119	32.6605	11.9712	27.1308	8.7752	21.9481
49.0000	31.0000	63.4721	25.4859	51.8351	20.8399	43.2022	16.6741	35.9592	12.8167	29.5178	9.1692	23.5826	5.6673	17.9765
50.0000	30.0000	62.1915	24.0384	50.0637	19.0292	41.0089	14.5371	33.3656	10.3698	26.5231	6.4171	20.1711	2.6058	14.1193
51.0000	29.0000	61.0009	22.6072	48.4013	17.2466	38.9341	12.4358	30.8921	7.9621	23.6421	3.7030	16.8568	-0.4245	10.3293
52.0000	28.0000	59.8862	21.1906	46.8300	15.4885	36.9570	10.3648	28.5150	5.5861	20.8472	1.0168	13.6066	-3.4371	6.5644
53.0000	27.0000	58.8359	19.7870	45.3359	13.7518	35.0612	8.3193	26.2152	3.2351	18.1156	-1.6505	10.3916	-6.4448	2.7847
54.0000	26.0000	57.8413	18.3950	43.9078	12.0338	33.2332	6.2951	23.9767	0.9033	15.4273	-4.3073	7.1848	-9.4598	-1.0513
55.0000	25.0000	56.8951	17.0135	42.5365	10.3321	31.4621	4.2888	21.7858	-1.4146	12.7646	-6.9615	3.9596	-12.4951	-4.9894
56.0000	24.0000	55.9914	15.6416	41.2143	8.6448	29.7383	2.2969	19.6306	-3.7236	10.1105	-9.6210	0.6885	-15.5642	-9.0843
57.0000	23.0000	55.1250	14.2782	39.9346	6.9699	28.0538	0.3166	17.5003	-6.0284	7.4484	-12.2938	-2.6591	-18.6826	-13.4062
58.0000	22.0000	54.2919	12.9226	38.6921	5.3058	26.4013	-1.6549	15.3848	-8.3337	4.7617	-14.9884	-6.1188	-21.8683	-18.0527
59.0000	21.0000	53.4884	11.5740	37.4818	3.6510	24.7745	-3.6202	13.2744	-10.6439	2.0321	-17.7140	-9.7344	-25.1432	-23.1710
60.0000	20.0000	52.7114	10.2317	36.2994	2.0041	23.1675	-5.5818	11.1596	-12.9639	-0.7601	-20.4811	-13.5631	-28.5358	-29.0106
61.0000	19.0000	51.9581	8.8953	35.1413	0.3638	21.5748	-7.5422	9.0308	-15.2986	-3.6382	-23.3018	-17.6845	-32.0848	-36.0703
62.0000	18.0000	51.2261	7.5639	34.0040	-1.2712	19.9913	-9.5037	6.8778	-17.6532	-6.6301	-26.1907	-22.2177	-35.8463	-45.7303
63.0000	17.0000	50.5134	6.2373	32.8845	-2.9020	18.4119	-11.4688	4.6898	-20.0338	-9.7709	-29.1661	-27.3592	-39.9094	
64.0000	16.0000	49.8180	4.9148	31.7798	-4.5297	16.8318	-13.4399	2.4547	-22.4467	-13.1069	-32.2518	-33.4837	-44.4363	
65.0000	15.0000	49.1383	3.5961	30.6874	-6.1555	15.2459	-15.4196	0.1587	-24.8996	-16.7021	-35.4802	-41.5201	-49.8047	
66.0000	14.0000	48.4726	2.2806	29.6048	-7.7804	13.6493	-17.4106	-2.2145	-27.4014	-20.6517	-38.8980	-56.9333	-58.0291	
67.0000	13.0000	47.8196	0.9680	28.5295	-9.4054	12.0365	-19.4158	-4.6843	-29.9628	-25.1084	-42.5786			
68.0000	12.0000	47.1780	-0.3421	27.4594	-11.0317	10.4019	-21.4383	-7.2754	-32.5973	-30.3516	-46.6512			
69.0000	11.0000	46.5465	-1.6501	26.3923	-12.6602	8.7394	-23.4816	-10.0195	-35.3220	-37.0135	-51.3957			
70.0000	10.0000	45.9242	-2.9563	25.3259	-14.2921	7.0423	-25.5496	-12.9592	-38.1598	-47.5353	-57.8309			
71.0000	9.0000	45.3100	-4.2612	24.2580	-15.9284	5.3027	-27.6467	-16.1550	-41.1426					
72.0000	8.0000	44.7028	-5.5649	23.1865	-17.5704	3.5119	-29.7781	-19.6982	-44.3176	Total internal reflection occurs at the interface, causing loss L_{br}				
73.0000	7.0000	44.1019	-6.8679	22.1092	-19.2192	1.6595	-31.9498	-23.7389	-47.7610					
74.0000	6.0000	43.5063	-8.1705	21.0236	-20.8762	-0.2670	-34.1690	-28.5602	-51.6125					
75.0000	5.0000	42.9151	-9.4730	19.9274	-22.5427	-2.2828	-36.4446	-34.8422	-56.1974					

2.4.2.2 Calculation of cumulative transmission (T_{cab})

To calculate the light intensity at the different faces, the Fresnel equation (refer to Equations 1.7 and 1.8) of light through the interfaces is used as follows:

$$T_{\perp a1} = \frac{4n_{material}\cos(i_{a1}) * n_{air}\cos(r_{a1})}{[n_{material}\cos(i_{a1}) + n_{air}\cos(r_{a1})]^2} \tag{2.16}$$

$$T_{\perp a2} = \frac{4n_{air}\cos(i_{a2}) * n_{material}\cos(r_{a2})}{[n_{air}\cos(i_{a2}) + n_{material}\cos(r_{a2})]^2} \tag{2.17}$$

$$T_{\parallel a1} = \frac{4n_{material}\cos(i_{a1}) * n_{air}\cos(r_{a1})}{[n_{material}\cos(r_{a1}) + n_{air}\cos(i_{a1})]^2} \tag{2.18}$$

$$T_{\perp a2} = \frac{4n_{air}\cos(i_{a2}) * n_{material}\cos(r_{a2})}{[n_{air}\cos(r_{a2}) + n_{material}\cos(i_{a2})]^2} \quad (2.19)$$

The mean of $T_\perp$ and $T_\parallel$ is the T_c value of an interface. $T_{\perp a1}, T_{\perp a2}, T_{\parallel a1}, T_{\parallel a2}$ are transmittance of s and p polarized light rays at different faces, where a1 and a2 represent the annotation of faces as discussed in the Design & Methodology section.

T_c (in %) at the different interfaces of the different parameter settings of the SV-PLC with materials with RI 1.49, 1.52, and 1.58 is tabulated as shown in Tables 2.4, 2.5, and 2.6, respectively. The red-marked region shows very meagre T_c values, which are attributed to the higher incident angles at the interfaces, causing high $L_{fresnel}$ losses. The tabulated values, along with the number of grooves the individual rays (range of rays in length) are passing, and the length of the SV-PLC, determine the basis of the developed mathematical model, which will be discussed in the following sections.

Table 2.4. Cumulative light transmission (%) at the different faces of the SV-PLC with varying α angles for material of RI 1.49.

Material Refractive Index: 1.49 | Reflective face angle, θ: 43°														
α	(%)T_{C11}	(%)T_{C12}	(%)T_{C21}	(%)T_{C22}	(%)T_{C31}	(%)T_{C32}	(%)T_{C41}	(%)T_{C42}	(%)T_{C51}	(%)T_{C52}	(%)T_{C61}	(%)T_{C62}	(%)T_{C71}	(%)T_{C72}
44.0000	33.8905	9.2092	6.1659	3.9418	3.0072	2.2328	1.8150	1.4479	1.2230	1.0184	0.8827	0.7566	0.6680	0.5845
45.0000	67.8474	41.8460	34.2703	27.0155	23.5275	20.0304	17.9938	15.9175	14.5662	13.1813	12.2091	11.2131	10.4739	9.7187
46.0000	78.0454	56.0992	49.1272	41.5882	37.8672	33.8138	31.3848	28.7628	26.9934	25.1096	23.7298	22.2818	21.1555	19.9896
47.0000	83.4371	64.5634	58.4395	51.3100	47.7232	43.6463	41.1233	38.3407	36.3840	34.2854	32.6767	30.9918	29.6193	28.2091
48.0000	86.7833	70.2099	64.7778	58.1468	54.7254	50.7602	48.2096	45.3893	43.3171	41.1098	39.3421	37.5118	35.9593	34.3850
49.0000	89.0398	74.2352	69.3249	63.1521	59.8631	56.0331	53.4639	50.6447	48.4829	46.2096	44.3170	42.3849	40.6907	38.9957
50.0000	90.6420	77.2342	72.7106	66.9315	63.7362	60.0323	57.4404	54.6324	52.3935	50.0732	48.0773	46.0672	44.2579	42.4688
51.0000	91.8206	79.5408	75.3032	69.8558	66.7221	63.1267	60.5070	57.7105	55.4029	53.0453	50.9620	48.8889	46.9849	45.1200
52.0000	92.7102	81.3586	77.3328	72.1638	69.0673	65.5626	62.9116	60.1239	57.7548	55.3653	53.2077	51.0819	49.1001	47.1724
53.0000	93.3948	82.8192	78.9502	74.0154	70.9388	67.5088	64.8248	62.0427	59.6187	57.2009	54.9803	52.8096	50.7636	48.7836
54.0000	93.9297	84.0114	80.2586	75.5217	72.4525	69.0838	66.3668	63.5872	61.1145	58.6711	56.3974	54.1878	52.0892	50.0651
55.0000	94.3525	84.9977	81.3304	76.7618	73.6915	70.3729	67.6239	64.8443	62.3289	59.8622	57.5436	55.3003	53.1588	51.0971
56.0000	94.6900	85.8228	82.2182	77.7933	74.7163	71.4386	68.6595	65.8777	63.3252	60.8371	58.4811	56.2082	54.0315	51.9381
57.0000	94.9613	86.5200	82.9607	78.6593	75.5718	72.3275	69.5205	66.7352	64.1505	61.6427	59.2556	56.9568	54.7510	52.6305
58.0000	95.1808	87.1142	83.5869	79.3923	76.2922	73.0751	70.2427	67.4526	64.8405	62.3146	59.9014	57.5799	55.3490	53.2056
59.0000	95.3591	87.6245	84.1193	80.0174	76.9036	73.7086	70.8533	68.0577	65.4221	62.8796	60.4444	58.1030	55.8486	53.6858
60.0000	95.5045	88.0658	84.5752	80.5540	77.4262	74.2491	71.3736	68.5717	65.9162	63.3585	60.9037	58.5451	56.2653	54.0864
61.0000	95.6233	88.4499	84.9681	81.0176	77.8759	74.7133	71.8200	69.0115	66.3389	63.7673	61.2937	58.9201	56.6081	54.4159
62.0000	95.7206	88.7861	85.3089	81.4205	78.2655	75.1144	72.2056	69.3903	66.7026	64.1183	61.6244	59.2379	56.8786	54.6754
63.0000	95.8003	89.0821	85.6062	81.7725	78.6051	75.4630	72.5407	69.7185	67.0166	64.4209	61.9015	59.5044	57.0686	54.8563
64.0000	95.8655	89.3439	85.8670	82.0816	78.9028	75.7678	72.8336	70.0045	67.2880	64.6821	62.1271	59.7212	57.1539	54.9336
65.0000	95.9188	89.5766	86.0970	82.3545	79.1653	76.0355	73.0907	70.2549	67.5215	64.9067	62.2977	59.8848	57.0798	54.8508
66.0000	95.9623	89.7843	86.3011	82.5965	79.3979	76.2721	73.3173	70.4748	67.7199	65.0974	62.4025	59.9845	56.7219	54.4801
67.0000	95.9977	89.9706	86.4829	82.8121	79.6052	76.4820	73.5170	70.6683	67.8833	65.2546	62.4185	59.9970	55.7629	53.4955
68.0000	96.0264	90.1382	86.6458	83.0051	79.7907	76.6691	73.6929	70.8383	68.0095	65.3758	62.3001	59.8763	53.1536	50.8243
69.0000	96.0495	90.2898	86.7925	83.1786	79.9574	76.8366	73.8467	70.9866	68.0920	65.4550	61.9540	59.5285	41.8401	39.4077
70.0000	96.0681	90.4273	86.9252	83.3352	80.1076	76.9868	73.9792	71.1142	68.1186	65.4801	61.1716	58.7434		
71.0000	96.0828	90.5525	87.0458	83.4771	80.2432	77.1219	74.0899	71.2207	68.0677	65.4298	59.3969	56.9616		
72.0000	96.0944	90.6670	87.1559	83.6062	80.3656	77.2433	74.1771	71.3046	67.9007	65.2659	54.5222	52.0782		
73.0000	96.1034	90.7720	87.2568	83.7241	80.4759	77.3523	74.2372	71.3624	67.5457	64.9175	Total internal reflection occurs at the interface, causing loss L_{br}			
74.0000	96.1104	90.8686	87.3497	83.8320	80.5746	77.4494	74.2640	71.3881	66.8597	64.2429				
75.0000	96.1156	90.9578	87.4355	83.9313	80.6619	77.5350	74.2475	71.3722	65.5187	62.9217				

Table 2.5. Cumulative light transmission (%) at the different faces of the SV-PLC with varying α angles for material of RI 1.52.

Material Refractive Index: 1.52 | Reflective face angle, θ: 42˚														
α	$(\%)T_{C11}$	$(\%)T_{C12}$	$(\%)T_{C21}$	$(\%)T_{C22}$	$(\%)T_{C31}$	$(\%)T_{C32}$	$(\%)T_{C41}$	$(\%)T_{C42}$	$(\%)T_{C51}$	$(\%)T_{C52}$	$(\%)T_{C61}$	$(\%)T_{C62}$	$(\%)T_{C71}$	$(\%)T_{C72}$
43.0000	32.5424	8.3826	5.6042	3.5806	2.7287	2.0254	1.6444	1.3109	1.1057	0.9198	0.7959	0.6813	0.6004	0.5245
44.0000	67.6813	41.7090	34.1042	26.8709	23.3573	19.8627	17.8041	15.7241	14.3543	12.9638	11.9763	10.9744	10.2224	9.4619
45.0000	77.8947	55.9931	48.9320	41.3824	37.5879	33.5075	31.0162	28.3635	26.5409	24.6271	23.2018	21.7262	20.5614	19.3711
46.0000	83.2595	64.4222	58.1679	51.0020	47.3039	43.1730	40.5534	37.7141	35.6736	33.5209	31.8400	30.1058	28.6719	27.2183
47.0000	86.5772	70.0240	64.4288	57.7374	54.1739	50.1303	47.4551	44.5548	42.3740	40.0913	38.2301	36.3318	34.7000	33.0666
48.0000	88.8088	74.0065	68.9064	62.6515	59.1955	55.2655	52.5493	49.6300	47.3403	44.9738	42.9715	40.9563	39.1697	37.4031
49.0000	90.3901	76.9668	72.2317	66.3512	62.9686	59.1461	56.3894	53.4644	51.0826	48.6546	46.5369	44.4316	42.5206	40.6504
50.0000	91.5512	79.2393	74.7721	69.2061	65.8687	62.1386	59.3401	56.4125	53.9505	51.4733	49.2594	47.0816	45.0696	43.1162
51.0000	92.4261	81.0271	76.7565	71.4537	68.1401	64.4869	61.6459	58.7152	56.1831	53.6643	51.3698	49.1320	47.0378	45.0165
52.0000	93.0981	82.4611	78.3346	73.2526	69.9478	66.3573	63.4746	60.5395	57.9459	55.3910	53.0292	50.7406	48.5797	46.5020
53.0000	93.6223	83.6297	79.6086	74.7125	71.4061	67.8665	64.9439	62.0029	59.3559	56.7690	54.3510	52.0190	49.8041	47.6794
54.0000	94.0358	84.5949	80.6502	75.9116	72.5967	69.0981	66.1382	63.1900	60.4968	57.8814	55.4167	53.0476	50.7888	48.6248
55.0000	94.3652	85.4010	81.5113	76.9067	73.5791	70.1134	67.1192	64.1628	61.4301	58.7890	56.2858	53.8845	51.5900	49.3930
56.0000	94.6294	86.0811	82.2299	77.7402	74.3972	70.9579	67.9326	64.9675	62.2011	59.5368	57.0017	54.5726	52.2483	50.0235
57.0000	94.8426	86.6597	82.8350	78.4440	75.0844	71.6661	68.6131	65.6388	62.8439	60.1588	57.5971	55.1439	52.7928	50.5449
58.0000	95.0154	87.1558	83.3483	79.0428	75.6663	72.2645	69.1871	66.2033	63.3844	60.6804	58.0958	55.6220	53.2435	50.9764
59.0000	95.1558	87.5841	83.7870	79.5556	76.1626	72.7738	69.6750	66.6817	63.8424	61.1215	58.5156	56.0240	53.6124	51.3295
60.0000	95.2702	87.9563	84.1645	79.9977	76.5888	73.2100	70.0927	67.0900	64.2329	61.4968	58.8688	56.3621	53.9030	51.6071
61.0000	95.3635	88.2816	84.4912	80.3809	76.9573	73.5860	70.4527	67.4408	64.5675	61.8178	59.1629	56.6437	54.1076	51.8009
62.0000	95.4396	88.5673	84.7758	80.7149	77.2778	73.9120	70.7648	67.7440	64.8544	62.0928	59.4006	56.8712	54.2008	51.8842
63.0000	95.5016	88.8197	85.0250	81.0077	77.5583	74.1963	71.0368	68.0075	65.0994	62.3274	59.5785	57.0411	54.1217	51.7940
64.0000	95.5521	89.0436	85.2446	81.2655	77.8052	74.4456	71.2746	68.2372	65.3058	62.5250	59.6846	57.1410	53.7262	51.3809
65.0000	95.5931	89.2431	85.4390	81.4937	78.0237	74.6653	71.4829	68.4379	65.4739	62.6860	59.6920	57.1439	52.6235	50.2410
66.0000	95.6262	89.4218	85.6120	81.6966	78.2180	74.8598	71.6649	68.6128	65.6010	62.8076	59.5458	56.9941	49.3545	46.8780
67.0000	95.6528	89.5823	85.7669	81.8778	78.3914	75.0327	71.8227	68.7643	65.6793	62.8823	59.1286	56.5726	25.4656	23.2545
68.0000	95.6741	89.7271	85.9062	82.0404	78.5467	75.1869	71.9571	68.8931	65.6940	62.8954	58.1601	55.5959		
69.0000	95.6910	89.8583	86.0321	82.1869	78.6861	75.3246	72.0676	68.9989	65.6178	62.8200	55.8037	53.2204		
70.0000	95.7043	89.9776	86.1464	82.3194	78.8111	75.4476	72.1518	69.0796	65.4007	62.6064	47.8683	45.2761		
71.0000	95.7146	90.0865	86.2506	82.4397	78.9229	75.5571	72.2053	69.1308	64.9454	62.1584	Total internal reflection occurs at the interface, causing loss L_{br}			
72.0000	95.7225	90.1863	86.3461	82.5493	79.0221	75.6539	72.2201	69.1450	64.0445	61.2700				
73.0000	95.7285	90.2779	86.4339	82.6495	79.1088	75.7383	72.1836	69.1098	62.1768	59.4252				
74.0000	95.7330	90.3625	86.5148	82.7414	79.1826	75.8098	72.0748	69.0051	57.5686	54.8759				
75.0000	95.7362	90.4407	86.5895	82.8256	79.2423	75.8676	71.8592	68.7972	34.2153	32.1547				

Table 2.6. Cumulative light transmission (%) at the different faces of the SV-PLC with varying α angles for material of RI 1.58.

Material Refractive Index: 1.58 | Reflective face angle, θ: 40°														
α	$(\%)T_{C11}$	$(\%)T_{C12}$	$(\%)T_{C21}$	$(\%)T_{C22}$	$(\%)T_{C31}$	$(\%)T_{C32}$	$(\%)T_{C41}$	$(\%)T_{C42}$	$(\%)T_{C51}$	$(\%)T_{C52}$	$(\%)T_{C61}$	$(\%)T_{C62}$	$(\%)T_{C71}$	$(\%)T_{C72}$
41.0000	42.9750	16.1328	11.0600	7.2888	5.6088	4.2155	3.4368	2.7560	2.3275	1.9412	1.6789	1.4378	1.2649	1.1040
42.0000	69.6007	44.7142	36.7229	29.1759	25.3474	21.5908	19.3008	17.0250	15.4805	13.9411	12.8178	11.6998	10.8399	9.9868
43.0000	78.6589	57.6458	50.3320	42.6710	38.6179	34.3669	31.6549	28.8427	26.8352	24.7820	23.2021	21.6072	20.3132	19.0219
44.0000	83.5277	65.3636	58.8261	51.5667	47.5835	43.2822	40.4108	37.3990	35.1419	32.8317	30.9670	29.0947	27.5068	25.9355
45.0000	86.5664	70.5158	64.5832	57.7708	53.8812	49.6413	46.6775	43.5783	41.1489	38.6839	36.6127	34.5553	32.7492	30.9815
46.0000	88.6194	74.1857	68.6961	62.2816	58.4600	54.3023	51.2645	48.1184	45.5533	42.9811	40.7484	38.5554	36.5803	34.6660
47.0000	90.0770	76.9154	71.7455	65.6662	61.8840	57.8030	54.6976	51.5202	48.8424	46.1883	43.8254	41.5274	39.4187	37.3907
48.0000	91.1479	79.0104	74.0704	68.2692	64.5037	60.4873	57.3183	54.1161	51.3426	48.6225	46.1534	43.7712	41.5562	39.4379
49.0000	91.9544	80.6573	75.8821	70.3112	66.5464	62.5820	59.3537	56.1296	53.2745	50.4992	47.9431	45.4919	43.1923	41.0013
50.0000	92.5732	81.9766	77.3192	71.9396	68.1647	64.2415	60.9584	57.7139	54.7894	51.9670	49.3398	46.8312	44.4644	42.2142
51.0000	93.0548	83.0502	78.4761	73.2562	69.4644	65.5732	62.2404	58.9764	55.9932	53.1301	50.4449	47.8882	45.4681	43.1693
52.0000	93.4339	83.9352	79.4190	74.3333	70.5208	66.6540	63.2766	59.9941	56.9615	54.0629	51.3306	48.7334	46.2705	43.9319
53.0000	93.7347	84.6729	80.1961	75.2235	71.3884	67.5402	64.1232	60.8231	57.7491	54.8194	52.0489	49.4174	46.9191	44.5479
54.0000	93.9752	85.2937	80.8425	75.9660	72.1078	68.2733	64.8217	61.5048	58.3964	55.4393	52.6374	49.9769	47.4467	45.0488
55.0000	94.1683	85.8206	81.3849	76.5903	72.7095	68.8848	65.4033	62.0704	58.9335	55.9524	53.1232	50.4385	47.8746	45.4551
56.0000	94.3240	86.2712	81.8435	77.1191	73.2168	69.3988	65.8916	62.5436	59.3827	56.3805	53.5257	50.8206	48.2132	45.7761
57.0000	94.4497	86.6591	82.2342	77.5700	73.6477	69.8340	66.3048	62.9427	59.7608	56.7403	53.8572	51.1354	48.4604	46.0086
58.0000	94.5515	86.9952	82.5691	77.9568	74.0164	70.2050	66.6569	63.2816	60.0801	57.0437	54.1239	51.3884	48.5946	46.1294
59.0000	94.6338	87.2880	82.8581	78.2907	74.3340	70.5232	66.9590	63.5714	60.3491	57.2992	54.3242	51.5779	48.5571	46.0766
60.0000	94.7004	87.5444	83.1091	78.5805	74.6092	70.7978	67.2191	63.8202	60.5729	57.5117	54.4464	51.6916	48.1982	45.6928
61.0000	94.7540	87.7701	83.3282	78.8334	74.8493	71.0363	67.4438	64.0345	60.7528	57.6825	54.4607	51.6987	47.0814	44.5213
62.0000	94.7972	87.9697	83.5207	79.0551	75.0598	71.2444	67.6373	64.2188	60.8859	57.8087	54.3016	51.5325	43.3306	40.6219
63.0000	94.8318	88.1470	83.6908	79.2506	75.2454	71.4269	67.8026	64.3760	60.9630	57.8811	53.8194	51.0394		
64.0000	94.8593	88.3052	83.8419	79.4237	75.4094	71.5875	67.9408	64.5073	60.9650	57.8808	52.6177	49.8148		
65.0000	94.8811	88.4469	83.9769	79.5777	75.5547	71.7291	68.0513	64.6121	60.8552	57.7713	49.2594	46.4030		
66.0000	94.8982	88.5744	84.0980	79.7153	75.6834	71.8540	68.1309	64.6877	60.5620	57.4809	27.8035	25.3349		
67.0000	94.9114	88.6896	84.2074	79.8388	75.7969	71.9635	68.1733	64.7279	59.9337	56.8586				
68.0000	94.9215	88.7939	84.3065	79.9502	75.8958	72.0587	68.1674	64.7221	58.6036	55.5388				
69.0000	94.9291	88.8889	84.3967	80.0508	75.9803	72.1397	68.0944	64.6519	55.4214	52.3809				
70.0000	94.9348	88.9757	84.4790	80.1420	76.0497	72.2059	67.9222	64.4862	43.4275	40.6002				
71.0000	94.9388	89.0553	84.5543	80.2248	76.1021	72.2560	67.5941	64.1698						
72.0000	94.9417	89.1285	84.6232	80.3001	76.1349	72.2872	67.0034	63.5987						
73.0000	94.9436	89.1961	84.6861	80.3683	76.1435	72.2954	65.9290	62.5571	Total internal reflection occurs at the interface, causing loss L_{br}					
74.0000	94.9448	89.2587	84.7433	80.4298	76.1211	72.2741	63.8338	60.5219						
75.0000	94.9455	89.3169	84.7949	80.4850	76.0574	72.2137	58.9775	55.8038						

Figure 2.7 shows the graph of the cumulative light transmission percentage at different faces for varied α values, where face number 0 represents the ray condition before any refraction through the groove faces. With α values very close to θ values, there is a drastic reduction in transmitted light power in the initial refracting faces themselves. This is due to the higher incident angles at these interfaces (refer to Table 1.1, 1.2, and 1.3), as the angle of incidence increases, Fresnel reflection will be more (refer to Equations 1.7 and 1.8, Figures 1.3 and 1.5). With the increase in the α value, the reduction in transmitted ray power is minimised as the incident angles at the different interfaces are reduced.

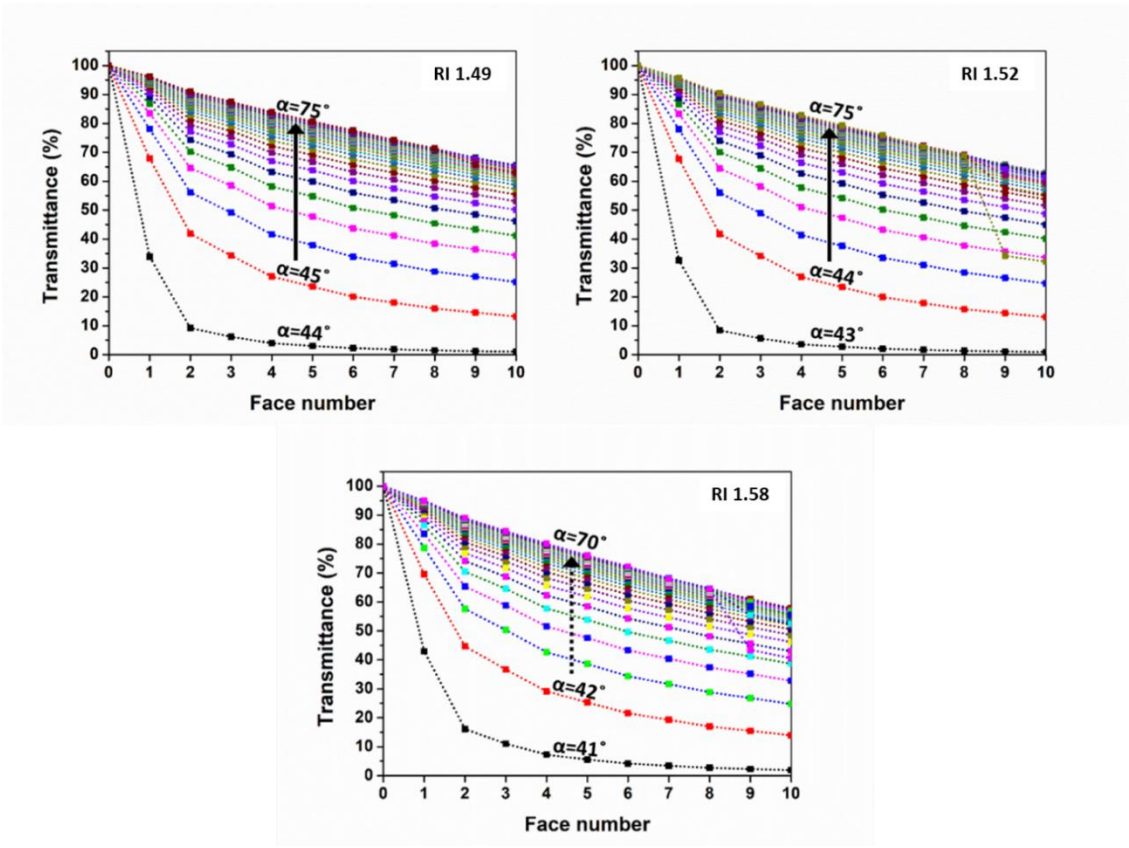

Figure 2.7. Cumulative light transmission (%) at the different faces of the SV-PLC with varying α angles for materials of RI 1.49, 1.52, and 1.58.

The maximum number of grooves a ray can pass within the SV-PLC decreases with the α value, as shown in Figure 2.11 (refer to section 2.4.4 for determination of N_{gmax} value). This is substantiated by the ray tracing simulation of an SV-PLC optics with varying α value. Figure 2.8a shows a 2D ray tracing simulation of an SV-PLC optics in a material of RI 1.49 with two α values (46° and 60°). The ray race shows that as the α value is increased, the N_{gmax} will be reduced due to the higher angular shift occurring in the ray. However, with the increase in the α, L_{100} (length of the SV-PLC, refer to section 2.4.5) will be reduced due to the higher exit angle (angle made by the ray with the horizontal). In material selection, the higher RI will result in more deviation at the interfaces, resulting in a minimum number of groove passages (Figure 2.11), thus reducing the total $L_{fresnel}$ losses. Figures 2.8b and 2.8c show the 2D ray tracing simulation of SV-PLC optics with materials of RI 1.49 and 1.58, respectively. The design considerations are taken similarly, except for the optimised parameters (θ and S). The α value is fixed (taken as 46°) to provide the comparison. The ray trace shows that for similar parameters, the material with higher RI provided fewer interfaces of ray travel (7 grooves), compared to the material with lower RI (3 grooves).

This provides less total Fresnel reflection loss for higher RI material. However, the exit angle of rays from the grooves is higher for SV-PLC with high RI material. This reduces the L_{100} of the SV-PLC compared with the SV-PLC of lower RI material, as shown in Figures 2.8b and 2.8c.

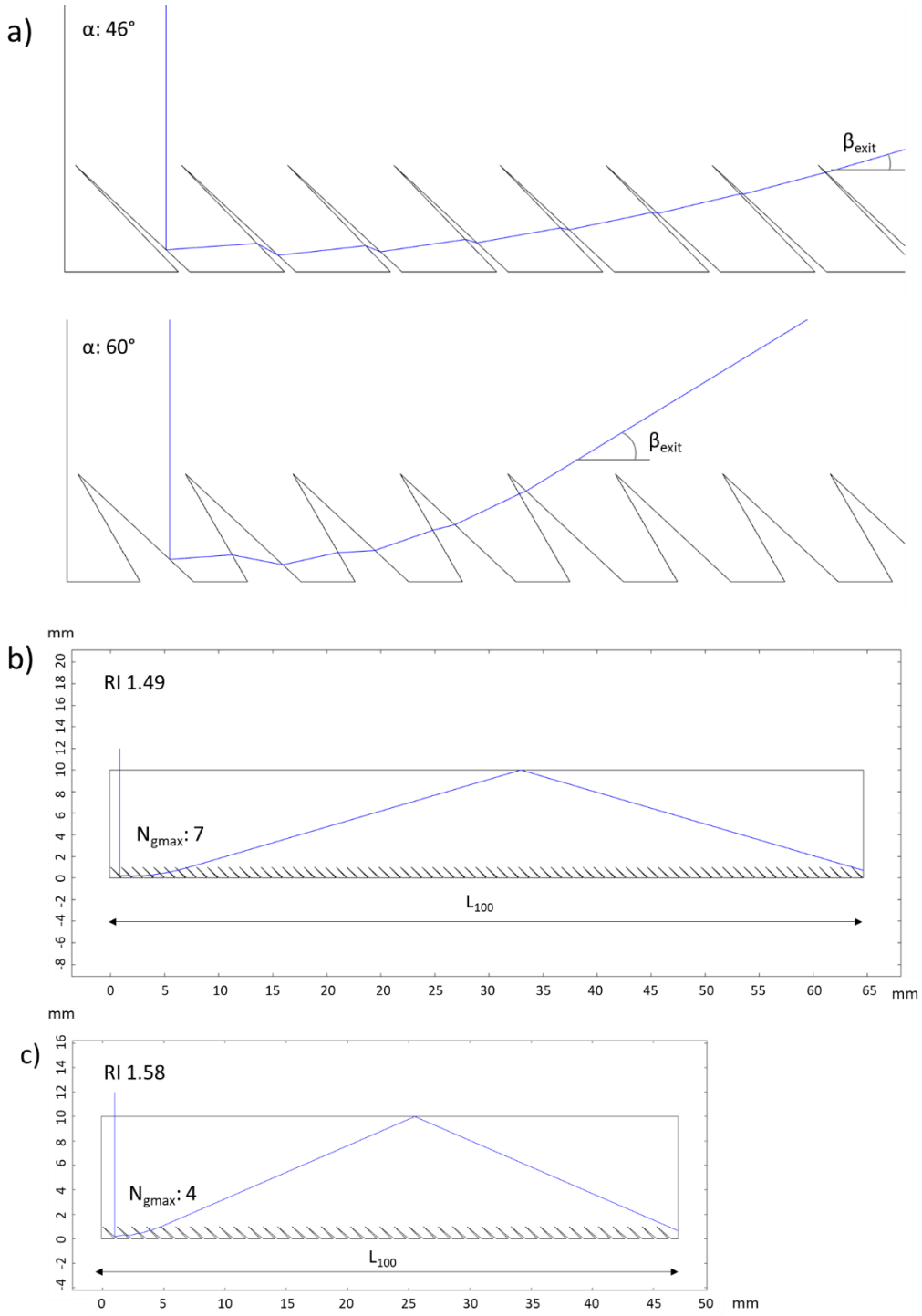

Figure 2.8. a) 2D ray tracing simulation of an SV-PLC with varying α angle (42° and 60°); b) 2D ray tracing simulation of an SV-PLC in a material of RI 1.49 and α 46°; c) 2D ray tracing simulation of an SV-PLC in a material of RI 1.52 and α 46°.

To predict the effectiveness of an SV-PLC, every possible ray trajectory and condition from a groove should be considered, i.e., not every ray assumes the same number of refractions. To predict the condition of rays from a groove, the coordinates of rays at the different interfaces should be traced. The height (h_{ab}) and the range of rays (constitutes the horizontal distance, X^n, where n is the number of grooves the ray passes, which is 0 to N_{gmax}) form the basis of the total groove analysis.

2.4.3 Derivation of h_{ab}

Consider the reflection of a random ray at the reflecting face of an SV-PLC, as shown in Figure 2.9.

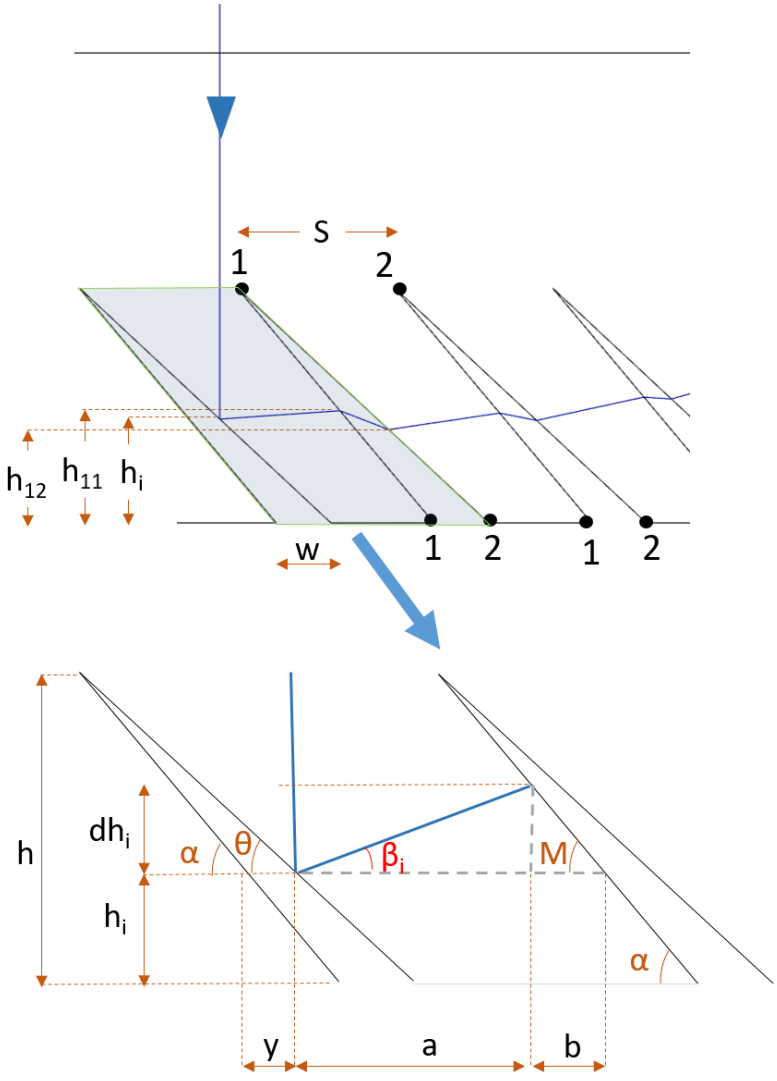

Figure 2.9. Schematic representation of ray travel (in blue color) in an SV-PLC optics showing the height position of the ray at the different interfaces (top). The highlighted area showing TIR at the incident face is detailed (bottom) with the parameters and variables.

$$a+b+y = S$$

$$y = S-(a+b) \tag{2.20}$$

$$\tan(\beta_i) = {dh_i}/{a}$$

$$\tan(M) = {dh_i}/{b}$$

Where dh represents the vertical displacement of rays.

$$M = \alpha \text{ (Corresponding angles)}$$

$$\Rightarrow \quad a+b = dh_i\left[\cot(\beta_i) + \cot(\alpha)\right] \tag{2.21}$$

$$y = (h-h_i)[\cot\theta - \cot\alpha] \tag{2.22}$$

$$\Rightarrow \quad dh_i = \frac{S+(h-h_i)[\cot(\alpha) - \cot(\theta)]}{\cot(\beta_i) + \cot(\alpha)} \text{ (from Equations 2.20, 2.21, and 2.22)}$$

where dh represents the vertical shift of the ray

Since $\beta_i = 90°-2\theta$ (Equation 2.3)

$$dh_i = \frac{S+(h-h_i)[\cot(\alpha) - \cot(\theta)]}{\tan(2\theta) + \cot(\alpha)} \tag{2.23}$$

$$h_{11} = h_i+dh_i$$

Similarly, $\beta_{a2} = 90°-\theta-r_{a2}$ (Equation 2.11)

$$\Rightarrow \quad dh_{a2} = \frac{S+(h-h_{a1})[\cot(\alpha) - \cot(\theta)]}{\tan(\theta+r_{a2}) + \cot(\alpha)} \tag{2.24}$$

$$h_{a1} = h_{(a-1)2}+dh_{(a-1)2}$$

Consider the first refraction occurring in the same ray as shown in Figure 2.10,

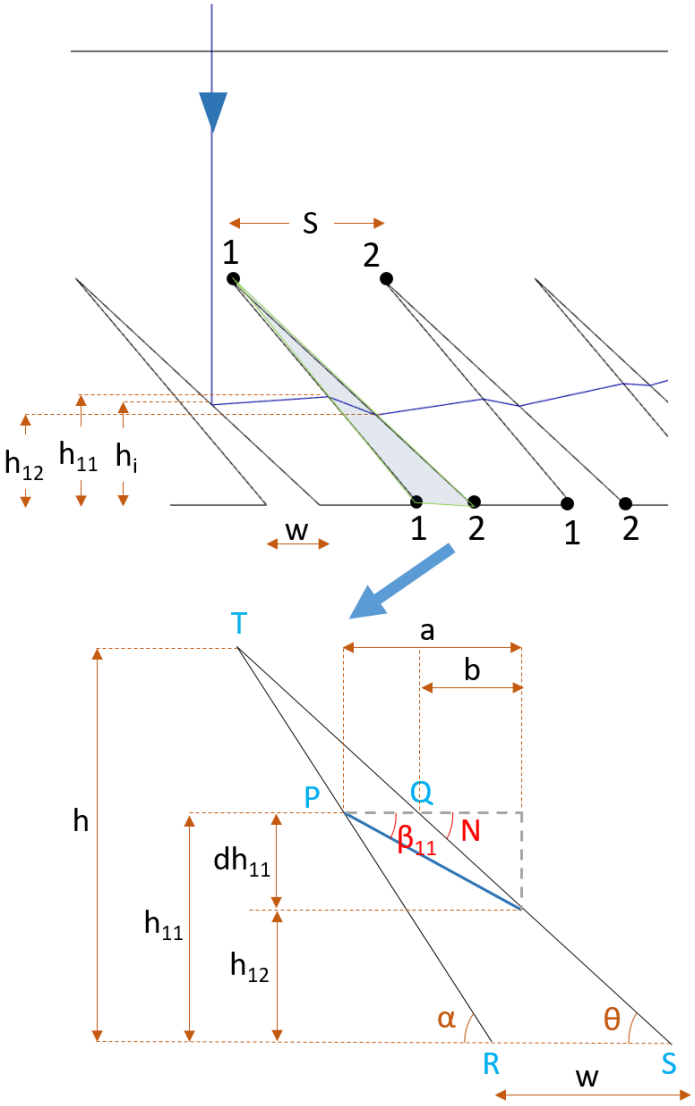

Figure 2.10. Schematic representation of ray travel (in blue color) in an SV-PLC optics showing the height position of the ray at the different interfaces (top). The highlighted area showing refraction at the incident groove interface is detailed (bottom) with the parameters and variables.

$\Delta TPQ \sim \Delta TRS$ (AAA Similarity criterion)

$$\Rightarrow \quad \frac{h-h_{11}}{h} = \frac{a-b}{w} \tag{2.25}$$

$$\tan(\beta_{11}) = {dh_{11}}/{a}$$

$$\tan(N) = {dh_{11}}/{b}$$

$N = \theta$ (Alternate interior angles)

$$\Rightarrow \quad a\text{-}b = dh_{11}\left[\cot\left(\beta_{11}\right) - \cot(\theta)\right] \tag{2.26}$$

Also, $w = h[\cot(\theta) - \cot(\alpha)]$ (2.27)

$$\Rightarrow \quad dh_{11} = \frac{(h\text{-}h_{11})[\cot(\theta) - \cot(\alpha)]}{\cot\left(\beta_{11}\right) - \cot(\theta)} \text{ (from Equations 2.25, 2.26, and 2.27)}$$

Since $\beta_{11} = \alpha + r_{11} - 90°$ (Equation 2.10)

$$\Rightarrow \quad dh_{11} = \frac{(h\text{-}h_{11})[\cot(\alpha) - \cot(\theta)]}{\tan(\alpha+r_{11}) + \cot(\theta)} \tag{2.28}$$

$$h_{12} = h_{11} + dh_{11}$$

Similarly, $\beta_{a1} = \alpha + r_{a1} - 90°$ (Equation 2.10)

$$\Rightarrow \quad dh_{a1} = \frac{(h\text{-}h_{a1})[\cot(\alpha) - \cot(\theta)]}{\tan(\alpha+r_{a1}) + \cot(\theta)} \tag{2.29}$$

$$h_{a2} = h_{a1} + dh_{a1}$$

2.4.4 Derivation of N_{gmax}

To calculate the maximum number of grooves (N_{gmax}) through which a light ray can travel in a specific SV-PLC design, the total height of light ray travel is as follows:

Total height of light ray travel $= h_i + dh_i - \sum_{k=1}^{n} dh_{a1} + \sum_{k=1}^{n} dh_{a2}$, which should be less than or equal to h, where n is the number of grooves through which the light ray is traveling, and it satisfies the above equation. Figure 2.11 shows the variation in N_{gmax} with α for different materials (RI 1.49, 1.52, and 1.58). Even though higher index materials show lower N_{gmax}, i.e., lower Fresnel losses, the length of the SV-PLC also needs to be considered, which is also a determining factor of the FC.

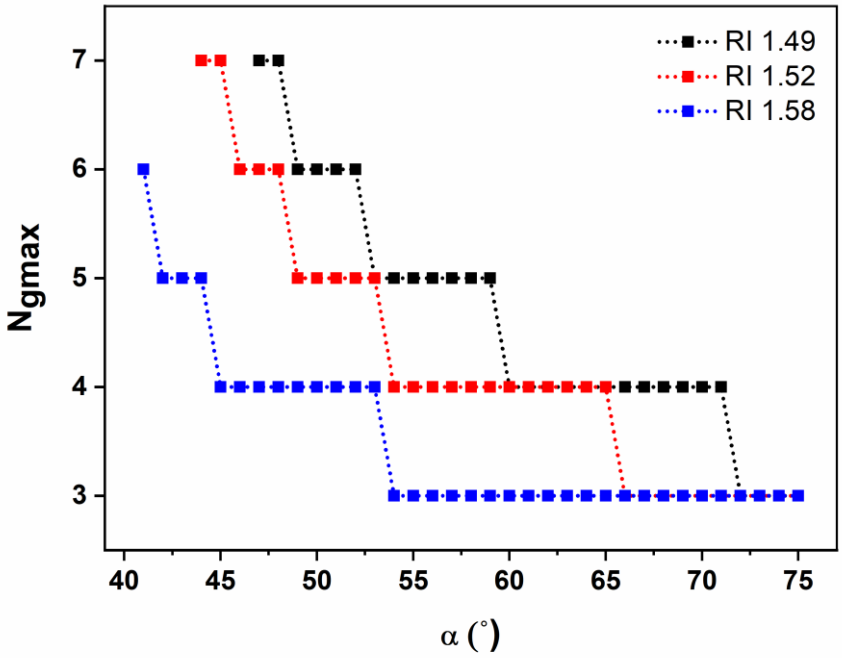

Figure 2.11. Plot depicting the relation of N_{gmax} and α for SV-PLCs with materials of RI 1.49, 1.52, and 1.58.

2.4.5 Determination of L_{100} and L_{max}

L_{100} represents the maximum length of the PLC, which can translate 100% of the light falling on the SV-PLC to the lateral face. L_{max} represents the length of the SV-PLC, from which a further increase in length does not produce any ray at the lateral face. It can include the ray loss occurring through the grooves themselves. The distinction between L_{100} and L_{max} is depicted in Figure 2.12a. Both L_{100} and L_{max} are determined by light rays coming from the bottom and top of the first groove, respectively. From L_{100} to L_{max} there will be an increased reduction in the OE, at the expense of the FC (shown in Figure 2.12b; results are simulated in COMSOL Multiphysics 6.1 (parameters: H: 10mm, h: 1mm; S: 0.98 (as per the mathematical model discussed in the section 2.4.6), α: 49°, θ: 43°). This loss can be justified by the very high FC in radial designs compared to linear designs (discussed in Chapter 4).

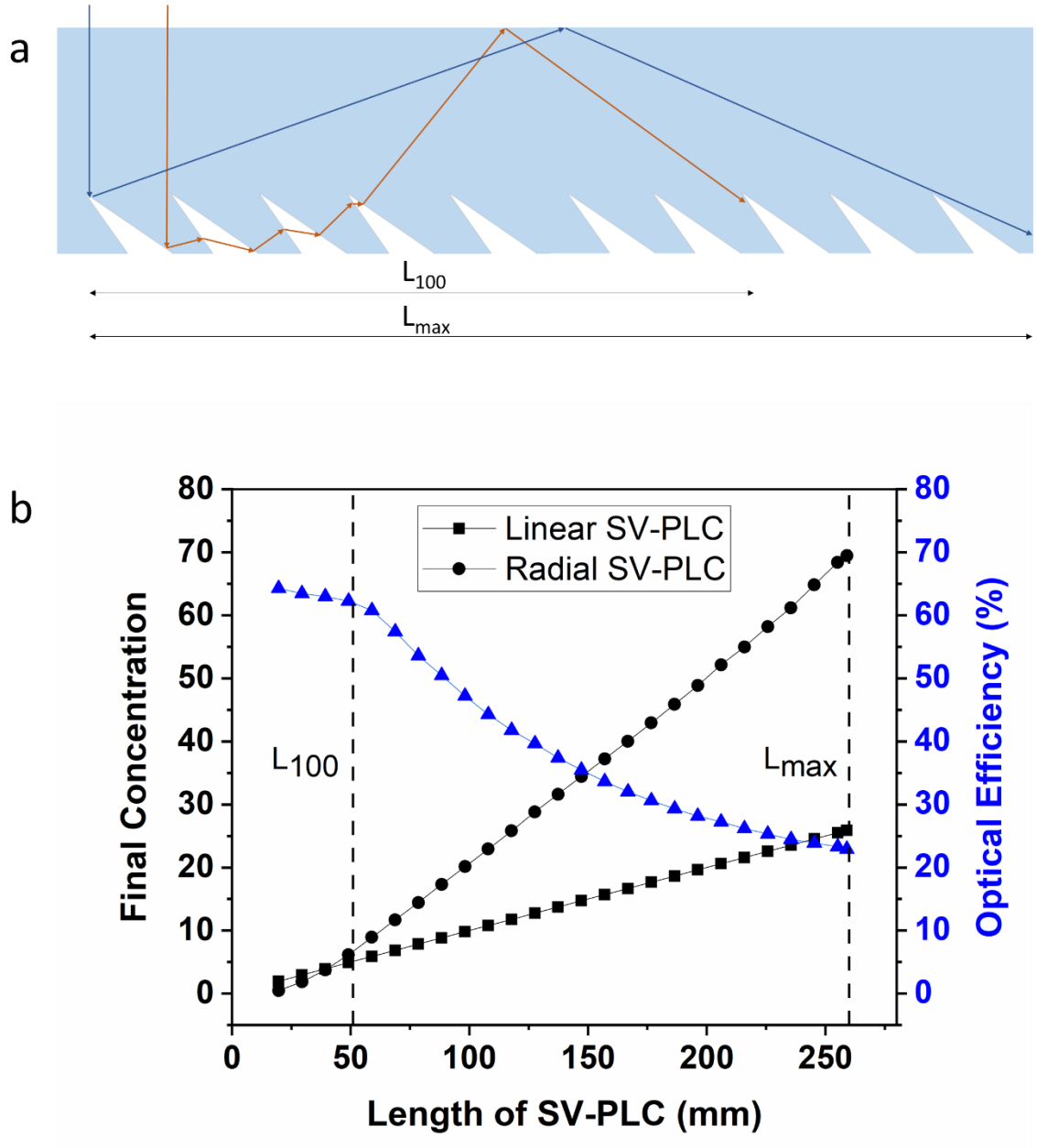

Figure 2.12. a) Schematic representation showing the distinction between L_{100} and L_{max}; b) Plot showing the relation of length of SV-PLC with the final concentration (for radial and linear designs) and Optical efficiency between L_{100} and L_{max}.

L_{100} is related to the exit angle of the ray that passes through the maximum possible number of rays in a specific SV-PLC design. Thus, L_{100} is wholly dependent on the different design parameters of the SV-PLC. Figure 2.13 shows the variation of L_{100} with varying α (the rest of the parameters are fixed) for materials of RI 1.49, 1.52, and 1.58. Unlike L_{100}, L_{max} only depends on the θ value (as L_{max} is determined with the rays that are non-refracted), which will be optimized to a minimum.

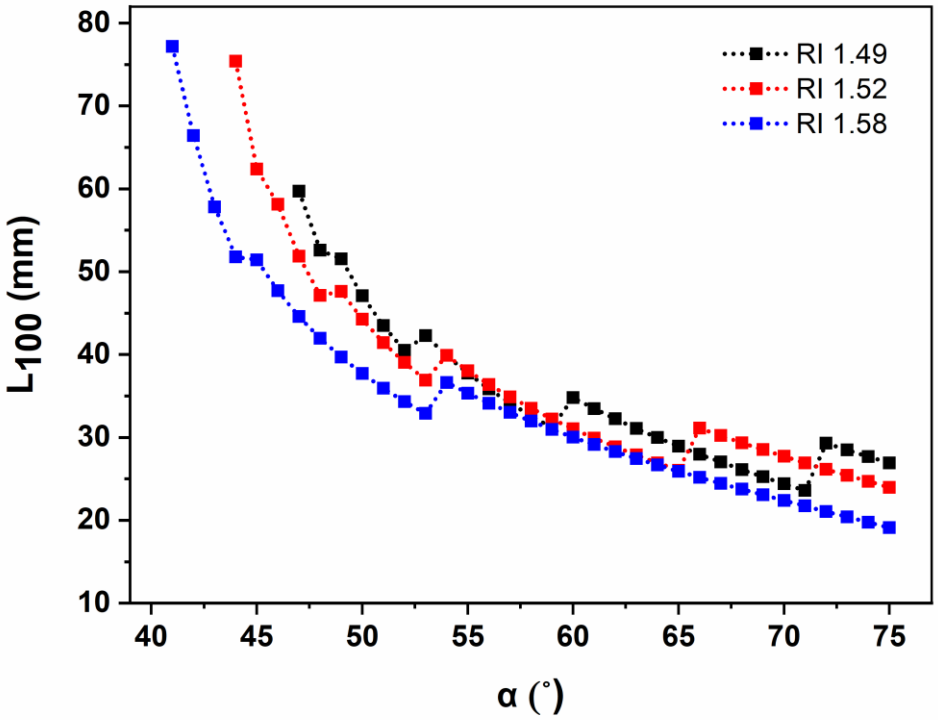

Figure 2.13. Plot depicting the value of L_{100} with varying α for SV-PLCs with materials of RI 1.49, 1.52, and 1.58.

2.4.6 Optimisation of intergroove distance (S)

For determining the transported ray power across the length of a groove in SV-PLC, the inter-groove spacing (S) for specific angular consideration of the faces is required. The inter-groove spacing is always set to a maximum value without any direct ray leakage (refer to L_{leak} loss in Figure 2.1) in the SV-PLC.

Consider the reflection and first refraction of a ray as shown in Figure 2.14. To maximize the S value without any ray leakage, the ray should coincide with point 2 of the (12) face, as shown in Figure 2.14.

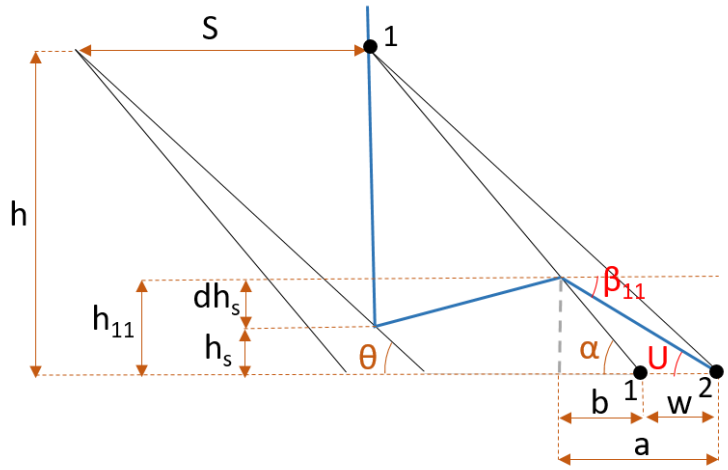

Figure 2.14. Schematic representation of ray travel (in blue color) in an SV-PLC optics representing the maximum groove space without ray leakage from the bottom; the parameters and variables are marked.

$$a-b = w \tag{2.30}$$

$$\tan(U) = {h_{11}}/{a}$$

$U = \beta_{11}$ (Alternate interior angles)

$$\Rightarrow \quad \tan(\beta_{11}) = {h_{11}}/{a}$$

$$\tan(\alpha) = {h_{11}}/{b}$$

$$\Rightarrow \quad a-b = h_{11}[\cot(\beta_{11}) - \cot(\alpha)] \tag{2.31}$$

Also $w = h[\cot(\theta) - \cot(\alpha)]$ (2.32)

$$\Rightarrow \quad h_{11} = \frac{h[\cot(\theta) - \cot(\alpha)]}{\cot(\beta_{11}) - \cot(\alpha)}$$

Since $\beta_{11} = \alpha + r_{11} - 90°$ (Equation 2.10)

$$\Rightarrow \quad h_{11} = \frac{h[\cot(\alpha) - \cot(\theta)]}{\tan(\alpha + r_{11}) + \cot(\alpha)} \tag{2.33}$$

Also $h_s + dh_s = h_{11}$

$$dh_s = \frac{S+(h-h_s)[\cot(\alpha) - \cot(\theta)]}{\tan(2\theta) + \cot(\alpha)} \text{ (from Equation 2.23)}$$

$$\Rightarrow \quad h_s = \frac{h_{11}[\tan(2\theta) + \cot(\alpha)] - h\cot(\alpha)}{\tan(2\theta)} \tag{2.34}$$

$$S = (h-h_s)\cot(\theta) \tag{2.35}$$

Keeping the θ and h values constant, the required S value is plotted against α (Figure 2.15). For materials with low RI, like PMMA, the S value is less than the groove width (the horizontal length of a groove) value to eliminate the L_{leak} loss. With the increase in RI of the material, the S value reaches the groove width at higher α values. For much higher RI materials, S will be the same as the groove width, hence the possibility of L_{leak} loss is directly eliminated for such materials, and thus helps in improving the L_{100} of the SV-PLC.

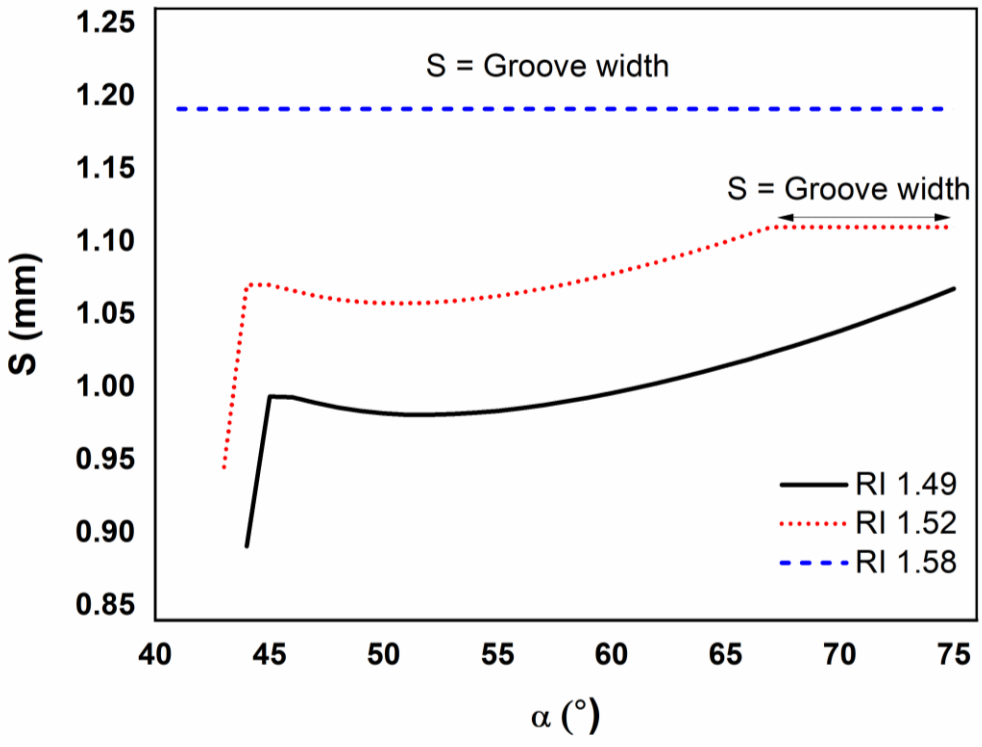

Figure 2.15. Plot showing the dependency of refraction face angle (α) on the inter-groove spacing (S) in SV-PLC for different materials with RI 1.49, 1.52, and 1.58.

2.4.7 Derivation of X^n

X^n represents the horizontal length from the groove tip up to which a ray passes through n number of grooves. X^n helps to evaluate the effectiveness of an SV-PLC by calculating the OE and FC by analyzing a single groove.

Consider the reflection of a ray as shown in Figure 2.16, showing zero fractions. To calculate X^0, the ray path should coincide with point 1 of face (11).

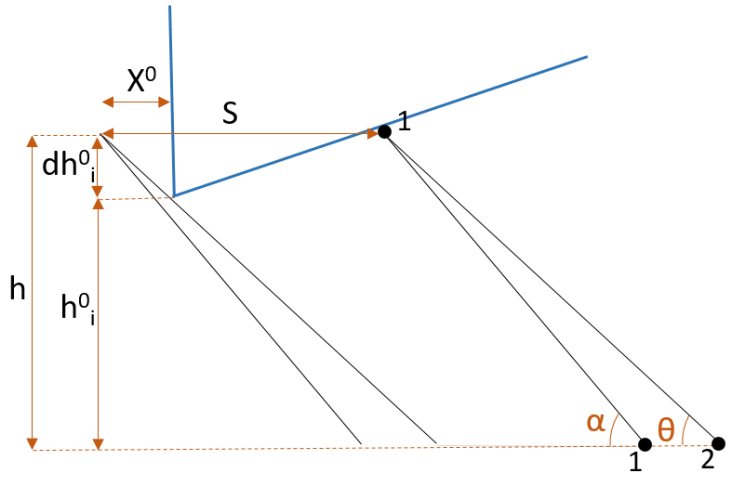

Figure 2.16. Schematic representation of ray travel (in blue color) in an SV-PLC optics representing the maximum point of length (X^0) from the tip of the groove for ray travel without any refraction; the parameters and variables are marked.

$$h_i^0 + dh_i^0 = h$$

$$dh_i^0 = \frac{S + (h - h_i^0)[\cot(\alpha) - \cot(\theta)]}{\tan(2\theta) + \cot(\alpha)} \quad \text{(from Equation 2.23)}$$

$$\Rightarrow \quad h_i^0 = \frac{h[\tan(2\theta) + \cot(\theta)] - S}{\tan(2\theta) + \cot(\theta)} \tag{2.36}$$

$$X^0 = \frac{h - h_i^0}{\tan(\theta)} \tag{2.37}$$

$$\Rightarrow \quad X^0 = \frac{S}{\tan(2\theta)\tan(\theta) + 1} \tag{2.38}$$

Consider the trajectory of a ray passing through a single groove (i.e., two refractions) as shown in Figure 2.17. To calculate X^1, the ray path should coincide with point 2 of face (21).

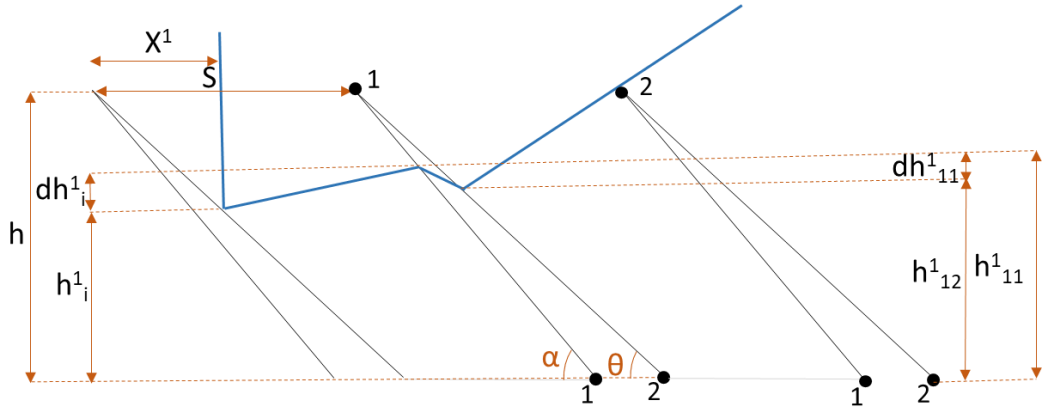

Figure 2.17. Schematic representation of ray travel (in blue color) in an SV-PLC optics representing the maximum point of length (X^0) from the tip of the groove for ray travel with single groove refractions; the parameters and variables are marked.

$$h^1_{12}+dh^1_{12} = h$$

$$dh^1_{12} = \frac{S+(h-h^1_{12})[\cot(\alpha) - \cot(\theta)]}{\tan(\theta+r_{12}) + \cot(\alpha)} \text{ (from Equation 2.24)}$$

$$\Rightarrow \quad h^1_{12} = \frac{h[\tan(\theta+r_{12}) + \cot(\theta)]-S}{\tan(\theta+r_{12}) + \cot(\theta)} \tag{2.39}$$

Also $h^1_{11}-dh^1_{11} = h^1_{12}$

$$dh^1_{11} = \frac{(h-h^1_{11})[\cot(\alpha) - \cot(\theta)]}{\tan(\alpha+r_{11}) + \cot(\theta)} \text{ (from Equation 2.29)}$$

$$\Rightarrow \quad h^1_{11} = \frac{h^1_{12}[\tan(\alpha+r_{11}) + \cot(\theta)]+h[\cot(\alpha) - \cot(\theta)]}{\tan(\alpha+r_{11}) + \cot(\alpha)} \tag{2.40}$$

$$h^1_i+dh^1_i = h^1_{11}$$

$$dh^1_i = \frac{S+(h-h^1_i)[\cot(\alpha) - \cot(\theta)]}{\tan(2\theta) + \cot(\alpha)} \text{ (from Equation 2.23)}$$

$$\Rightarrow \quad h_i^1 = \frac{h_{11}^1[\tan(2\theta) + \cot(\alpha)]\text{-}h[\cot(\alpha) - \cot(\theta)]\text{-}S}{\tan(2\theta) + \cot(\theta)} \tag{2.41}$$

$$X^1 = \frac{h\text{-}h_i^1}{\tan(\theta)} \tag{2.42}$$

Similarly,

For the final groove,

$$h_{a2}^n = \frac{h[\tan(\theta+r_{a2}) + \cot(\theta)]\text{-}S}{\tan(\theta+r_{a2}) + \cot(\theta)} \tag{2.43}$$

By using the same method of derivation, for the even face of the corresponding intermediate grooves,

$$h_{b2}^n = \frac{h_{(b+1)1}^n[tan(\theta + r_{b2}) + cot(\alpha)] - h[cot(\alpha) - cot(\theta)] - S}{tan(\theta + r_{b2}) + cot(\theta)} \tag{2.44}$$

$$h_{b1}^n = \frac{h_{b2}^n[\tan(\alpha+r_{b1}) + \cot(\theta)]+h[\cot(\alpha) - \cot(\theta)]}{\tan(\alpha+r_{b1}) + \cot(\alpha)} \tag{2.45}$$

For the corresponding incident groove,

$$h_i^n = \frac{h_{11}^n[\tan(2\theta) + \cot(\alpha)]\text{-}h[\cot(\alpha) - \cot(\theta)]\text{-}S}{\tan(2\theta) + \cot(\theta)} \tag{2.46}$$

$$X^n = \frac{h\text{-}h_i^n}{\tan(\theta)} \tag{2.47}$$

2.4.8 Optical evaluation of SV-PLC designs with the mathematical model

Considering the ambiguity created by the interdependence of different factors with the variables as discussed, the total merit of the grooves along with SV-PLC should be evaluated properly with OE, GC, and FC and length variables (L_{100} & L_{max}), which is evaluated mathematically in this chapter. For determining the efficiency of an SV-PLC, the

transported ray power from a typical groove (considered grooves with the possibility of light traveling with the maximum possible interface) should be studied. For this, the range (distance, X^n) of rays undergoing n (from 0 to a maximum number of grooves through which the rays can pass in a design) refractions should be studied individually. From Equation 2.47, this range has been determined. The T_c of light rays from a single groove was also determined earlier. The total intensity ($\Sigma T_c X^n$) from a groove has been tabulated for different materials with varying α in Tables 2.7 to 2.9. The factor $\Sigma T_c X^n/S$ (OE of a typical groove) has been used to normalize the result with the length, and its value for different materials with varying α is shown in Figure 2.18a (also tabulated in Tables 2.7 to 2.9). It shows that increasing α drastically increases the light intensity from a groove up to a limit. Further increasing α does not show much increment. This can be attributed to the higher Fresnel losses at the interfaces at lower α angles (refer to Tables 1.4 to 1.6). At lower α values, the angle of incidence at the groove interfaces will be higher (refer to Tables 1.1 to 1.3). When considering the Fresnel laws (refer to Equations 1.3 and 1.5 and Figures 1.7 and 1.8), higher angles of incidence provide drastically higher light transmission loss, which is non-linear. This creates a drastic increase in light intensity with the increase in α initially. However, higher α provides a lesser angle of incidence at different groove interfaces, which does not cause much optical transmission loss compared to the other case. Hence, the graph tends to straighten after a certain value of α. Also, the fact that it reduces the L_{100} (Figure 2.13) value should also be pointed out (refer to Figure 2.8a).

For conducting the selection of an SV-PLC, the FC (OE of a typical groove X L_{100}/H, i.e., OEXGC) should be plotted against the length of the concentration (herein, the study has been conducted for L_{100}). Figure 2.18b shows the effectiveness factor (simulated results) of different SV-PLC designs on different materials. The factor can be correlated to the theoretical FC factor of the SV-PLC. Even though the FC graph shows an overall decrease in the longer range, it also produces irregular steps in the short range. This can be attributed to the irregularity in the L_{100} value (Figure 2.13), as different designs have different ray directional paths depending on the number of grooves the rays pass. Herein, the design considerations are kept for the SV-PLC length of L_{100}, since after L_{100} there will be a drastic reduction in the OE even though the GC is high (as shown in Figure 2.12b), as much of the light rays will not reach the lateral face and will be lost through the bottom of the SV-PLC. This is the reason that there is a reducing trend in FC upon the α after L_{100}, and the design has been considered for the L_{100} length of SV-PLC.

Table 2.7. Tabulation of Optical efficiency (normalized with inter-groove spacing) ($\Sigma T_c X^n/S$) with varying α angles for material of RI 1.49.

Material Refractive Index: 1.49 | Reflective face angle, θ: 43˚																					
α	hs	S	X^0	T_0X^0	X^l	$T_{C12}X^l$	X^2	$T_{C22}X^2$	X^3	$T_{C32}X^3$	X^4	$T_{C42}X^4$	X^5	$T_{C52}X^5$	X^6	$T_{C62}X^6$	X^7	$T_{C72}X^7$	N_{gmax}	$\Sigma T_C X^n$	$\Sigma T_C X^n/S$
47.0000	0.0767	0.9895	0.0684	0.0684	0.0973	0.0628	0.1174	0.0602	0.1329	0.0580	0.1456	0.0558	0.1563	0.0536	0.1658	0.0514	0.1057	0.0298	7	0.4401	44.4804
48.0000	0.0799	0.9861	0.0682	0.0682	0.1036	0.0727	0.1271	0.0739	0.1448	0.0735	0.1592	0.0723	0.1714	0.0705	0.1821	0.0683	0.0297	0.0102	7	0.5096	51.6761
49.0000	0.0822	0.9836	0.0680	0.0680	0.1094	0.0812	0.1360	0.0859	0.1558	0.0873	0.1718	0.0870	0.1854	0.0857	0.1571	0.0666			6	0.5618	57.1098
50.0000	0.0837	0.9820	0.0679	0.0679	0.1150	0.0888	0.1444	0.0967	0.1662	0.0998	0.1838	0.1004	0.1989	0.0996	0.1058	0.0488			6	0.6019	61.2918
51.0000	0.0845	0.9812	0.0679	0.0679	0.1203	0.0957	0.1525	0.1065	0.1762	0.1112	0.1954	0.1128	0.2121	0.1125	0.0569	0.0278			6	0.6344	64.6511
52.0000	0.0846	0.9810	0.0678	0.0678	0.1254	0.1021	0.1603	0.1157	0.1859	0.1219	0.2069	0.1244	0.2252	0.1247	0.0095	0.0048			6	0.6614	67.4145
53.0000	0.0842	0.9815	0.0679	0.0679	0.1305	0.1081	0.1679	0.1243	0.1955	0.1320	0.2183	0.1354	0.2014	0.1152					5	0.6828	69.5727
54.0000	0.0833	0.9824	0.0679	0.0679	0.1354	0.1137	0.1754	0.1325	0.2051	0.1417	0.2298	0.1461	0.1688	0.0991					5	0.7010	71.3535
55.0000	0.0820	0.9838	0.0680	0.0680	0.1403	0.1192	0.1829	0.1404	0.2146	0.1510	0.2414	0.1565	0.1366	0.0818					5	0.7170	72.8777
56.0000	0.0804	0.9856	0.0682	0.0682	0.1451	0.1245	0.1903	0.1480	0.2242	0.1602	0.2533	0.1669	0.1045	0.0636					5	0.7314	74.2038
57.0000	0.0784	0.9877	0.0683	0.0683	0.1498	0.1296	0.1977	0.1555	0.2340	0.1693	0.2656	0.1772	0.0723	0.0446					5	0.7445	75.3751
58.0000	0.0760	0.9902	0.0685	0.0685	0.1546	0.1346	0.2052	0.1629	0.2439	0.1783	0.2782	0.1877	0.0399	0.0248					5	0.7568	76.4245
59.0000	0.0735	0.9930	0.0687	0.0687	0.1593	0.1396	0.2127	0.1702	0.2541	0.1873	0.2913	0.1983	0.0069	0.0043					5	0.7683	77.3773
60.0000	0.0706	0.9960	0.0689	0.0689	0.1640	0.1445	0.2203	0.1775	0.2645	0.1964	0.2783	0.1908							4	0.7780	78.1137
61.0000	0.0675	0.9993	0.0691	0.0691	0.1688	0.1493	0.2280	0.1847	0.2752	0.2056	0.2582	0.1782							4	0.7869	78.7477
62.0000	0.0642	1.0029	0.0694	0.0694	0.1736	0.1541	0.2359	0.1921	0.2863	0.2150	0.2378	0.1650							4	0.7955	79.3278
63.0000	0.0607	1.0066	0.0696	0.0696	0.1784	0.1589	0.2439	0.1994	0.2978	0.2247	0.2170	0.1513							4	0.8039	79.8638
64.0000	0.0570	1.0106	0.0699	0.0699	0.1832	0.1637	0.2521	0.2069	0.3097	0.2346	0.1957	0.1370							4	0.8122	80.3639
65.0000	0.0531	1.0148	0.0702	0.0702	0.1881	0.1685	0.2605	0.2145	0.3221	0.2449	0.1739	0.1222							4	0.8203	80.8345
66.0000	0.0490	1.0192	0.0705	0.0705	0.1931	0.1734	0.2691	0.2222	0.3351	0.2556	0.1515	0.1067							4	0.8284	81.2813
67.0000	0.0447	1.0238	0.0708	0.0708	0.1981	0.1783	0.2779	0.2302	0.3487	0.2667	0.1283	0.0906							4	0.8365	81.7090
68.0000	0.0402	1.0286	0.0711	0.0711	0.2032	0.1832	0.2870	0.2383	0.3630	0.2783	0.1042	0.0738							4	0.8447	82.1215
69.0000	0.0356	1.0336	0.0715	0.0715	0.2084	0.1882	0.2965	0.2466	0.3780	0.2905	0.0792	0.0562							4	0.8529	82.5225
70.0000	0.0308	1.0387	0.0718	0.0718	0.2137	0.1933	0.3062	0.2552	0.3940	0.3033	0.0530	0.0377							4	0.8613	82.9152
71.0000	0.0258	1.0441	0.0722	0.0722	0.2191	0.1984	0.3163	0.2640	0.4109	0.3169	0.0257	0.0183							4	0.8698	83.3027
72.0000	0.0206	1.0497	0.0726	0.0726	0.2246	0.2036	0.3268	0.2732	0.4257	0.3288									3	0.8783	83.6702
73.0000	0.0152	1.0554	0.0730	0.0730	0.2302	0.2090	0.3377	0.2827	0.4146	0.3207									3	0.8854	83.8842
74.0000	0.0096	1.0614	0.0734	0.0734	0.2360	0.2144	0.3490	0.2926	0.4030	0.3121									3	0.8926	84.0910
75.0000	0.0039	1.0676	0.0738	0.0738	0.2419	0.2200	0.3609	0.3029	0.3910	0.3032									3	0.8999	84.2917

Table 2.8. Tabulation of Optical efficiency (normalized with inter-groove spacing) ($\Sigma T_c X^n/S$) with varying α angles for material of RI 1.52.

α	hs	S	X^0	T_0X^0	X^1	$T_{C1}X^1$	X^2	$T_{C2}X^2$	X^3	$T_{C3}X^3$	X^4	$T_{C4}X^4$	X^5	$T_{C5}X^5$	X^6	$T_{C6}X^6$	N_{gmax}	$\Sigma T_c X^n$	$\Sigma T_c X^n/S$
46.0000	0.0393	1.0664	0.1108	0.1108	0.1359	0.0875	0.1546	0.0788	0.1694	0.0731	0.1818	0.0685	0.1924	0.0645	0.1215	0.0366	6	0.5200	48.7608
47.0000	0.0424	1.0628	0.1105	0.1105	0.1423	0.0996	0.1646	0.0951	0.1820	0.0912	0.1962	0.0874	0.2085	0.0836	0.0587	0.0213	6	0.5888	55.3946
48.0000	0.0448	1.0602	0.1102	0.1102	0.1484	0.1098	0.1740	0.1090	0.1936	0.1070	0.2097	0.1041	0.2243	0.1009			6	0.6410	60.4578
49.0000	0.0463	1.0586	0.1100	0.1100	0.1542	0.1186	0.1829	0.1214	0.2048	0.1211	0.2227	0.1191	0.1840	0.0895			5	0.6797	64.2141
50.0000	0.0471	1.0577	0.1099	0.1099	0.1598	0.1266	0.1916	0.1326	0.2156	0.1339	0.2354	0.1328	0.1455	0.0749			5	0.7107	67.1959
51.0000	0.0472	1.0576	0.1099	0.1099	0.1653	0.1339	0.2000	0.1429	0.2262	0.1459	0.2481	0.1457	0.1082	0.0581			5	0.7363	69.6195
52.0000	0.0467	1.0581	0.1100	0.1100	0.1707	0.1407	0.2083	0.1526	0.2367	0.1571	0.2608	0.1579	0.0717	0.0397			5	0.7579	71.6323
53.0000	0.0458	1.0592	0.1101	0.1101	0.1760	0.1472	0.2165	0.1618	0.2473	0.1678	0.2736	0.1697	0.0356	0.0202			5	0.7768	73.3374
54.0000	0.0444	1.0607	0.1103	0.1103	0.1813	0.1534	0.2247	0.1706	0.2580	0.1783	0.2865	0.1810					4	0.7935	74.8068
55.0000	0.0426	1.0627	0.1105	0.1105	0.1866	0.1593	0.2329	0.1791	0.2688	0.1884	0.2639	0.1693					4	0.8067	75.9152
56.0000	0.0404	1.0651	0.1107	0.1107	0.1919	0.1651	0.2412	0.1875	0.2798	0.1985	0.2415	0.1569					4	0.8188	76.8786
57.0000	0.0380	1.0678	0.1110	0.1110	0.1971	0.1708	0.2496	0.1958	0.2911	0.2086	0.2190	0.1438					4	0.8300	77.7271
58.0000	0.0352	1.0709	0.1113	0.1113	0.2024	0.1764	0.2581	0.2040	0.3026	0.2187	0.1964	0.1300					4	0.8405	78.4841
59.0000	0.0322	1.0742	0.1117	0.1117	0.2077	0.1820	0.2667	0.2122	0.3146	0.2289	0.1735	0.1157					4	0.8504	79.1674
60.0000	0.0289	1.0779	0.1120	0.1120	0.2131	0.1874	0.2755	0.2204	0.3269	0.2394	0.1503	0.1008					4	0.8600	79.7914
61.0000	0.0254	1.0818	0.1124	0.1124	0.2185	0.1929	0.2844	0.2286	0.3398	0.2500	0.1266	0.0854					4	0.8694	80.3675
62.0000	0.0216	1.0859	0.1129	0.1129	0.2240	0.1984	0.2936	0.2370	0.3531	0.2610	0.1023	0.0693					4	0.8786	80.9048
63.0000	0.0177	1.0904	0.1133	0.1133	0.2295	0.2039	0.3030	0.2455	0.3670	0.2723	0.0774	0.0526					4	0.8877	81.4108
64.0000	0.0135	1.0950	0.1138	0.1138	0.2352	0.2094	0.3127	0.2541	0.3816	0.2841	0.0517	0.0353					4	0.8967	81.8918
65.0000	0.0091	1.0999	0.1143	0.1143	0.2409	0.2150	0.3227	0.2630	0.3969	0.2964	0.0250	0.0171					4	0.9058	82.3532
66.0000	0.0045	1.1050	0.1149	0.1149	0.2467	0.2206	0.3330	0.2721	0.4104	0.3072							3	0.9148	82.7845
67.0000	< 0	1.1100	0.1154	0.1154	0.2525	0.2262	0.3436	0.2813	0.3985	0.2990							3	0.9219	83.0569
68.0000		1.1100	0.1154	0.1154	0.2573	0.2309	0.3528	0.2895	0.3845	0.2891							3	0.9248	83.3150
69.0000		1.1100	0.1154	0.1154	0.2621	0.2355	0.3624	0.2978	0.3702	0.2788							3	0.9275	83.5611
70.0000		1.1100	0.1154	0.1154	0.2669	0.2401	0.3722	0.3064	0.3556	0.2683							3	0.9301	83.7972
71.0000		1.1100	0.1154	0.1154	0.2717	0.2448	0.3823	0.3152	0.3406	0.2573							3	0.9326	84.0250
72.0000		1.1100	0.1154	0.1154	0.2766	0.2495	0.3927	0.3242	0.3252	0.2460							3	0.9351	84.2460
73.0000		1.1100	0.1154	0.1154	0.2816	0.2542	0.4036	0.3336	0.3094	0.2344							3	0.9375	84.4614
74.0000		1.1100	0.1154	0.1154	0.2866	0.2590	0.4149	0.3433	0.2931	0.2222							3	0.9398	84.6723
75.0000		1.1100	0.1154	0.1154	0.2917	0.2638	0.4266	0.3533	0.2763	0.2096							3	0.9421	84.8795

Table 2.9. Tabulation of Optical efficiency (normalized with inter-groove spacing) ($\Sigma T_c X^n/S$) with varying α angles for material of RI 1.58.

α	hs	S	X^0	T_0X^0	X^1	$T_{C12}X^1$	X^2	$T_{C22}X^2$	X^3	$T_{C32}X^3$	X^4	$T_{C42}X^4$	X^5	$T_{C52}X^5$	N_{gmax}	ΣT_cX^n	$\Sigma T_cX^n/S$
44.0000	< 0	1.1911	0.2062	0.2062	0.2218	0.1450	0.2365	0.1220	0.2493	0.1079	0.2604	0.0974	0.0169	0.0055	5	0.6839	57.4227
45.0000		1.1911	0.2062	0.2062	0.2288	0.1614	0.2476	0.1430	0.2632	0.1307	0.2453	0.1069			4	0.7481	62.8099
46.0000		1.1911	0.2062	0.2062	0.2355	0.1747	0.2580	0.1607	0.2764	0.1501	0.2150	0.1034			4	0.7951	66.7562
47.0000		1.1911	0.2062	0.2062	0.2419	0.1860	0.2680	0.1760	0.2891	0.1671	0.1858	0.0957			4	0.8311	69.7777
48.0000		1.1911	0.2062	0.2062	0.2481	0.1960	0.2777	0.1896	0.3016	0.1824	0.1576	0.0853			4	0.8594	72.1564
49.0000		1.1911	0.2062	0.2062	0.2541	0.2049	0.2872	0.2019	0.3138	0.1964	0.1298	0.0729			4	0.8823	74.0750
50.0000		1.1911	0.2062	0.2062	0.2599	0.2131	0.2965	0.2133	0.3260	0.2094	0.1025	0.0592			4	0.9011	75.6563
51.0000		1.1911	0.2062	0.2062	0.2657	0.2207	0.3057	0.2239	0.3381	0.2217	0.0754	0.0444			4	0.9170	76.9854
52.0000		1.1911	0.2062	0.2062	0.2713	0.2278	0.3148	0.2340	0.3504	0.2336	0.0483	0.0290			4	0.9305	78.1228
53.0000		1.1911	0.2062	0.2062	0.2769	0.2345	0.3240	0.2437	0.3628	0.2451	0.0212	0.0129			4	0.9423	79.1125
54.0000		1.1911	0.2062	0.2062	0.2824	0.2409	0.3331	0.2530	0.3694	0.2522					3	0.9523	79.9524
55.0000		1.1911	0.2062	0.2062	0.2879	0.2471	0.3423	0.2621	0.3547	0.2444					3	0.9598	80.5787
56.0000		1.1911	0.2062	0.2062	0.2933	0.2531	0.3515	0.2711	0.3400	0.2360					3	0.9663	81.1296
57.0000		1.1911	0.2062	0.2062	0.2988	0.2589	0.3609	0.2799	0.3253	0.2272					3	0.9721	81.6196
58.0000		1.1911	0.2062	0.2062	0.3042	0.2646	0.3703	0.2887	0.3104	0.2179					3	0.9774	82.0601
59.0000		1.1911	0.2062	0.2062	0.3096	0.2702	0.3799	0.2975	0.2954	0.2083					3	0.9822	82.4603
60.0000		1.1911	0.2062	0.2062	0.3150	0.2757	0.3898	0.3063	0.2802	0.1984					3	0.9865	82.8275
61.0000		1.1911	0.2062	0.2062	0.3204	0.2812	0.3998	0.3152	0.2648	0.1881					3	0.9906	83.1677
62.0000		1.1911	0.2062	0.2062	0.3258	0.2866	0.4100	0.3241	0.2491	0.1775					3	0.9944	83.4856
63.0000		1.1911	0.2062	0.2062	0.3313	0.2920	0.4205	0.3333	0.2331	0.1665					3	0.9979	83.7853
64.0000		1.1911	0.2062	0.2062	0.3368	0.2974	0.4313	0.3426	0.2168	0.1552					3	1.0013	84.0703
65.0000		1.1911	0.2062	0.2062	0.3423	0.3028	0.4425	0.3521	0.2001	0.1435					3	1.0046	84.3433
66.0000		1.1911	0.2062	0.2062	0.3479	0.3082	0.4540	0.3619	0.1830	0.1315					3	1.0077	84.6067
67.0000		1.1911	0.2062	0.2062	0.3536	0.3136	0.4659	0.3720	0.1654	0.1190					3	1.0108	84.8626
68.0000		1.1911	0.2062	0.2062	0.3593	0.3191	0.4783	0.3824	0.1473	0.1061					3	1.0138	85.1130
69.0000		1.1911	0.2062	0.2062	0.3652	0.3246	0.4911	0.3932	0.1286	0.0928					3	1.0167	85.3594
70.0000		1.1911	0.2062	0.2062	0.3711	0.3302	0.5046	0.4044	0.1093	0.0789					3	1.0196	85.6033
71.0000		1.1911	0.2062	0.2062	0.3771	0.3358	0.5186	0.4160	0.0892	0.0645					3	1.0225	85.8463
72.0000		1.1911	0.2062	0.2062	0.3832	0.3415	0.5333	0.4282	0.0684	0.0495					3	1.0254	86.0899
73.0000		1.1911	0.2062	0.2062	0.3894	0.3474	0.5487	0.4410	0.0467	0.0338					3	1.0283	86.3359
74.0000		1.1911	0.2062	0.2062	0.3958	0.3533	0.5650	0.4545	0.0241	0.0174					3	1.0313	86.5861
75.0000		1.1911	0.2062	0.2062	0.4023	0.3593	0.5823	0.4686	0.0004	0.0003					3	1.0344	86.8434

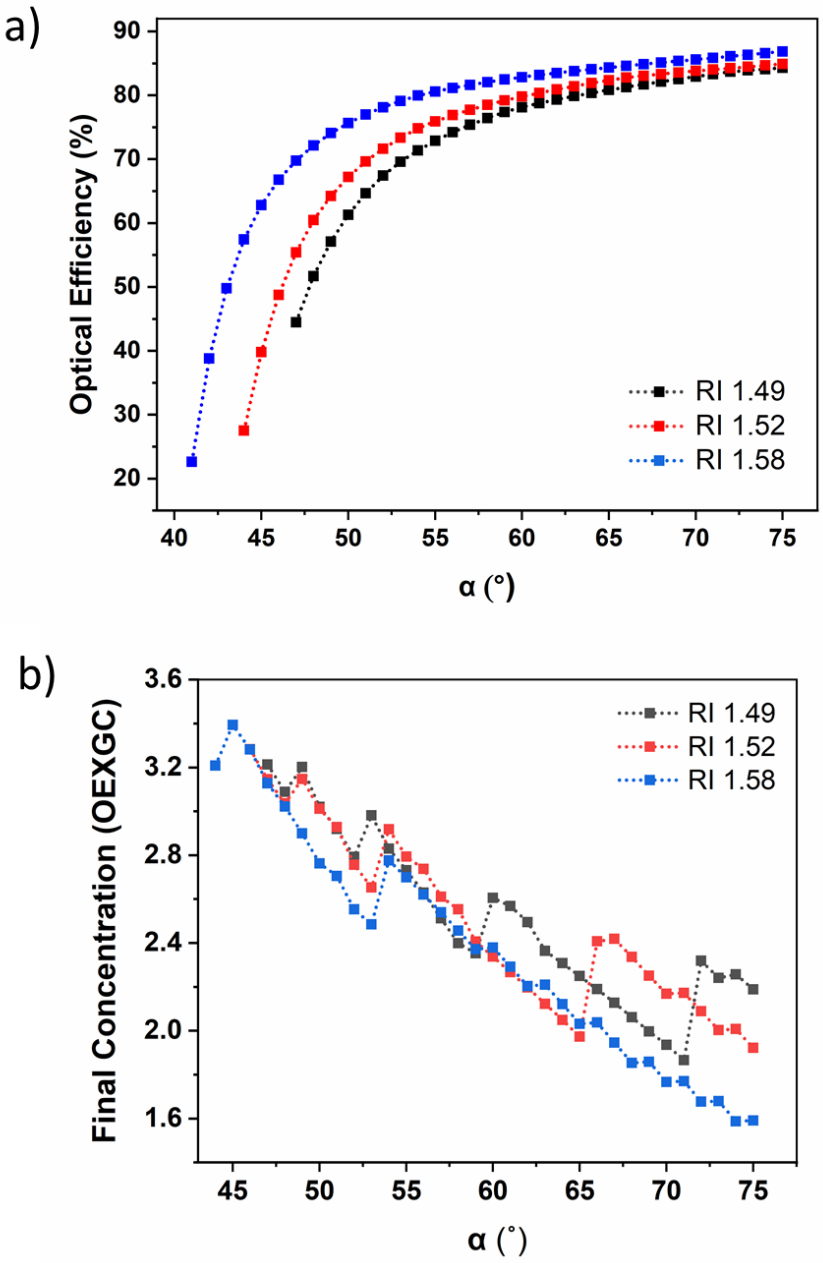

Figure 2.18. a) Optical efficiency of typical grooves (i.e., initial grooves with maximum possible refraction) vs α plot for different materials (RI: 1.49, 1.52, and 1.58); b) Final concentration vs α based on the Optical efficiency of typical grooves for the different materials.

2.5 Conclusions

A novel waveguide-based PLC optics design has been introduced in this chapter. The design constitutes an array of skewed V-groove optics patterns in an optics slab, which creates a unidirectional light transport to its lateral side. The design can be employed as an optics solution, which is:

1) Non-sequential
2) Single-elemental
3) Translatable to both longitudinal (for better solar acceptance) and radial (for medium concentration) designs (detailed in Chapter 4)
4) Manufactured with an industrial production route

The detailed mechanism of light transport and its mathematical model have been developed in this chapter. The mathematical model helps in understanding the different parameters and variables of SV-PLC optics. The model constitutes the base for simulation studies, as there are a lot of parameters to be studied and optimized before developing the simulation models. Detailed derivation and optimization have been conducted for the different parameters. Finally, the effectiveness (i.e., the OE and FC) of the SV-PLC design has been predicted with the present mathematical model of a single groove.

Chapter 3

Fabrication methods of Skewed V-groove based Planar Light Concentrator optics

3 Fabrication methods of Skewed V-groove based Planar Light Concentrator Optics

3.1 Abstract

Optics manufacturing has been translated from conventional glass material to lightweight polymer materials, due to the high flexibility offered in the manufacturing, ease, and cost of manufacturing, and enhanced production rates. Compared to the fragility of glass, polymer materials can be made adaptable for SV-PLC optics manufacturing, which is composed of an array of grooved structures. The present chapter discusses the manufacturing possibilities of SV-PLC optics in transparent polymer materials. Three different methods have been adopted for the fabrication of SV-PLC optics in levels of rapid prototyping up to industrial manufacturing. The optics design validation has been conducted with a rapid prototyping method of laser machining in PMMA plates. The limitations of lower cutting depth and thermal deformation with laser machining make the process utilizable for initial optical validation. Further, large-area prototypes have been developed with SLA 3D printing in optically transparent resin. Finally, the injection molding technique was adopted as a large-scale manufacturing method of SV-PLC optics. The different fabrication routes are explained in detail, drawing out the limitations and advantages of the same for the SV-PLC optics. The workflow in the chapter is illustrated in the flow chart below.

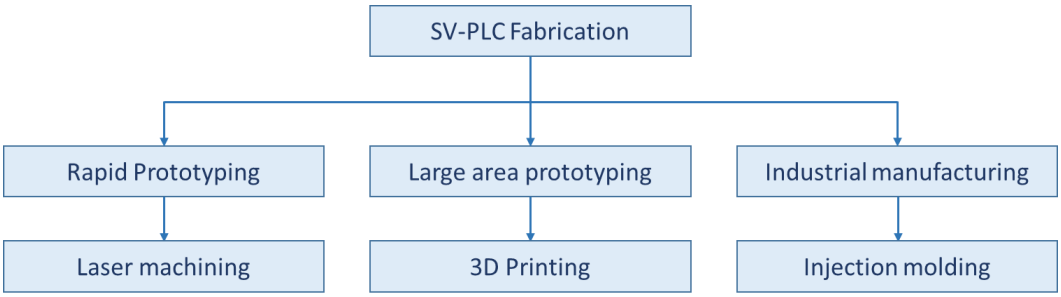

3.2 Introduction

Optics manufacturing is highly complex due to the requirement for high dimensional precision, surface quality, and sustenance of material properties during the selected manufacturing process [111, 112]. Optics elements can be manufactured predominantly with three methods: 1) Machining [113. 114], 2) Additive manufacturing [115, 116], and 3) Molding and forging [117-119]. Additionally, surface improvements are attained with

polishing and coating techniques [120-123]. Conventional machining process, such as cutting and grinding, often involves ultra-fine polishing of optical surfaces using machining or chemical methods. The processes have been more advanced recently, especially for custom applications such as the fabrication of spectacle glasses, with computer-controlled grinding [124]. Machining with methods like laser cutting has recently been more widely used for rapid prototyping or precise fabrication in optics materials such as PMMA [125, 126]. Additive manufacturing recently evolved to incorporate more optical fabrication, with more emphasis on the development of material libraries and precise machine capabilities [127-129]. Molding in glass optics is conventionally carried out through hot pressing for optics manufacturing [130], especially for lenses and mirror profiles. Nowadays, methods like hot embossing [131] and injection molding [132] in polymer optics materials are widely adopted if mass production is a requirement.

Apart from the manufacturing process, the selection of optics material is crucial when the requirements are critical with the combination of precision, optical properties such as transparency and refractive index (RI), mechanical and material stability under the operating or manufacturing conditions, additional functional requirements such as the need for additional optical coatings, etc. Glass material is often adopted for their advantage of material stability and less interaction with harsh environments, making it a better option as optical components for precision instruments or requirement under harsh conditions. However, for mass manufacturing or if the lifespan required is less (such as optics for spectacles), polymer materials are nowadays mostly used due to less sophistication and cost in manufacturing. Compared to glass, it is easier to achieve complex designs using injection molding of polymers such as PMMA or PC due to their high flowability and process flexibility. Recently, innovative approaches such as injection molding and 3D printing in silica glass material have been achieved through a glass powder and organic binder mix optics matrix [133]. This can provide huge potential in optics manufacturing of complex features in glass. The technology offers a very high surface finish (~3 nm) and transparency (~ 92%), which is very much comparable to optical glasses. However, the manufacturing process needs optimization and reproducibility for a large-scale optics manufacturing process [129]. The surface finish and optical clarity depend on the method of fabrication; for example, 3D techniques can suffer from less transparency and surface finish compared to injection molding. Also, the process has an additional step of sintering compared to

injection molding, increasing the cost of fabrication. Table 3.1 shows the general comparison of glass and polymer materials for optics fabrication [134].

Table 3.1. General comparison of glass and polymer materials for optics fabrication.

Properties	Material comparison for SV-PLC optics
Light transmittance	Compared to standard optical N-BK7 crown glass which has high transmittance of 91.6% polymers also shows similar transmittance values, such as PMMA (around 92%), PC (85-91%), Polystyrene (PS, 87-92%), Cyclic Olefin Copolymer (COC, around 92%), Cyclic Olefin Polymer (COP, around 92%) (data for material thickness of 3.2 mm). A high transmittance value is required for SV-PLC optics to reduce the light absorbance within the optics matrix.
RI	Crown glass: 1.51 - 1.52; polymer optics materials are available in varied RI, such as PMMA: 1.49, PC: 1.58 – 1.59, PS: 1.58 – 1.6, COC: 1.52 – 1.54, COP: 1.52 – 1.53. Any RI material can be utilized for SV-PLC optics, and the design parameters will be changed accordingly.
Abbe number	Crown glass matrix has a high Abbe number of 64, compared to polymer materials. PMMA, COC, and COP show a better Abbe number of 56 compared to PC and PS (30 and 31, respectively). A higher Abbe number yields low light dispersion, which is beneficial for any optical system. Parameter designs should be fixed accordingly, such that the functionality of SV-PLC should not be sabotaged.
Thermal expansion coefficient	Glass is superior to polymer materials in terms of the coefficient of linear thermal expansion. For glass, it is around 0.7 $°C^{-1}$, and for polymers, it is around 7 $°C^{-1}$. A lower thermal expansion material has a better dimensional stability and fixed optical properties (such as RI), which is beneficial for any optical system, especially for high temperature applications.
Mechanical properties	Glass matrices generally have higher tensile strength, however, polymers have better flexibility, lower density, high impact resistance, and ease of processing. Material flexibility is of utmost importance for SV-PLC fabrication due to their intricate shape.
Design flexibility	Polymer materials offer high and complex design flexibility compared to glass due to the process flexibility and material advantage. This is important for SV-PLC fabrication due to their complex design
Cost	Polymer materials like PMMA, PC, and PS offer both process (requiring only low-temperature processes such as injection molding) and material cost-effectiveness compared to glass. Compared to PMMA, PC, and PS, COP and COC are more expensive.

Even though glass matrix offers better durability, thermal resistance, and optical properties such as Abbe number, herein, the fabrication of SV-PLC optics has been explored in polymer materials, since the geometry of a skewed V-groove is difficult to achieve and preserve in brittle materials such as glass. In addition, the material and processes involved in polymer manufacturing are flexible and much cheaper [135]. The techniques adopted are laser machining, 3D printing, and injection molding, which are elaborated in the following sections. Materials have been selected with similar RI to compare the different processes. PMMA (for laser machining and injection molding) and similar RI materials (for 3D printing) have been opted for the fabrication due to their superior optical properties, including transmittance and Abbe number. Even though polymer materials provide better design and manufacturing flexibility, over time, UV degradation in the material happens, which can reduce the mechanical (tensile strength) and optical performance (transmittance) [136, 137]. However, commercially, UV-stabilizing additives or UV-protection coatings are used to extend the impact caused by UV-degradation in polymer materials.

3.2.1 Laser Cutting

Laser cutting is a non-contact thermal machining method, where a high-power focused laser is traversed in an input path to get the desired cut in a material. When a laser beam hits the material, it melts and penetrates through it. The laser is then allowed to move through the desired pattern, making the material melt or vaporize, creating the separation of material through the cut. Since the process depends only on the thermal capacity of the material, rather than any other properties like electrical conductivity, laser cutting has been used for wide applicability in both organic and inorganic materials. Compared to conventional mechanical cutting processes, the Kerf width (amount of material removed) is minimal with laser machining [138]. With laser cutting, the requirement of post-processing is very minimal in most cases. For generally used applications such as cutting metals, plastics, or leather, the process yields high surface quality, smaller heat-affected zones, and high flexibility in designs in the vertical direction. However, for cutting materials such as PMMA for optical applications, the effects produced must be carefully observed according to the application [139, 140].

Figure 3.1 shows the schematic of the laser cutting process. A high-power laser generated in the laser resonator is focused through a lens on the material to be machined through a single or a series of mirrors placed in the focusing head. The laser is supplied coaxially

with the laser through the nozzle to support the machining process. The workpiece is positioned according to the focal length of the lens used, as it can provide maximum energy density at the laser spot.

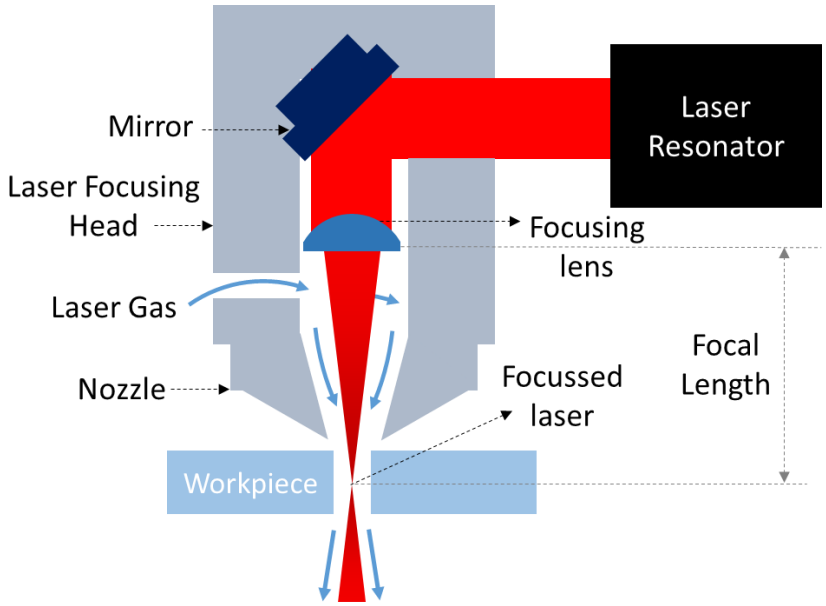

Figure 3.1. Schematic of a laser cutting process.

For smooth machining and better surface finish, it is important to set the parameters of operating laser machining according to the material and its thickness [141]. The parameters that control the laser-cutting process are:

1) Laser Power (P): Laser power refers to the total energy of the emitted laser per second. Power is an important parameter because it defines the energy for the operation, and thus, how deep the cutting process will be. Different laser systems provide different power ratings. Optical materials like PMMA require a higher energy compared to wood. A higher frequency system can provide even energy distribution in the material, which can create even melting of edges, making it smooth and clear. The laser system can be in continuous or pulsed mode. Pulsed lasers can provide higher energy than continuous ones, as they can accumulate energy for a period. Thus, it can create a finer machining surface.

2) Laser wavelength (λ): The wavelength, i.e., the type of laser, determines the range of material that can be used for a particular machine. The material absorption and reflectivity are the determining factors for the selection of a laser. Even though laser systems such as neodymium: yttrium aluminium garnet (Nd:YAG lasers) or fiber lasers are available in the market, the most commonly used system is continuous wave CO_2 lasers

(wavelength of 10.6μm) since it has more material coverage (with its wavelength range), relatively better beam quality with the high power rating, and fewer maintenance issues.

3) Laser spot size (ϕ): Laser spot size is the direct indication of the power of the laser, i.e., how concentrated the laser light is falling on the workpiece. Finally, the Laser power must be balanced with the spot size to achieve the right energy density to make the machining process in a given material of a specific thickness. The spot size is also an indication of the minimum Kerf width, and it defines the resolution of machining. For a laser beam of wavelength λ, lens focal length f, and beam diameter D,

$$\phi = 1.27 f\lambda \frac{M^2}{D}$$ (Rayleigh criterion) [138],

Where M^2 is the beam quality factor, which is the degree of beam variation from the ideal Gaussian beam. Even though focal length is inversely proportional to the spot size, a focal length shorter than 50 mm is not used, as it can cause lens damage due to the temperature.

4) Depth of focus (DOF):

Depth of focus is another important factor to be considered when cutting thicker materials. It is calculated as the distance between the converging and diverging points of the laser, where the size of the laser is 1.4 times that of the minimal spot size, as shown in Figure 3.2.

$$DOF = 2.5\lambda \left(\frac{f}{D}\right)^2$$ [24]

Hence, for larger DOF, longer focal length lenses are required. However, to create higher laser power, it may require a large area light collection, which increases the lens size, hence the cost. The point of focus of the laser is kept nearer to the middle of the workpiece to reduce the Kerf width and ensure uniformity of the cut throughout the depth.

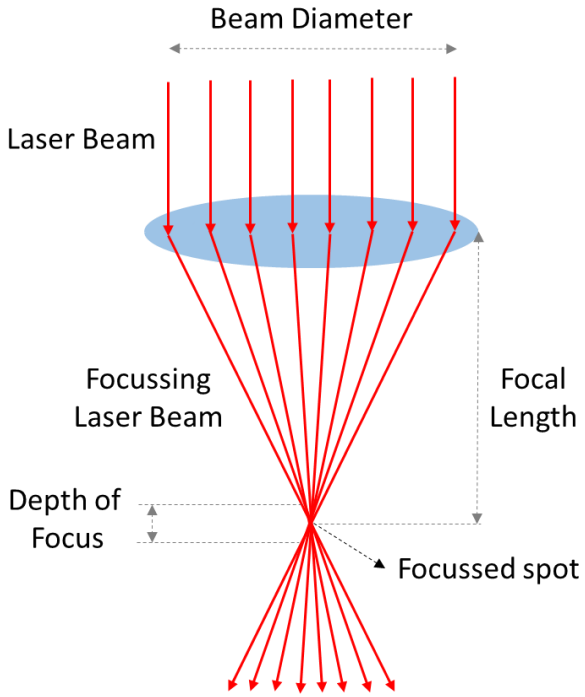

Figure 3.2. Schematic of a pointed laser beam in laser cutting, showing the depth of focus.

5) Laser speed (S):

The speed of the laser travel (i.e., distance travelled per time) is another important factor that determines the quality and efficiency of the laser cutting. The speed required for a machining process is related to the power of the laser and the thickness of the sample to be machined. The speed is proportional to the power, i.e., the higher the power of the laser, the working speed can be increased. The speed is also inversely proportional to the thickness of the sample, i.e., the working speed should be reduced for thicker materials.

$$S \propto \frac{P}{t} \text{ [24]}$$

where S is the speed of traverse of the laser, P is the power, and t is the thickness of the workpiece.

In a nutshell, for cutting material of thickness t, the higher the power of the laser, the lower the speed required, and vice versa. When the speed is kept higher than the optimized value, cutting ridges may appear on the faces. Also, when the speed is kept lower than the optimized value, burning or irregularities due to the larger heat-affected zone prevail on the cuts. This can also create increased kerf width due to the larger material vaporization zone occurring due to the lower speed.

6) Pulses per inch (PPI) (or Frequency): PPI is the number of times the laser will make a pulse within a distance of laser travel. If the PPI is kept higher, it will make more overlapping of laser cuts, hence providing a smoother finish. However, if the PPI is much larger, it can cause melting, irregularities, and charring in the material.

The optimization of the mentioned laser parameters should be effectively carried out for a material with a specific thickness to receive a high dimensional accuracy and surface finish of the cut. For intricate shapes that have patterns or cutting lines adjacent to each other, extra care must be taken to maintain dimensional accuracy.

3.2.2 3D Printing

Unlike other fabrication methods, the 3D printing method offers very high flexibility for design customization without any additional cost [142]. Traditional optics manufacturing methods, like grinding and polishing, do not offer applicability in complex and intricate shapes or profiles. The 3D printing technology paves its way to mitigate this limitation and can be used to fabricate complex shapes with decent precision and efficiency [143, 144]. Considering the cost and time of optics fabrication with conventional methods, 3D printing can be best utilized as a rapid prototyping solution to check and validate the optics designs. Apart from that, the material library provided for 3D printing can produce application-oriented optics parts to create compact and lightweight systems [145, 146]. However, the possibilities of mass production have also been recently explored more with this additive manufacturing technology [147]. Although comparing the cost of fabrication (higher material cost) for mass production with conventional methods like injection molding, 3D printing will be well suited for customization applications, such as the development of eyeglasses.

For optics manufacturing, the following class of methods of 3D printing can be adopted for manufacturing transparent parts.

1) Fused Deposition Modelling (FDM): It is a method of 2D layering technique, where materials are melted and made into 2D layers to create a 3D model. Thermosetting polymer materials in filament or pellet forms are generally used for this. Common optical materials include Polylactic acid (PLA), PMMA, PC, etc. The polymer filament is forced through a heated nozzle, which melts and is transferred to a platform. The nozzle moves according to the geometry input, where the 2D layers are deposited layer by layer to create the 3D geometry. The layers get bonded through fusion in their melted state. The size of the nozzle

determines the layer dimension, which will be visible in the final fabricated part. This additive manufacturing technique requires post-processing to acquire any desired surface finish, essential for any optic parts.

2) Vat Polymerization: This is a class of techniques that utilize the polymerization of a photopolymer, layer by layer, to create the final 3D geometry. Ultraviolet (UV) light is used for polymerization, which can be a laser light source (a process termed Stereolithography (SLA)), or a projection system using Light Emitting Diodes (LEDs) (a process termed Digital Light Processing (DLP)). SLA makes rastering of the light source to create layers of polymerization, whereas the DLP technique uses a digital light projector to project sectional layers, making a faster 3D printing process. Generally, SLA printing has better resolution compared to DLP due to the large area configuration limitation of DLP. Vat polymerization can provide a higher surface finish and accuracy compared to the FDM technique, since it creates a continuous line of cured material, making it smoother. The provision of material selection is limited with vat polymerization, compared to the FDM technique, as the latter involves only direct heating. Many advancements are going on in this technique. One such example is the utilization of a ceramic (amorphous silica) slurry to polymerize and subsequently sinter to create a glass 3D printed part [133].

3) Selective Laser Sintering (SLS): This process involves a laser source to melt and fuse powder material in the form of layers to create the final 3D geometry. Optic ceramic material glass can be easily 3D printed with the SLS technique. Even though intricate shapes can be manufactured with a better finish compared to the FDM technique, the surface finish is inferior to vat polymerization techniques.

Table 3.2 shows the performance comparison of different 3D printing techniques, drawing their applicability in optics manufacturing [148]. From this general comparison, it is evident that the SLA technique has more advantages in optics parts manufacturing, because of its better resolution and surface finish, which is a prerequisite for the SV-PLC fabrication.

Table 3.2. Table of comparison of the performance of different 3D printing technologies [148].

3D Printing Technique	FDM	SLA	SLS
Accuracy	Better	Best	Best
Resolution	Average	Best	Better
Surface Finish	Average	Best	Better
Design flexibility	Average	Better	Best

3.2.2.1 Stereolithography (SLA)

The SLA technique uses a UV laser to cure transparent liquid resin layer by layer to create the required optical part. The method is abstracted in Figure 3.3. The part to be fabricated is built upon a mobile platform, where the platform will be moved vertically with a resolution. Compared to other commonly used additive manufacturing technologies like FDM, SLA produces better accuracy, surface finish, and precision. This can be attributed to the resolution of layer thickness, which depends on the fineness of the vertical movement of the stage. Generally, machines capable of producing a fine layer thickness of 50 to 150 μm are used, however, precise machines use layer thickness in the range of 10 μm. Nowadays, microstereolithography techniques are also emerging, which can provide resolution up to 2 μm. The layer thickness also determines the printing speed in SLA, i.e., it is proportional to each other [149]. Laser spot size is another important factor that matters for very fine shapes and patterns. Apart from the resolution of vertical movement and laser spot size, the laser power and laser exposure time (i.e., the printing speed) are other factors that affect the quality of the final product [150]. The increase in printing speed lowers the exposure time, which may result in incomplete curing. However, reducing speed to a very minimal level may result in excessive polymerization. The resin material is also a dependent factor for the polymerization rate and depth of polymerization. Hence, an optical condition should be assigned to the process to get parts with good surface finish, dimensional accuracy, and material stability. Secondary UV treatment as a post-processing method is also employed after the 3D printing to avoid the possibility of incomplete polymerization.

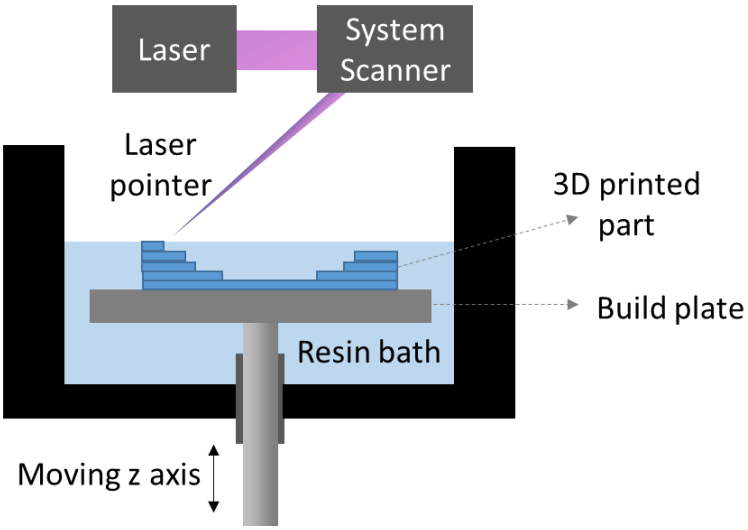

Figure 3.3. Schematic of SLA 3D printing.

3.2.3 Injection molding

For any product innovation to bloom, the efficient production feasibility should coincide with the innovation. For easy reachability in the market, the product should be adaptable to any current mass production routes. Injection molding is the most widely adopted efficient plastic manufacturing technique when considering the production rate and capacity of the mold. The utilization of injection molding can be extensively adopted for applications that require optical materials. This can replace conventional glass manufacturing techniques in many applications, which are tedious, expensive, and energy-consuming.

In operation, the injection molding technique involves the introduction of material in a molten plastic state/ liquid state into the mold under pressure, where it is allowed to cool/ cure, and harden. The schematic of the injection molding machine is shown in Figure 3.4. For thermosetting plastic optics materials such as PMMA or PC, the granules of the polymer are initially fed to a hopper and passed through a heated barrel through the rotary motion of the screw inside the barrel. The material is converted to its plastic state, and then it is forced into the mold under pressure to fill the mold cavity. The filled material is then allowed to cool under controlled conditions, which is dependent on the material properties. The mold is then opened, and the sample is ejected from the mold cavity. The clamping unit in the injection molding machine closes the mold during the injection and subsequent cooling process.

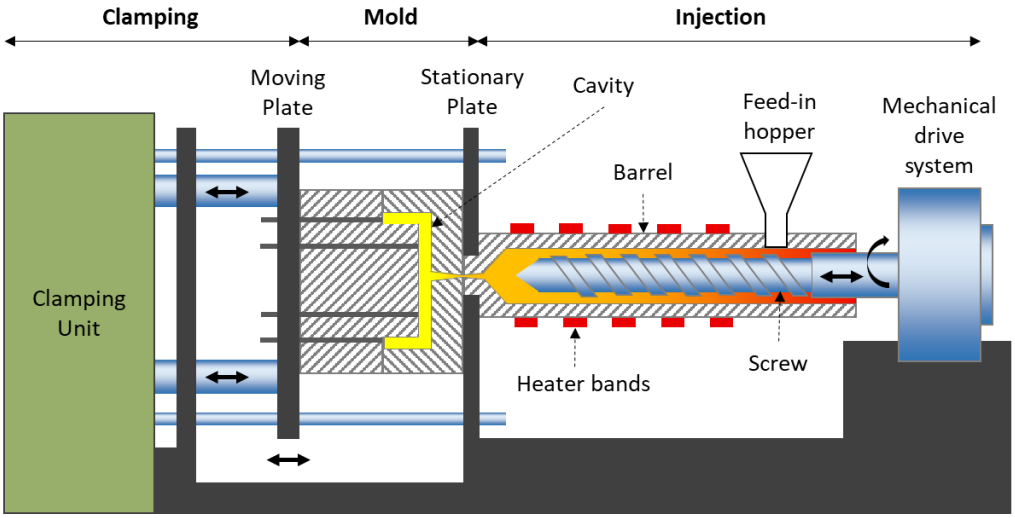

Figure 3.4. Schematic of an injection molding machine.

Setting the parameters of injection molding is crucial in obtaining a consistent, flaw-free end product [151, 152]. The mold temperature, barrel temperature, injection pressure, and clamping pressure are all fixed according to the material in use. For example, PMMA material has a melting point above 160°C and starts the degradation process above 220°C. Hence, the window of operation should be set between these temperature limits. If the product to be molded has intricate shapes or thin walls, the material can be heated to higher temperature points, which increases the flowability of the material. However, for optical applications, the temperature should be adjusted such that there will not be any discoloration or material degradation. For PMMA, the injection pressure should be kept considerably high (typically 80 to 120 MPa), since PMMA has poor flowability and high melt viscosity. Maintaining high injection pressure properly fills the cavity and provides the strength and optical clarity for the final product. However, excessive pressure may create stress marks in the product and reduce the life of the mold. The holding pressure is usually kept between 40-60 MPa to withstand the injection pressure and avoid flashing, and is usually kept at 50-65% of the injection pressure. Maintaining this pressure is crucial to avoid sink marks (depression in the final product) and to create uniform weight and dimensions. The holding pressure is determined according to the complexity and size of the part and the injection pressure.

Mold temperature is another important process factor, especially for the production of optical parts, as it is connected with the cooling and solidification of the parts. The surface finish and dimensional stability of the molded parts are critically affected by the cooling

rate provided by the mold section. For materials like PMMA that cool quickly, the mold temperature is usually kept raised to 40°C - 80°C to avoid the shrinkage stress occurring in the rapid cooling, which affects the optical clarity, dimensional uniformity, and surface finish of the final product. Also, materials with a high shrinkage rate need higher cooling time to reduce the defects occurring in the final part, hence, proper temperature control should be maintained in the mold.

Apart from pressure and temperature, injection speed is another important parameter to be checked for the injection molding process. It affects the surface quality and final product stability. An optimal speed should be maintained for this. If the speed is too low, there will be partial solidification before the complete filling of the mold, leading to defects and instability. Too high a speed can create stress in the mold and may create warping and other surface defects.

3.3 Materials & Methods

The fabrication of SV-PLC optics has been conducted on three levels: 1) Initial validation of the optics design by rapid prototyping using the laser cutting process; 2) Prototype validation using the 3D printing technique (direct 3D printing and solution casting with 3D printed mold); 3) Industrial-scale injection molding process. The materials and methods of fabrication are described below.

3.3.1 Laser Cutting

3.3.1.1 Machine details

The equipment employed was the Trotec Speedy 100 CO_2 laser machine (machining conducted at Fab Lab Kerala in Technopark, Thiruvananthapuram). The machine specifications are listed in Table 3.3.

Table 3.3. Specifications of the laser cutting machine.

Specification	Description
Working area	610 mm X 305 mm
Maximum height of the workpiece	157 mm with a 2-inch lens
Accuracy	± 15 μm

Laser system	Air-cooled class 2 CO_2 laser (laser wavelength: 10.6 μm)
Laser power	60 W
Laser Pointer size	120 μm
Software interface	Job Control™ Expert

3.3.1.2 Material details

Commercially available cast PMMA sheets (brand: Gujpol-S) with an RI of 1.49 at 589 nm and a visible transmittance of 92% (for 3 mm thickness) were used for the laser cutting. The thickness of the PMMA sheet is limited to 8 mm according to the capacity of the machine to provide a satisfactory cut (without obliqueness and many surface irregularities) for the design.

3.3.1.3 Method details

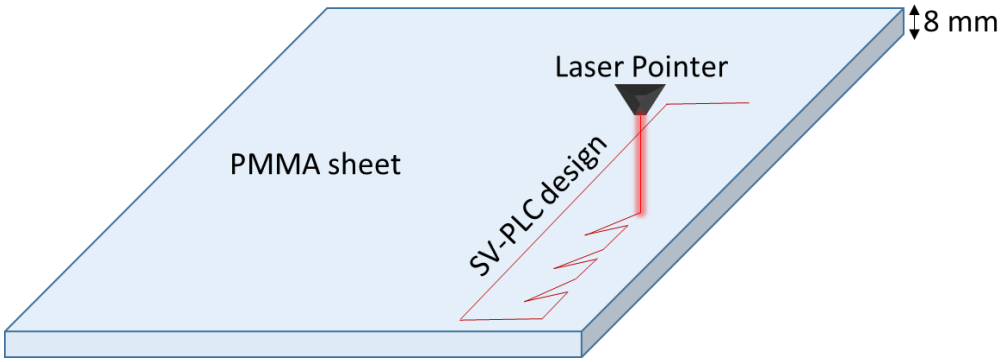

Figure 3.5. Schematic showing the method of fabrication of SV-PLC optics using laser machining

The schematic of laser cutting is as shown in Figure 3.5, where a laser pointer is used to cut through the material (8 mm thick PMMA sheet; size: 610 mm X 305 mm) in the SV-PLC pattern. The design parameters were set as follows: θ to 43°, α to 49°, H to 10 mm. To improve the profile cut by the laser, the h value was increased to 4 mm. This adjustment compensates for any local heat zones that can cause material softening and deformation during machining [140]. The vector drawing of the design was fed into the TROTEC JobControl X software. The parameters were fixed with the software by the trial-and-error method to get a better finish with a straight and single cut. The optimized parameters for the process include:

1) Laser head speed of 15 mm/s
2) Laser power setting to maximum (60 W)
3) Laser pulses per inch (PPI) of 500

Once the 8mm width SV-PLC pieces were cut, they were cleaned with a water jet for any residual removal, dried, and stacked together with Sylgard 184 optical sealant for final visual inspection. The machined parts were then inspected using a Carson MM-380 microscope with 20X magnification to check for cut angles, defects, and finish.

3.3.2 3D Printing

3.3.2.1 Machine details

From the background study conducted in the Introduction section, SLA 3D printing can be considered the best solution for getting higher accuracy, surface finish, and resolution. Herein, SLA 3D printing fabrication has been carried out in the Magform SL-600 machine (3D printing carried out at Quick Parts Solutions Pvt. Ltd., Mumbai). The machine specifications are listed in Table 3.4.

Table 3.4. Magform SL-600 3D printer machine specifications.

Specification	Description
Working size	600 mm X 600 mm X 400 mm
Accuracy	0.1 mm (for length ≤ 100 mm) 0.001 X L mm (for length > 100 mm) *Accuracy is dependent on other conditions like post-processing, geometry, size, resin material, and other machine parameters.
X-Y Resolution	25 μm
Layer thickness	50 – 150 μm
Laser system	Solid-state frequency tripled Nd:YVO4 (355 nm)
Software interface	Magforms iBuild 2.0

3.3.2.2 Material details

For any optical 3D printing material, its properties in the final prototype must be comparable to those of PMMA (as a benchmark). Herein, Magforms Crysplus 1801 is selected as the SLA photopolymer resin for the optics 3D printing. The properties of the resin are listed in Table 3.5 in comparison with a standard cast PMMA sheet (Gujpol-S):

Table 3.5. Comparison of properties of Crysplus 1801 3D printer resin with a commercially available PMMA sheet.

Properties	**Crysplus 1801**	**PMMA (Gujpol S)**
Transparency	90.8%	92%
Tensile strength	48 Mpa	55.9 – 74.5 Mpa
Elongation at break	12%	2-7%
Water absorption	0.48%	0.3%
Heat Distortion Temperature	52 °C	100 °C

The heat distortion temperature of Crysplus 1801 is far inferior to that of the standard PMMA sheet, thus, the operation temperature should be below that point. Apart from that, Crysplus 1801 has additional advantages such that it is less viscous (200 cps) and creates no bubbles upon the printed part. The RI of Crysplus 1801 is similar to that of PMMA (~ 1.49). The composition of Crysplus 1801 is described in Table 3.6.

Table 3.6. Composition of Crysplus 1801 3D printer resin.

Chemical Name	**CAS-No.**	**Concentration (%)**
Cyclohexanol, 4,4-(1-methylethylidene)bis-,polymer with (chloromethyl)oxirane	0583-72-3	10-60%
3.4-Epoxycyclohexanemethyl-3',4'-epoxycyclohexylcarboxylate	2386-87-0	5-30%
3-Ethyl-3-oxetanemethanol	3047-32-3	5-30%
Polyols(polyether triols)	9003-11-6	0.1-10%
Propylene carbonate	108-32-7	0.1-10%
Photoinitiator(the mixture of benzophenone and hexafluorophosphate)	947-193 & 68156-13-8	1-10%

3.3.2.3 Method details

The 3D printing of SV-PLC has been carried out with two methods:

Method 1: Direct 3D printing of the SV-PLC

Method 2: Converting SV-PLC into several individual elements to conduct efficient post-processing after 3D printing.

Figure 3.6 shows the illustration of method 1 and method 2 of 3D printing of SV-PLC. Method 1 involves the complete PLC design 3D printed as a single entity. Method 2 involves converting an SV-PLC design to multiple individual geometries (marked from 1 to 9 in Figure 3.6). Individual elements are then optically joined together with Sylgard 184 optical sealant to receive the final SV-PLC optics.

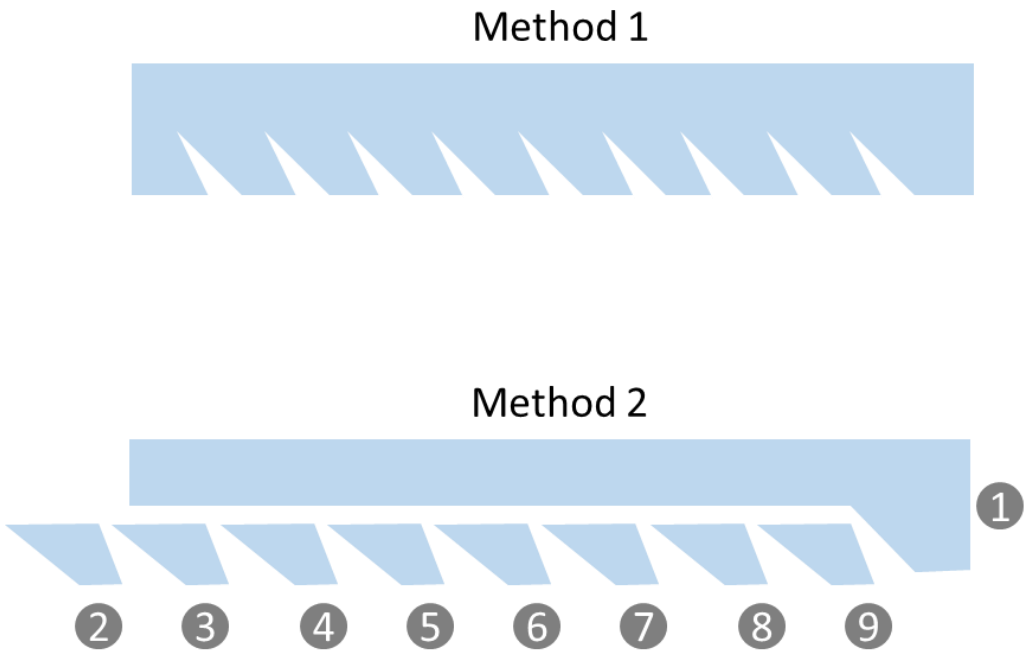

Figure 3.6. Schematic of 3D printing of SV-PLC optics through Method 1 and Method 2.

The steps of 3D printing carried out are described in the flow chart below (Figure 3.7). The parts to be printed (whole SV-PLC design for method 1 and split parts for method 2) were designed, and the Stl files were uploaded to the Magforms iBuild 2.0 software. The parts were 3D printed in the Magforms SL 600 printer from the Crysplus 1801 resin bath with a laser speed of 5800 mm per second. The printed parts were then cleaned properly using

isopropyl alcohol (IPA) to remove the residual uncured resin from the surface. An additional 20 minutes of curing was also provided in the Magforms PCA 600 post-processing unit for the printed parts to complete the polymerization. The 3D-printed parts were then taken to improve the surface finish with polishing and subsequent lacquer coating. Polishing was carried out to remove the support marks and scratches from the part surfaces with different grit sizes (the polishing method starts with grit sizes 320, 400,600, and 800 and ends with 2000 grit size for a better finish). Finally, lacquer coating was carried out with ESDEE Deco lacquer, and subsequently buffed to make the surface more transparent and glossy. Compared to other surface finishing methods like chemical polishing, coating techniques can yield better surface finish and optical clarity and surface finish [153, 154].

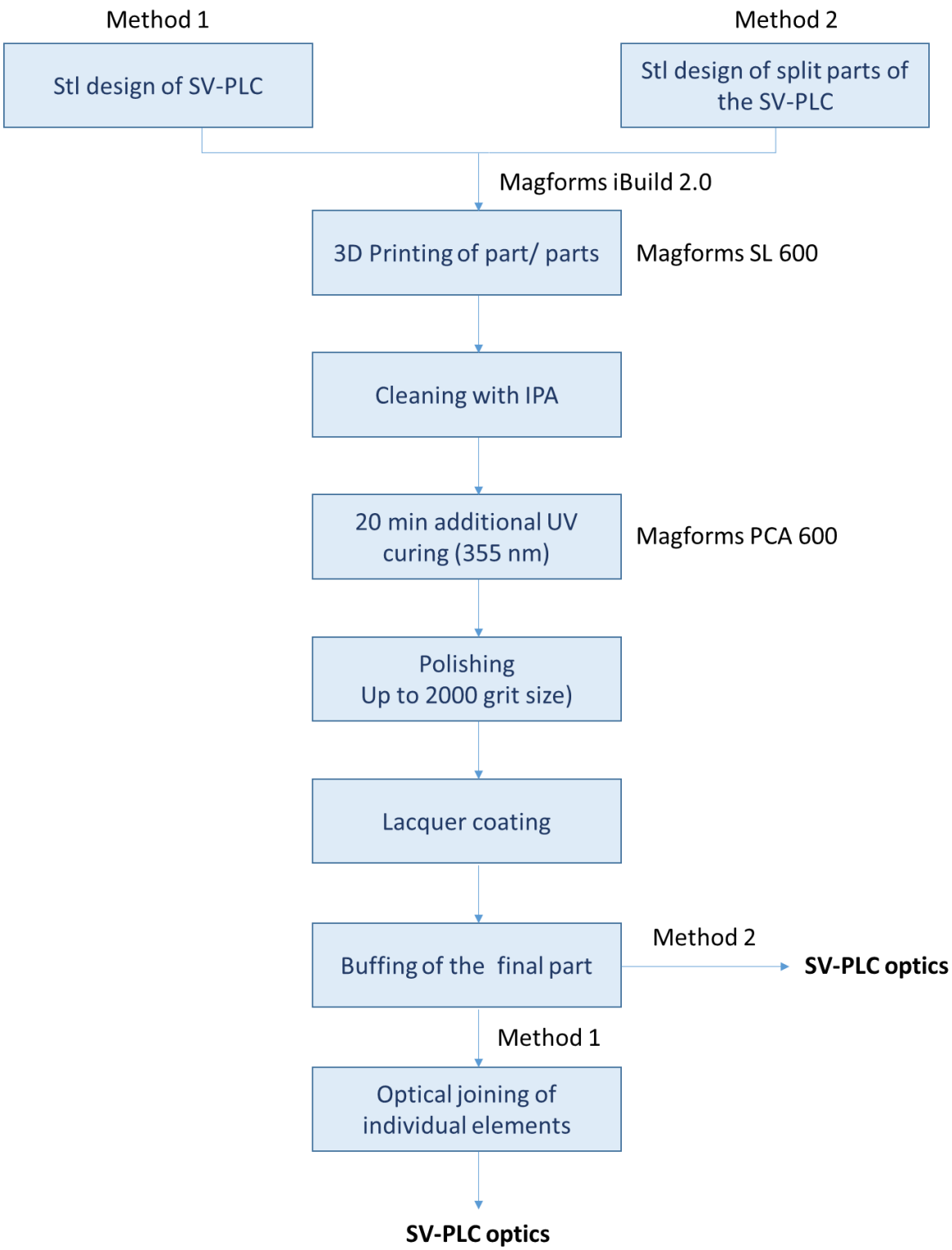

Figure 3.7. Flow chart representation of steps in 3D printing of SV-PLC optics through Method 1 and Method 2.

3.3.3 Injection molding

3.3.3.1 Machine details

The SV-PLC optics have been fabricated through injection molding in the PMMA matrix (Acrypet VH of Mitsubishi Rayon Co. Ltd.), due to its better optical properties (92% visible transmittance with RI 1.49). To select the tonnage requirement of the machine, the following calculation is made.

Tonnage = Projected Area x Clamp Factor, where the area (area of final molded part) is measured in sq. inches and the clamp factor is projected in tons per sq. inch, which is material dependent. For our SV-PLC optics, the area is 16.3 sq. inches. For PMMA, the clamp factor is taken as 3-5 tons per sq. inch, making the requirement 49 to 82 tonnes. Considering a safety factor of 1.5, the projected injection molding machine's requirement is 150 tonnes.

The equipment employed for the manufacturing was the Shibaura TD 150T injection molding machine (machining conducted at Raini Industries India Private Limited, Chennai). The machine details and optimized operating parameters for the injection molding are mentioned in Table 3.7.

Table 3.7. Machine specifications of Shibaura TD 150T injection molding machine and operating parameters for the fabrication of SV-PLC.

Specification	Description
Machine Tonnage	150 tonnes
Melt temperature/ Nozzle temperature	~ 210 °C
Mold temperature	~ 80 °C to avoid rapid cooling and shrinkage stress
Injection pressure	~ 120 Mpa

3.3.3.2 Material and Methods details

The skewed V-groove pattern of the SV-PLC optics forms an interlocking structure during the mold release in injection molding (as shown in Figure 3.8a). To circumvent this issue,

the mold cavity is positioned at 45° to the horizontal movement of mold release, as shown in Figure 3.8b.

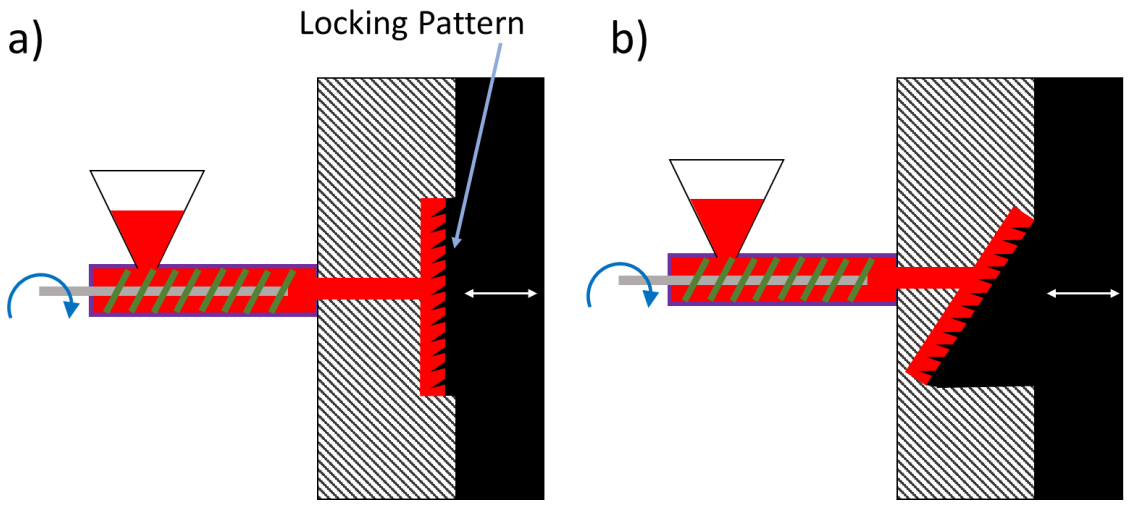

Figure 3.8. a) Schematic of injection molding of SV-PLC optics with the mold core placed vertically, making an interlocking pattern of skewed V-groove upon mold release. b) Schematic of injection molding of SV-PLC optics with the mold core placed at 45° to vertically, making the smooth release of the mold core from the SV-PLC optics.

The materials and machining details of the mold are specified in Table 3.8.

Table 3.8. Materials and machining details of the mold for the injection molding of SV-PLC optics.

Specification	Description
Manufacturing method of skewed V-groove pattern	Wire EDM (0.2 mm wire diameter)
Mold materials	Core and Cavity – 1.2083 steel Mold base – P20 steel
Polishing Methods	• Pride abrasive stone-600 • Emery-1000 • Emery2000 • 7-carat artificial diamond powder • Diamond buffing for R -0.06-0.07µm

The design considerations for fabrication have been carried out to incorporate the limitations of mold manufacturing and injection molding techniques. The difference

between α and θ was set to a higher value, rather than the optimized value, to increase the width of the pin-like structure in the mold (reverse pattern of the groove). Decreasing the width to the minimum values may cause mold damage. Apart from that, the height of the groove was scaled three times to that of the simulation design (height of 3 mm) for better fabrication feasibility of the mold, and for finishing the mold surface. The total height of the SV-PLC optics was limited to 4.5 mm to avoid any warpage or optical clouding, as the material thickness and rate of cooling contribute to the optical clarity of the final product. To increase the thickness of the SV-PLC, additional PMMA plates (brand: Gujpol-S) were optically coupled together with PDMS encapsulant. The SV-PLC optics have been designed for a length of 100 mm, such that the thickness of the SV-PLC optics can be flexibly increased to higher values to collect more rays. The final design and dimensions of the SV-PLC optics are shown in Figure 3.9a. Figure 3.9b shows the final mold core design for the fabrication of SV-PLC.

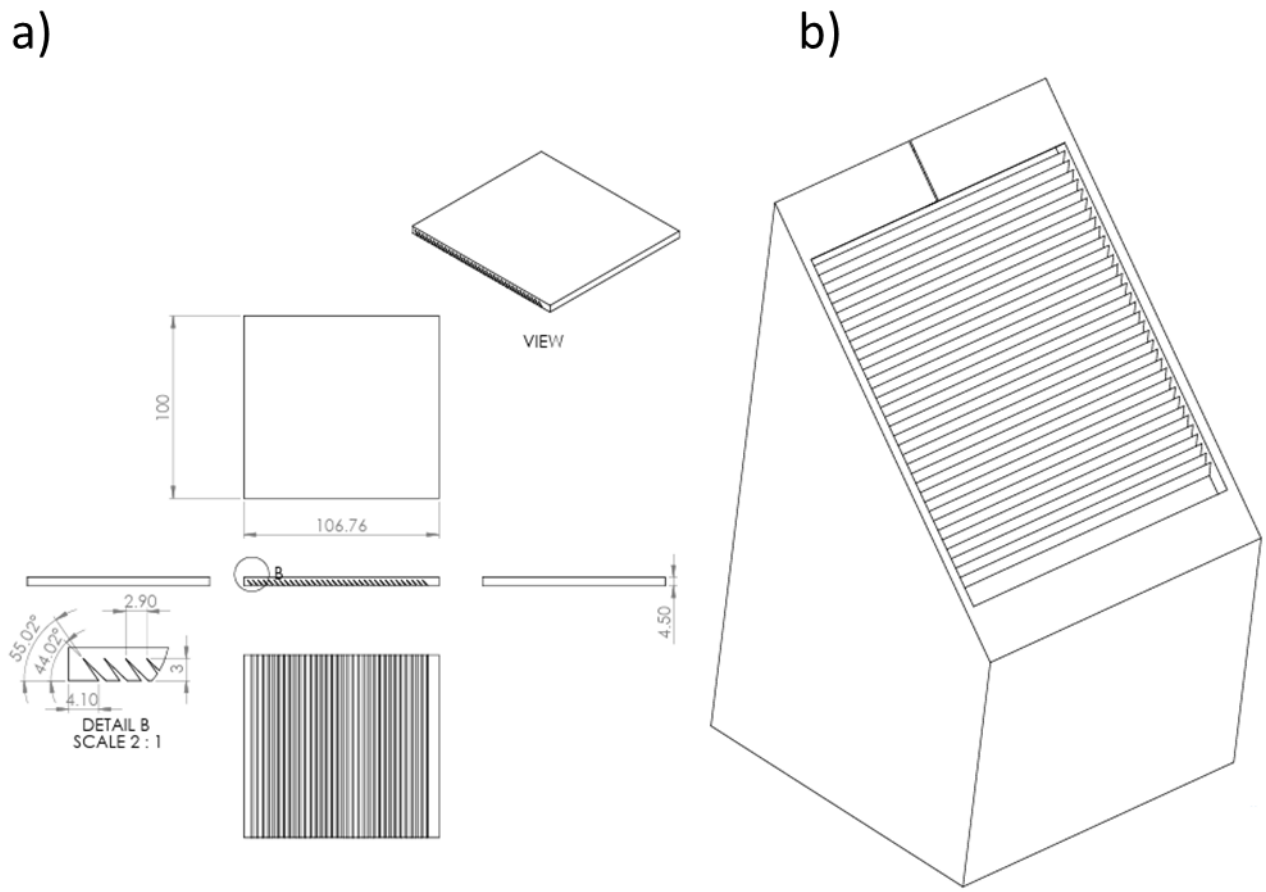

Figure 3.9. a) The final design and dimensions of the SV-PLC optics. b) Final mold core design for the fabrication of SV-PLC optics.

3.4 Results & Discussion

Figure 3.10a shows a single piece of PMMA SV-PLC optics (with θ: 43°, α: 49°, H: 10 mm, h: 4 mm) fabricated by laser machining. To attain a better surface finish and avoid obliqueness on the cuts, the thickness of the PMMA sheet was kept to 8mm. Since the laser machining process has limitations in the depth of cutting, the complete SV-PLC optics have been fabricated by optically assembling the individual 8 mm-thick pieces with transparent epoxy resins. Figure 3.10b shows the completely assembled SV-PLC optics showing lateral light redirection under direct sunlight. The optics validation has been conducted visually with varying angles of incidence of light (approx. 0°, 15°, 30°, 40°) along an axis. Colored PC sheets were attached with the SV-PLC optics for improved visual distinction. The major drawback of the laser cutting technique is the limitation of cutting thickness, which makes the individual pieces optically coupled, resulting in a high loss of light intensity through the interfaces. Also, the material was subjected to slight thermal bulging due to the heat-induced effects, especially at the adjacent groove faces. Yet, the laser machining method can be adopted for quick validation of the optics, and the cost of customized fabrication will be minimal. Detailed evaluation of the fabrication routes of SV-PLC optics was carried out with optical microscopy and direct light transmission, which are elaborated in Chapter 4.

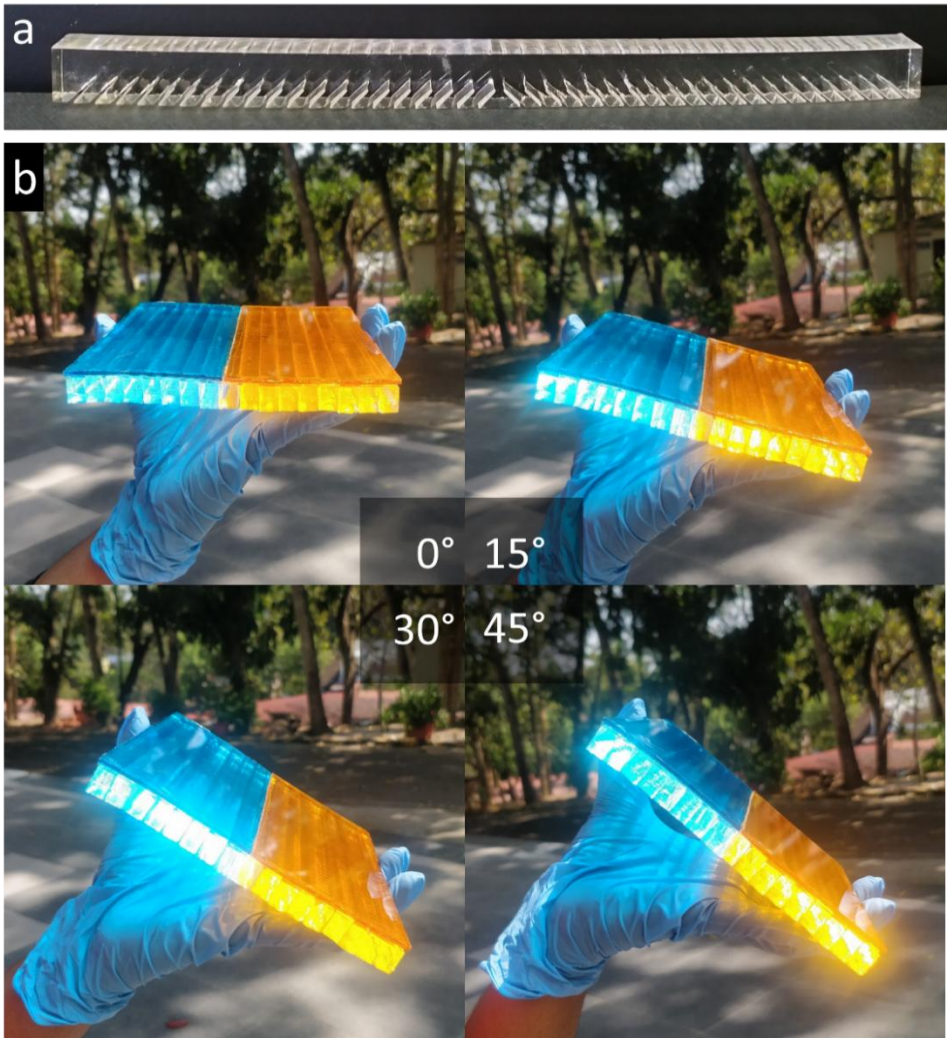

Figure 3.10. a) Photograph of a single piece of SV-PLC optics fabricated through laser machining in a PMMA plate. b) Photographs showing visual validation of high angular acceptance in SV-PLC optics fabricated through laser machining. Individual SV-PLC pieces are optically coupled and attached to colored PC sheets to enhance the visual distinction.

The SLA 3D printing of SV-PLC optics has been conducted in two methods. The directly printed optics with Magforms Crysplus 1801 resin are shown in Figure 3.11a. As shown, the light scattering surfaces formed at the groove interfaces in this method cannot be polished, lacquer-coated, chemical-treated, or vapour-treated for surface improvement. The light scattering point makes the incident light disperse in every direction, resulting in more loss of light rays rather than lateral concentration. To mitigate this issue, the SV-PLC optics have been split into individual components, 3D printed, and optically joined together in a single 3D printed plate (as explained in section 3.3.2.3 of Materials and Methods). Figure

3.11b shows the final part fabricated with the second method. Even though it yielded better optical clarity, the polishing and lacquer coating yielded dimensional and shape variations, with more rounded edges, as evident from the photograph. Vapor polishing or chemical polishing should be explored more in the future to obtain the required surface finish without compromising the optical quality for different 3D printing resins. Apart from that, meticulously aligning individual elements of the optics and losses occurring at the interfaces was found to be more disadvantageous. Even though large-scale optics (> 10 cm) can be fabricated easily with the provision of easy customization through 3D printing, the precision of fabrication depends more on the machine settings and post-processing. 3D printing techniques can be non-arguably adopted for technology validation and prototype development. Pointing out that the heat distortion temperature of the resin is 52 °C, for applications like this, the resin should function well with the required environmental conditions, other than the optical properties.

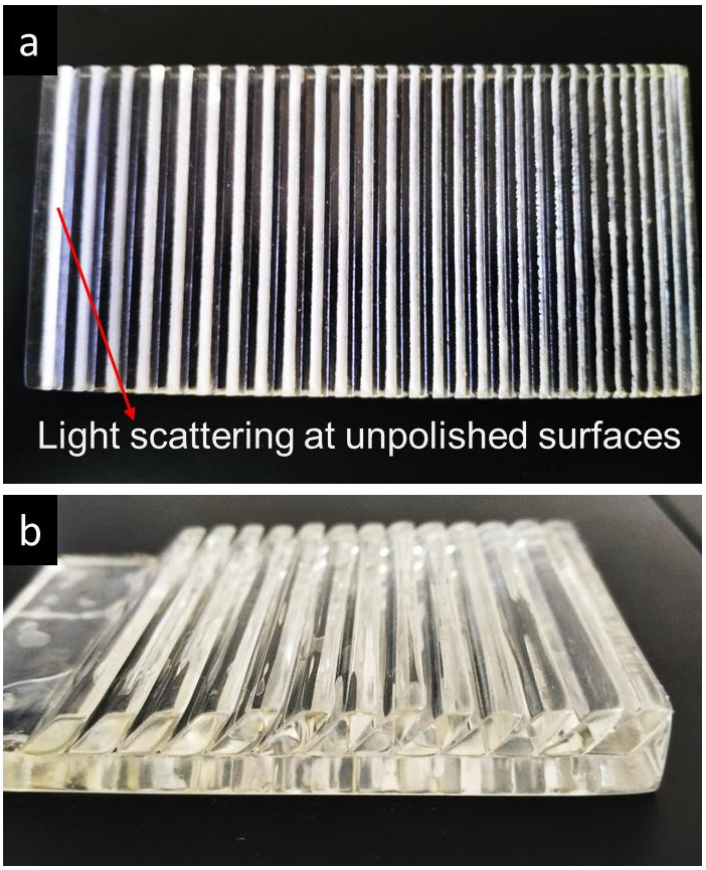

Figure 3.11. a) SLA 3D printed SV-PLC optics with Crysplus 1801 resin using Method 1, showing light scattering surfaces at the unpolished groove interfaces. b) SLA 3D printed SV-PLC optics with Crysplus 1801 resin using Method 2, showing improved optical clarity.

Finally, the SV-PLC optics fabrication has been translated to industrial-scale injection molding manufacturing. As detailed in the Materials and Methods section, the angle between θ and α was set to a higher value to increase the pin thickness in the mold. Also, the thickness of the SV-PLC was limited to 4.5 mm to avoid warpage and optical clarity issues. Hence, the parameters were θ: 44°, α: 55°, H: 4.5 mm, and h: 3 mm. The mold core has been fabricated accordingly with a cavity thickness of 4.5 mm. Figure 3.12a shows the CAD model of the mold with a blue-marked region as the SV-PLC optics part. The mold core consists of the groove pins, which are aligned horizontally with a 45° tilt in the SV-PLC optics. Since melt PMMA has much higher viscosity compared to other thermoplastic materials, a nine-runner design area (as shown in Figure 3.12a and Figure 3.12b) is made to properly fill the mold cavity, especially in the groove. The gate was placed at the bottom face of the SV-PLC to avoid any large marks at the top face that would hamper the optical efficiency of the SV-PLC. Also, the gate size was kept to a minimum (Figure 3.12b) of 1.7 mm X 4 mm. Figure 3.12c shows the final injection molded part to be released from the mold cavity attached to the machine.

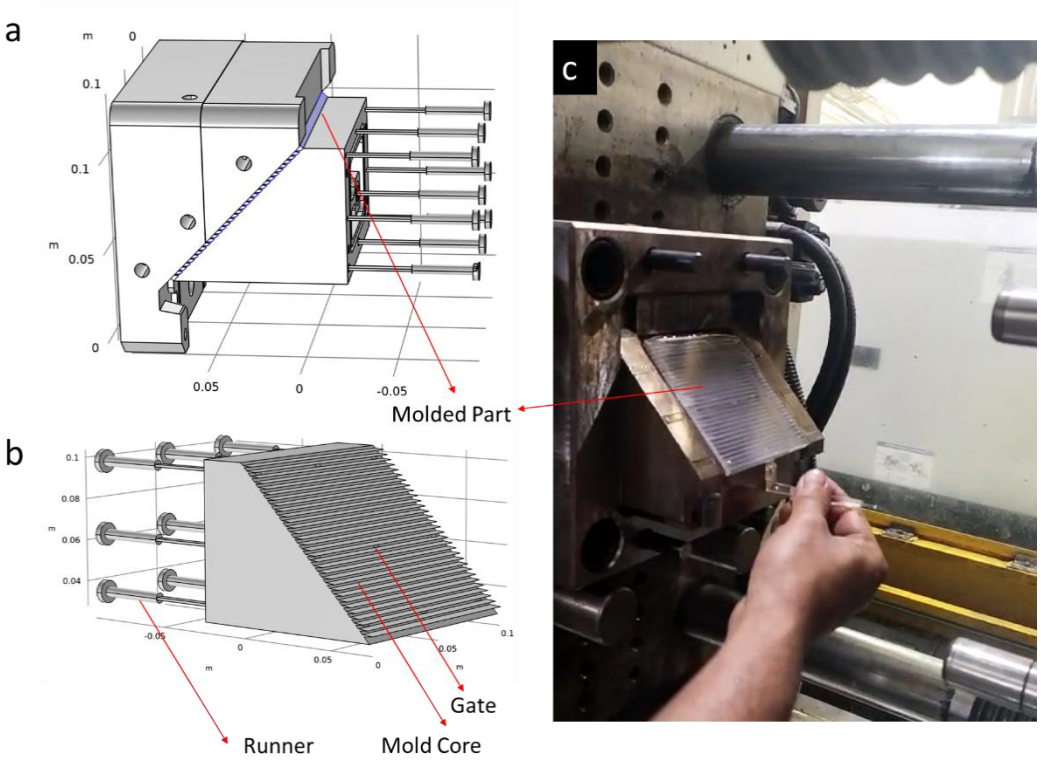

Figure 3.12. a) CAD model of the SV-PLC optics mold for injection molding with the blue marked region being the SV-PLC optics part. b) CAD model of the SV-PLC optics mold for injection molding showing the mold core, runner, and gates. c) Final injection molded SV-PLC optics part to be released from the mold cavity attached to the machine.

Figure 3.13a shows the final injection molded SV-PLC optics, which show a better groove profile compared to laser machining or 3D printing on initial visual inspection. As mentioned in the Materials and Methods section, the size of the SV-PLC optics was kept to a minimum of 4.5 mm to avoid warpage and issues with optical clarity. However, with the (H-h) value of 1.5 mm, the losses from the SV-PLC optics will be very large, since there is less room for light transport. The time-dependent ray tracing simulation result (Figure 3.13b) of the injection molded SV-PLC optics (simulations carried out in COMSOL Multiphysics Ray Optics Platform; the details are elaborated in Chapter 4) explains this, showing higher ray leakage through the bottom. To improve the collection, additional PMMA plates were optically coupled to the SV-PLC. This makes more room for light transport, as the TIR does not happen at the SV-PLC top surface, but is transported to the coupled PMMA and reflected at the top surface of PMMA, increasing the light collection. Figure 3.13c shows the time-dependent ray tracing simulation result of the injection molded SV-PLC optics coupled to a 5 mm PMMA plate. The improvement in the light collection was clearly visible with reduced ray leakage through the bottom, with more room for light transport. By increasing the thickness of the whole SV-PLC optics even more, it can again improve the collection of light rays. Figure 3.13d and Figure 3.13e show the lateral light concentration in the injection molded SV-PLC optics and the injection molded SV-PLC optics coupled with a PMMA plate, respectively, under direct sun. The evaluation of the SV-PLC optics has been detailed in Chapter 4.

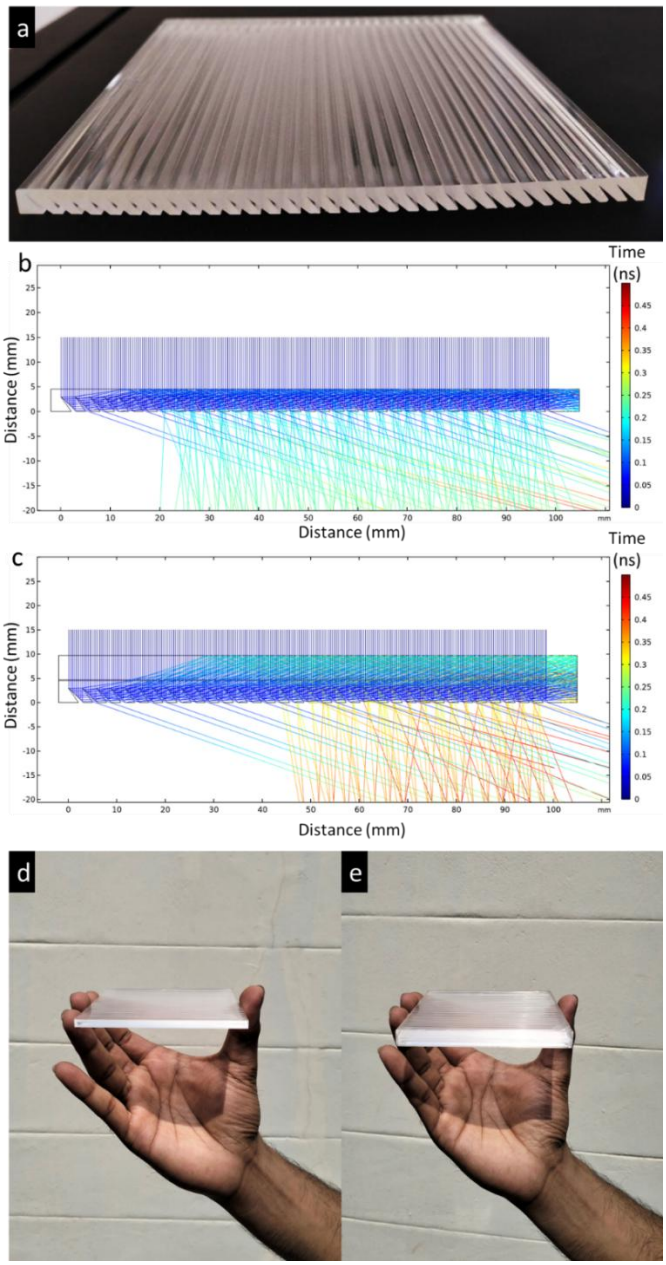

Figure 3.13. a) Injection molded SV-PLC optics part with a thickness of 4.5 mm. b) Time-dependent ray tracing simulation of the injection molded SV-PLC optics (4.5 mm thickness) showing high loss of light rays. c) Time-dependent ray tracing simulation of the injection molded SV-PLC optics optically coupled with a 5 mm PMMA plate (total ~ 10 mm thickness) showing an improved collection of light rays. d) Photograph showing the lateral light concentration in the injection molded SV-PLC optics under direct sun. e) Photograph showing the lateral light concentration in the injection molded SV-PLC optics coupled with the PMMA plate, under direct sun.

The cost comparison of the three methods of fabrication of SV-PLC optics is detailed in Table 3.9. From the manufacturing quality (detailed in Chapter 4), replicability, and cost-

effectiveness point of view, injection molding can be stated as the best fabrication route for the SV-PLC optics, especially for mass manufacturing.

Table 3.9. Cost comparison of different fabrication routes of SV-PLC optics.

Fabrication method	Cost of fabrication (INR per m_2 of SV-PLC optics)
Laser machining	5985 (1945 for fabrication, and 4040 for material)
3D printing	10,39,000 for material & fabrication
Injection molding	6,00,000 for mold development; 12,987 for material & fabrication (cost can be reduced with the quantity)

3.5 Summary

SV-PLC optics have been successfully fabricated with laser machining, SLA 3D printing, and injection molding. The laser machining process has limitations in the depth of cutting, hence, individual pieces are optically coupled to each other, resulting in a loss of light intensity through the interfaces. Also, the machining yields heat-induced bulges at the groove interfaces. Apart from that, the method can be adopted for quick validation of the optics with minimal cost of fabrication. The SLA 3D printing of SV-PLC optics has been conducted in two methods. Method one adopted the direct 3D printing of the SV-PLC optics. This method does not provide a provision for polishing and coating to improve the surface finish. This yielded light-scattering surfaces at the groove interfaces, reducing the efficiency of the SV-PLC optics. To mitigate this issue, the second method has been utilized. In the second method, the SV-PLC optics have been split into individual components, 3D printed, and optically joined together. The method provides optical clarity, however, the polishing and lacquer coating yielded dimensional and shape variations, with more rounded edges in the individual pieces. Also, aligning individual elements of the optics and losses occurring at the interfaces is disadvantageous in this method. Even though large-scale optics (> 10 cm) can be fabricated easily with easy customization, the precision of fabrication sets the limit of 3D printing to large-area prototypes for technology validation. When compared to the other two techniques of fabrication, injection molding can be considered a better manufacturing process for SV-PLC optics on a larger scale and with a better possibility of combining dimensional accuracy, surface profiles, and optical clarity. The evaluation of the SV-PLC optics fabricated through different methods has been conducted through optical microscopy and direct light transmission and is detailed in Chapter 4.

Chapter 4

Evaluation of Skewed V-groove based Planar Light Concentrator Optics

4 Evaluation of Skewed V-groove based Planar Light Concentrator Optics

4.1 Abstract

Planar waveguide-based light concentrators are emerging as a compact solution to conventional solar concentrators. However, it has its design limitations due to the conflict between intricate designs and performance factors. The solution of SV-PLC offers a non-sequential, single-elemental design, which can be translatable to both longitudinal (for better solar acceptance) and radial (for medium concentration) designs. Apart from that, it can be manufactured with a single industrial production route, as discussed in the previous chapters. Herein, the different fabrication routes opted for the fabrication of SV-PLC have been evaluated, and concluded that injection molding offered better optical clarity and dimensional accuracy. The SV-PLC optics are evaluated with the performance indicators, i.e., the optical efficiency (OE), final concentration (FC), acceptance angle in an axis, and flexibility to adapt for both longitudinal and radial designs through simulation models using the COMSOL Multiphysics Ray Optics platform. The simulation models validated the mathematical models with slight variations in the OE and FC, due to the difference in the method adopted for the models. Finally, the final light concentration and angular acceptance are measured using an amorphous silicon solar cell optically coupled to the injection-molded 10X GC SV-PLC optics. The chapter workflow is illustrated in the flow chart below.

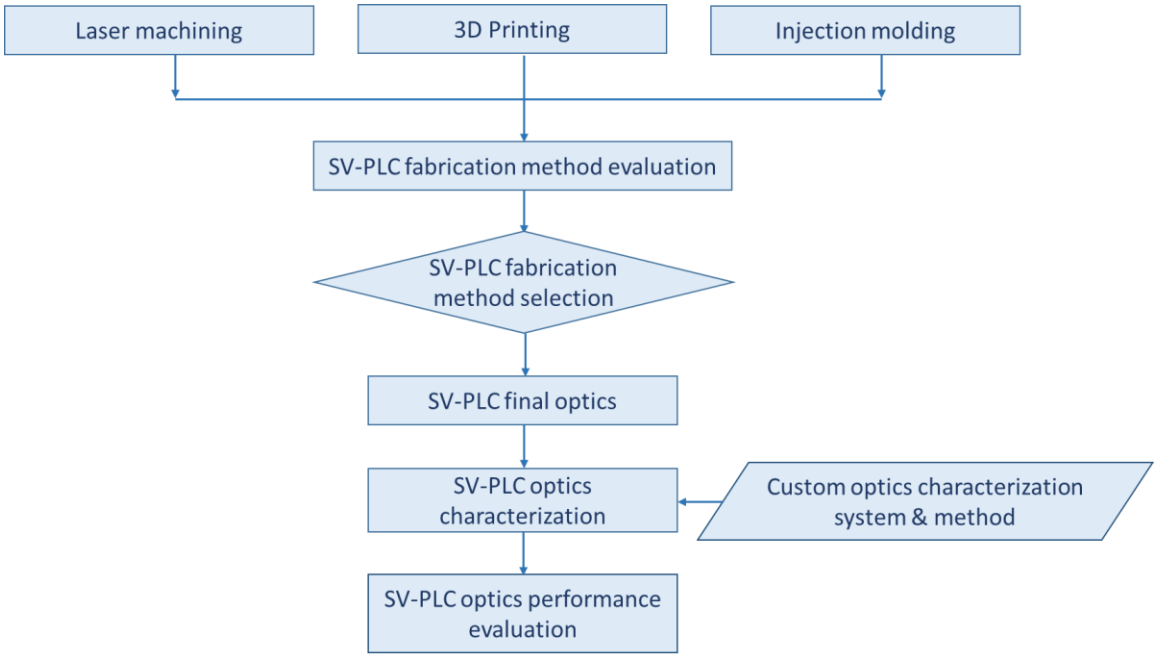

4.2 Introduction

With a global trend of reduced cost of photovoltaic installations [155], the significance of CPV systems has shifted from large power plant installations to their applicability in built environments. To accomplish the targets of the Paris Climate Agreement [156] and the recent COP26 meeting [157], it is of the utmost essential to meet the energy demand in industry, commercial, and residential building spaces by adopting renewable energy technologies for Decentralized Distributed Generation (DDG). Most of the initiatives to tackle this vast energy demand rely on the efficient utilization of solar energy, where light energy management is an essential prerequisite. The role of PV in buildings [158-160], building-vehicle integration [161, 162], and urban environments [163, 164] for city planning has been indicated extensively for the past five years globally. Compact CPV systems for BIPV, solar urban planning and developments, and solar vehicles are some of the major focuses in this regard. In that, BIPV is considered the most promising approach to utilize built spaces for solar energy conversion, where conventional building elements are replaced with resembling PV products [165]. This can promote the widespread construction of energy-efficient solar/green buildings, which are considered the backbone of DDG.

In this context, waveguide-based compact PLC systems play a pivotal role in developing efficient light trapping and guiding systems. Such systems are of utmost importance for sustainable light energy management and BIPV product development from the point of view of energy efficiency (through light concentration) and aesthetic appeal. Because of their compact design architecture, PV concealed architecture, aesthetic inclusions, and reduction in size and structural elements compared to conventional CPV technologies, waveguide-based planar CPV systems can exhibit superiority in BIPV systems. However, waveguide-based planar CPV systems are considered to be in their infant stage in the technological forefront of PV solutions. The requirement of complex R&D development and product-specific manufacturing automation is a major technical hindrance to product development. Also, the BIPV implementation challenges, the requirement of product multi-specifications, and vigorous technical planning for deployments such as building

information modeling and solar-specific architectural innovations [34] create an ecosystem of both opportunity and challenges for the future.

The typical designs followed similar approaches, i.e., the utilization of multiple cylindrical [92], or spherical [16,166] microlenses, or mirror designs [55, 167] and dispersing elements to redirect the light rays to the receiver by trapping them through a waveguide. Here also, optical alignment and precise microfabrication seem to be the challenge as they involve multiple optical elements to transfer the light rays to the waveguide. The waveguide-based PLCs are designed either longitudinally [93, 94] or radially [52, 101]. Longitudinal approaches are mainly used for creating designs with better solar angular acceptance [56, 91]. However, radial designs (that concentrate light to the centre), even though they lack angular acceptance, can produce very high geometric concentration (GC). Creating a single elemental radial design seems to be the most challenging in waveguide-based PLCs, as the design freedom is very limited. Even though it requires 2-axis solar tracking, any such innovative approach will be a boon considering their final light concentration value, and ease of fabrication and operation.

From the introduction and status of the current waveguide-based PLC (refer to Chapter 1), it is evident that the existing design innovations conducted on planar waveguide-based CPVs have more prominence for geometric optics-based designs (advantages are discussed in Chapter 1). Table 4.1 shows the summary of the review of different design configurations (optics and optics materials) of geometric optics-based PLCs for comparative analysis.

Table 4.1. Summary of review on different design configurations (optics and optics materials) of geometric optics-based PLC (in chronological order)

Reference, year	Research method E: Experimental S: Simulated	Optical material data	Structure form	Dimensions	Optical performance (OE/PCE (%)), GC	Acceptance angle (˚)
Geometric Optics-based PLC P: Primary Optics; W: Waveguide; C: Light coupler						
[98-100], 2007	E	P: Acrylic W: Acrylic + Centre piece for light collection: Glass	P: Total internal reflecting surface (parabolic/ cubic/ hyperbolic/ flat) W: Wedge shaped	200 mm X 200 mm square (Generation 2)	GC claimed: ~ 1000 X	± 0.75
				200 mm hexagonal (Generation 3)		± 0.9
[16], 2010	E and S	P: BK7 glass W: F2 glass	P: Hexagonal lens array	P: 2.3 mm diameter F/1.1	OE: 81.9 GC: 300 X	± 1

		P: F/1.1 lens array W: BK7	W: Slab waveguide C: Air prism	hexagonal lens array W: 75 mm long by 1 mm thick	OE: 32.4 GC: 37.5 X	
[93], 2010	S	P, W: RI 1.51 Low index layer RI 1.38	P: Staggered microlens array W: Stepped guide layer + Low index layer	P: Lens aperture of 3 mm x 1.5 mm W: Thickness of 2.42 mm	GC: 112.5 X	± 1
[91], 2012	S	P: f⁄1.2 lens array W: RI 1.7	P: Cylindrical lens array W: Planar waveguide C: Air prism	P: Lens pitch 2.6 mm W: 10.4 mm × 30 mm, core thickness of 1 mm C: width of 1.5 mm	OE: 80	North-South axis: ± 9 East-West axis: ± 54
[92], 2014	S	P: BK7 glass W: F2 glass	P: Array of cylindrical lens W: Planar waveguide C: Air prism	P: Lens pitch - 5 mm Lens F/#: 1.81 Air-gap thickness of 0.2 mm W: Thickness of 1 mm C: Width of 90 μm	OE: 70 GC: 50 X	± 7.5
[95], 2014	E and S	P: Plastic W: Fused Silica Actuator: Paraffin wax	P: Aspheric lens pair W: Planar waveguide + dichroic membrane + actuation element	53 x 53 mm^2	OE: 2.8 GC: 8 X (Simulated) GC: 3.5 X (Experimental)	± 16 (Experimental)
[56], 2014	S	P: Polymer W: Polymer	P: Cylindrical microlens W: Curved light guide	20 cm long, 1.1 cm thick	GC: 39 PCE: 20% (module efficiency) (Si based solar cells)	± 15
[97], 2015	E	P: Glass coated with silver W: Caged air	P: Reflector (square, hexagonal, circular) W: Cage waveguide	-	Hexagonal reflector showed better light transmission to waveguide (used GC: 6 X)	± 1
[96], 2016	E and S	P, W: PMMA C: Al and SiO_2 coated reflective grooves	V grooved single elemental	30 × 30 mm^2 with solar cell size of 30 × 3 mm^2	GC: 5 X PCE: 24.8 and 25.1 at the two ends of concentration (used Single-junction GaAs solar cells)	2
[94], 2017	Trigonometric analysis and simulation	P: PMMA W: PMMA	P: Square lens array W: Planar waveguide C: Air prism + fibre optic ribbon for daylighting	P: Lens array period of 2 mm W: Thickness of 2 mm C: Prism base width of 80 μm	OE: changed from 1 to 0.1 with incident angle direction of 0˚ to 40˚ GC: Study conducted for varied concentrator length	0.38 (trigonometric analysis)

[52], 2020	S	P, C, W, Compound parabolic collector (CPC): PMMA	P: Sheet collector with arc-segment lens structures W: Concentric light guide channel with additional CPC C: Embedded prism	Optimised mode with Length: 413.7mm Width: 300 mm Height: 25 mm Length of CPC: 21.2 mm	OE: 87.6 GC: 739	0.35 to -1.65 -12 to 12 In two directional axis
		P, CPC: PMMA C, W: NBK7 glass			OE: 87.5 GC: 738	

The current technology gap for the waveguide-based PLC technology is to achieve an optical solution that is:

1) Non-sequential
2) Single-elemental
3) Translatable to both longitudinal (for better solar acceptance) and radial (for medium concentration) designs
4) Manufacturable with a single industrial production route

The evaluation of waveguide-based PLCs is generally considered with the following factors:

Optical efficiency: This is a merit value that determines how much light energy (for the concerned spectral range) is transported from the inlet aperture to the final output area. OE encompasses the merits of different optical elements, optical material efficiency, and system fabrication efficiency. It is the ratio of the power of radiation received at the receiver to that of the light concentrator. It incorporates the loss of energy in the system.

$$\mathrm{OE} = \frac{\text{Output power}}{\text{Input power}} = \frac{\mathrm{E_{receiver}}}{\mathrm{E_{concentrator}}} \tag{4.1}$$

Final concentration: This is the final performance factor of the whole concentrator system; i.e., the ratio of the intensity of the output radiation (at the receiver) to that at the light concentrator. It is the product of GC and OE.

$$\mathrm{FC} = \mathrm{GC}^{*}\mathrm{OE} \tag{4.2}$$

Acceptance angle: The acceptance angle of a system refers to the incident light angular range up to which the performance (OE) of the concentrator does not degrade to a required percentage limit.

Design flexibility: Refers to the flexibility to adopt longitudinal or radial designs upon application.

4.3 Design & Methodology

4.3.1 Simulation modeling

The optics simulation models are used to predict the performance of SV-PLC with common optical materials like PMMA, Glass, and PC with Refractive Indices (RI) taken as 1.49, 1.52, and 1.58, respectively. Two-dimensional simulations have been conducted to gauge the effectiveness of SV-PLC and expand to three-dimensional simulations for an in-depth analysis of angular acceptance along a given axis (for linear design). The simulation studies are conducted in the Ray Optics module of the COMSOL Multiphysics 6.1 platform.

The optimization parameters and variables for the skewed V-groove optical design are generally θ, α, (H-h), S, L_{100}, and L_{max}, as elaborated in Chapter 2. However, for conducting the simulation studies for efficient evaluation of the SV-PLC, certain parameters need to be fixed based on the mathematical modeling. From the mathematical correlations developed, for efficient light transport to longer lengths, θ is kept as small as possible, but ensuring the reflection occurs at the face. The θ value is equal to the incident angle at the reflecting face (refer to Chapter 2). Thus, to keep θ to a minimum, it is kept at the critical angle of the material for total internal reflection (TIR) to happen. The space for light transport (H-h, where H is the PLC height and h is the groove height) is one factor that determines the L_{100} or L_{max} of the PLC. A higher H-h value provides higher room for light collection, increasing the length, thus producing more light collection. Hence, for a fixed H, the h value should be kept as low as possible, depending on the manufacturing capability. Herein, (H-h) is made a constant for the comparison studies, and S is fixed to minimum values (refer to Chapter 2). The inter-groove spacing (S) for an SV-PLC design is kept as wide as possible up to the width of a groove (refer to Chapter 2) to avoid ray leakage loss (L_{leak}). The fixing of S value is based on the mathematical model developed in Chapter 2. The fixed parameters and associated variables are provided as input parameters for the simulation. The final parameter, α, is the most critical parameter for optimizing SV-PLC. The simulation studies are mainly carried out by parametrizing α for L_{100} or L_{max}.

The designs of SV-PLC are considered for two types of configurations:

1) Linear design for PLC with angular acceptance in an axis: Herein, the skewed V-grooves are arranged in a linear pattern (Figure 4.1a), providing the unidirectional light concentration to the lateral face (Figure 4.1b, showing the 3D time-dependent ray trace simulation model). The light will spread from the lateral face if uncoupled from any collector. Figure 4.1c shows the 2D time-dependent ray trace simulation of the SV-PLC for linear design, where the light collector can be directly coupled to the lateral face. The linear design will be evaluated for its OE, FC, and angular acceptance in the longitudinal axis.

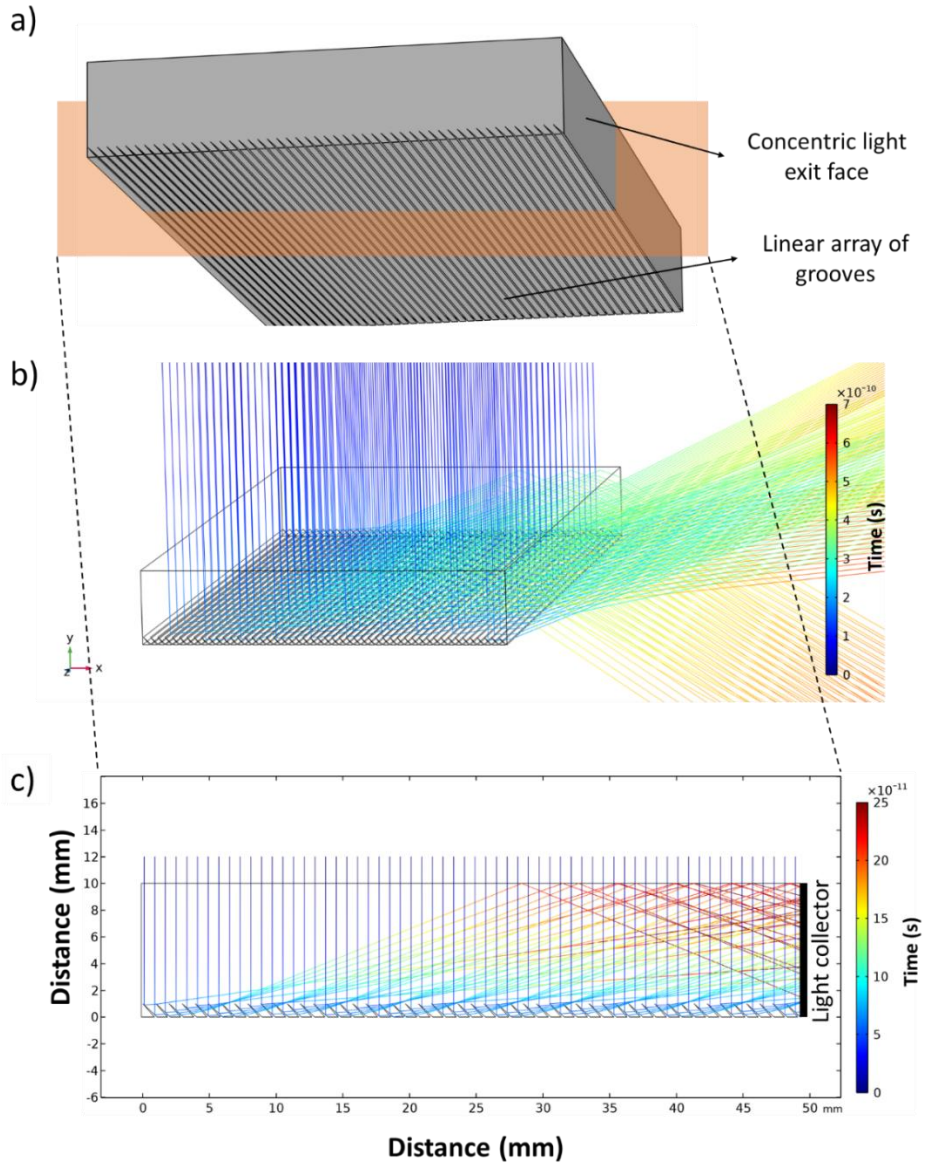

Figure 4.1. a) 3D geometric design of a typical linear SV-PLC; b) Time-dependent 3D ray tracing simulation of a linear SV-PLC showing lateral light concentration to the edge; c) Time-dependent 2D ray tracing simulation of the linear SV-PLC (cross-sectional profile of Figure 4.1a).

The following parameters and conditions were applied for the 2D simulation, for the linear design configuration.

1. All the simulations were carried out for the SV-PLC length kept at L_{100} (since for linear designs the FC does not justify the OE reduction after L_{100}).

2. The input power of light rays was set as 1W across the L_{100}.

3. A uniform ray density was considered, with a spacing of 0.05 units (mm) distance per ray across the L_{100}.

4. Material absorption losses were excluded from consideration, focusing the study on the design features of the SV-PLC.

5. The secondary rays (Fresnel reflection) were considered but not shown in the simulation images.

6. The angle θ was set to a minimum value as detailed in the design section, according to the RI of the material.

7. For comparative analysis, values of H and h were set at 10 mm and 1 mm, respectively.

8. The spacing value S was maximized while ensuring zero L_{leak} as outlined in the design section.

9. The α parameter was varied above the θ angle up to a maximum of 75˚.

2) Radial design for higher GC: The architecture of the radial design is shown in Figure 4.2a. The array of skewed V-grooves is arranged in concentric circles in this design. The concentrated light from every point is collected from the bottom of the centre of the SV-PLC (Figure b, showing the 3D time-dependent ray tracing simulation model) with the help of a mirrored surface, as shown in Figure 4.2a & Figure 4.2c. The light will spread from the bottom of the SV-PLC if uncoupled to any collector, as shown in Figure 4.2b. Figure 4.2c shows the 2D time-dependent ray trace simulation of the SV-PLC for radial design, where the light collector can be directly coupled to the bottom of the centre of the SV-PLC. The radial design is evaluated for its OE and FC.

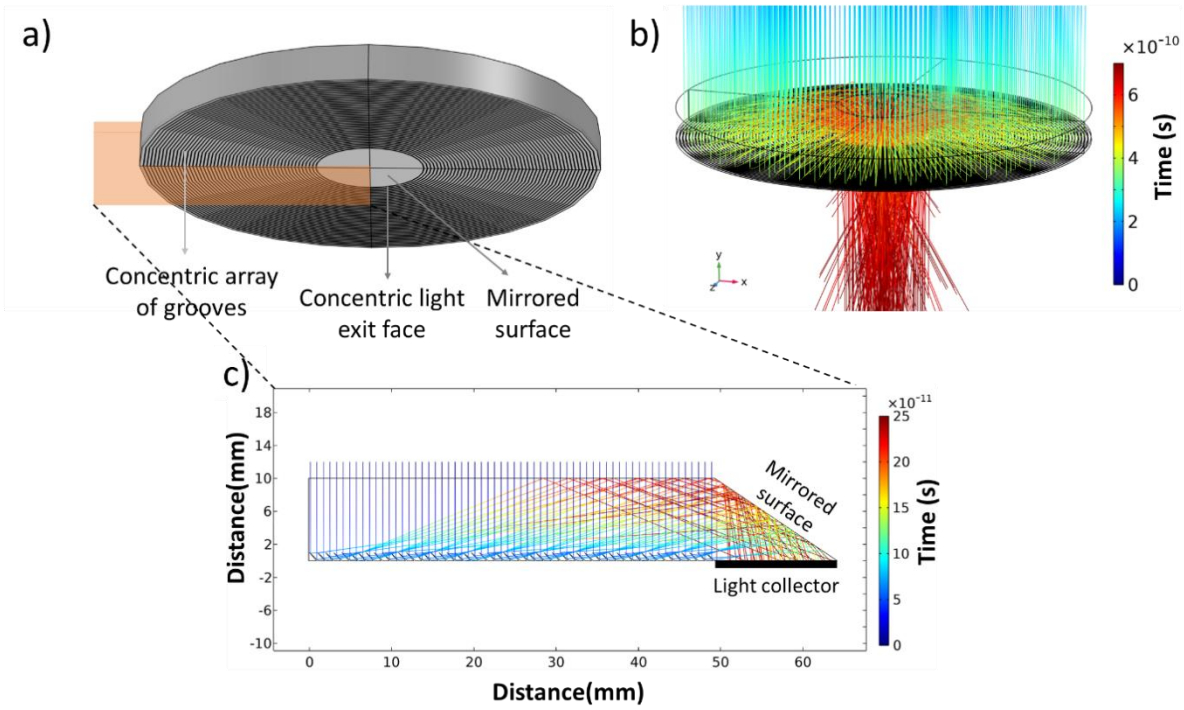

Figure 4.2. a) 3D geometric design of a typical radial SV-PLC; b) Time-dependent 3D ray tracing simulation of a radial SV-PLC showing radial light concentration to the centre; c) Time-dependent 2D ray tracing simulation of the SV-PLC (cross-sectional profile of Figure 4.2a).

Apart from the groove design, the collector end design should also be conceived for maximum light collection in a minimal area without any design loss in radial SV-PLCs. The design loss can be attributed to the low apex angle (γ) of the mirrored surface, making the concentrated light reflect back to the grooves, as shown in Figure 4.3a. By increasing γ, the loss can be avoided, compromising on the final light concentration (as the area of collection is increased), as shown in Figure 4.3b. Thus, it requires the optimization of γ, which is dependent on the maximum exit angle (β_{exit}) of the directed light from the grooves.

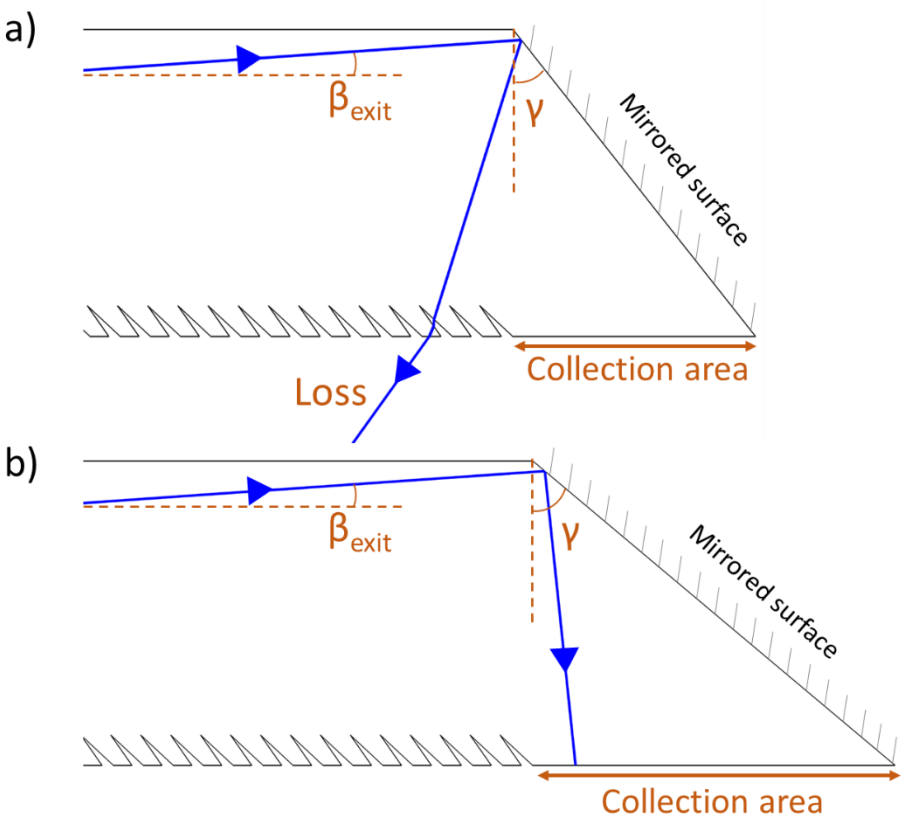

Figure 4.3. a) Design of the collection end of a radial SV-PLC showing incorrect γ angle creating loss of light rays; b) Design of the collection end of a radial SV-PLC showing the proper direction of light rays to the collection area.

The β_{exit} is dependent on θ, α, RI of the material, and the maximum number of grooves the rays pass through (N_{gmax}). Any β value (β represents the angle of the ray with the horizontal after reflection or refraction) of a particular design can be determined as mentioned in the mathematical equations in Chapter 2.

Consider a ray traveling with a maximum β_{exit} value on the mirrored surface of the radial SV-PLC design as shown in Figure 4.4.

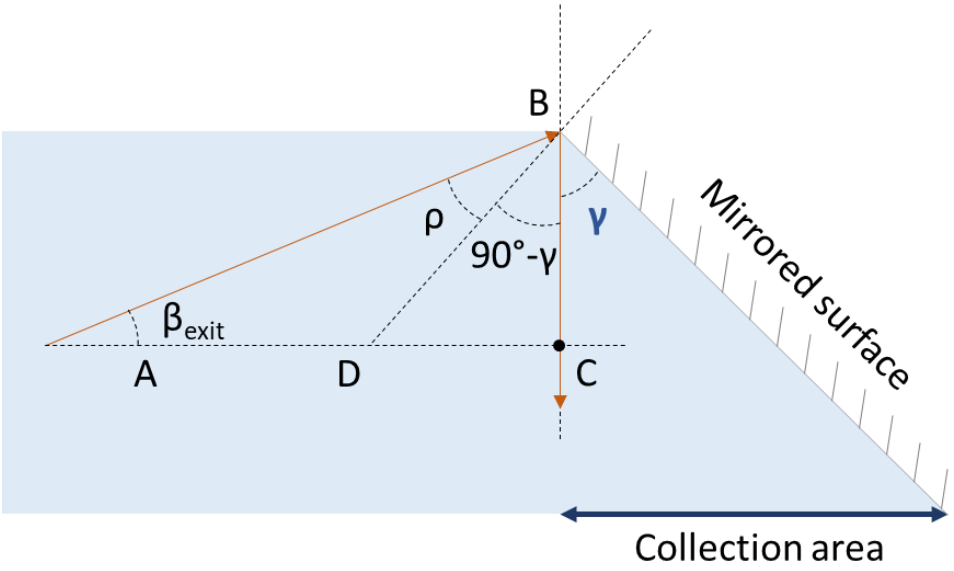

Figure 4.4. Representative illustration of ray travel (in orange color) in the collector end of an SV-PLC showing optimized apex angle (γ) of the mirrored edge.

For light to redirect to the collection area, point C must coincide with the vertical line from point B.

$$\Rightarrow \rho = 90°-\gamma \text{ (Snell's law of reflection of light)}$$

$$\beta_{exit}+\rho+90°-\gamma+90° = 180° \text{ (Sum of interior angles of a triangle)}$$

$$\Rightarrow \beta_{exit}+90°-\gamma+90°-\gamma+90° = 180°$$

$$\Rightarrow \gamma = \frac{\beta_{exit}+90°}{2} \tag{4.3}$$

The final collection area of the radial SV-PLC is:

$$\text{Area} = \pi\left(H\tan\left(\beta_{exit}\right)\right)^2 \tag{4.4}$$

The following boundary conditions and parameter settings were applied for the 2D ray tracing study for radial design:

1. All the simulations were carried out for the length of the PLC from 20 groove length to L_{max} (since radial design gives maximum light concentration, even though there is an OE drop after L_{100}).

2. The input power of light rays was set as 1W across the length taken for the OE study.

3. Uniform ray density was considered, with a spacing of 0.05 units (mm) distance per ray across the length of the PLC.

4. The angle θ was taken as small as possible (refer to the Design section).

5. For comparative analysis, values of H and h were set at 10 mm and 1 mm, respectively.

6. The inter-groove spacing was kept as wide as possible without any ray leakage (refer to design section).

7. The α parameter was varied from 45˚ to 55˚, with a 1˚ period to generate the trend for study.

8. The collection side of the PLC was designed as per the mathematical equations derived in Chapters 2 and 4.

8. Material absorption losses were not considered for the study, as it is focused on the design efficiency study of the system.

9. The secondary rays (Fresnel reflection) were considered but not shown in the simulation images.

10. The mirrored surface at the collection point is taken as 100% reflective.

The OE (i.e., the output energy received at the lateral edge/input energy) and final light concentration (OE X GC) are determined by measuring the power of light received at the lateral edge (the lateral edge boundary is taken as the detector) in the 2D simulation models. For linear designs, the FC remains the same in 3D considerations (since GC (input area/ output area) remains the same). For radial designs, the GC varies with the concentrator area and angular considerations (light collector area is dependent on θ and α). Hence, results from the 2D simulation are converted with mathematical calculations to get the FC in a 3D radial SV-PLC concentrator.

4.3.2 SV-PLC module fabrication evaluation

SV-PLC optics modules have been fabricated through laser cutting, 3D printing, and injection molding, as explained in Chapter 3. Optical microscopic imaging is carried out with a Carson MM-380 microscope with 20X magnification to check for cut angles, profiles, defects, and finish. In addition, the direct transmittance is also measured with the fabricated SV-PLCs as a qualitative measure of dimensional inaccuracies, as shown in

Figure 4.5. The SV-PLC optics are kept at a distance of 25 cm from an integrating sphere. The majority of the losses from the SV-PLC will be deviated outside of the integrating sphere. However, a portion of the losses due to dimensional inaccuracies will be transmitted to the integrating sphere, where it is detected. The light source used is a single-wavelength light (540 nm) from a monochromator.

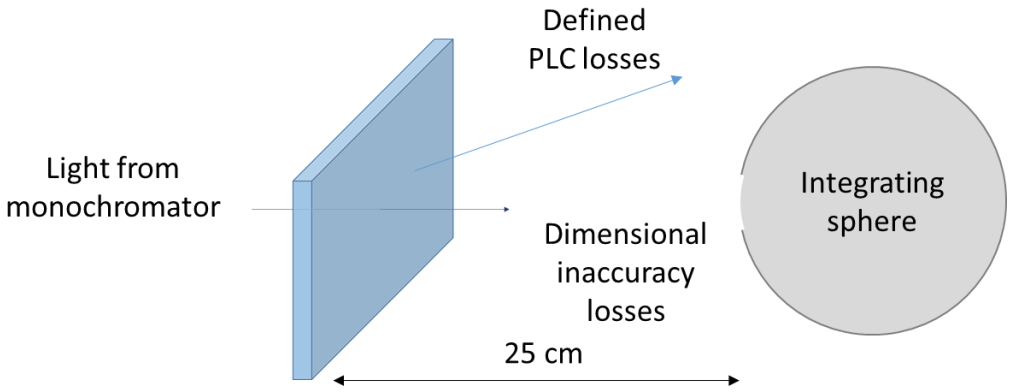

Figure 4.5. Schematic of the optical characterization layout of SV-PLC for analyzing the direct light transmission

4.3.3 SV-PLC Optics Characterisation

The OE of the selected SV-PLC is evaluated using a standard thin-film amorphous silicon flexible solar cell (supplied by PowerFilm Solar, USA; active area: 1 cm X 1 cm; 4 mW under 1 sun). The photograph and cell architecture are shown in Figure 4.6a. The solar cell is optically coupled to the SV-PLC with PDMS, and electrical contacts are taken from the rear end, as shown in Figure 4.6b. The output power from the bare cell and cell optically coupled with the SV-PLC are evaluated under 1 sun conditions using an AM1.5G ACA solar simulator (supplied by HOLMARC, India). For evaluating the cell performance under concentrated light, the cell is initially characterized from low light to concentrated light using a concave lens.

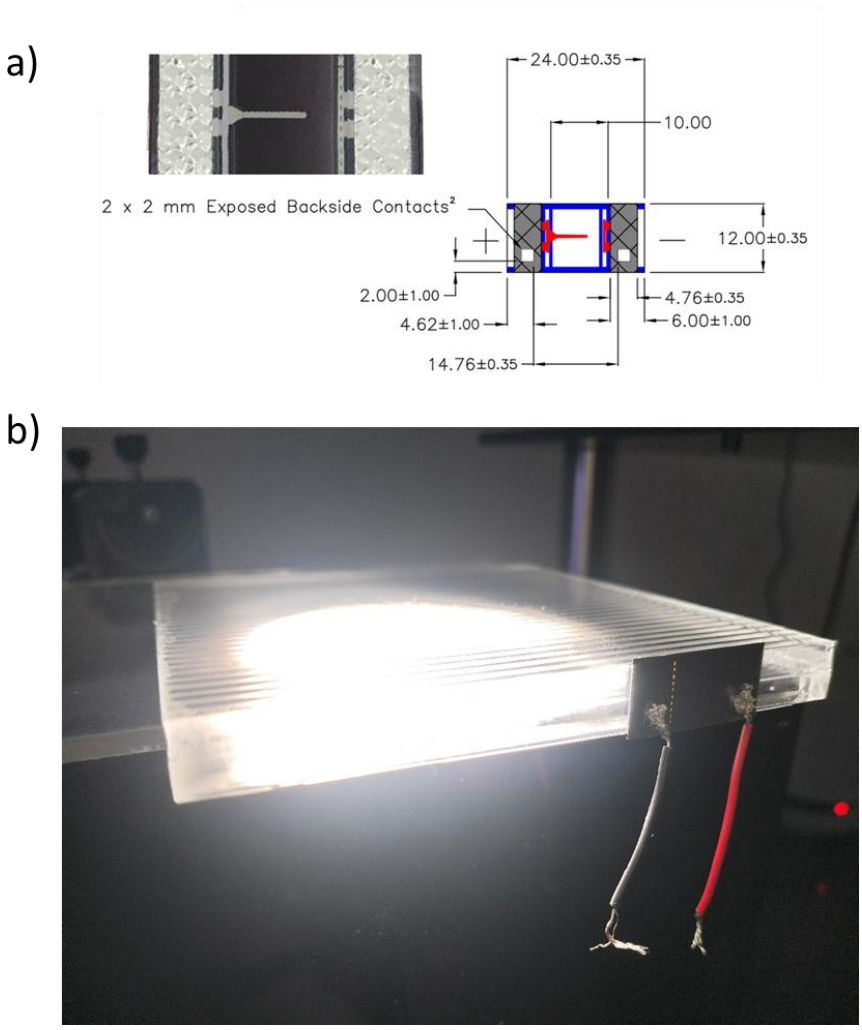

Figure 4.6. a) Amorphous silicon thin film solar cell used for the characterization of the SV-PLC and its dimensional details. b) Photograph of the SV-PLC optics module assembled with the solar cell for electrical characterization and kept under a solar simulator showing lateral light concentration.

The size of the simulator light source is 50 mm. To mitigate the non-uniformity of the solar simulator light and to convert it to a rectangular shape, the light source is masked to a definite geometric size at its entry point and also at the exit point. The schematic of this is shown in Figure 4.7. The sample will be moved from point to point to evaluate the light concentration. The final light concentration is calculated by adding up the results for the whole length of the concentrator. To expedite the optics in real conditions, a solar tracker setup is used for the study. All the measurements were taken around a light intensity of 1000 W/m^2.

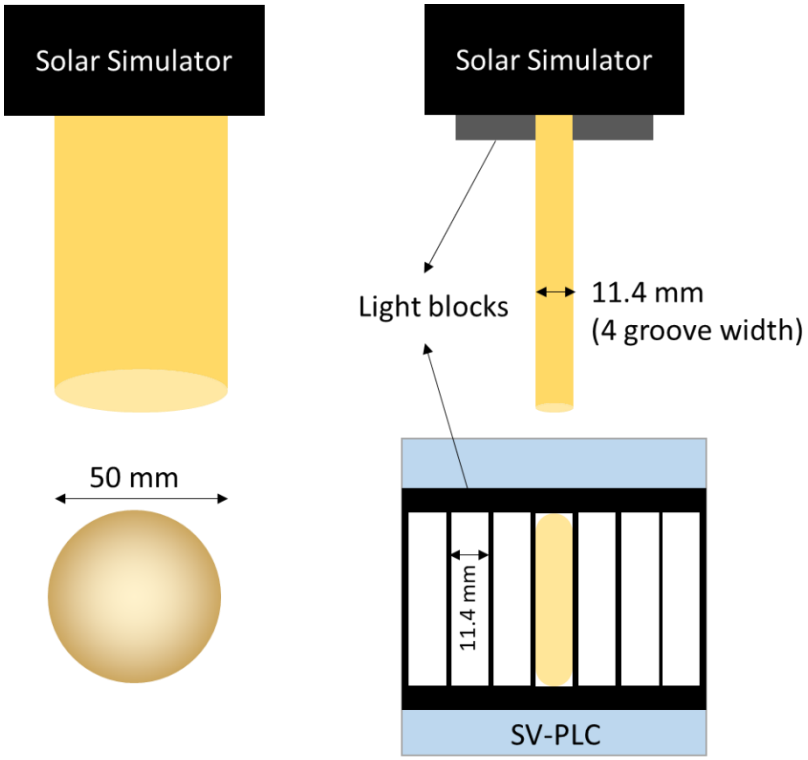

Figure 4.7. Schematic of the optical characterization setup layout used for the electrical output characterization of SV-PLC optics.

To conduct the angular acceptance study, a digital goniometer is used to vary the angle of incidence to the SV-PLC optics, and the output power is measured accordingly. The efficiency drop for different angles of incidence was measured relative to the respective 0° light incidences, as different cases have different power outputs. Hence, the efficiency drop is taken to 0 at 0°. The investigation focuses on the longitudinal axis and involves changing the incident angle from 0° to 25° since the angular shift of the sun through different seasons is ±23.5°.

4.4 Results & Discussion

Following the mathematical modeling (refer to Chapter 2), a parametrized simulation has been carried out in the COMSOL Multiphysics Ray tracing simulation platform. The study mainly focused on analyzing the OE and FC with varying α values for different RI materials (1.49, 1.52, and 1.58). The value input for other parameters is fixed according to the mathematical models (refer to Chapter 2) and assumptions (refer to the Design and Methodology section). The primary difference between the mathematical and simulation models is that the mathematical model is based on a single groove (typical groove) analysis, whereas simulation models are based on the whole SV-PLC optics. Figure 4.8 shows the

comparison of results from both models, analyzing the OE (Figure 4.8a) and FC (Figure 4.8b) with α. Even though the graphs follow the same pattern, a slight variation is there. This can be attributed to the difference in the basic method of modeling. The primary difference between the mathematical and simulation models is that the mathematical model is based on a single groove (typical groove) analysis, and extrapolated to the whole length of the concentrator. Whereas, the simulation models are based on the whole SV-PLC optics. Thus, the mathematical model does not include the final grooves that yield rays with fewer refractions through the grooves compared to the typical groove. Hence, there will be an upward shift to the values in the simulation models, and it tends to be more accurate. The Root Mean Squared Error between the models for OE is 3.02%, 3.65%, and 3.28% for RI 1.49, 1.52, and 1.58, respectively. The Root Mean Squared Error between the models for FC is 0.20, 0.31, and 0.56 for RI 1.49, 1.52, and 1.58, respectively. The model difference will be distinctive for low α values, since N_{gmax} (maximum number of grooves a ray passes through in an SV-PLC) will be higher. Even though the simulation models can be considered more accurate, the mathematical model is used for understanding the SV-PLC optics in detail, and for several parametric optimisations, which are used in the simulation studies.

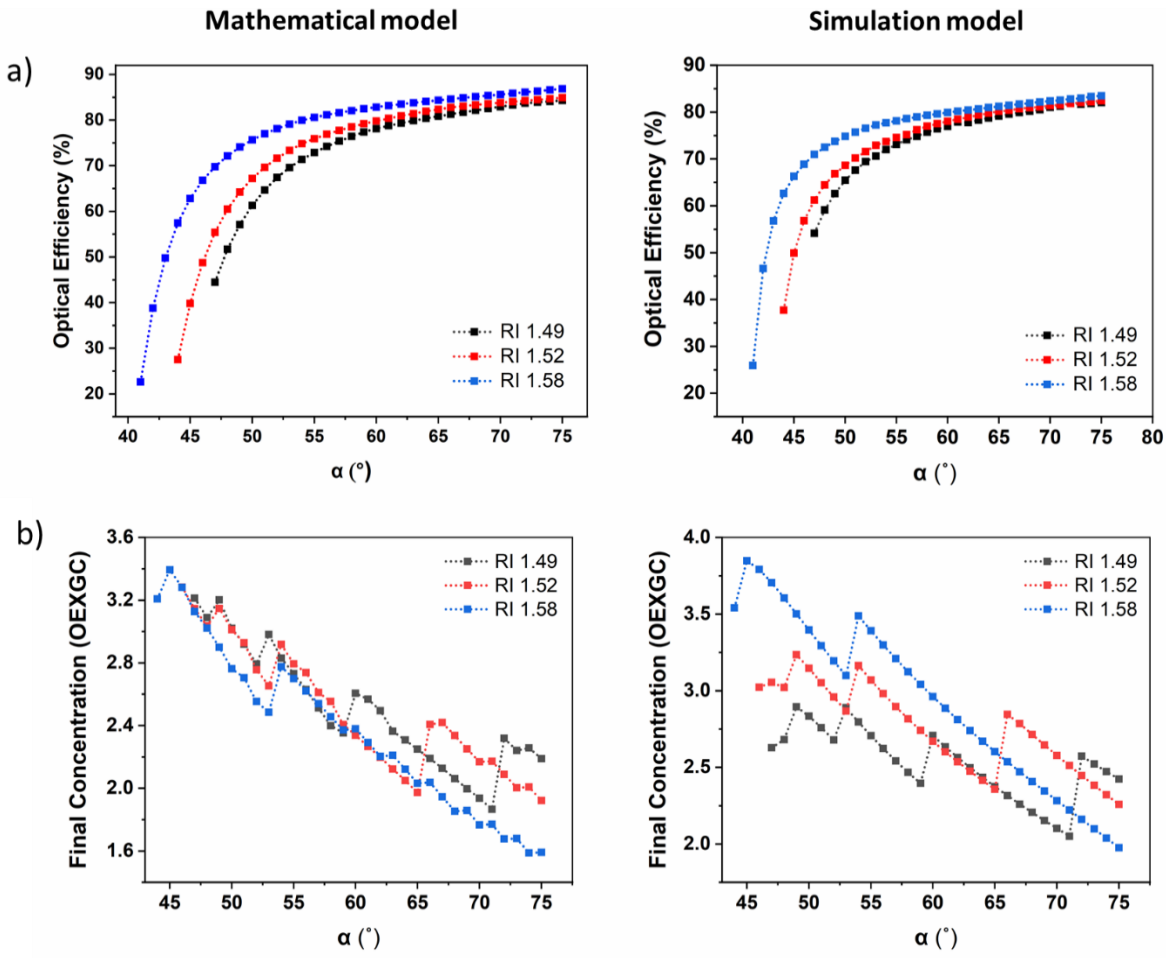

Figure 4.8. Plots obtained from the mathematical and simulation models of the SV-PLC optics show the relation of a) OE with α, and b) FC with α.

The 2D evaluation of the SV-PLC can be identified as the same for the linear design (refer to the Design and Methodology section), since the ratio of SV-PLC top area and lateral area remains the same in the 2D and linear designs. However, for radial designs, the GC value or the ratio of the SV-PLC top area to the final light collection area will be different according to the length of the PLC. Moreover, studies need to be conducted with lengths higher than L_{100} up to L_{max} (refer to section Determination of L_{100} and L_{max} in Chapter 2).

For radial design, the 2D ray-tracing model of the radial SV-PLC has been conducted with an output time of 1.5 nanoseconds and a period of 0.5 picoseconds to get an accurate model. OE has been calculated as the ratio of the power received at the collector (taken as a detector) and the input power. The simulations have been carried out with the length of the PLC from 20 grooves to L_{max}. L_{max} for the present study is 260 mm for the material RI taken as 1.49, θ as 43°, H as 10 mm, and h as 1 mm (refer to the section Determination of

L100 and L_{max} in Chapter 2). For designing the collector section, i.e., determining the γ value, the maximum number of grooves (G_{max}) any ray will pass is estimated through simulation models for individual groove designs (i.e., varying α). β_{exit} for each design is calculated separately from the refraction angle at the exit point (r_{exit}). γ and the final collection area are calculated using Equation 4.3 and Equation 4.4, respectively. Figure 4.9a shows the plots of OE with varying GC (i.e., radius of the radial SV-PLC) with α ranging from 45° to 55° for a material with RI 1.49. The dotted curve indicates the point of OE drop, pointing to the position of L_{100}. After L_{100}, there will be a drastic reduction in OE due to the increased losses. Figure 4.9b shows the FC value with varying radial SV-PLC area with α ranging from 45° to 55° for material with RI 1.49, which can be considered a method of selection of SV-PLC design. Except for a very low α design (i.e., 45°) with high Fresnel reflection losses, low α designs tend to perform better in FC for a fixed concentrator area. The plot can be used for design selection according to the manufacturing capability, as lower α design faces difficulties in manufacturing since they reduce the groove thickness. As an example, the dotted line in Figure 4.9b shows an FC of 50X. According to the results for achieving 50X, the SV-PLC with α 46° requires approximately 1.8 times less concentrator area compared with the PLC of α 54°. Any PLC design (with material RI of 1.49, H as 10 mm, and h as 1 mm) with an α value less than 54° cannot theoretically achieve the 50X FC mark.

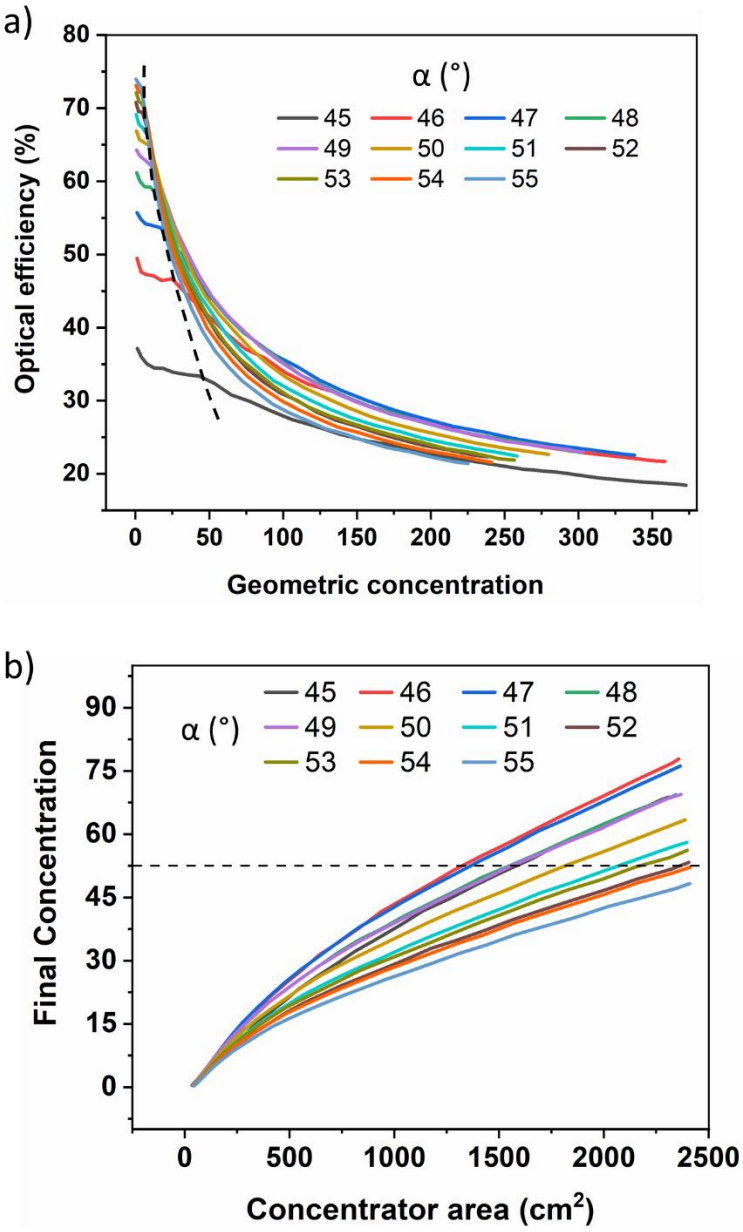

Figure 4.9. a) OE vs GC plot of radial skewed V-groove PLCs with varying α in a material of RI 1.49. b) FC vs Concentrator area plot of radial SV-PLC with varying α in a material of RI 1.49.

The different fabrication routes adopted for the SV-PLC are elaborated in Chapter 3. The fabrication evaluation is conducted with optical microscopy imaging and direct light transmission study, as explained in the Design and Methodology section. Figure 4.10 shows the optical microscopy images (20X) of the grooves of SV-PLC fabricated with laser cutting, 3D printing, and injection molding. The images of samples of laser cutting revealed several issues with the process, including low dimensional accuracy, profile deformation, and low surface quality. The designed angle between the reflecting and refracting faces was

6°, however, the final contour shows an angle of 2° after laser cutting. This was likely due to damaged and deformed edges caused by local heat produced. The profile also seems to be unsuitable for the laser cutting process, since the cuts for the profile are very close to each other, creating heat-induced deformations. Analyzing images of 3D printing, they also showed lower dimensional accuracy due to the edge irregularities and rounded-off edges. The limitations of printing accuracy and additional polishing and lacquer coating processes can lead to these limitations. When compared to the two processes, injection molding yielded better straight-cut surface profiles with minimal rounded-off edges. The angular difference between the faces (11°, $\alpha = 55°$, $\theta = 44°$) was also accurate.

The limitations in fabrication using laser cutting and 3D printing compared to injection molding were also validated with direct light transmittance measurement (Refer to the Design and Methodology section). The direct transmittance offered by SV-PLC fabricated by laser cutting is higher (38.5 ± 0.8%), followed by 3D printing (23.1 ± 1.4%) and injection molding (12.8 ± 0.5%). The dimensional inaccuracies contribute to the major portion of this direct light transmittance.

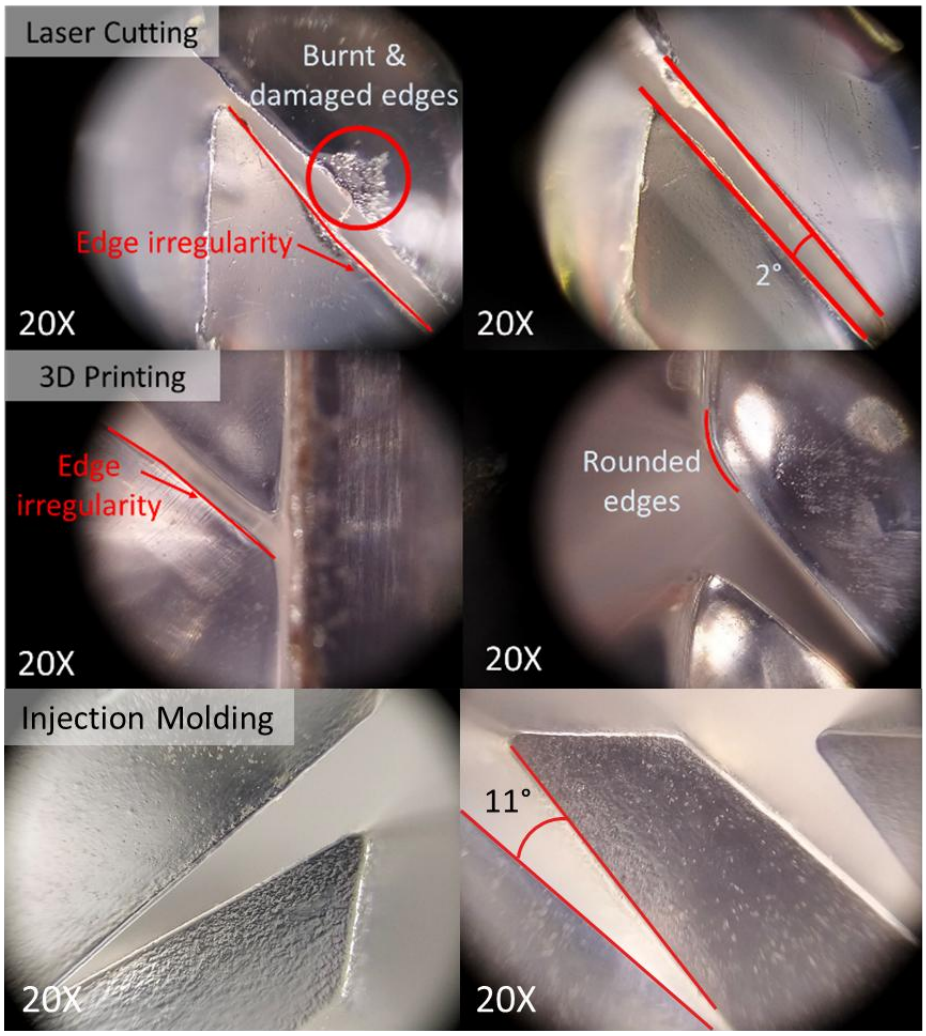

Figure 4.10. 20X optical microscopy images of SV-PLC optics fabricated through laser machining, 3D printing, and injection molding showing groove profiles and defects.

After the evaluation of the SV-PLC optics fabricated through the different methods, injection molded samples yielded samples were selected for the concentration studies due to their better groove profiles. The injection molded samples (Specifications: H: 4.5 mm, h: 3 mm, θ: 44°, α: 55°) were optically coupled with a PMMA plate of 5 mm with epoxy resin to increase the H value to around 10 mm, to attain the size of the solar cell. The samples were characterized to measure the final output power from the solar cell. Figure 4.11 shows the photograph of the characterization setup at the standard conditions (bottom left) and real-time conditions (bottom right). All the measurements were taken around a light intensity of 1000 W/m^2 (1 sun). The results show an FC of 2.3X and 2.2X in the STC and real-time conditions, respectively, compared to the non-concentrated solar cell reading at 1 sun condition.

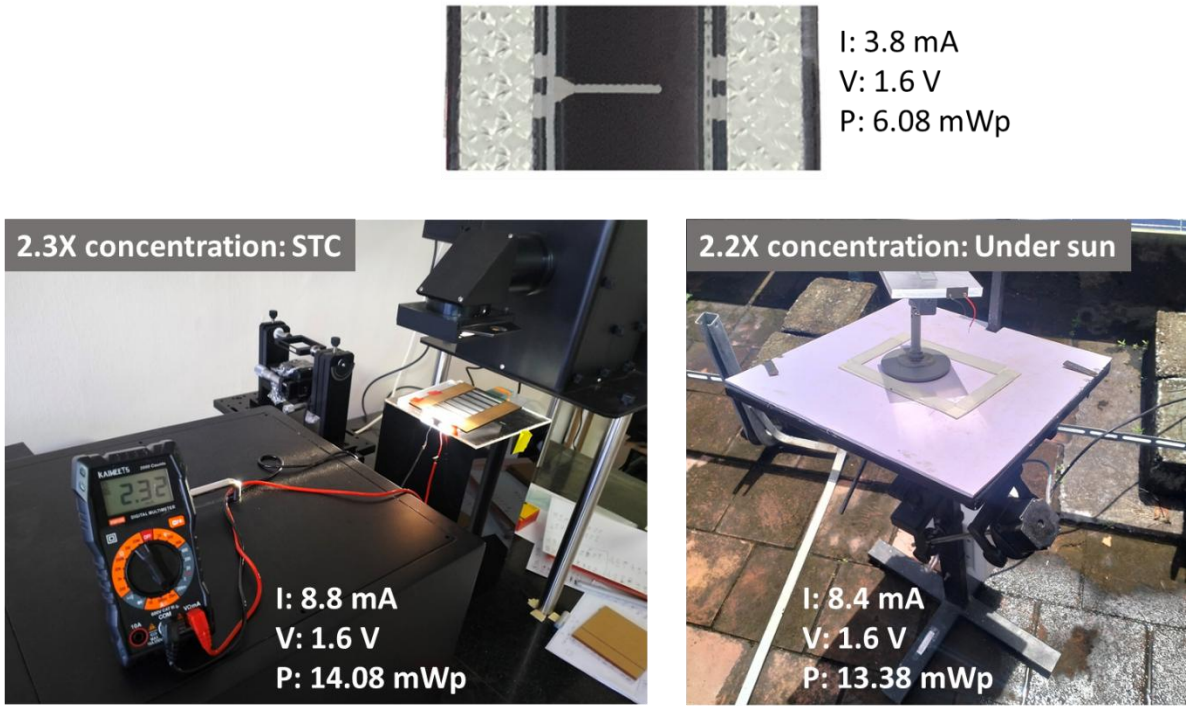

Figure 4.11. Photograph of the experimental setups (standard condition (left) and on-field condition (right)) used for the electrical output characterization of SV-PLC optics, and showing the corresponding results obtained. The top image shows the results of bare solar cells under 1 sun conditions.

The angular acceptance study along the longitudinal axis has been conducted by both a simulation study and experimentally (for 1.6X GC to accommodate the size and uniformity of the solar simulator) under STC using a goniometer. Figure 4.12a shows a typical ray tracing image of SV-PLC with an angular shift of 25° light incidence to the normal, showing the lateral light concentration. Figure 4.12b presents the results of the simulated single directional efficiency drop angular study for SV-PLC (RI: 1.49, θ: 43°, α: 49°, H: 10 mm, h: 1 mm) with GC of 10X, 7.5X, 5X, and 2.5X, and an experimental study in a 1.6X GC SV-PLC. The efficiency drop for different angles of incidence was measured relative to the respective 0° light incidences, as different cases have different power outputs. Hence, the efficiency drop is taken to 0 at 0°. The investigation focuses on the longitudinal axis and involves changing the incident from 0° to 25°. In the graph, the highlighted rectangle represents the angular acceptance zone till 23.5°, which corresponds to the angular shift of the sun (± 23.5°) through different seasons. The results showed a low-efficiency drop of less than 10% within 15° and a maximum drop of 30% within the 23.5° zone. Figure 4.12c shows the photographs of SV-PLC optics showing lateral light concentration with varying angles of incidence under direct sunlight.

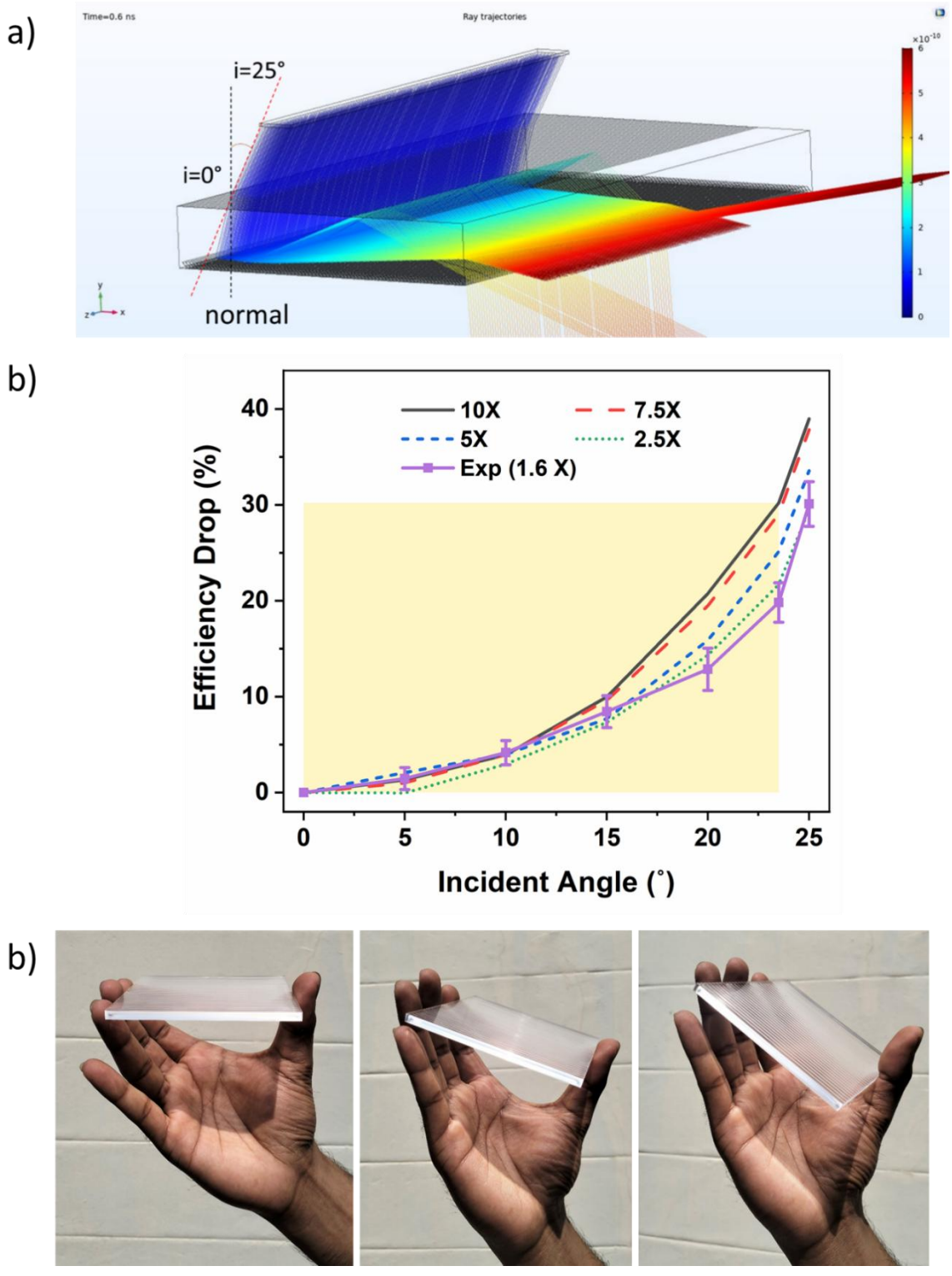

Figure 4.12. a) Typical 3D ray tracing simulation of SV-PLC optics with inclined light incidence (25°) in the longitudinal axis. c) Simulation and experimental study plot demonstrating the efficiency drop in SV-PLC with varying incident angles in the longitudinal axis. c) Photographs validating the high angular acceptance of SV-PLC in the longitudinal axis.

4.5 Conclusions

The evaluation of the SV-PLC optics has been carried out for different fabrication routes through optical microscopy and direct light transmittance to assess the dimensional accuracy and surface profiles of the skewed V-grooves. The results revealed injection molding to be a more suitable manufacturing method for better groove profiles and optical clarity. The simulation models have been developed for SV-PLC optics with different RI materials (1.49, 1.52, and 1.58). Accordingly, the FC of <5X can be achieved with the linear design of SV-PLC (length up to L_{100} only taken for evaluation) with a low-efficiency drop of less than 10% within ±15° angular shift in the light incidence and a maximum drop of 30% within the ±23.5° zone. More design modifications can be made in SV-PLC linear designs, such as gradient-sized grooves (discussed in Chapter 6) to improve the FC. The radial SV-PLC designs simulated revealed that it can achieve an FC up to 75X at the expense of the angular acceptance. The simulated models (the method used whole SV-PLC optics) align well with mathematical models (the method used a typical single SV-PLC groove), except for the slight performance increment in simulation models because of the methods adopted. Upon the experimental evaluation, the 10X GC injection molded SV-PLC optics (H: 10 mm, h: 3 mm, length: 100 mm, θ: 44°, α:55°) showed a maximum FC of 2.3X and 2.2X under standard conditions and on-field conditions, respectively, under 1 sun conditions. The experimental angular acceptance study (for 1.6X GC) also showed a similar graphical trend to the simulation results.

Chapter 5

Dynamic Power Window Technology

5 Dynamic Power Window Technology

5.1 Abstract

Dynamic windows are widely used in buildings/vehicles to obtain switchable transparency modes, which enable advanced privacy settings as well as improve the energy efficiency of the built environment. The incorporation of energy generation capability in dynamic windows is a highly welcomed technological advancement, hence listed by the U.S. Department of Energy (DOE) as a high-priority early-stage R&D topic. The current status of state-of-the-art active dynamic renewable energy-generating window technologies reveals a huge gap due to their multifunctionality and technological feasibility. As of now, both BIPV window glazing and active dynamic window technologies suffer from cost competitiveness and functional limitations. The exploitation of material experimentation for BIPV windows either compromises their energy efficiency or transparency state, both of which are conduits for their technological excellence. Considering the cost-effectiveness, the implementation/ modification of existing dynamic window technology will be impractical. However, the design-oriented approach has the greater advantage of better BIPV techno-economics and cost reduction potential for active dynamicity. Combining the two in a single platform will emerge as a prospective solution to the cause. Herein, a novel window technology is demonstrated that enables switchable transparency modes along with energy generation capability, a first-of-its-kind technology using Skewed V-groove based Planar Light Concentrator (SV-PLC) optics and optofluidics transparency switching. The solution attained transparency switching states (directly transmitted light) of 90% (transparent state) to 15% (translucent state) for privacy, with an energy generation of ~20 Wp/m^2 (using polycrystalline silicon solar cells). Apart from that, the window can offer a 50% daylight transmittance (diffused transmitted light) in its translucent state. The chapter workflow is illustrated in the flow chart below.

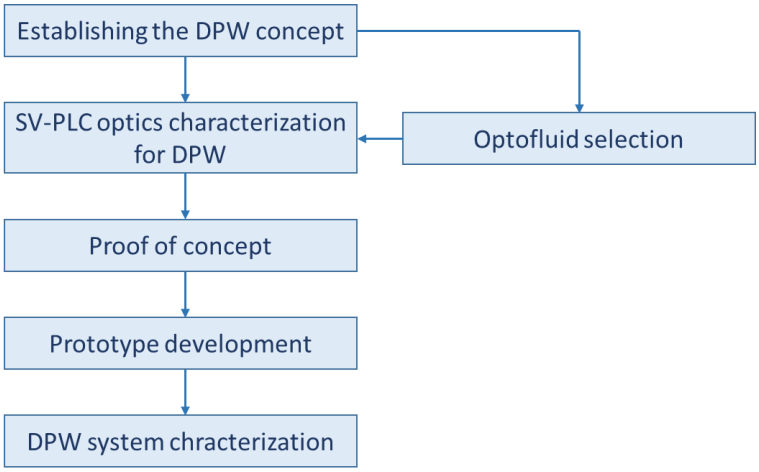

5.2 Introduction

To accomplish the targets of the Paris Climate Agreement and the recent COP26 meeting, it is of the utmost importance to meet the energy demand in industry, commercial, and residential building spaces by adopting renewable energy technologies. Most of the initiatives to tackle this vast energy demand rely on the efficient utilization of solar energy, where light energy management is an essential prerequisite. Hence, the development of efficient light trapping and guiding systems is of utmost importance for sustainable light energy management, which promotes the widespread construction of energy-efficient solar/green buildings. The concept of Building Integrated Photovoltaic (BIPV) is the most promising method to use built space for solar energy capture, conversion, and distribution. However, BIPV is limited to the rooftop or facade space due to the serious constraints of the standard module; mainly, the components are opaque and have a standard size and shape. The constraints of the standard module limit its use in the vertical glazing space of skyscrapers, which require aesthetic appearance and on-demand transparency for energy-efficient dynamic windows that can control daylight guiding into the built environment [168].

Different PV materials and product design considerations have evolved in the R&D of BIPV windows. Even though crystalline silicon PV is the best solution from an energy generation point of view, the technology can be considered less exploitable for glazing solutions due to the lack of visible light transmission (V_T) [169]. For incorporating comparatively better light transmittivity for daylighting, thin film solar cells (such as cadmium telluride (CdTe), gallium arsenide (GaAs), and copper indium gallium selenium compounds (CIGS)) and other third solar cells (such as dye-sensitized solar cells (DSSCs),

perovskite solar cells (PSCs), quantum dot solar cells (QDSCs), etc.) have been accommodated both in R&D and product level [170-172]. Another approach that was carried out is the modification in system design, such as that of PV solar blinds, BIPV windows with cut cell strips, etc., which also has its limitations of shading and low energy performance [173-175]. Luminescent Solar Concentrators (LSC) are also employed as semi-transparent planar concentrators that can be integrated with a photovoltaic cell to generate energy [82, 176]. However, the low light collection and photon density of LSC compared with direct sun exposure and optics-based concentrator technologies [59], limit the scope of LSC, where high illuminance is required for enhancing the performance of PV cells.

It is worth mentioning that the active dynamic performance in windows is also an essential requirement for achieving better energy efficiency and privacy settings in a built environment; this is mainly attained by controlling the light intensity using different approaches, which utilize the principles of electrochromism, liquid crystal technology, and suspended particle technology. Among them, the most commercially adopted products are electrochromic (EC) [177, 178], Suspended Particle Devices (SPDs) [179], and Polymer-Dispersed Liquid Crystals (PDLCs) [180, 181]. One of the major advantages of EC windows is that the switching states can be stopped at intermediate levels without requiring any power to maintain [182]. However, the switching time of EC windows is comparatively very large, around 10 to 20 min for standard-size windows [183]. PDLC windows have a faster discoloration speed than EC, and the transmittance can be adjusted depending on the amount of voltage applied. However, PDLC requires the continuous application of power to maintain a low transparency state, which is limited to 50%, and cannot be used for privacy windows [184, 185]. Like PDLC, the switching speed is higher for SPD, and the V_T can be controlled, but requires power to maintain the state [186]. Even though these technologies are available in the commercial market, the transparency state is limited to around 60% to 75% V_T [187]. Other technologies in this regard include Gasochromic, Nanocrystal in-glass composite, Electrokinetic pixel, Elastomer-deformation tunable, Liquid infill tunable windows, etc., except for Nanocrystal in-glass composite, these technologies also possess limited V_T in their transparent state [187]. Also, the cost analysis of active dynamic window technologies in the market shows their limited feasibility for a mass audience [188, 189]. In this regard, optofluidic smart glass offers a cheaper, simpler, and more efficient dynamicity of 8% to 85% V_T states [188]. The window matrix is

designed to block the light from transmitting through in its opaque state. The method of dynamicity involves the incorporation of an optofluid that has a refractive index (RI) matched with the optics-based opaque window matrix to make the transparent state. The matrix design has a retroreflective pattern on it and has been 3D printed in an optically transparent material (Veroclear, RI: 1.52). The fluid used is methyl salicylate, having an RI similar to the matrix. Figure 5.1 shows the different states of optofluidic dynamic glass, in which the first and last photographs show the opaque and transparent states achieved through fluid incorporation. The middle figure shows the water-filled matrix, showing diffused transmittance and the importance of RI matching in optofluidic dynamic windows.

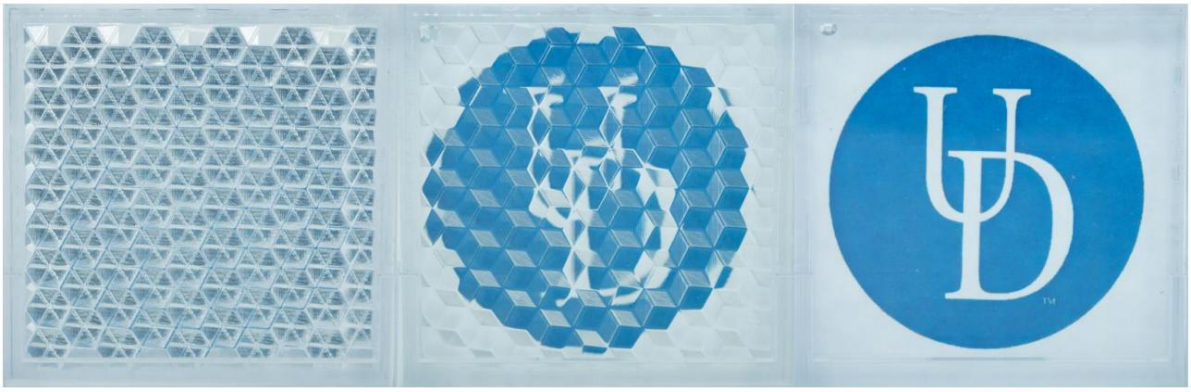

Figure 5.1. Optofluidic-based dynamic window, showing its opaque state (left photograph), diffuse transmittance state (middle photograph), and transparent state (right photograph). Source: Reproduced with permission from [188]. Copyright © 2017, OSA.

Even though active dynamic windows are available in the market, and BIPV glazing solutions are hitting the market with new advancements, till now, there is no such window technology available where renewable energy generation, active dynamism for privacy, and daylighting have been developed. The only closer concept carried out was Lance M. Wheeler et.al., in 2017, demonstrated the proof of concept of a passively dynamic power-generating window, that relies on a thin coating of a perovskite material for energy generation, and methylammonium lead iodide-methylamine complex to demonstrate a cohesive thermally switchable PV window when sunlight falls on it [190]. The transparency switching was 68% to 3% V_T over 20 cycles, and the energy conversion efficiency was 11.3% in the opaque state. The scalability and material stability are major concerns for this type of power window, as perovskites are only in the development stage.

Herein, a novel concept of integrating active dynamicity and power generation in a single platform is been introduced, as a BIPV glazing solution. The technology utilized SV-PLC

as the energy-generating segment, which is integrated with optofluidics to attain active dynamism.

5.3 Concept

The concept of DPW using SV-PLC can be conceived with the combination of energy generation through planar light concentration from SV-PLC and optofluidic-based dynamicity in transparency. Through that, DPW works in two modes of operation, as represented in Figure 5.2:

1) Translucent mode (Figure 5.2a): This is the fluid-uncoupled energy generation mode, where light will be redirected by the SV-PLC for energy generation. The mode provides the Privacy-ON setting, and the losses from the SV-PLC (Refer to Chapter 2) will be utilized for daylighting. Also, part of the diffused light will be utilized for energy generation, and a part will be transmitted through the window.
2) Transparent mode (Figure 5.2b): This is the fluid-coupled transparent mode of DPW, where direct and diffuse light will be transmitted through the window, providing the Privacy-OFF setting with no power generation. By matching the RI of the optics matrix with the optofluid, the light will follow the same path as the incident direction, providing visual clarity. Any power generation in this mode can be attributed to the collection of direct or diffuse light by the solar cell.

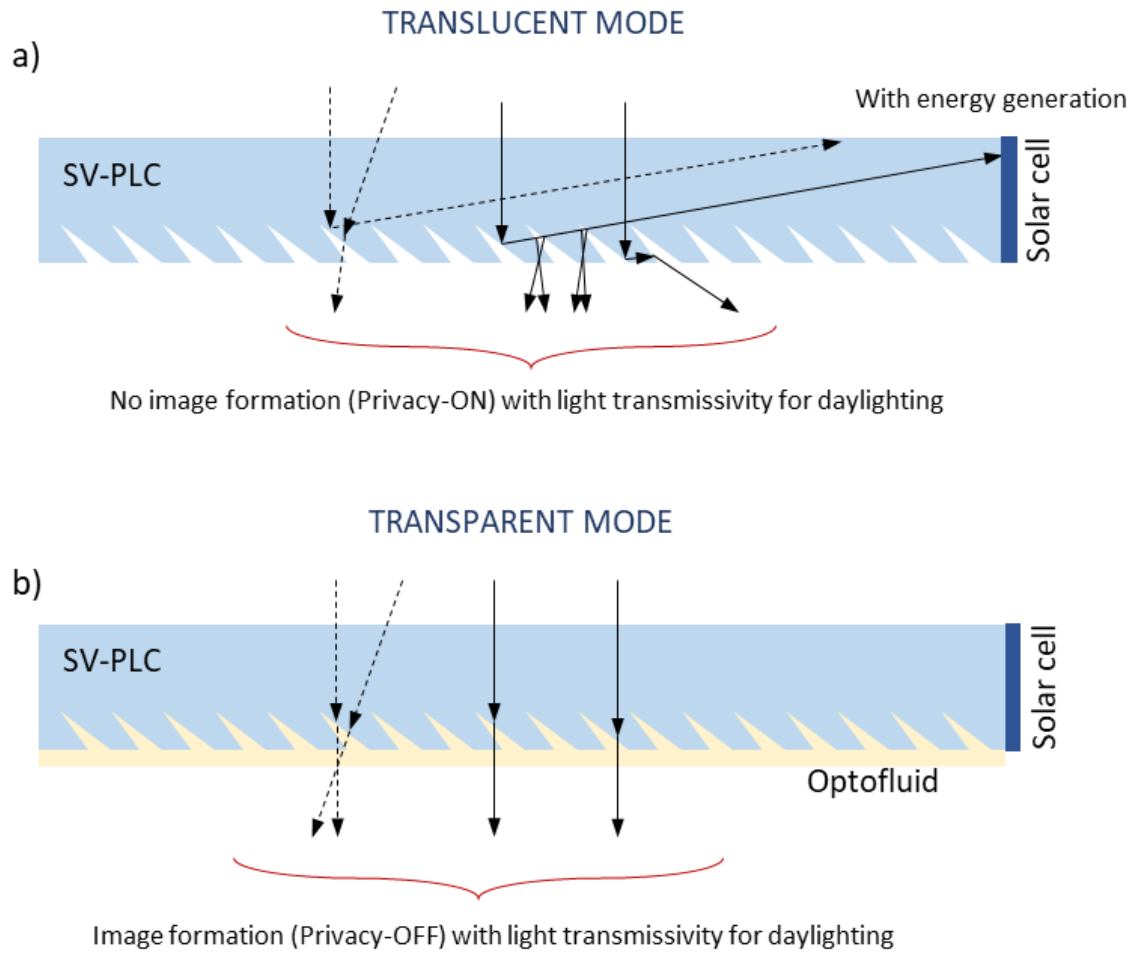

Figure 5.2. Schematic representing the concept of DPW using SV-PLC optics in its a) Translucent mode, having privacy ON, partial daylighting, and energy generation, and b) Transparent mode, having privacy OFF and daylighting.

5.4 Materials and Methods

5.4.1 Design

The transparency switching in DPW is achieved through gravitational fluid flow with a rotating window design. A fluid storage tank is placed adjacent to the SV-PLC unit to store the optofluid in the unfilled translucent mode. When the window is rotated, the fluid flows to the SV-PLC unit, filling the skewed V-groove voids to have the transparent state. The different parts and design of the DPW are shown in Figure 5.3.

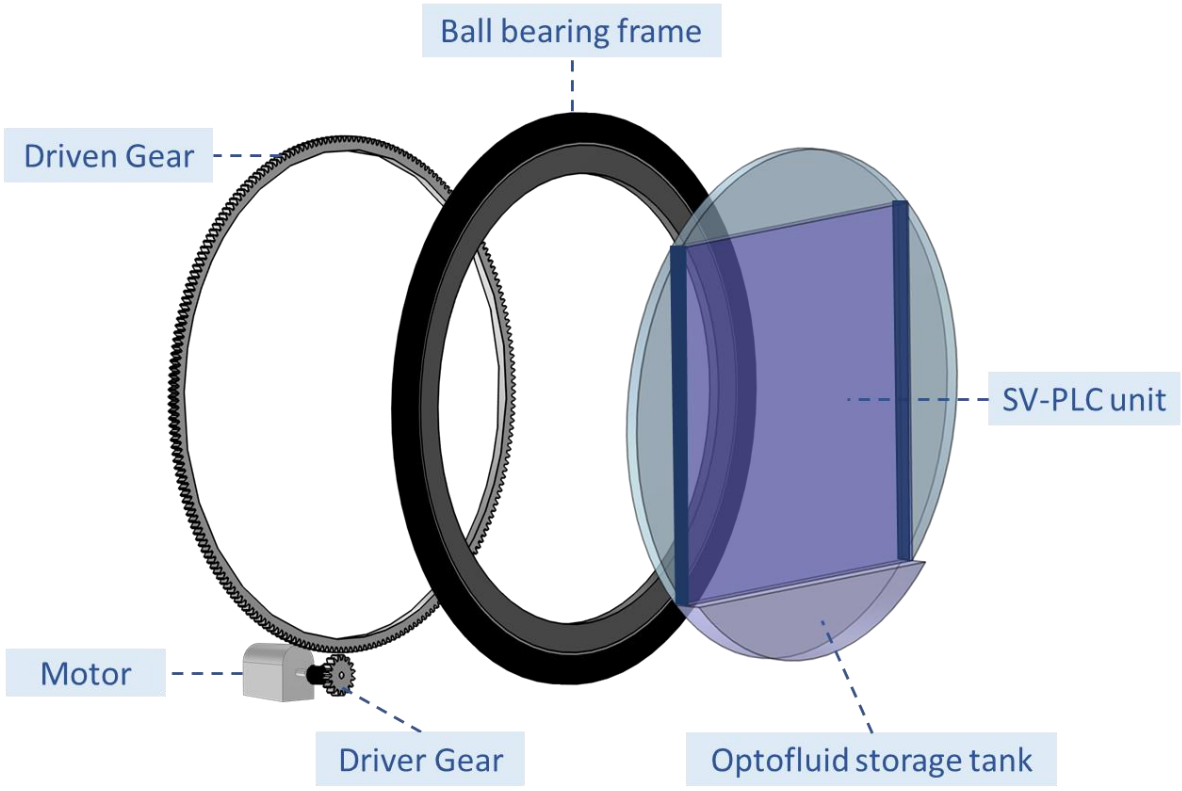

Figure 5.3. Schematic showing different parts and architecture of DPW.

SV-PLC unit: The SV-PLC unit constitutes the SV-PLC optics (H: 4.5 mm, h: 3 mm, θ: 44°, α: 55°) array within a closed enclosure (fabricated with PMMA), with one end opening to the optofluid storage tank, as shown in Figure 5.4. The solar cell array is isolated from the enclosure and is on the lateral edge of the unit. The current design includes four SV-PLC optics modules of size 105 mm X 100 mm, making the whole window of size 210 mm X 200 mm. Six individual solar cells of size 17 mm X 34 mm X 3mm have been optically coupled to the enclosure on one side of the unit, and electrically connected in series. The series-connected cells from both are connected in parallel to each other. A gap of 2.5 mm has been incorporated in the SV-PLC enclosure for the fluid flow from and to the storage tank.

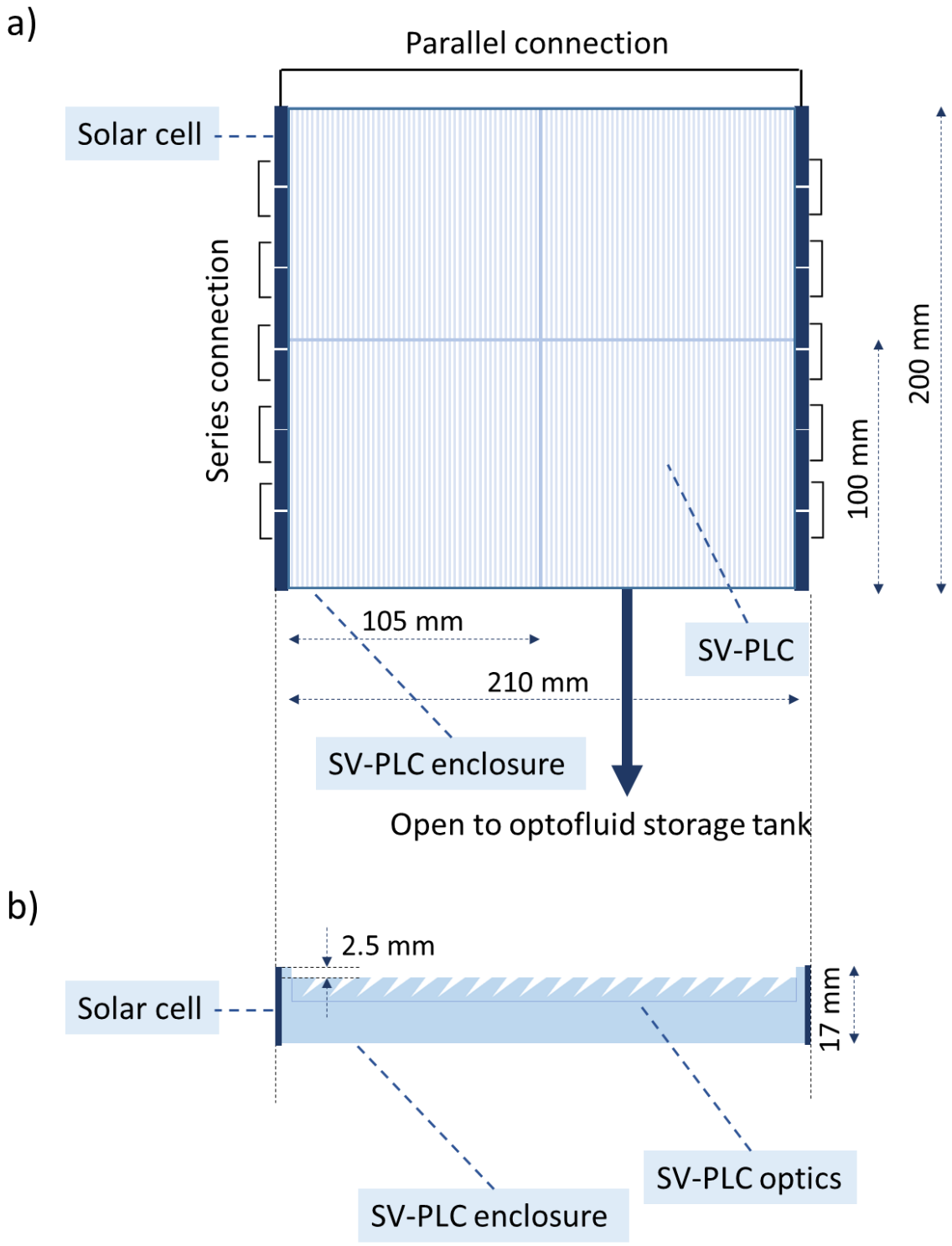

Figure 5.4. Drawing showing a) front view of the SV-PLC unit with the dimensions and solar cell architecture, b) top view of the SV-PLC unit with the dimensions, and gap for optofluid flow.

Optofluid storage tank: It is an arc-shaped enclosed PMMA tank with one end open to the SV-PLC unit. The volume of the tank is kept above the volume of space to be filled in the SV-PLC unit.

Window rotation arrangement: As mentioned, the transparency switching states in the DPW have been achieved with the filled and non-filled state of the optofluid, which has been carried out with gravity steering. A rotatable turntable bearing (outer diameter of 510 mm and inner diameter of 340 mm) unit has been attached to the window unit with a PMMA plate to allow the rotation. To automate the motion, a 12 V motor with a gear arrangement is attached to the bearing unit, and the whole system is operated with a connected electrical push switch. The gear system fabricated for the system has the following dimensions:

- Driver gear (Pinion): Pressure angle: 20°, module: 1.6 mm, pitch diameter: 25.6 mm; circular thickness: 2.2 mm; face width: 6.4 mm
- Driven gear: Pressure angle: 20°, module: 1.6 mm, pitch diameter: 356 mm; circular thickness: 2.2 mm; addendum: 1.5 mm; face width: 6.4 mm

5.4.2 Materials

SV-PLC Unit: SV-PLC optics in PMMA material (Acrypet VH of Mitsubishi Rayon Co. Ltd.; RI: 1.49) have been manufactured through injection molding (Refer to Chapter 3 for details), which is used for the DPW demonstration. SV-PLC enclosure: SV-PLC optics have been optically coupled to the enclosure with transparent epoxy resin. The enclosure and optofluid storage tank have been fabricated using transparent PMMA sheets (brand: Gujpol-S, RI: 1.49)

Optofluid: The optofluid selection for technology demonstration has been carried out under three conditions:

1) High visible light transmission (> 90%)
2) RI approximately similar to that of PMMA (1.49)
3) Compatibility with PMMA

Commercially available RI matching liquid (Acrylic matching liquid (Product code: 5032) of Cargille Laboratories, USA, with RI 1.4917) has been used as a standard fluid for the DPW. Apart from that, commercially available α-tocopheryl acetate, having a RI of 1.492

and visible transmittance above 90%, is also evaluated for the current technology demonstration. The fluid is also shown to be inert with PMMA material.

Solar Cell: Commercially available solar cells of the required size are made to attach to the lateral face of the SV-PLC enclosure. Polycrystalline silicon solar cells (17 mm X 34 mm X 3mm) with a rating of 1V, 40 mA have been used.

Gear system: The gear system is fabricated using the FDM 3D printing technique in ABS plastic material.

5.4.3 Characterisation methods

5.4.3.1 Direct transmittance of light and privacy

A direct transmittance of light study has been conducted to evaluate the privacy offered by the DPW in its translucent state. The fluid selection for DPW is conducted with the selected RI fluids through visual inspection. As represented in Figure 5.2, the image formation only occurs when the rays exiting the SV-PLC follow the path in parallel. For the direct transmission characterization, the light source from a monochromator is used with the spectral scan in the visible region (400 nm to 700 nm). As represented in Figure 5.2, a major portion of the exited light rays will be in an angular shift with the normal to the PLC. To evaluate direct transmittance as a measure of privacy, an integrating sphere with a photodetector is kept at a distance of 25 cm (Figure 5.5a), such that the SV-PLC losses will be omitted from the measurement. The privacy offered by the DPW is also affirmed with visual evaluation, in which the quality of the image formation is visually inspected with varying object distances from the window pane (Figure 5.5b).

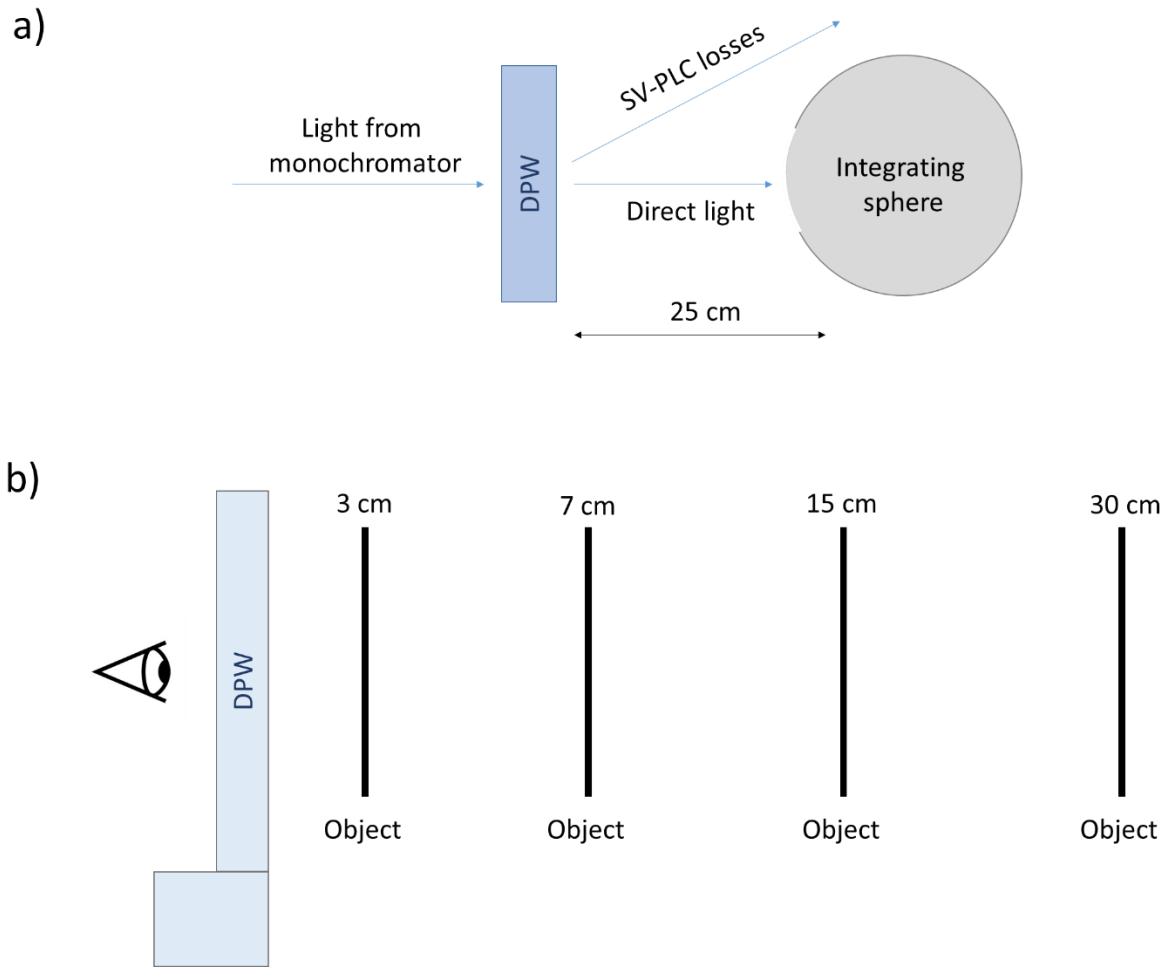

Figure 5.5. a) Schematic showing the characterization method for evaluating privacy with direct transmittance of light in DPW. b) Schematic showing the experimental evaluation setup for analyzing the privacy offered by DPW in its opaque state.

5.4.3.2 Diffuse transmittance of light and daylighting Potential

As represented in Figure 5.2, in the translucent mode of DPW, there will be transmission of light in diffusion mode. This is attributed to the losses from the direct light, and also the penetration of diffused light. This mode of transmission will not form the image of the object across the DPW, but can be utilized for daylighting. The diffuse transmission of light is measured in DLI using an Apogee MS-100 Spectroradiometer. The light from the solar simulator is used for the study. The 6 mm diameter sensor window is kept directly beneath (with zero gap) the DPW, which is exposed directly to the simulator rays (Figure 5.6). The method can collect all the diffused and direct light rays from the DPW and can be correlated to the daylighting potential as the transmittance value.

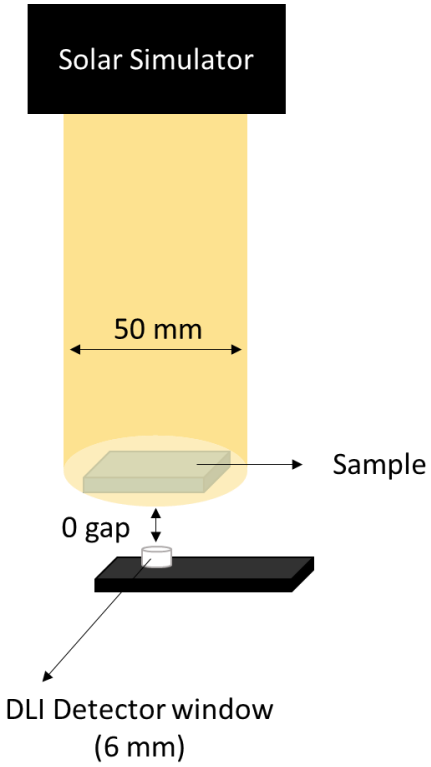

Figure 5.6. Schematic showing the characterization method for evaluating the daylighting potential with diffuse transmittance of light in DPW.

5.4.3.3 Power generation

The power generation in DPW is measured at its peak in direct solar insolation, facing normal to the sun.

5.5 Results & Discussion

The influence of optofluid in transparency switching through RI matching in DPW is distinctly shown in Figure 5.7. The ray tracing simulation shows the different cases of unmatching RI fluids (RI: 1.33 (water), 1.48, 1.485, 1.488) and matching RI fluid (RI 1.49) as the optofluids. If the RI of the fluid matches exactly with that of the SV-PLC, there will be no deflection of light, and the image formation will be perfect. As the RI difference between SV-PLC and opto-fluid was increased, the image formation was more distorted, as shown by the dispersing light with the distance. When there is a higher RI difference between the SV-PLC and fluid (for example, water (RI: 1.33)), there will be no image formation.

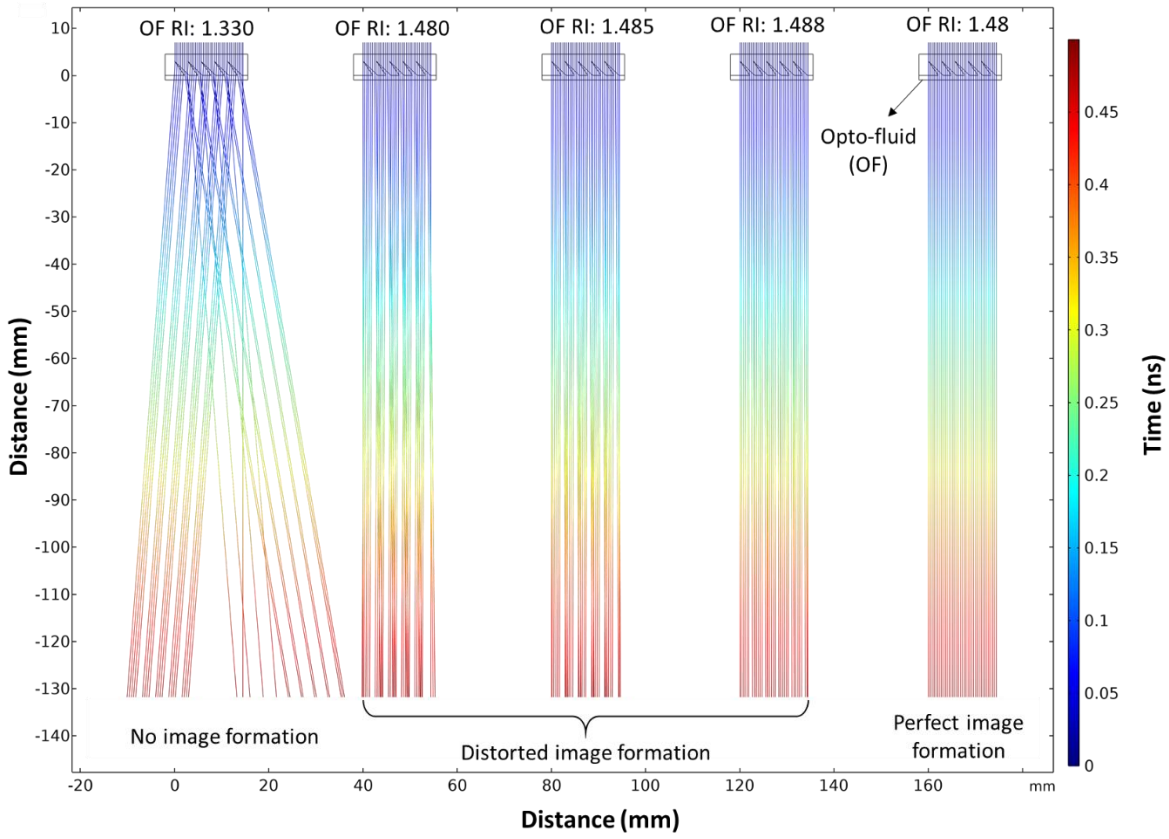

Figure 5.7. Ray tracing simulation of SV-PLC optics grooves filled with varying RI optofluids, showing the image distortion occurring with the distinction in the RI of optofluid and SV-PLC.

Figure 5.8 shows the photographs of the experimental evaluation of image formation by the selected opto-fluids for DPW. The object was kept at an equal distance (5 cm) from the sample in every case. The top-left photograph shows the unfilled state of SV-PLC, where the voids are not filled, causing light redirection. The top-right photograph shows the SV-PLC voids filled with water (RI: 1.33). No image formation is made as the refracted light from the PLC is made to diverge. The bottom left photograph shows the case SV-PLC voids filled with acrylic matching liquid, which claims to have a good clarity of image. However, some short-range distortion is visible in the image formed, due to some slight variation in the RI. Also, there is high bubble entrapment within the fluid in the course of its motion, due to the high viscosity of the fluid. Surface tension of the fluid in the channel and the viscosity favors the bubble formation and drag the bubble movement within the liquid [191-193]. Apart from that, the width of the fluid channel also determines (which is inversely proportional) the fluid velocity and the bubble movement [191]. However, increasing the channel width increase the optofluid volume required for the DPW. Hence, a low viscous

fluid will always be beneficial for DPW for better flow control. α-tocopheryl acetate was found to be the best choice of opto-fluid for DPW, providing less distortion and more clarity in the image it forms (bottom right image of Figure 5.8).

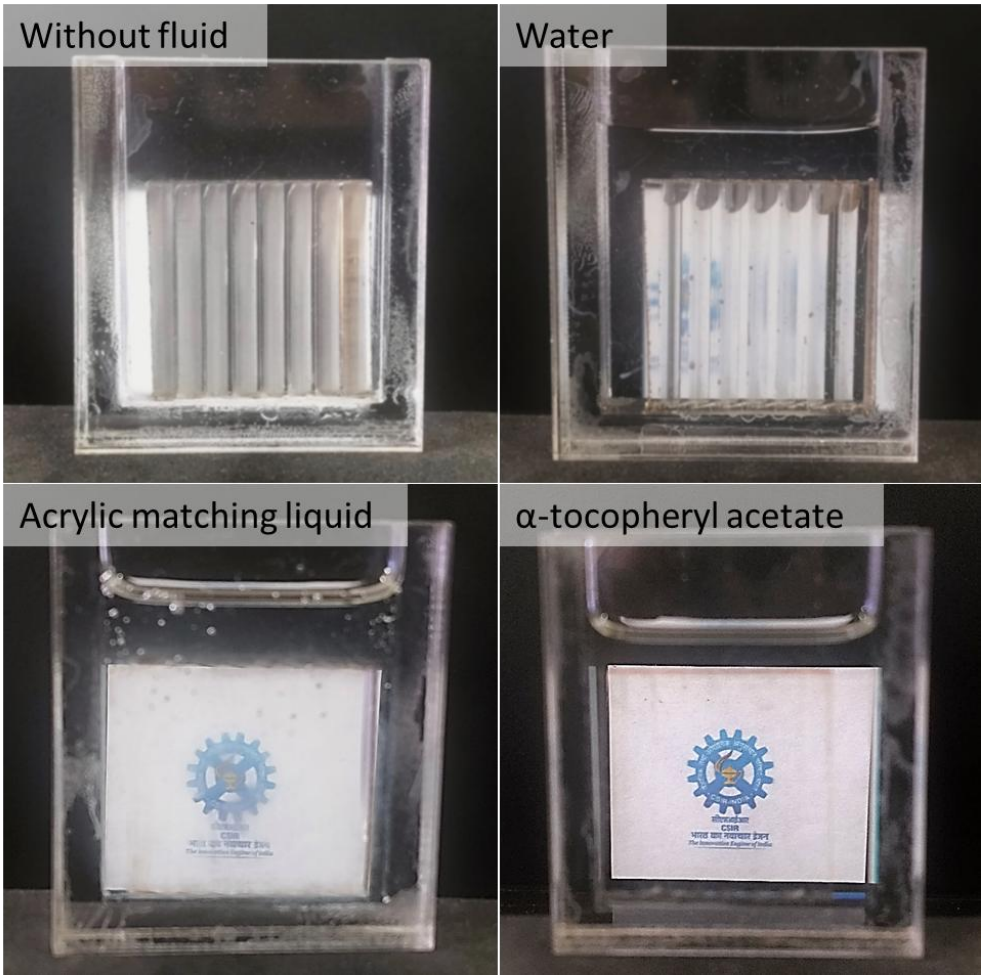

Figure 5.8. Photographs showing image formation offered SV-PLC in its unfilled state (top left), and filled states with water (top right), acrylic matching liquid (bottom left), and α-tocopheryl acetate (bottom right).

Figure 5.9 shows the assembled DPW prototype. The size of the window is 210 mm X 200 mm. The solar cell assembly and fluid tank are kept on the rear side, making it masked.

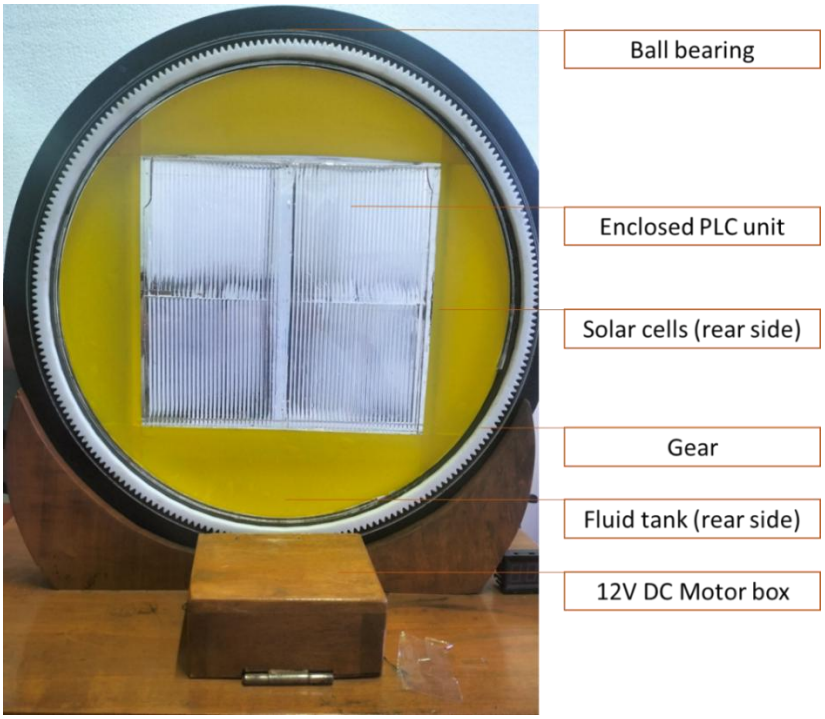

Figure 5.9. Prototype of DPW technology

Figure 5.10a shows the transparency switched states in the DPW prototype, where it shows the distorted image of the background in its translucent state. When the window is rotated, a clean image of the background will be visible upon the filling of the SV-PLC groove with optofluid. The switching time for the prototype was around 4.5 minutes, which is dependent on the height of the DPW. The moderately high time for switching can be attributed to the high viscosity of the optofluid used and the low fluid channel width. A more engineered optofluid with low viscosity can provide very fast switching of the states. Also, design changes such as increased channel width can substantially reduce the switching time [191], compromising the total opto-fluid volume requirement. Apart from that, the viscosity of the fluid at the operating conditions is also considered important, since temperature can affect the fluid viscosity. The direct transmission of light measured in the visible region for the unfilled and filled state (with α-tocopheryl acetate) of DPW is shown in Figure 5.10b. The drastic change in the direct transmittance of light, i.e., ~15% in the translucent state to ~90% in the transparent state, suggests the high privacy switching offered by the DPW technology using SV-PLC. Apart from the privacy offered by DPW, it can also provide the daylighting component in both states. In the translucent state, the measured diffused transmittance of the light is around 50.13 ± 0.83%, which is switched to 90.50 ± 0.85% in the transparent state. The high diffuse transmittance of light can be attributed to the

different losses occurring in the SV-PLC optics (Ll_{eak}, $L_{fresnel}$, and initial Fresnel reflection loss at the top surface), and is also a measure of the same.

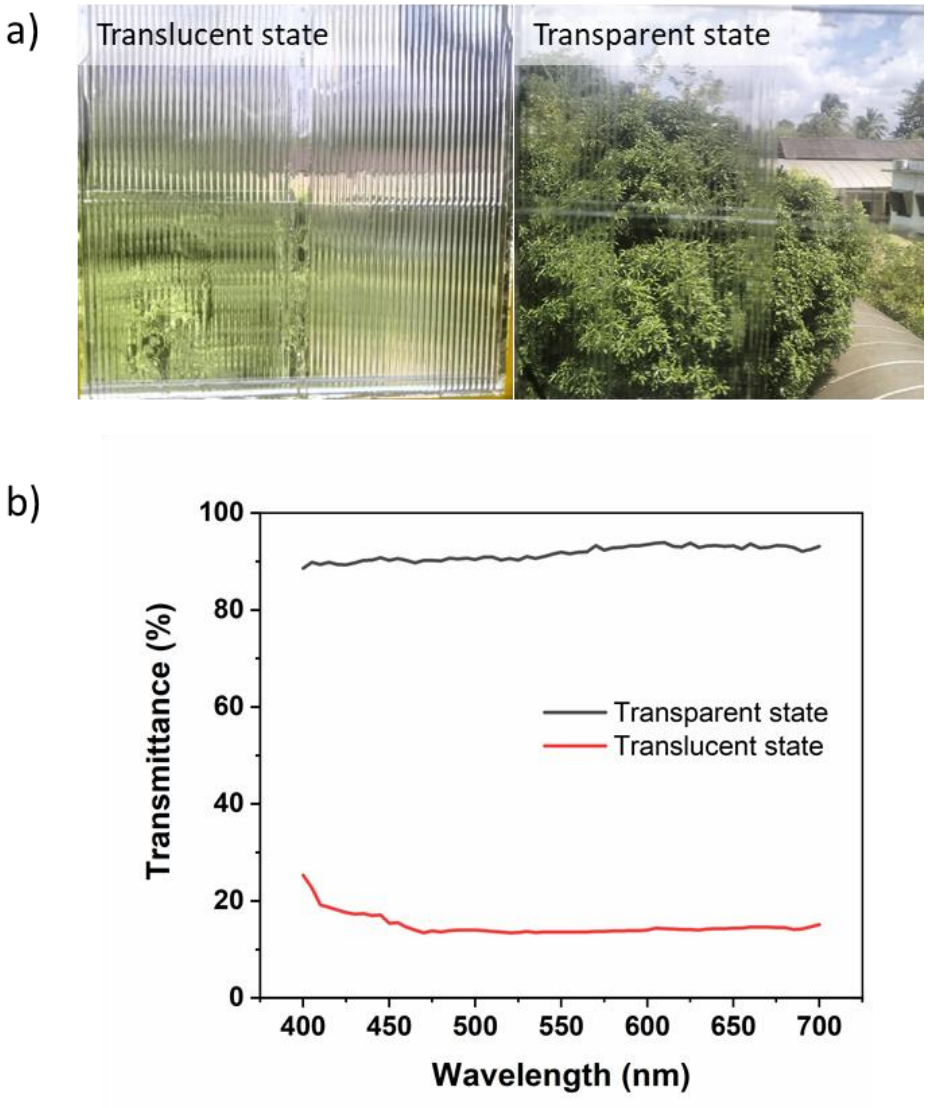

Figure 5.10. a) Photographs showing the view of DPW in the translucent and transparent states, showing its privacy offerings. b) Plot showing the transmittance (direct transmittance of light) of the transparency switching states in DPW with α-tocopheryl acetate as the optofluid.

The privacy offered by the window in its translucent state is also evaluated with an object (size around 13 cm X 12 cm) and varying its distance from the window pane (as explained in the characterization method section). The results are shown in Figure 5.11. By changing the distance from 3 cm to 15 cm, the image of the object almost vanished. Upon increasing the distance to 30 cm, the object cannot be spotted.

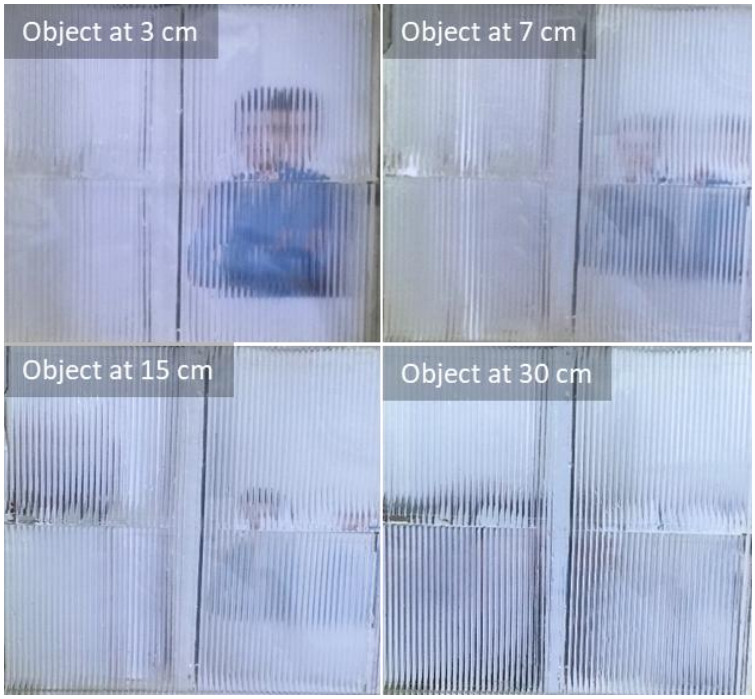

Figure 5.11. Photographs showing the privacy offered by DPW in its translucent state with varying distances of the object from the window pane.

Finally, the maximum power generation offered by the DPW prototype under field conditions is around 20 Wp/m^2 (under one sun condition) using polycrystalline solar cells. Improvement in power generation can be attained with better SV-PLC designs (refer to the Future outlook chapter (Chapter 6)), improved manufacturing, better solar cells, architecture, and their coupling with the DPW.

5.6 Conclusions

Dynamic Power Window, a novel concept and approach for integrating power generation, active dynamism, and daylighting as a glazing solution, has been conceptualized and demonstrated. The SV-PLC optics have been utilized as the optics platform for energy generation and transparency modulation. The transparent state of the DPW has been achieved by incorporating optofluid within the SV-PLC optics grooves having a matching RI. The demonstrated DPW technology has distinct transparency switching states of 90% to 15% (direct transmittance of light) in around 4.5 minutes. The maximum energy generation potential has been ~20 Wp/m^2 using polycrystalline silicon solar cells with the demonstrated prototype. Apart from that, the technology can offer a daylighting transmittance (diffuse transmittance of light) of ~50% and 90% in the translucent and transparent states, respectively.

Chapter 6

Summary and Future Perspectives

6 Summary and Future Perspectives

6.1 Summary

Planar optics, such as Fresnel lenses and mirrors, emerged as compact light concentrator solutions to address the drawbacks of large imaging optics-based systems. However, creative solutions were required to solve the focus gap problem instead of relying solely on imaging optics. Since it allows for a single point of energy collection, the zero focal length idea, diffused light collection from the waveguide, and reduced size of the entire light concentrating system, waveguide-based PLC has emerged as the greatest option in this regard. Notwithstanding these benefits, waveguide-based PLCs have drawbacks in their current designs, such as the requirement for exact microfabrication methods, bulkier components (having a higher width-to-length ratio), numerous optical components that require exact alignments, or restricted solar acceptance angles.

The thesis focuses on designing and developing a novel compact Planar Light Concentrator (PLC) optics solution to replace conventional bulky light concentrators. The design essentially consists of an array of skewed V-grooves in an optics slab, and light falling on it will be transported to the lateral face in a direction. The low-concentration system can be effectively used in built environments such as Building Integrated Photovoltaics, where the concept of focal length limits conventional light concentrators in their applicability. A basic introduction to the current designs of waveguide-based PLCs was discussed in Chapter 1, which defines the research gap. As of now, the existing design innovations conducted on planar waveguide-based CPVs have more prominence for geometric optics-based designs. However, the primary design challenge is to achieve a scalable design solution without compromising on geometrical concentration, OE, and solar acceptance. The key attributes of the skewed V-groove based PLC (SV-PLC) optics design include 1) Non-sequential design approach employing a single optics element; this avoids the need for precise positioning of the optics 2) Low-concentration optics, eliminating the need for intricate thermal management systems; 3) Manufacturable through a single process; 4) Higher solar acceptance in an axis eliminating the need for 2-axis tracking; 5) A zero focal length configuration that negates the necessity for spacing before the collectors; 6) Unidirectional light concentration design for higher concentration factor; 7) Design flexibility for converting to radial design for higher concentration factor.

The detailed mechanism of light transport and its mathematical model have been developed in Chapter 2. Understanding the various SV-PLC optical parameters and variables is aided by the mathematical model. Since many parameters need to be examined and optimized before creating simulation models, the model serves as the foundation for simulation investigations. For the various parameters, thorough derivation and optimization have been carried out. Lastly, the current mathematical model of a single groove has been used to forecast the efficacy, i.e., the Optical Efficiency (OE) and Final Concentration (FC) of the SV-PLC design.

The various fabrication routes that can be used for the SV-PLC optics are described in depth in Chapter 3. From quick prototyping to industrial manufacture, three distinct techniques have been used to fabricate SV-PLC optics. Laser machining in PMMA plates, a quick prototyping technique, has been used to validate the optics design. Furthermore, stereolithography 3D printing in optically transparent resin has been used to create large-area prototypes. In the end, SV-PLC optics were manufactured on a wide scale using injection molding technology. The laser machining process has limitations in the depth of cutting (8 mm, for mediocre cuts without obliqueness), hence, individual pieces were cut and optically coupled to each other, resulting in a loss of light intensity through the interfaces. Also, the machining yields heat-induced bulges at the groove interfaces. Apart from that, the technique can be used for quick validation of the optics with minimal cost of fabrication. After that, the SV-PLC optics were fabricated with SLA 3D printing by two different methods. Method one adopted the direct 3D printing of the SV-PLC optics. This method does not provide a provision for polishing and coating to improve the surface finish. This yielded light-scattering surfaces at the groove interfaces, reducing the efficiency of the SV-PLC optics. To mitigate this issue, the second method has been utilized. The SV-PLC optics have been divided into separate parts, 3D printed, and optically connected in the second technique. Although the technique produces visual clarity, the individual pieces yielded rounded edges with dimensional and shape variances, caused by the polishing and lacquer coating. Additionally, the system will suffer from higher losses due to improper alignment of the individual elements and losses occurring at the interfaces. Large-scale optics (> 10 cm) can be readily customized and manufactured, but the accuracy of the process limits 3D printing to large-area prototypes for technology validation. The third method, injection molding, can be regarded as a better manufacturing procedure for SV-

PLC optics on a larger scale and with a greater chance of integrating dimensional accuracy, surface profiles, and optical clarity when compared to laser machining and 3D printing.

Chapter 4 conducts the evaluation of the SV-PLC optics. The evaluation of different fabrication routes was conducted through optical microscopy and direct light transmittance to assess the dimensional accuracy and surface profiles of the skewed V-grooves. The results revealed injection molding to be a more suitable manufacturing method for attaining better groove profiles and optical properties. The simulation models have been developed for SV-PLC optics in the COMSOL Multiphysics Ray Optics module. The simulated models align well with the mathematical models developed for analyzing the OE, with a slight performance increment in the simulation models because of the difference in the methodology adopted. The FC of <5X can be achieved with the linear design of SV-PLC. Analyzing the angular acceptance, a low-efficiency drop of less than 10% is only suffered within ±15° angular shift in the light incidence, and a maximum drop of 30% within the ±23.5° zone. However, the design can be elevated to an FC in the range of 75X with the radial SV-PLC designs. Finally, experimental evaluations were carried out with a 10X GC injection molded SV-PLC optics in both standard conditions and direct sunlight using an amorphous silicon solar cell. The FC measured are 2.3X and 2.2X under standard conditions and on-field conditions, respectively, under 1 sun conditions. The angular acceptance study (under standard conditions) also shows a similar graphical trend to the simulation results.

Energy efficiency in buildings is always connected with both energy conservation and energy generation. Glazing provides a huge opportunity to integrate both in a single platform, where light transmissivity switching provides the energy efficiency component, and photovoltaic integration provides the energy generation. However, the integration of photovoltaics compromises light transmissivity in glazings. Conventional methods like electrochromism, suspended particles, or liquid crystals for transparency switching have their limitations in cost and switching efficiency. Chapter 6 conceptualized and demonstrated the Dynamic Power Window, a novel concept and approach for integrating power generation, active dynamism, and daylighting as a glazing solution. The SV-PLC optics were used for power generation and transparency modulation. The transparent state of the DPW has been achieved by incorporating a matching RI optofluid (α-tocopheryl acetate) within the SV-PLC optics grooves. The fluid flow has been driven by gravity in the rotating window prototype model developed. The demonstrated DPW technology has

distinct transparency switching states of 90% to 15% (direct transmittance of light) in around 4.5 minutes. The maximum energy generation potential has been ~20 Wp/m^2 using polycrystalline silicon solar cells with the demonstrated prototype. Apart from that, the technology can offer a daylighting transmittance (diffuse transmittance of light) of ~50% and 90% in the translucent and transparent states, respectively.

6.2 Future Perspectives

The present thesis could provide new insights into the straightforward design and fabrication of SV-PLC optics and offer a wide range of opportunities for future research for design approaches, product development, and extended studies. Some of the possibilities are:

1. Gradient skewed V-groove design for higher optical efficiency: The proposition is to have an array of skewed V-grooves with increasing size from the end near to collector to the other end. This will increase the optical efficiency by reducing the percentage of rays passing through the maximum number of grooves.

2. Development of radial Skewed V-groove Planar Optics for Medium Light Concentrators: As shown with the simulation results, radial SV-PLC optics can achieve an FC of up to 75X at the expense of the angular acceptance. However, translating the optics to industrial manufacturing seems to be challenging. The possibility of fabricating a sector of the circular design can be explored with injection molding since the circular, skewed V-groove pattern makes an interlocking arrangement.

3. Fast transparency switching in DPW: The current switching time of the transparency in DPW is around 4.5 minutes for a 0.2 m high window. The viscosity of the fluid plays a major role in switching time, as the process depends on the flowability of fluid in the channel. The possibility of low-viscosity liquids can be explored in the future for fast switching of the transparency states in the DPW.

4. Concentrated Photovoltaics (CPV): The possibility of indoor and outdoor CPV product development with proper solar cell architecture and thermal management should be explored in the future.

5. Daylighting application: The possibility of daylighting can be explored with the radial design of SV-PLC optics by connecting a light pipe to the center of the optics.

References

[1] Layton BE. A Comparison of Energy Densities of Prevalent Energy Sources in Units of Joules Per Cubic Meter. 2008;5:438–55. https://doi.org/10.1080/15435070802498036.

[2] Hernandez RR, Hoffacker MK, Murphy-Mariscal ML, Wu GC, Allen MF. Solar energy development impacts on land cover change and protected areas. Proc Natl Acad Sci U S A 2015;112:13579–84. https://doi.org/10.1073/PNAS.1517656112/SUPPL_FILE/PNAS.1517656112.ST05.DOCX.

[3] van de Ven DJ, Capellan-Peréz I, Arto I, Cazcarro I, de Castro C, Patel P, et al. The potential land requirements and related land use change emissions of solar energy. Sci Reports 2021;11:1–12. https://doi.org/10.1038/s41598-021-82042-5.

[4] Turney D, Fthenakis V. Environmental impacts from the installation and operation of large-scale solar power plants. Renew Sustain Energy Rev 2011;15:3261–70. https://doi.org/10.1016/J.RSER.2011.04.023.

[5] PV FAQs: What's New in Concentrating PV? (Miscellaneous) | OSTI.GOV n.d. https://www.osti.gov/biblio/15015121 (accessed November 30, 2024).

[6] Shanks K, Senthilarasu S, Mallick TK. Optics for concentrating photovoltaics: Trends, limits and opportunities for materials and design. Renew Sustain Energy Rev 2016;60:394–407. https://doi.org/10.1016/J.RSER.2016.01.089.

[7] Sharma VK, Singh R, Gehlot A, Buddhi D, Braccio S, Priyadarshi N, et al. Imperative Role of Photovoltaic and Concentrating Solar Power Technologies towards Renewable Energy Generation. Int J Photoenergy 2022;3852484. https://doi.org/10.1155/2022/3852484.

[8] Simms DL. Archimedes and the Burning Mirrors of Syracuse. Technol Cult 1977;18:1. https://doi.org/10.2307/3103202.

[9] Africa TW. Archimedes through the Looking-Glass. Class World 1975;68:305. https://doi.org/10.2307/4348211.

[10] Karellas S, Roumpedakis TC. Solar thermal power plants. Sol Hydrog Prod Process Syst Technol 2019:179–235. https://doi.org/10.1016/B978-0-12-814853-2.00007-2.

[11] Cuce E, Cuce PM. A comprehensive review on solar cookers. Appl Energy 2013;102:1399–421. https://doi.org/10.1016/J.APENERGY.2012.09.002.

[12] Pfahl A, Coventry J, Röger M, Wolfertstetter F, Vásquez-Arango JF, Gross F, et al. Progress in heliostat development. Sol Energy 2017;152:3–37. https://doi.org/10.1016/J.SOLENER.2017.03.029.

[13] Xie WT, Dai YJ, Wang RZ, Sumathy K. Concentrated solar energy applications using Fresnel lenses: A review. Renew Sustain Energy Rev 2011;15:2588–606. https://doi.org/10.1016/J.RSER.2011.03.031.

[14] El Gharbi N, Derbal H, Bouaichaoui S, Said N. A comparative study between parabolic trough collector and linear Fresnel reflector technologies. Energy Procedia 2011;6:565–72. https://doi.org/10.1016/J.EGYPRO.2011.05.065.

[15] Ma X, Zheng H, Liu S. A review on solar concentrators with multi-surface and multielement combinations. J Daylighting 2019;6:80–96. https://doi.org/10.15627/JD.2019.9.

[16] Tremblay EJ, Karp JH, Ford JE. Planar micro-optic solar concentrator. Opt Express 2010;18:1122–33. https://doi.org/10.1364/OE.18.001122.

[17] Karp JH, Ford JE. Planar micro-optic solar concentration using multiple imaging lenses into a common slab waveguide. Proc. SPIE 7407 2009;7407:76–86. https://doi.org/10.1117/12.826531.

[18] Xuan Q, Li G, Lu Y, Zhao B, Zhao X, Pei G. The design, construction and experimental characterization of a novel concentrating photovoltaic/daylighting window for green building roof. Energy 2019;175:1138–52. https://doi.org/10.1016/J.ENERGY.2019.03.135.

[19] Lumiduct | Wellsun n.d. https://www.wellsun.nl/lumiduct (accessed May 7, 2024).

[20] Li G, Xuan Q, Akram MW, Golizadeh Akhlaghi Y, Liu H, Shittu S. Building integrated solar concentrating systems: A review. Appl Energy 2020;260:114288. https://doi.org/10.1016/J.APENERGY.2019.114288.

[21] Vu NH, Pham TT, Shin S. Flat concentrator photovoltaic system for automotive applications. Sol Energy 2019;190:246–54. https://doi.org/10.1016/J.SOLENER.2019.08.025.

[22] Zhou B, He K, Chen Z, Zhong S. Fixed Fiber Light Guide System with Concave Outlet Concentrators. Energies 2022, Vol 15, Page 982 2022;15:982. https://doi.org/10.3390/EN15030982.

[23] Sripadmanabhan Indira S, Vaithilingam CA, Chong KK, Saidur R, Faizal M, Abubakar S, et al. A review on various configurations of hybrid concentrator photovoltaic and thermoelectric generator system. Sol Energy 2020;201:122–48. https://doi.org/10.1016/J.SOLENER.2020.02.090.

[24] Parthiban A, Mallick TK, Reddy KS. Integrated optical-thermal-electrical modeling of compound parabolic concentrator based photovoltaic-thermal system. Energy Convers Manag 2022;251:115009. https://doi.org/10.1016/J.ENCONMAN.2021.115009.

[25] Essahili O, Ouafi M, Moudam O. Recent progress in organic luminescent solar concentrators for agrivoltaics: Opportunities for rare-earth complexes. Sol Energy 2022;245:58–66. https://doi.org/10.1016/J.SOLENER.2022.08.054.

[26] Ernst Kussul. Combinations of Solar Concentrators with Agricultural Plants. J Environ Sci Eng B 2020;9. https://doi.org/10.17265/2162-5263/2020.05.002.

[27] Elliott AD. Confocal Microscopy: Principles and Modern Practices. Curr Protoc Cytom 2020;92:e68. https://doi.org/10.1002/CPCY.68.

[28] Li J, Hu J, Lin M. A flexibly controllable high-flux solar simulator for concentrated solar energy research from extreme magnitudes to uniform distributions. Renew Sustain Energy Rev 2022;157:112084. https://doi.org/10.1016/J.RSER.2022.112084.

[29] Liang X, Wang R, Li H. Complementary Concentrating Solar LED Lighting Device and Its Application in Architectural Design. J Nanoelectron Optoelectron 2021;16:1120–8. https://doi.org/10.1166/JNO.2021.3073.

[30] Coppola S, Vespini V, Nasti G, Ferraro P. Transmitting Light through Biocompatible and Biodegradable Drug Delivery Micro Needles. IEEE J Sel Top Quantum Electron 2021;27. https://doi.org/10.1109/JSTQE.2021.3057834.

[31] Martín-Sómer M, Moreno-SanSegundo J, Álvarez-Fernández C, van Grieken R, Marugán J. High-performance low-cost solar collectors for water treatment fabricated with recycled materials, open-source hardware and 3d-printing technologies. Sci Total Environ 2021;784:147119. https://doi.org/10.1016/J.SCITOTENV.2021.147119.

[32] Gowda B N VK, Gauni S, Gurushankar K, Maik V. Application in optical design: Optimization for high intensity and aberration free camera lens system. Optik (Stuttg) 2022;262:168764. https://doi.org/10.1016/J.IJLEO.2022.168764.

[33] Zhan T, Yin K, Xiong J, He Z, Wu ST. Augmented Reality and Virtual Reality Displays: Perspectives and Challenges. IScience 2020;23:101397. https://doi.org/10.1016/J.ISCI.2020.101397.

[34] Animesh M Ramachandran, Paolo Corti, Adersh Asok, Pierluigi Bonomo. Indian BIPV Report 2022: Status and Roadmap. 2022. https://solarchitecture.ch/wp-content/uploads/2022/08/BIPV-Report-India_v01.pdf.

[35] Badr F, Radwan A, Ahmed M, Hamed AM. Performance assessment of a dual-axis solar tracker for concentrator photovoltaic systems. Int J Energy Res 2022;46:13424–40. https://doi.org/10.1002/ER.8052.

[36] Wang L, Yu J. Principles of photocatalysis. Interface Sci Technol 2023;35:1–52. https://doi.org/10.1016/B978-0-443-18786-5.00002-0.

[37] Freier D, Ramirez-Iniguez R, Jafry T, Muhammad-Sukki F, Gamio C. A review of optical concentrators for portable solar photovoltaic systems for developing countries. Renew Sustain Energy Rev 2018;90:957–68. https://doi.org/10.1016/J.RSER.2018.03.039.

[38] Khamooshi M, Salati H, Egelioglu F, Hooshyar Faghiri A, Tarabishi J, Babadi S. A review of solar photovoltaic concentrators. Int J Photoenergy 2014;958521. https://doi.org/10.1155/2014/958521.

[39] Caron S, Röger M, Wullenkord M. Selection of Solar Concentrator Design Concepts for Planar Photoelectrochemical Water Splitting Devices. Energies 2020; 13:5196. https://doi.org/10.3390/EN13195196.

[40] Price JS, Giebink NC, Grede AJ. Fundamental and practical limits of planar tracking solar concentrators. Opt Express 2016;24:A1635–46. https://doi.org/10.1364/OE.24.0A1635.

[41] Peatross Justin, Ware Michael. Physics of Light and Optics Optics Textbook. 2015; ISBN978-1-312-92927-2. https://optics.byu.edu/textbook.

[42] Teets TS. Photoluminescence, American Chemical Society 2021.ISBN: 9780841299429. https://doi.org/10.1021/ACSINFOCUS.7E5014.

[43] Canavarro D, Chaves J, Collares-Pereira M. New Optical Designs for Large Parabolic Troughs. Energy Procedia 2014;49:1279–87. https://doi.org/10.1016/J.EGYPRO.2014.03.137.

[44] Abed AA, El-Marghany MR, El-Awady WM, Hamed AM. Recent advances in parabolic dish solar concentrators: Receiver design, heat loss reduction, and nanofluid optimization for enhanced efficiency and applications. Sol Energy Mater Sol Cells 2024;273:112930. https://doi.org/10.1016/J.SOLMAT.2024.112930.

[45] Sen PK, Ashutosh K, Bhuwanesh K, Engineer Z, Hegde S, Sen P V., et al. Linear Fresnel Mirror Solar Concentrator with Tracking. Procedia Eng 2013;56:613–8. https://doi.org/10.1016/J.PROENG.2013.03.167.

[46] Chittalakkotte V, Lazzar Vincent V, Valiyaparambil P. Development of a solar energy based desalination system using a hyperboloid concentrator. Mater Today Proc 2021;46:9771–5. https://doi.org/10.1016/J.MATPR.2020.09.555.

[47] Jiang C, Yu L, Yang S, Li K, Wang J, Lund PD, et al. A Review of the Compound Parabolic Concentrator (CPC) with a Tubular Absorber. Energies 2020;13:695. https://doi.org/10.3390/EN13030695.

[48] Song J, Dessie BB. Concentration performance evaluation of sunlight concentrators: Fresnel lens, plano-convex lens, and parabolic mirrors for daylighting application. Int J Green Energy 2024;21:2457–76. https://doi.org/10.1080/15435075.2024.2315429.

[49] Qandil H. Application-based design of the Fresnel-lens Solar Concentrator. AEE World Energy Eng Congr 2019 2019;6:4861–9. https://doi.org/10.1186/S40807-019-0057-8/TABLES/5.

[50] Alves M, Pérez-Rodríguez A, Dale PJ, Domínguez C, Sadewasser S. Thin-film micro-concentrator solar cells. J Phys Energy 2019;2:012001. https://doi.org/10.1088/2515-7655/AB4289.

[51] Price JS, Sheng X, Meulblok BM, Rogers JA, Giebink NC. Wide-angle planar microtracking for quasi-static microcell concentrating photovoltaics. Nat Commun 2015;6:1–8. https://doi.org/10.1038/ncomms7223.

[52] Kuo C-H, Teng T-C, Li Y-J. Planar solar concentrator composed of stacked waveguides with arc-segment structures and movable receiving assemblies. Opt Express 2020;28:34362–77. https://doi.org/10.1364/OE.405909.

[53] Hasan AB, Husain SA. Design of Light Trapping Solar Cell System by Using Zemax Program. J Phys Conf Ser 2018;1003:012074. https://doi.org/10.1088/1742-6596/1003/1/012074.

[54] Vu DT, Kieu NM, Tien TQ, Nguyen TP, Vu H, Shin S, et al. Solar Concentrator Bio-Inspired by the Superposition Compound Eye for High-Concentration Photovoltaic System up to Thousands Fold Factor. Energies 2022;15:3406. https://doi.org/10.3390/EN15093406.

[55] Vu NH, Shin S. Flat Optical Fiber Daylighting System with Lateral Displacement Sun-Tracking Mechanism for Indoor Lighting. Energies 2017;10:1679. https://doi.org/10.3390/EN10101679.

[56] Kim J, Lee J, Dhakal R. Bio-inspired thin and flat solar concentrator for efficient, wide acceptance angle light collection. Appl Opt 2014;53:306–15. https://doi.org/10.1364/AO.53.000306.

[57] Elikkottil A, Tahersima MH, Gupta MVNS, Maiti R, Sorger VJ, Pesala B. A Spectrally Tunable Dielectric Subwavelength Grating based Broadband Planar Light Concentrator. Sci Reports 2019;9:1–9. https://doi.org/10.1038/s41598-019-48025-3.

[58] Meinardi F, Bruni F, Brovelli S. Luminescent solar concentrators for building-integrated photovoltaics. Nat Rev Mater 2017;2:1–9. https://doi.org/10.1038/natrevmats.2017.72.

[59] Mohan BVG, Vasu V, Benjamin AR, Kottaisamy M. Luminescent solar concentrators-the solar waveguides. Rev Artic Curr Sci 2018;114.

[60] Reddy DS, Khan MK. Stationary point focus solar concentrators—A review. Int J Energy Res 2022;46:5678–702. https://doi.org/10.1002/ER.7612.

[61] Iqbal W, Ullah I, Shin S. Optical Developments in Concentrator Photovoltaic Systems—A Review. Sustain 2023;15:10554. https://doi.org/10.3390/SU151310554.

[62] Baharoon DA, Rahman HA, Omar WZW, Fadhl SO. Historical development of concentrating solar power technologies to generate clean electricity efficiently – A review. Renew Sustain Energy Rev 2015;41:996–1027. https://doi.org/10.1016/J.RSER.2014.09.008.

[63] Masood F, Nor NBM, Nallagownden P, Elamvazuthi I, Saidur R, Alam MA, et al. A Review of Recent Developments and Applications of Compound Parabolic Concentrator-Based Hybrid Solar Photovoltaic/Thermal Collectors. Sustain 2022;14:5529. https://doi.org/10.3390/SU14095529.

[64] Faye K, Thiam A, Faye M. Optimum Height and Tilt Angle of the Solar Receiver for a 30 kWe Solar Tower Power Plant for the Electricity Production in the Sahelian Zone. Int J Photoenergy 2021;1961134. https://doi.org/10.1155/2021/1961134.

[65] Xianglong L, Guang H, Zhi Z, - al, Bongungu JL, Francisco PW, et al. Analysis of solar water heater with parabolic dish concentrator and conical absorber. IOP Conf Ser Mater Sci Eng 2017;206:012030. https://doi.org/10.1088/1757-899X/206/1/012030.

[66] Lv J, Xu X, Yin P. Design of leak-free sawtooth planar solar concentrator for daylighting system. J Clean Prod 2020;266:121895. https://doi.org/10.1016/J.JCLEPRO.2020.121895.

[67] Liang S, He Q, Zheng H, Zhao Z, Kang H, Ma X, et al. Optical and thermal performance of a uniaxial bidirectional tracked linear-focusing Fresnel lens solar concentrator. Int J Energy Res 2022;46:18768–80. https://doi.org/10.1002/ER.8496.

[68] Babu M, Raj SS, Valan Arasu A. Experimental analysis on Linear Fresnel reflector solar concentrating hot water system with varying width reflectors. Case Stud Therm Eng 2019;14:100444. https://doi.org/10.1016/J.CSITE.2019.100444.

[69] Tien NX, Shin S. A Novel Concentrator Photovoltaic (CPV) System with the Improvement of Irradiance Uniformity and the Capturing of Diffuse Solar Radiation. Appl Sci 2016;6:251. https://doi.org/10.3390/APP6090251.

[70] Wang L, Yuan Z, Zhao Y, Guo Z. Review on Development of Small Point-Focusing Solar Concentrators. J Therm Sci 2019;28:929–47. https://doi.org/10.1007/S11630-019-1134-4.

[71] Lee KT, Yao Y, He J, Fisher B, Sheng X, Lumb M, et al. Concentrator photovoltaic module architectures with capabilities for capture and conversion of full global solar radiation. Proc Natl Acad Sci U S A 2016;113:E8210–8. https://doi.org/10.1073/PNAS.1617391113.

[72] Alves M, Pérez-Rodríguez A, Dale PJ, Domínguez C, Sadewasser S. Thin-film micro-concentrator solar cells. J Phys Energy 2019;2:012001. https://doi.org/10.1088/2515-7655/AB4289.

[73] Vu NH, Pham TT, Shin S. Large Scale Spectral Splitting Concentrator Photovoltaic System Based on Double Flat Waveguides. Energies 2020;13:2360. https://doi.org/10.3390/EN13092360.

[74] Jost N, Jacobo-Martín A, Vallerotto G, Hernández JJ, Garcia-Sanchez A, Domínguez C, et al. Fabrication of high-performance lens arrays for micro-concentrator photovoltaics using ultraviolet imprinting. Int J Adv Manuf Technol 2024;131:5961–70. https://doi.org/10.1007/S00170-024-13350-Z/TABLES/3.

[75] Michel C, Blain P, Clermont L, Languy F, Lenaerts C, Fleury-Frenette K, et al. Waveguide solar concentrator design with spectrally separated light. Sol Energy 2017;157:1005–16. https://doi.org/10.1016/J.SOLENER.2017.09.015.

[76] University of Rochester | arpa-e.energy.gov n.d. https://arpa-e.energy.gov/technologies/projects/planar-light-guide-concentrated-photovoltaics (accessed November 30, 2024).

[77] Ramachandran AM, S SM, Thampi AS, Singh M, Asok A. A comprehensive review on optics and optical materials for planar waveguide-based compact concentrated solar photovoltaics. Results Eng 2022;16:100665. https://doi.org/10.1016/J.RINENG.2022.100665.

[78] Moraitis P, Schropp REI, van Sark WGJHM. Nanoparticles for Luminescent Solar Concentrators - A review. Opt Mater (Amst) 2018;84:636–45. https://doi.org/10.1016/J.OPTMAT.2018.07.034.

[79] Kim A, Hosseinmardi A, Annamalai PK, Kumar P, Patel R. Review on Colloidal Quantum Dots Luminescent Solar Concentrators. ChemistrySelect 2021;6:4948–67. https://doi.org/10.1002/SLCT.202100674.

[80] Elikkottil A, Elikkottil A, Tahersima MH, Gupta S, Gupta S, Sorger VJ, et al. Silicon nitride grating based planar spectral splitting concentrator for NIR light harvesting. Opt Express 2020;28:21474–80. https://doi.org/10.1364/OE.390666.

[81] Parola I, Zaremba D, Evert R, Kielhorn J, Jakobs F, Illarramendi MA, et al. High performance fluorescent fiber solar concentrators employing double-doped polymer optical fibers. Sol Energy Mater Sol Cells 2018;178:20–8. https://doi.org/10.1016/J.SOLMAT.2018.01.013.

[82] GJHM van Sark W, Barnham KW, Slooff LH, Chatten AJ, Büchtemann A, Meyer A, et al. Luminescent Solar Concentrators - A review of recent results. Opt Express 2008;16:21773–92. https://doi.org/10.1364/OE.16.021773.

[83] Rafiee M, Chandra S, Ahmed H, McCormack SJ. An overview of various configurations of Luminescent Solar Concentrators for photovoltaic applications. Opt Mater (Amst) 2019;91:212–27. https://doi.org/10.1016/J.OPTMAT.2019.01.007.

[84] Zdražil L, Kalytchuk S, Langer M, Ahmad R, Pospíšil J, Zmeškal O, et al. Transparent and Low-Loss Luminescent Solar Concentrators Based on Self-Trapped Exciton Emission in Lead-Free Double Perovskite Nanocrystals. ACS Appl Energy Mater 2021;4:6445–53. https://doi.org/10.1021/ACSAEM.1C00360/SUPPL_FILE/AE1C00360_SI_001.PDF.

[85] Griffini G. Host matrix materials for luminescent solar concentrators: Recent achievements and forthcoming challenges. Front Mater 2019;6:29. https://doi.org/10.3389/FMATS.2019.00029/BIBTEX.

[86] Winston R, Welford WT. Nonconventional optical systems and the brightness theorem. Appl Opt 1982;21:1531–3. https://doi.org/10.1364/AO.21.001531.

[87] Winston R, Welford WT. Efficiency of nonimaging concentrators in the physical-optics model. JOSA 1982;72:1564–6. https://doi.org/10.1364/JOSA.72.001564.

[88] Eisler CN, Parsons LE, Nett Z, Love C, Schwartzberg AM, Alivisatos AP. Photonic Luminescent Solar Concentrator Design for High Efficiency, Low Cost Multijunction Photovoltaics. Front Photonics 2022;3:932913. https://doi.org/10.3389/FPHOT.2022.932913/BIBTEX.

[89] Ferrara MA, Striano V, Coppola G. Volume Holographic Optical Elements as Solar Concentrators: An Overview. Appl Sci 2019;9:193. https://doi.org/10.3390/APP9010193.

[90] Chien MC, Tung YL, Tien CH. Ultracompact backlight-reversed concentration optics. Appl Opt 2009;48:4142–8. https://doi.org/10.1364/AO.48.004142.

[91] Bouchard S, Thibault S. Planar waveguide concentrator used with a seasonal tracker. Appl Opt 2012;51:6848–54. https://doi.org/10.1364/AO.51.006848.

[92] Li B, Lin H, Xie P, Liu Y. Total internal reflection-based planar waveguide solar concentrator with symmetric air prisms as couplers. Opt Express 2014;22:A1389–98. https://doi.org/10.1364/OE.22.0A1389.

[93] Moore D, Schmidt G, Unger B. Concentrated photovoltaics stepped planar light guide. 2010;7652:382–7. https://doi.org/10.1117/12.877725.

[94] Ong JR, Chu HS, Png CE, Ong K, Bera LK. Planar micro-optic solar concentrator for natural daylighting systems in tropics. 2016 Asian Conf Energy, Power Transp Electrif ACEPT 2016;1-5. https://doi.org/10.1109/ACEPT.2016.7811514.

[95] Zagolla V, Dominé D, Tremblay E, Moser C, Slooff LH, Bende EE, et al. Self-tracking solar concentrator with an acceptance angle of 32°. Opt Express 2014;22:A1880–94. https://doi.org/10.1364/OE.22.0A1880.

[96] Wei AC, Chen ZR, Sze JR. Planar solar concentrator with a v-groove array for a side-absorption concentrated photovoltaic system. Optik (Stuttg) 2016;127:10858–67. https://doi.org/10.1016/J.IJLEO.2016.08.045.

[97] Van Dijk L, Marcus EAP, Oostra AJ, Schropp REI, Di Vece M. 3D-printed concentrator arrays for external light trapping on thin film solar cells. Sol Energy Mater Sol Cells 2015;139:19–26. https://doi.org/10.1016/J.SOLMAT.2015.03.002.

[98] John Paul Morgan; Morgan Solar Inc. Light-guide solar panel and method of fabrication thereof. US Patent 7873257B2. January 18, 2011.

[99] Buljan M, Mendes-Lopes J, Benítez P, Miñano JC. Recent trends in concentrated photovoltaics concentrators' architecture. ournal of Photonics for Energy 2014;4:040995. https://doi.org/10.1117/1.JPE.4.040995.

[100] What We Presented at CPV-7: The Gen 3 Sun Simba Optic | The Unofficial Morgan Solar Weblog n.d. https://morgansolar.wordpress.com/2011/04/27/what-we-presented-at-cpv-7-the-gen-3-sun-simba-optic/ (accessed May 26, 2022).

[101] Miñano . J C, Benítez P, Liu J, Infante J, Chaves J, Wang ; 5 L, et al. Orthogonal and secondary concentration in planar micro-optic solar collectors. Opt Express 2011;19:A673–85. https://doi.org/10.1364/OE.19.00A673.

[102] Zhang X, Muneer T. Mathematical model for the performance of light pipes. International Journal of Lighting Research & Technology 2000;32:141–6. https://doi.org/10.1177/096032710003200306.

[103] Singh S, Bisht DS, Garg H. Designing a laser-cut panel for light collection for daylighting using a generalised mathematical model. Lighting Research & Technology 2020;53:147–70. https://doi.org/10.1177/1477153520932626.

[104] García JR, Cota RCA, Almeida DIR, Osuna NL, Machado MZ, García JRH, et al. A mathematical model to generate a light reflector that produces a uniform irradiance distribution from a point light source. Optik (Stuttg) 2024;312:171951. https://doi.org/10.1016/J.IJLEO.2024.171951.

[105] Muhammad-Sukki F, Farooq H, Abu-Bakar SH, Ardila-Rey JA, Sellami N, Kilpatrick C, et al. Mathematical Modelling of a Static Concentrating Photovoltaic: Simulation and Experimental Validation. Appl. Sci. 2021;11:3894. https://doi.org/10.3390/APP11093894.

[106] Pereira JCG, Fernandes JC, Rosa LG. Mathematical Models for Simulation and Optimization of High-Flux Solar Furnaces. Math Comput Appl 2019;24:65. https://doi.org/10.3390/MCA24020065.

[107] Shoeibi H, Jarrahian A, Mehrpooya M, Assaerh E, Izadi M, Pourfayaz F. Mathematical Modeling and Simulation of a Compound Parabolic Concentrators Collector with an Absorber Tube. Energies 2022;16:287. https://doi.org/10.3390/EN16010287.

[108] Song J, Dessie BB. Concentration performance evaluation of sunlight concentrators: Fresnel lens, plano-convex lens, and parabolic mirrors for daylighting application. Int J Green Energy 2024;21:2457–76. https://doi.org/10.1080/15435075.2024.2315429.

[109] Ejaz A, Babar H, Ali HM, Jamil F, Janjua MM, Fattah IMR, et al. Concentrated photovoltaics as light harvesters: Outlook, recent progress, and challenges. Sustain Energy Technol Assessments 2021;46:101199. https://doi.org/10.1016/J.SETA.2021.101199.

[110] Wu HY, Shin CW, Kwon KC, Lee KY, Gil SK, Kim N. Holographic solar concentrator with wide band using multi-wavelength transmission grating. Optik (Stuttg) 2024;318:172106. https://doi.org/10.1016/J.IJLEO.2024.172106.

[111] Fang FZ, Zhang XD, Weckenmann A, Zhang GX, Evans C. Manufacturing and measurement of freeform optics. CIRP Ann 2013;62:823–46. https://doi.org/10.1016/J.CIRP.2013.05.003.

[112] Tan NYJ, Zhang X, Neo DWK, Huang R, Liu K, Senthil Kumar A. A review of recent advances in fabrication of optical Fresnel lenses. J Manuf Process 2021;71:113–33. https://doi.org/10.1016/J.JMAPRO.2021.09.021.

[113] Yuan J, Lyu B, Hang W, Deng Q. Review on the progress of ultra-precision machining technologies. Front Mech Eng 2017;12:158–80. https://doi.org/10.1007/S11465-017-0455-9/METRICS.

[114] Brinksmeier E, Gläbe R, Schönemann L. Review on diamond-machining processes for the generation of functional surface structures. CIRP J Manuf Sci Technol 2012;5:1–7. https://doi.org/10.1016/J.CIRPJ.2011.10.003.

[115] Zhu Y, Tang T, Zhao S, Joralmon D, Poit Z, Ahire B, et al. Recent advancements and applications in 3D printing of functional optics. Addit Manuf 2022;52:102682. https://doi.org/10.1016/J.ADDMA.2022.102682.

[116] Zolfaghari A, Chen T, Yi AY. Additive manufacturing of precision optics at micro and nanoscale. Int J Extrem Manuf 2019;1:012005. https://doi.org/10.1088/2631-7990/AB0FA5.

[117] Forest CR, Saez MA, Hunter IW. Microforging technique for rapid, low-cost fabrication of lens array molds. Appl Opt 2007;46:8668–73. https://doi.org/10.1364/AO.46.008668.

[118] Zhou T, Yan J. Glass molding process for microstructures. Microfabr Precis Eng Res Dev 2017:213–62. https://doi.org/10.1016/B978-0-85709-485-8.00008-5.

[119] Li K, Huang X, Chen Q, Xu G, Xie Z, Wan Y, et al. Flexible fabrication of optical glass micro-lens array by using contactless hot embossing process. J Manuf Process 2020;57:469–76. https://doi.org/10.1016/J.JMAPRO.2020.07.019.

[120] Ghosh G, Sidpara A, Bandyopadhyay PP. Review of several precision finishing processes for optics manufacturing. Journal of Micromanufacturing 2018;1:170–88. https://doi.org/10.1177/2516598418777315.

[121] Xie M, Pan Y, An Z, Huang S, Dong M. Review on Surface Polishing Methods of Optical Parts. Adv Mater Sci Eng 2022;8723269. https://doi.org/10.1155/2022/8723269.

[122] Yadav HNS, Das M. Advances in finishing of optical complex substrates: A comprehensive review. Opt Laser Technol 2024;176:110938. https://doi.org/10.1016/J.OPTLASTEC.2024.110938.

[123] De La Rie ER, Delaney JK, Morales KM, Maines CA, Sung LP. Modification of Surface Roughness by Various Varnishes and Effect on Light Reflection. Stud Conserv 2010;55:134–43. https://doi.org/10.1179/SIC.2010.55.2.134.

[124] Kumar S, Tong Z, Jiang X. Advances in the design and manufacturing of novel freeform optics. Int J Extrem Manuf 2022;4:032004. https://doi.org/10.1088/2631-7990/AC7617.

[125] Chen M qing, He T yue, Zhao Y. Review of femtosecond laser machining technologies for optical fiber microstructures fabrication. Opt Laser Technol 2022;147:107628. https://doi.org/10.1016/J.OPTLASTEC.2021.107628.

[126] Shaker LM, Al-Amiery A, Wan Isahak WNR. Revolutionizing contact lens manufacturing: exploring cutting-edge techniques and innovations for enhanced vision and comfort. Int J Low-Carbon Technol 2024;19:359–85. https://doi.org/10.1093/IJLCT/CTAD136.

[127] Berglund G, Wisniowiecki A, Wisniowiecki A, Gawedzinski J, Applegate B, Applegate B, et al. Additive manufacturing for the development of optical/photonic systems and components. Opt 2022;9:623–38. https://doi.org/10.1364/OPTICA.451642.

[128] Alam F, Elsherif M, Alqattan B, Salih A, Lee SM, Yetisen AK, et al. 3D Printed Contact Lenses. ACS Biomater Sci Eng 2021;7:794–803. https://doi.org/10.1021/ACSBIOMATERIALS.0C01470/ASSET/IMAGES/LARGE/AB0C01470_0009.JPEG.

[129] Xin C, Li Z, Hao L, Li Y. A comprehensive review on additive manufacturing of glass: Recent progress and future outlook. Mater Des 2023;227:111736. https://doi.org/10.1016/J.MATDES.2023.111736.

[130] Ming W, Chen Z, Du J, Zhang Z, Zhang G, He W, et al. A comprehensive review of theory and technology of glass molding process. Int J Adv Manuf Technol 2020;107:2671–706. https://doi.org/10.1007/S00170-020-05051-0/METRICS.

[131] Li Y, Li K, Gong F. Fabrication and Optical Characterization of Polymeric Aspherical Microlens Array Using Hot Embossing Technology. Appl Sci 2021;11:882. https://doi.org/10.3390/APP11020882.

[132] Peixoto C, Valentim PT, Sousa PC, Dias D, Araújo C, Pereira D, et al. Injection molding of high-precision optical lenses: A review. Precis Eng 2022;76:29–51. https://doi.org/10.1016/J.PRECISIONENG.2022.02.002.

[133] Kotz F, Schneider N, Striegel A, Wolfschläger A, Keller N, Worgull M, et al. Glassomer—Processing Fused Silica Glass Like a Polymer. Adv Mater 2018;30:1707100. https://doi.org/10.1002/ADMA.201707100.

[134] Doushkina V, Fleming E. Optical and mechanical design advantages using polymer optics. Proc. SPIE 7424, Advances in Optomechanics 2009;7424:193–204. https://doi.org/10.1117/12.832319.

[135] Lee BK, Kim DS, Kwon TH. Replication of microlens arrays by injection molding. Microsyst Technol 2004;10:531–5. https://doi.org/10.1007/S00542-004-0387-2/METRICS.

[136] Rećko M, Aladag M, Błaszczak U, Dzierżek K, Kurzydłowski KJ. Effect of UV-C long-time irradiation on mechanical properties of PMMA. Results Mater 2024;22:100567. https://doi.org/10.1016/J.RINMA.2024.100567.

[137] Monsores KGDC, Silva AO Da, De Sant'Ana Oliveira S, Rodrigues JGP, Weber RP. Influence of ultraviolet radiation on polymethylmethacrylate (PMMA). J Mater Res Technol 2019;8:3713–8. https://doi.org/10.1016/J.JMRT.2019.06.023.

[138] Martínez-Conde A, Krenke T, Frybort S, Müller U. Review: Comparative analysis of CO2 laser and conventional sawing for cutting of lumber and wood-based materials. Wood Sci Technol 2017;51:943–66. https://doi.org/10.1007/S00226-017-0914-9/METRICS.

[139] Elsheikh AH, Deng W, Showaib EA. Improving laser cutting quality of polymethylmethacrylate sheet: experimental investigation and optimization. J Mater Res Technol 2020;9:1325–39. https://doi.org/10.1016/J.JMRT.2019.11.059.

[140] Moradi M, Rezayat M, Meiabadi S, Karamimoghadam M, Hillyard S, Mateo A, et al. Capability Enhancing of CO2 Laser Cutting for PMMA Sheet Using Statistical Modeling and Optimization. Appl Sci 2023;13:12601. https://doi.org/10.3390/APP132312601.

[141] Khoshaim AB, Elsheikh AH, Moustafa EB, Basha M, Showaib EA. Experimental investigation on laser cutting of PMMA sheets: Effects of process factors on kerf characteristics. J Mater Res Technol 2021;11:235–46. https://doi.org/10.1016/J.JMRT.2021.01.012.

[142] Shao G, Hai R, Sun C. 3D Printing Customized Optical Lens in Minutes. Adv Opt Mater 2020;8:1901646. https://doi.org/10.1002/ADOM.201901646.

[143] Jeong HY, Lee E, An SC, Lim Y, Jun YC. 3D and 4D printing for optics and metaphotonics. Nanophotonics 2020;9:1139–60. https://doi.org/10.1515/NANOPH-2019-0483/ASSET/GRAPHIC/J_NANOPH-2019-0483_FIG_006.JPG.

[144] Wang H, Wang H, Zhang W, Yang JKW. Toward Near-Perfect Diffractive Optical Elements via Nanoscale 3D Printing. ACS Nano 2020;14:10452–61. https://doi.org/10.1021/ACSNANO.0C04313/ASSET/IMAGES/LARGE/NN0C04313_0005.JPEG.

[145] Nseowo Udofia E, Zhou W. 3D printed optics with a soft and stretchable optical material. Addit Manuf 2020;31:100912. https://doi.org/10.1016/J.ADDMA.2019.100912.

[146] Ding G, He R, Zhang K, Zhou N, Xu H. Stereolithography 3D printing of SiC ceramic with potential for lightweight optical mirror. Ceram Int 2020;46:18785–90. https://doi.org/10.1016/J.CERAMINT.2020.04.196.

[147] Prashar G, Vasudev H, Bhuddhi D. Additive manufacturing: expanding 3D printing horizon in industry 4.0. Int J Interact Des Manuf 2023;17:2221–35. https://doi.org/10.1007/S12008-022-00956-4/FIGURES/9.

[148] Kafle A, Luis E, Silwal R, Pan HM, Shrestha PL, Bastola AK. 3D/4D Printing of Polymers: Fused Deposition Modelling (FDM), Selective Laser Sintering (SLS), and Stereolithography (SLA). Polym 2021;13:3101. https://doi.org/10.3390/POLYM13183101.

[149] Zeng YS, Hsueh MH, Hsiao TC. Effect of ultraviolet post-curing, laser power, and layer thickness on the mechanical properties of acrylate used in stereolithography 3D printing. Mater Res Express 2023;10:025303. https://doi.org/10.1088/2053-1591/ACB751.

[150] Badanova N, Perveen A, Talamona D. Study of SLA Printing Parameters Affecting the Dimensional Accuracy of the Pattern and Casting in Rapid Investment Casting. J Manuf Mater Process 2022;6:109. https://doi.org/10.3390/JMMP6050109.

[151] Gim J, Turng LS. A review of current advancements in high surface quality injection molding: Measurement, influencing factors, prediction, and control. Polym Test 2022;115:107718. https://doi.org/10.1016/J.POLYMERTESTING.2022.107718.

[152] PMMA Injection Molding - FOW Mould n.d. https://www.immould.com/pmma-injection/ (accessed November 30, 2024).

[153] Kumar A, Kumar N, Puttapati SK. Advancing optical transparency in 3D-printed PLA parts using chemical post-processing. Polym Eng Sci 2025;65:299–314. https://doi.org/10.1002/PEN.27010.

[154] Dizon JRC, Gache CCL, Cascolan HMS, Cancino LT, Advincula RC. Post-Processing of 3D-Printed Polymers. Technol 2021;9:61. https://doi.org/10.3390/TECHNOLOGIES9030061.

[155] Renewable Power Generation Costs in 2021 | IRENA. https://www.irena.org/publications/2022/Jul/Renewable-Power-Generation-Costs-in-2021 (accessed November 30, 2024).

[156] The Paris Agreement | UNFCCC n.d. https://unfccc.int/process-and-meetings/the-paris-agreement (accessed November 30, 2024).

[157] COP26: Together for our planet | United Nations n.d. https://www.un.org/en/climatechange/cop26 (accessed November 30, 2024).

[158] Sheikh YA, Maqbool MU, Butt AD, Bhatti AR, Awan AB, Paracha KN, et al. Impact of rooftop photovoltaic on energy demand of a building in a hot semi-arid climate. J Renew Sustain Energy 2021;13:065101. https://doi.org/10.1063/5.0063044.

[159] Arabkoohsar A, Xie G, Wei J, Asok A, Behzadi A, Mahian O. Perspectives and review of photovoltaic-thermal panels in net-zero energy buildings. J Therm Anal Calorim 2022;147:8621–30. https://doi.org/10.1007/S10973-021-11191-6/METRICS.

[160] Gholami H, Røstvik HN, Müller-Eie D. Holistic economic analysis of building integrated photovoltaics (BIPV) system: Case studies evaluation. Energy Build 2019;203:109461. https://doi.org/10.1016/J.ENBUILD.2019.109461.

[161] Martin H, Buffat R, Bucher D, Hamper J, Raubal M. Using rooftop photovoltaic generation to cover individual electric vehicle demand—A detailed case study. Renew Sustain Energy Rev 2022;157:111969. https://doi.org/10.1016/J.RSER.2021.111969.

[162] Zhou Y, Cao S, Kosonen R, Hamdy M. Multi-objective optimisation of an interactive buildings-vehicles energy sharing network with high energy flexibility using the Pareto archive NSGA-II algorithm. Energy Convers Manag 2020;218:113017. https://doi.org/10.1016/J.ENCONMAN.2020.113017.

[163] Formolli M, Croce S, Vettorato D, Paparella R, Scognamiglio A, Mainini AG, et al. Solar Energy in Urban Planning: Lesson Learned and Recommendations from Six Italian Case Studies. Appl Sci 2022;12:2950. https://doi.org/10.3390/APP12062950.

[164] He Y, Zhou Y, Yuan J, Liu Z, Wang Z, Zhang G. Transformation towards a carbon-neutral residential community with hydrogen economy and advanced energy management strategies. Energy Convers Manag 2021;249:114834. https://doi.org/10.1016/J.ENCONMAN.2021.114834.

[165] Kuhn TE, Erban C, Heinrich M, Eisenlohr J, Ensslen F, Neuhaus DH. Review of technological design options for building integrated photovoltaics (BIPV). Energy Build 2021;231:110381. https://doi.org/10.1016/J.ENBUILD.2020.110381.

[166] Pan JW, Su YC, Lee SY. Optimized planar micro-optic concentrator design. J Opt 2016;18:065901. https://doi.org/10.1088/2040-8978/18/6/065901.

[167] Lv J, Xu X, Yin P. Design method of a planar solar concentrator for natural illumination. Sol Energy 2019;194:554–62. https://doi.org/10.1016/J.SOLENER.2019.10.056.

[168] Attoye DE, Aoul KAT, Hassan A. A Review on Building Integrated Photovoltaic Façade Customization Potentials. Sustain 2017;9:2287. https://doi.org/10.3390/SU9122287.

[169] Reddy P, Surendra Gupta MVN, Nundy S, Karthick A, Ghosh A. Status of BIPV and BAPV System for Less Energy-Hungry Building in India—A Review. Appl Sci 2020;10:2337. https://doi.org/10.3390/APP10072337.

[170] Yu G, Yang H, Luo D, Cheng X, Ansah MK. A review on developments and researches of building integrated photovoltaic (BIPV) windows and shading blinds. Renew Sustain Energy Rev 2021;149:111355. https://doi.org/10.1016/J.RSER.2021.111355.

[171] Ghosh A, Sundaram S, Mallick TK. Colour properties and glazing factors evaluation of multicrystalline based semi-transparent Photovoltaic-vacuum glazing for BIPV application. Renew Energy 2019;131:730–6. https://doi.org/10.1016/J.RENENE.2018.07.088.

[172] Mirabi E, Akrami Abarghuie F, Arazi R. Integration of buildings with third-generation photovoltaic solar cells: a review. Clean Energy 2021;5:505–26. https://doi.org/10.1093/CE/ZKAB031.

[173] Hong T, Koo C, Oh J, Jeong K. Nonlinearity analysis of the shading effect on the technical–economic performance of the building-integrated photovoltaic blind. Appl Energy 2017;194:467–80. https://doi.org/10.1016/J.APENERGY.2016.05.027.

[174] Peng J, Curcija DC, Thanachareonkit A, Lee ES, Goudey H, Selkowitz SE. Study on the overall energy performance of a novel c-Si based semitransparent solar photovoltaic window. Appl Energy 2019;242:854–72. https://doi.org/10.1016/J.APENERGY.2019.03.107.

[175] Jeong K, Hong T, Koo C, Oh J, Lee M, Kim J. A Prototype Design and Development of the Smart Photovoltaic System Blind Considering the Photovoltaic Panel, Tracking System, and Monitoring System. Appl Sci 2017;7:1077. https://doi.org/10.3390/APP7101077.

[176] Brovelli S, Meinardi F, Carulli F. Colourless Luminescent Solar Concentrator, Free of Heavy Metals, based on at least Ternary Chalcogenide Semiconductor Nanocrystals with Absorption extending to the Near Infrared Region.WO/2016/116803. July 28, 2016.

[177] Smart Window Product Overview | SageGlass n.d. https://www.sageglass.com/smart-windows/product-overview (accessed November 30, 2024).

[178] Technology - Electrochromic glass - ChromoGenics AB n.d. https://chromogenics.com/technology/ (accessed November 30, 2024).

[179] Solar Control Glass | Switchable Smart Glass n.d. https://www.smartglassinternational.com/solar-smartglass/ (accessed November 30, 2024).

[180] Smart Glass : Switchable Smart Glass in India | AIS Glass n.d. https://www.aisglass.com/businesses-brands-architecture-by-category/value-added-glass/ais-swytchglas/ (accessed November 30, 2024).

[181] Royal Tint is India's leading brand of Switchable Film and Glass n.d. https://www.royaltint.in/ (accessed November 30, 2024).

[182] Anissa Tabet Aoul K, Efurosibina Attoye D, Al Ghatrif L. Performance of Electrochromic Glazing: State of the Art Review. IOP Conf Ser Mater Sci Eng 2019;603:022085. https://doi.org/10.1088/1757-899X/603/2/022085.

[183] Hillmer H, Al-Qargholi B, Khan MM, Worapattrakul N, Wilke H, Woidt C, et al. Optical MEMS-based micromirror arrays for active light steering in smart windows. Jpn J Appl Phys 2018;57:08PA07. https://doi.org/10.7567/JJAP.57.08PA07/XML.

[184] Ghosh A, Norton B. Advances in switchable and highly insulating autonomous (self-powered) glazing systems for adaptive low energy buildings. Renew Energy 2018;126:1003–31. https://doi.org/10.1016/J.RENENE.2018.04.038.

[185] Ghosh A, Mallick TK. Evaluation of colour properties due to switching behaviour of a PDLC glazing for adaptive building integration. Renew Energy 2018;120:126–33. https://doi.org/10.1016/J.RENENE.2017.12.094.

[186] Rezaei SD, Shannigrahi S, Ramakrishna S. A review of conventional, advanced, and smart glazing technologies and materials for improving indoor environment. Sol Energy Mater Sol Cells 2017;159:26–51. https://doi.org/10.1016/J.SOLMAT.2016.08.026.

[187] Casini M. Active dynamic windows for buildings: A review. Renew Energy 2018;119:923–34. https://doi.org/10.1016/J.RENENE.2017.12.049.

[188] Wolfe D, Goossen KW. Evaluation of 3D printed optofluidic smart glass prototypes. Opt Express 2018;26:A85–98. https://doi.org/10.1364/OE.26.000A85.

[189] Brzezicki M. A Systematic Review of the Most Recent Concepts in Smart Windows Technologies with a Focus on Electrochromics. Sustain 2021;13:9604. https://doi.org/10.3390/SU13179604.

[190] Wheeler LM, Moore DT, Ihly R, Stanton NJ, Miller EM, Tenent RC, et al. Switchable photovoltaic windows enabled by reversible photothermal complex dissociation from methylammonium lead iodide. Nat Commun 2017;8:1–9. https://doi.org/10.1038/s41467-017-01842-4.

[191] Eri A, Okumura K. Viscous drag friction acting on a fluid drop confined in between two plates. Soft Matter 2011;7:5648–53. https://doi.org/10.1039/C0SM01535K.

[192] Okumura K. Viscous dynamics of drops and bubbles in Hele-Shaw cells: Drainage, drag friction, coalescence, and bursting. Adv Colloid Interface Sci 2018;255:64–75. https://doi.org/10.1016/J.CIS.2017.07.021.

[193] Tanveer S. The effect of surface tension on the shape of a Hele–Shaw cell bubble. Phys Fluids 1986;29:3537–48. https://doi.org/10.1063/1.865831.

ABSTRACT

Name of the student: ANIMESH M R	**Registration No.: 20EE20A39003**
Faculty of Study: Engineering Sciences	**Year of Submission: 2024**
CSIR Lab: CSIR-National Institute for Interdisciplinary Science & Technology, Thiruvananthapuram, Kerala	**Name of the Supervisor: Dr. Adersh Asok**
Title of the thesis: Design & Development of Planar Light Concentrator based Solar Collectors	

This dissertation focuses on the design and development of a novel compact Planar Light Concentrator (PLC) as a solution to conventional bulky light concentrators. The design essentially consists of an array of skewed V-grooves in an optics slab, and light falling on it will be transported to the lateral face in a direction. The low-concentrating system can be effectively used in built environments such as Building Integrated Photovoltaics, where the concept of focal length limits conventional light concentrators in their applicability. The key features of the optics design include 1) Non-sequential design approach employing a single optics element; this avoids the need for precise positioning of the optics 2) Low-concentration optics, eliminating the need for intricate thermal management systems; 3) Manufacturable through a single process; 4) Higher solar acceptance in an axis eliminating the need for 2-axis tracking; 5) A zero focal length configuration that negates the necessity for spacing before the collectors; 6) Unidirectional light concentration design for higher concentration factor; 7) Flexibility for converting to radial design for higher concentration factor. A basic mathematical model was developed for the evaluation of the optics, defining the control parameters, and optimization of the parameters for the final simulation models. Fabrication of the skewed V-groove based PLC (SV-PLC) has been carried out with three different manufacturing processes: 1) Laser cutting, 2) Stereolithography 3D printing, and 3) Injection molding. The advantages and limitations of each process have been evaluated to carry the design solution from initial technological evaluation to mass production. The SV-PLC optics were experimentally evaluated using an amorphous silicon solar cell, under both standard conditions and direct solar radiation. Finally, a novel Building Integrated Photovoltaic glazing concept called Dynamic Power Window has been conceptualized and demonstrated using SV-PLC optics, which integrates active dynamicity and power generation in a single platform. The technology utilizes SV-PLC optics as the energy-generating component, which is integrated with optofluidics to attain the active dynamism.

List of publications

Emanating from the thesis work

Articles:

1. A.M. Ramachandran, A. Asok, Single elemental planar light concentrator using skewed V-groove optics, Results in Engineering. 24 (2024), 102923. https://doi.org/10.1016/j.rineng.2024.102923.
2. A.M. Ramachandran, S.M. S, A.S. Thampi, M. Singh, A. Asok, A comprehensive review on optics and optical materials for planar waveguide-based compact concentrated solar photovoltaics, Results Eng. 16 (2022) 100665. https://doi.org/10.1016/J.RINENG.2022.100665.
3. Mathematical Model of Skewed V-groove based Planar Light Concentrator (To be submitted).
4. Radial Skewed V-groove Planar Optics for Medium Light Concentrators (To be submitted).
5. Dynamic Power Window (To be submitted).

Patents:

1. Hybrid Planar Light Concentrator with Adaptable Transparency; Patent No. 483372; Granted: 15/12/2023.
2. Skewed V-groove-based Unidirectional Planar Light Concentrators; Application No. 202311075871; Filed: 6/11/2023
3. Light-sharing Energy Systems Based On Functional Optical Design Integrated Planar Waveguides; Filed: 6/12/2023.

Out of the thesis scope

Book Chapters:

1. A.M. Ramachandran, R. Joseph, A. Asok, Characterization techniques for morphological and physicochemical evaluation of nanomaterials. Nanobiotechnology, Elsevier, ISBN 9780128228784, (2021), 21-50, https://doi.org/10.1016/B978-0-12-822878-4.00002-X.

Reports:

1. A. M. Ramachandran, P. Corti, A. Asok, P. Bonomo, Indian BIPV Report 2022: Status and Roadmap. (2022). https://solarchitecture.ch/wp-content/uploads/2022/08/BIPV-Report-India_v01.pdf.

Patents:

1. Spectral Converting Diverging Optics for Even Solar Sharing systems. Filed December 2024.

List of Conference Presentations

1. A.M. Ramachandran, S.M. S, A. Asok, High Solar Acceptance Planar Waveguide-based Light Concentrator, COMSOL Conference, Bengaluru, 2023. (Poster)
2. A.M. Ramachandran, S.M. S, A.S. Thampi, A. Asok, Numerical Model for a High Solar Acceptance Planar Waveguide-Based Light Concentrator, ISES Solar World Congress, New Delhi, 2023 (SWC23_ABS_Q5641). (Poster)

Numerical Model for a High Solar Acceptance Planar Waveguide-Based Light Concentrator

Animesh M. Ramachandran†‡, Adhithya S. Thampi†‡ and Adersh Asok†‡*
†Centre for Sustainable Energy Technologies, CSIR-National Institute for Interdisciplinary Science and Technology (NIIST), Thiruvananthapuram, India
‡Academy of Scientific and Innovative Research (AcSIR), Ghaziabad, 201002, India
* Corresponding author: adersh.asok@niist.res.in

Solar energy, being the most abundant natural source of renewable energy, is playing a crucial role in the ongoing global renewable energy translation. However, energy converted utilization of solar energy has its limitation of lower input energy density. Light concentrators are the most sought-after technology for mitigating this limitation of solar radiation. However, the conventional optics systems such as mirrors and lenses suffer from bulkiness and low cost-effectiveness due to the large optics elements. Waveguide-based planar light concentrator (PLC) is an approach, where the system bulkiness is greatly reduced due to its prospectus of direct light collection from its lateral face. However, the existing designs mostly consist of multiple optics elements, resulting in the need for precise positioning and 2-axis point-to-point solar tracking. In this regard, we have designed and prototyped a novel PLC optics solution that is single elemental and has high solar acceptance in an axis.

High Solar Acceptance Planar Waveguide-Based Light Concentrator

Animesh M. Ramachandran†‡, and Adersh Asok†‡*
†Centre for Sustainable Energy Technologies, CSIR-National Institute for Interdisciplinary Science and Technology (NIIST), Thiruvananthapuram, India
‡Academy of Scientific and Innovative Research (AcSIR), Ghaziabad, 201002, India
* Corresponding author: adersh.asok@niist.res.in

Solar energy, being the most abundant natural source of renewable energy, will play a crucial role in the ongoing global renewable energy translation. However, energy converted utilization of solar energy, which can be either thermal or electrical, technologies have the limitation of lower input energy density. The area utilization of these solar power conversion systems, costs, and their environmental impacts will also become a major concern in the coming decades. The most sought-after and straightforward approach adopted to address this issue of lower energy density is by concentrating solar energy to a finite area using optics technology intervention.

Light concentration optics technologies have been classified with performance as low concentration (2X – 100X), medium concentration (100X – 1000X), and high concentration (>1000X) optics. Among them, low-concentration optics (LCO) have been identified with simpler approaches and minimalized requirements of active cooling methods upon different application systems. The additional prospectus of a compact system design of LCO technologies can be considered for small power plants or low-capacity decentralized solutions. Moreover, its applicability in built environments, such as for building integration/ retrofits has been discussed more recently. Recently, the low-concentration Planar Light Concentrator (PLC) technologies have been well acknowledged globally, and many research efforts have been put forward to develop new designs and solutions, indicating its prospect for Concentrated PV/Thermal technologies. Waveguide-based PLC has evolved as a major contender in PLC technologies. Recognizing its importance, the US Department of Energy acknowledged the potential of waveguide-based PLC through the Advanced Research Projects Agency-Energy (ARPA-E) project in 2016.

However, design development and optimization of any PLC technologies require elemental and subsequent system-level ray optics modelling, which is impractical with conventional optics drawing and numerical modelling. Also, the angular performance study of optics design, especially for solar applications is difficult to conduct conventionally. Herein, the

proprietary optics design for the PLC has been evaluated using the Ray Optics Module of COMSOL Multiphysics software. The multi-parameters have been well defined, parametrized individually, and optimized with their causality, leading to different designs correlated to different output requirements. The geometrical concentration factor depending on the system size, the final output light concentration, and the solar acceptance has been evaluated for the different design types and parameters and represented graphically to gain a better system and optics design selection process. Further, the secondary optics rays, analyzed through the simulation models give a better understanding of the fundamental optics phenomenon concerned with the optics designs. Data processing and data modelling has also been carried out through COMSOL post-processing elements to have better data visualization.

In conclusion, the proprietary PLC design has been developed with ray tracing models using COMSOL Multiphysics software. The optimized designs are fabricated and validated practically as a low-concentration solar optics solution.

Results in Engineering 24 (2024) 102923

Contents lists available at ScienceDirect

Results in Engineering

journal homepage: www.sciencedirect.com/journal/results-in-engineering

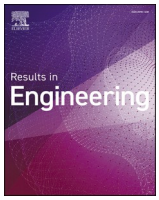

Micro-article

Single elemental planar light concentrator using skewed V-groove optics

Animesh M. Ramachandran [a,b], Adersh Asok [a,b,*]

[a] Centre for Sustainable Energy Technologies, CSIR-National Institute for Interdisciplinary Science and Technology (NIIST), Thiruvananthapuram, Kerala, 695 019, India
[b] Academy of Scientific and Innovative Research (AcSIR), Ghaziabad, 201002, India

A B S T R A C T

Light concentrators are widely used to address the challenges of solar radiation's limited energy density. However, traditional light concentrators suffer from bulkiness, higher focal length, low solar acceptance, and cost factor due to the usage of large imaging optics elements. Waveguide-based planar light concentrators (PLC) have been engineered as a solution to these challenges. They work by collecting light at the incident face and channeling it to the lateral face of the waveguides. However, the existing PLC designs mostly consist of multiple optics elements, resulting in the need for precise positioning and point-to-point solar tracking. Addressing these complexities, a new design for waveguide-based PLC is presented. It features a simplified array of skewed V-grooves within an optical slab, essentially creating a single elemental optics. This novel skewed V-groove-based PLC (SV-PLC) introduces a low-concentration (i.e., <10X geometric concentration (GC)) solution that offers high angular acceptance along one axis. The current study aims to establish the novel design concept, validate, optimize, and assess the design through the Ray-tracing simulation. Further, based on the simulation results, a functional prototype was successfully fabricated in PMMA using laser machining. The results of the optical characterization of the SV-PLC showed that the Optical Efficiency (OE) was approximately around half the theoretical OE. Angular-dependent ray trace results showed a lower OE drop (<10 %) for incident angles less than 15°, and a maximum drop of 30 % (for a 10X GC design) for an incident angle of 23.5° (i.e., half the angle shift of the sun through seasons).

1. Introduction

Solar electricity conversion stands out as a leading solution for renewable energy transformation, crucial for the required energy shift. Its ease of adaptability and prospectus of Decentralised Distributed Generation (DDG) highlight its significance [1,2]. Over the last two decades, the cost of solar modules has declined by more than 95 % [3]. However, the quest for enhancing the spatial efficiency of solar cells and reducing costs remains a critical issue [4]. Additionally, with the rapid adoption of solar technology, waste management, and recycling have emerged as pressing concerns for the industry in the upcoming decades [5]. This situation underscores the urgent need for strategies that maximize the effective use of solar cell area.

Concentrated solar power (CSP) technologies, due to their efficient resource and energy utilization attributes, are intended to have a higher impact on the renewable energy sector [6]. Originally developed for converting thermal energy [7,8], a growing focus is now on directly converting concentrated solar energy into electricity or electricity-thermal energy, which can reduce the need for extensive photovoltaic (PV) surface area and materials [9,10]. Compared to luminescent [11] and diffraction optics-based [12] solar Concentrated Photovoltaic (CPV) technologies, geometric optics (GO)-based CPV systems are particularly impactful due to their higher energy concentration factor and wide spectral selectivity [13]. These systems primarily have an optical element of a specific acceptance angle for solar radiation that concentrates the solar radiation onto a smaller desired area. While traditional GO - concentrators utilize bulky mirrors and lenses, that suffer from point-to-point solar tracking [6]. Efforts to scale down these components typically involve either reducing the concentration factor or increasing the number of elements used within the system [14].

In this context, GO-based Planar Light Concentrator (PLC) systems, which employ compact light-concentrating optics, are making a significant impact due to their reduced built volume. This reduction in size is mainly achieved by decreasing the optics' dimensions and/or the focal length [15,16]. Such advancements are propelling the use of PLCs in CPV, beneficial for both large-scale power generation [17] and integration into building designs, such as in Building Integrated Photovoltaics (BIPV) [18]. In PLCs, light waveguide-incorporated designs are developed later, that efficiently capture and transport light to their edges, where energy is concentrated and collected without any focal gap. Despite these advantages of waveguide-based PLCs, current designs face challenges including the need for precise microfabrication techniques [19], bulkier elements (larger width-to-length ratio) [20], complex optical alignments [21], or limited solar acceptance angles [22].

* Corresponding author. Centre for Sustainable Energy Technologies, CSIR-National Institute for Interdisciplinary Science and Technology (NIIST), Thiruvananthapuram, Kerala-695 019, India.
E-mail address: adersh.asok@niist.res.in (A. Asok).

https://doi.org/10.1016/j.rineng.2024.102923
Received 21 May 2024; Received in revised form 10 September 2024; Accepted 16 September 2024
Available online 17 September 2024

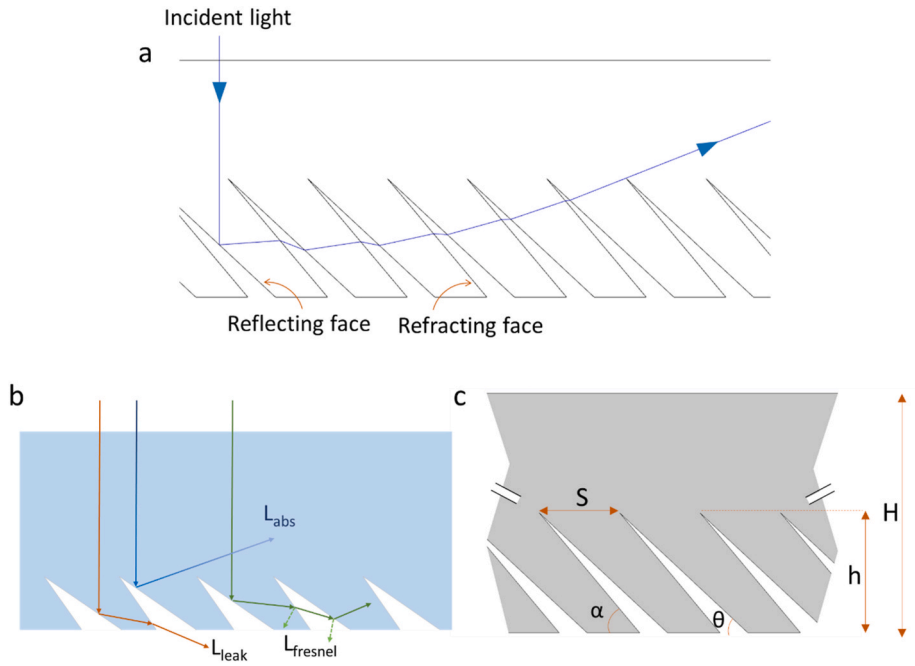

Fig. 1. a) Typical ray transport mechanism within an SV-PLC, illustrated using a ray-tracing simulation model; b) Key design parameters for SV-PLC optics; c) Principal loss mechanisms in an SV-PLC optics.

Current design approaches of GO-based PLC systems can be classified as.

1. Multi-elemental refractive: This is the most common approach, where refractive optics elements such as spherical or cylindrical microlenses are made to optically align with some light-dispersive elements such as prisms, wedges, mirrors, or scattering surfaces positioned in the waveguide. The light rays are initially made to focus on the dispersive elements through the microlenses, where it is transported within the waveguide after light dispersion. Eric J. Tremblay et al. fabricated one such system with spherical microlenses and 120° apex symmetric prisms [19]. The theoretical study shows an OE of 81.9 % for 300X GC, however, the prototype developed showed 32.4 % optical efficiency for 37.5X GC. The manufacturing and precise positioning of the specific optics elements seems to be challenging here. Also, the system has a very low acceptance angle and requires lateral alignment and rotational accuracy because of its architecture. The replacement of the spherical lens with cylindrical lens by S. Bouchard et al. provided high angular acceptance (±54°) in an axis at the expense of the GC [23]. The simulated results in LightTools showed an OE of 80 % for 8.1X. More studies are conducted in this similar approach with different design architectures [21,24–29], however, its scalability and optics design challenges remain unaddressed.
2. Multi-elemental reflective: This approach uses multiple reflective elements to direct the rays to the waveguide, which is architecturally separated. Kuo et al. showed one such design which uses waveguide sheets stacked with an array of arc segment structures which is reflective [30]. Light rays after reflection from the arc segment structures, it is directed to the sheet waveguide, and further transported to the desired area with a series of optics arrangement. The simulation studies conducted showed a GC of 738X with an OE of 87 %. The angular acceptance offered by the design is around ±12°. Here also, scalability and the positioning of optics elements seems to be challenging with multiple light guiding layers.
3. Single-elemental reflective: This approach uses an arrangement of reflective surfaces that transport the light rays to the waveguide, where it is directed to the desired output area. A typical design can be an array of reflective V-grooves on a planar optical waveguide [20]. Light falling on the grooves is redirected to the desired area (lateral edge), upon the design considerations. The design is a single-elemental approach, making the fabrication easier and eliminating the need for any inter-alignment of optics elements. The major drawback of the design is the high aspect ratio (length--to-height ratio) of the optics, and the lower acceptance angle (2°). The ray tracing simulation study (using LightTools software) suggested a moderate OE of 67.7 % for 5X GC. The PLC developed by Morgan Solar is one of the superior single-elemental reflective designs when considering the GC it can provide [22,31]. The architecture essentially consists of an array of reflective profiles placed above the waveguide. The light redirected from the reflective surfaces is made to pass through the entry point to the waveguide, where it is transported to the lateral side. The design offers a very low acceptance angle of ±0.9°, however, offers a very high GC (1000X) [32]. A comprehensive review summarizing various waveguide-based PLC designs, along with their advantages and limitations, has recently been published [33].

Herein, a novel optical design featuring skewed V-groove patterns has been developed for use in low-concentration solar energy systems. The first-of-its-kind design approach differs from the existing methods in its light transport mechanism and has the following attributes: 1) Utilization of a non-sequential design (one optics element is not followed by any other) approach, employing a single optics element; this avoids the need for precise positioning of the optics 2) Low-concentration optics (less than 10X GC), eliminating the need for intricate thermal management systems; 3) A straightforward waveguide-based construction, allowing for production through a single manufacturing process; 4) Higher solar acceptance in an axis eliminating the need for 2-axis tracking; 5) A zero focal length configuration that negates the necessity for spacing before the collectors. Design, being the first of its kind, has been assessed for its influence on performance factors such as OE, and concentration factor through optical ray trajectory simulation models, using COMSOL 6.1 Multiphysics simulation software. The skewed v-groove-based PLC has been fabricated using rapid prototyping laser cutting in PMMA plates, followed by a visual inspection and

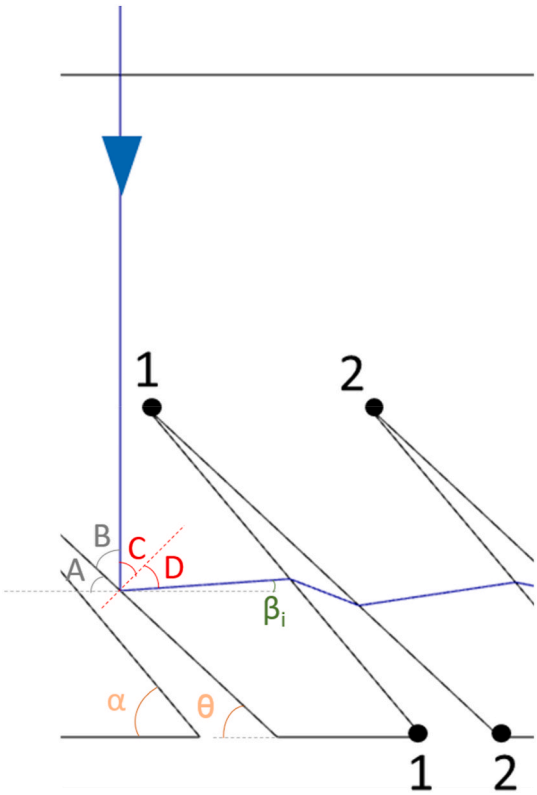

Fig. 2. Schematic representation of ray travel (in blue color) in a skewed V-groove PLC showing the angular parameters and variables at the incident face, where the light ray undergoes total internal reflection. (For interpretation of the references to color in this figure legend, the reader is referred to the Web version of this article.)

characterization to evaluate the optics.

2. Design

Fig. 1a depicts the typical simulated ray trajectory for lateral light concentration in SV-PLC using COMSOL Multiphysics 6.1. The design essentially consists of an array of skewed V-groove voids in an optically transparent slab. As illustrated, when a light ray hits the V-groove's reflecting face, it will undergo total internal reflection. This process steers the light horizontally through the SV-PLC, with multiple refractions at adjacent grooves causing an upward shift in the light rays within the SV-PLC, thereby enabling efficient light transmission. Ultimately, the rays redirected from the array of grooves lead to intensified light collection at the lateral edge of the SV-PLC.

The different losses that occur in an SV-PLC are depicted in Fig. 1b. The angle of incidence at the different faces determines the Fresnel loss ($L_{fresnel}$, represented as dotted lines), i.e., which is the light reflection loss during transmission. Additionally, material absorption loss (L_{abs}) significantly affects SV-PLC efficiency as light travels through the material. Beyond Fresnel and material absorption losses, there can also be leakage loss (L_{leak}) at the SV-PLC's base, as depicted in Fig. 1b. $L_{fresnel}$ and L_{leak} are influenced by the design parameters of SV-PLC. Therefore, optimizing the design to match the material characteristics can enhance its efficiency and improve final light concentration capabilities.

Fig. 1c illustrates the various design parameters for optimizing an SV-PLC. The methodology for this optimization of the parameters includes:

Reflecting face angle (θ): The angle θ must exceed the critical angle necessary for total internal reflection at the reflecting face. As defined by Snell's law, the critical angle for total internal reflection to occur is given by, $\theta_c = \sin^{-1}(RI_{air}/RI_m)$ or simply $\sin^{-1}(1/RI_m)$, where RI_{air} and RI_m are the refractive index of air and material respectively. Fig. 2 shows the schematic of the ray tracing of a single ray impinging on the SV-PLC.

$A = \theta$ (*Corresponding angles*)

$A + B = 90^\circ$ (*Considered ray at an angle of* 90° *with the PLC face*)

$\Rightarrow \quad B = 90^\circ - \theta$

$B + C = 90^\circ$ (*Angle made by normal to the groove face*)

$\Rightarrow \quad \theta = C$

$C + D + \beta_i = 90^\circ$

$\Rightarrow \quad \beta_i = 90^\circ - 2\theta$

Thus, the incident angle at the interface of total internal reflection is equal to the reflecting face angle. To ensure maximum light transmission with the fewest refractions possible, we maintain a minimal θ value. This minimization reduces Fresnel losses, thereby increasing the intensity of light rays reaching the lateral face. Consequently, for standard optic materials like PMMA (RI: 1.49), Glass (RI: 1.52), and Polycarbonate (RI: 1.58), we set θ to 43°, 42°, and 40° respectively.

Difference of Height of the slab & Height of the optical element (H-h): Reducing the size of the optical elements offers significant benefits by increasing the (H-h) factor, thereby extending the rays' path length. Consequently, this results in an increase in the L_{100} of the SV-PLC.

Length of the SV-PLC (L_{100}): L_{100} represents the maximum length of the PLC, capable of translating 100 % of the light from the incident plane onto the lateral face of the SV-PLC. It is a merit value rather than a variable and depends on the design parameters shown in Fig. 1c. After L_{100} the SV-PLC undergoes partial loss of light rays from the bottom (as represented in Fig. S1 of supplementary information showing a typical ray tracing simulation of SV-PLC). L_{max} (Fig. S2) represents the maximum length up to which the length of the SV-PLC can be extended, and it depends on only θ for a constant (H-h) value. After L_{max} there will be no additional gain of light to the lateral face.

Inter-groove spacing (S): The inter-groove spacing is always set to a maximum value without any L_{leak} loss in the SV-PLC.

Refracting face angle (α): The refracting face angle, α, is the critical factor in adjusting the optics of the SV-PLC to achieve the desired OE and light concentration, which is parameterized for this study.

3. Materials & methods

1. Simulation modelling

The optics simulation models are used to predict the performance of SV-PLC with common optical materials like PMMA, Glass, and Polycarbonate with Refractive Indices (RI) taken as 1.49, 1.52, and 1.58 respectively. We conduct two-dimensional simulations to gauge the effectiveness of SV-PLC and expand to 3D simulations for an in-depth analysis of angular acceptance along a given axis. Light rays are made to incident normal to the SV-PLC, and the simulation is carried out incorporating the interfacial light phenomena and the governing laws (Law of Reflection, Law of Refraction, Fresnel equations for light transmission through interfaces). The optical efficiency (OE, i.e., the output energy received at the lateral edge/input energy) and final light concentration (OE X GC (geometric concentration)) are determined by measuring the power of light received at the detector (lateral edge boundary is taken as the detector).

The ray optics module within COMSOL Multiphysics 6.1 was employed for the simulations, and the following considerations for the control parameters and boundary conditions were applied.

1. All the simulations are carried out for SV-PLC length kept at L_{100}.

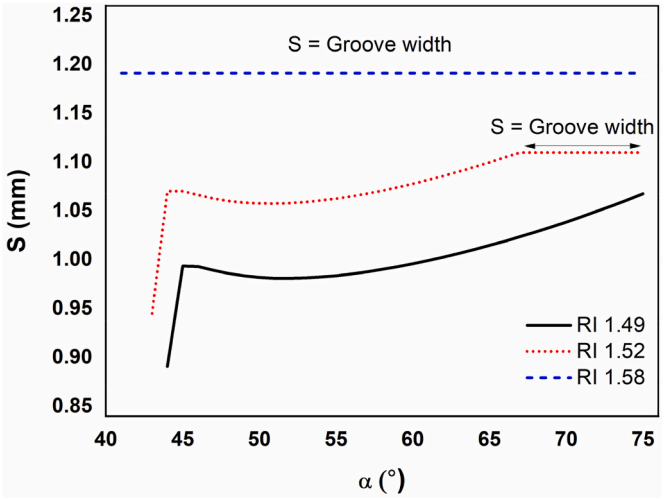

Fig. 3. Dependency of refraction face angle (α) on the inter-groove spacing (S) in SV-PLC for different materials (RI: 1.49, 1.52, and 1.58; results from simulation models).

2. The input power of light rays was set as 1W across the L_{100}. The light ray is taken as a singular wavelength (660 nm).
3. Uniform ray density is considered, with a spacing of 0.05 units' (mm) distance per ray across the L_{100}.
4. Material absorption losses were excluded from consideration, focusing the study on the design features of the SV-PLC.
5. The angle θ was set to a minimum value as detailed in the design section, according to the RI of the material.
6. For comparative analysis, values of H and h were set at 10 mm and 1 mm, respectively.
7. The spacing value S was maximized while ensuring zero L_{leak} as outlined in the design section.
8. The α parameter was swept above the θ angle up to a maximum of 75°.
9. The rays are made to freeze at the detector interface for computing the final ray power received at the detector.
9. Since the mesh size is independent of the simulation result (ray power at the detector), a coarser mesh size is selected.
10. The time step for the simulation is kept at 0.0001 ns for proper evaluation since a higher time step produces less accurate results.
10. Simulations are carried out up to 0.32 nanoseconds, for every ray to reach the detector where it is made to freeze to obtain the result.

2. Fabrication & Characterisation

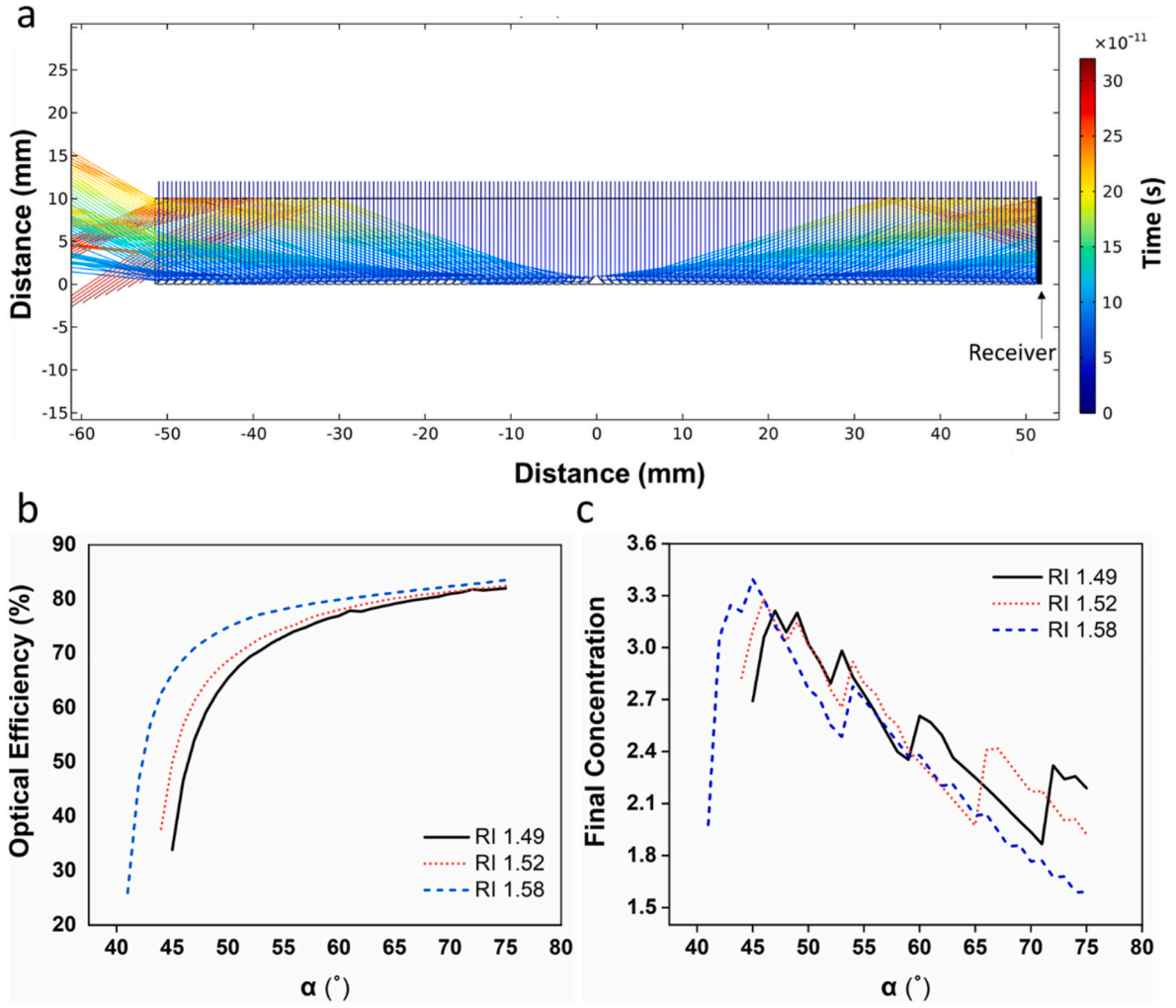

Fig. 4. a) A typical COMSOL Multiphysics simulation of ray-tracing within an SV-PLC showing complete lateral light concentration, a receiver placed on the lateral face to determine OE and final concentration; b) OE vs refracting face angle (α) plot in an SV-PLC for materials with RI 1.49, 1.52, and 1.58; c) Final light concentration vs α plot in an SV-PLC for the different RI materials.

The design was initially validated using a laser cutting process on PMMA sheets. Commercially available cast PMMA sheets (brand: Gujpol-S) with an RI of 1.49 at 589 nm, a visible transmittance of 92 % for 3 mm thickness, and a total thickness of 8 mm were used for creating the pattern. The equipment employed was the Trotec Speedy 100 CO_2 laser machine (accuracy of ±0.015 mm) which can operate at a maximum power of 60W for its 10.6 μm laser. The design parameters were set as follows: θ to 43°, α to 49°, H to 10 mm. To improve the profile cut by the laser, the h value was increased to 4 mm. This adjustment compensates for any local heat zones that can cause material softening and deformation during machining. The thickness of the PMMA sheet is limited to 8 mm according to the capacity of the machine to provide a satisfactory cut (without obliqueness) for the design. The vector drawing of the design is fed into the TROTEC JobControl X software. The parameters are fixed with the software by trial and error method to get a better finish with a straight and single cut. The machined parts are then inspected using a Carson MM-380 microscope with 20X magnification to check for cut angles, defects, and finish. The optimized parameters for the process include the laser head speed of 20 mm/s, with a laser power setting of 60 W, and the pulses per inch (PPI) of 500. Once the 8mm width SV-PLC pieces are cut, they are cleaned with a water jet for any residual removal, dried, and stacked together with epoxy resin for final visual inspection. In addition, colored Polycarbonate sheets are laminated above the SV-PLC for easy visual inspection. The OE of the fabricated SV-PLC pieces is evaluated using a standard thin-film amorphous silicon flexible solar cell (supplied by PowerFilm Solar, USA; active area: 1 cm × 1 cm; 4 mW under 1 sun). The output power from the bare cell and cell optically coupled with the SV-PLC are evaluated under 1 sun condition using an AM1.5G ACA solar simulator (supplied by HOLMARC, India).

4. Results and discussion

Fig. 4a depicts the typical time-dependent 2D ray-tracing model of an SV-PLC (RI: 1.49, α: 49°, H: 10 mm, h: 1 mm, ray density: 0.5 mm distance per ray (for analysis 0.05 mm distance per ray is used to improve the accuracy of models)). The inter-groove distance, S is taken for zero L_{leak}. Fig. 3 shows the S value for different α values for the considered materials. For higher RI material (RI: 1.58), the S value can be kept at maximum equalling the groove width.

The discussed SV-PLC design is mirrored to create bi-directional lateral concentration as shown in Fig. 4a. The receiver is identified as the position of the detector within the simulation model, which measures the SV-PLC's lateral power output. A parametric sweep was performed on the α value to analyse the OE and final light concentration. The results of the OE and final light concentration of the simulated models are shown in Fig. 4b & c (length of SV-PLC is taken as individual L_{100} of each design), respectively. The OE was calculated from the output light power (received at the detector) to the input light power (kept at 1 W) (the obtained results from the simulation are tabulated as Table S1 in the supplementary information). As the α value is increased, there was a drastic increase in the OE up to a limit, after that showing an almost straightened value. The trend is consistent with different optical materials under consideration, with slightly improved values for higher RI materials. The initial drastic increase is attributed to the lower $L_{fresnel}$ losses that occurred because of the reduced incident angles at the different groove interfaces and the reduced number of interfaces that the rays are passing. The graph tends to straighten after a limit due to less change in the Fresnel loss at interfaces. Nevertheless, the L_{100} value (which also influences the final concentration of light) typically decreases as α increases due to higher angular shifts occurring at the interfaces. The final light concentration, which is the product of the OE and GC (GC = L_{100}/H) was plotted against α, as shown in Fig. 4c. The graph shows a sharp increment initially, especially for higher RI material, owing to the drastic increase in the OE as discussed.

Even though the final concentration graph shows an overall decrease

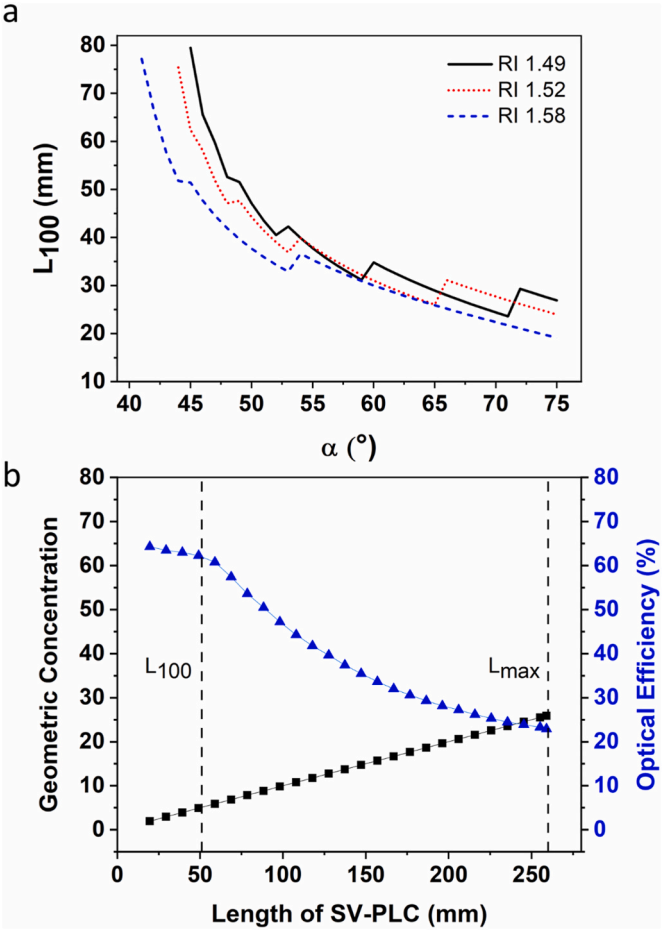

Fig. 5. a) Dependency of refraction face angle (α) on the L_{100} value in SV-PLC for different materials (RI: 1.49, 1.52, and 1.58; results from simulation models); b) Drop in OE and increase in the GC with the length of SV-PLC up to L_{max}.

in the longer range, it also produces irregular steps in the short range. This can be attributed to the irregularity in the L_{100} value (Fig. 5a), as different designs have different ray directional paths depending on the number of grooves the rays are passing. Herein, the design considerations are kept for the SV-PLC length of L_{100}, since after L_{100} there will be a drastic reduction in the OE even though the GC is high (as shown in Fig. 5b, where the design considerations are RI: 1.49, θ: 43°, α: 49°, H: 10 mm, h: 1 mm), as much of the light rays will not reach the lateral face and will be lost through the bottom of the SV-PLC. This is the reason that we have a reducing trend in final concentration upon the α after L_{100} and we are considering the design for L_{100} length of SV-PLC. In Fig. 5b, L_{max} represents the maximum length up to which the length of the SV-PLC can be extended (after L_{max} further increase in length does not provide any light concentration). The final concentration (product of OE and GC) can reach from 3.2X to 6X for L_{100} to L_{max}.

Fig. 6a shows the PMMA SV-PLC (RI: 1.49, θ: 43°, α: 49°, H: 10 mm, h: 4 mm) fabricated using laser cutting. Optical microscopy revealed several issues with the process including low dimensional accuracy, profile deformation, and low surface quality (Fig. 6b). The designed angle between the reflecting and refracting faces was 6°, however, the final contour shows an angle of 2° after laser cutting. This was likely due to damaged and deformed edges caused by local heat produced. The profile also seems to be unsuitable for the laser cutting process, since the cuts for the profile are very close to each other, creating heat-induced deformations. The measured optical efficiencies with the theoretical efficiency further validate these findings. The bare solar cell generates a power of 5.82 mW under the simulated conditions; the SV-PLC optics

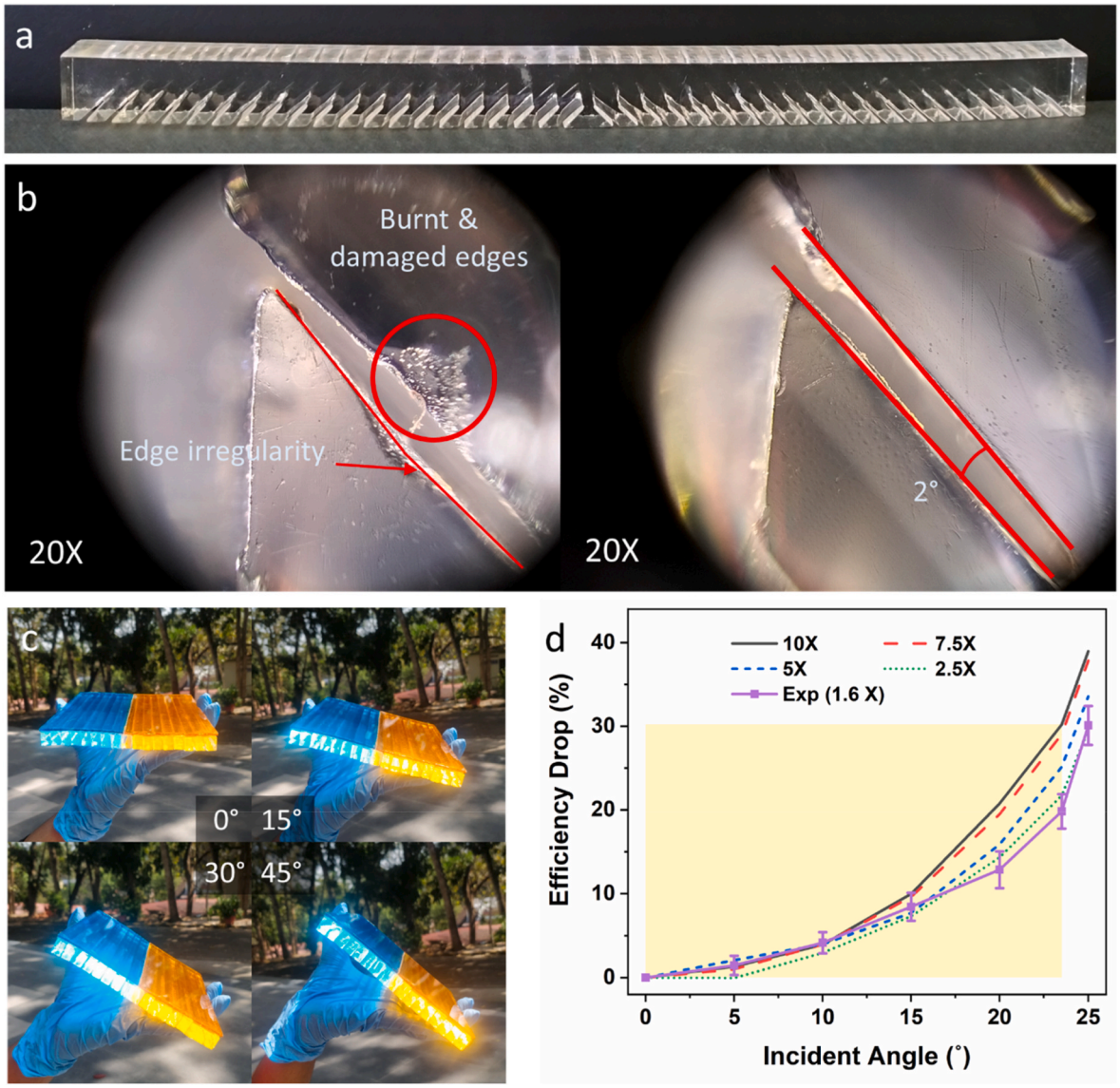

Fig. 6. a) A photograph showcasing the SV-PLC fabricated through laser cutting of PMMA sheet; b) Optical microscope images (20X magnified) of the fabricated SV-PLC using laser machining, showing the surface defects, low dimensional accuracy, and profile deformation; c) Photographs validating the high angular acceptance of SV-PLC in the longitudinal axis; d) Simulation study plot of efficiency drop in SV-PLC with varying incident angles in the longitudinal axis.

have an OE of 37.9 % (theoretical OE: 66.3 %) for 1.6X GC (3.52 mW), 26.4 % (theoretical OE: 58.3 %) for 3.2X GC (4.92 mW), 21.82 % (theoretical OE: 55.1 %) for 4.8X GC (6.01 mW), 18.8 % (theoretical OE: 45.4 %) for 6.4X GC (7 mW), and 15.43 % (theoretical OE: 36.4 %) (7.12 mW) for 8X GC. Apart from the limitations of the manufacturing process, lower H-h value also contributes to lower efficiency at higher GC. When compared, the measured OEs is around ~2 times less than that of the theoretical OE.

Fig. 6c showcases the visual validation (at 0°, 15°, 30°, and 45° light incidence) of the concept, illustrated with multiple laser-machined SV-PLCs coupled together with transparent epoxy resin. The angle of incidence is measured from the normal to the plane of SV-PLC, parallel to the groove direction. For enhanced visual detection, colored polycarbonate sheets are attached on top of the PLC, as shown in the accompanying photographs. Fig. 6d presents the results of the simulated single directional angular study (efficiency drop) of the SV-PLC (RI: 1.49, θ: 43°, α: 49°, H: 10 mm, h: 1 mm) with GC of 10X, 7.5X, 5X, and 2.5X, and an experimental study in a 1.5X GC SV-PLC. The efficiency drop for different angles of incidence was measured relative to the respective 0° light incidences as different cases have different power outputs. Hence the efficiency drop is taken 0 at 0°. The investigation focuses on the longitudinal axis and involves changing the incident angle from 0° to 25°. In the graph, the highlighted rectangle represents the angular acceptance zone till 23.5°, which corresponds to the angular shift of the sun (±23.5°) through different seasons. The results showed a low-efficiency drop of less than 10 % within ±15° and a maximum drop of 30 % within the ±23.5° zone. The experimental result also showed a similar trend even though the final laser cut optics have a slightly irregular graph pattern. The observed irregularity can be attributed to the presence of scattering points and irregular cuts due to the machining limitations and the loss of intensity of transmitted light due to its passage through individual SV-PLC elements. As a future applicability note, the products based on SV-PLC optics should be explored more in concentrated solar energy applications with geographic location-based feasibility study [34] and its techno-economics analysis.

5. Conclusion

A skewed V-groove design was introduced for a waveguide-based PLC, which is single elemental, non-sequential, and shows high

angular acceptance in an axis. This design underwent parametric optimization and was evaluated for OE and angular acceptance using the COMSOL Multiphysics 6.1 software. Rapid prototyping was performed on PMMA sheets using laser machining technique to verify the design concept; however, examination under an optical microscope exposed machining issues such as poor dimensional accuracy, profile deformation, and low surface quality. Simulation studies showed the final concentration of 6X can be obtained with the maximum length of the SV-PLC. The incident light angular study showed <10 % OE drop for incident angles less than 15°, and a maximum drop of 30 % for an incident angle of 23.5° (for 10X GC design). The OE results obtained from the experiment were around half the theoretical values. It suggests that a more refined optical fabrication process, like injection molding, should be considered for producing the skewed V-groove PLCs with better OE.

CRediT authorship contribution statement

Animesh M. Ramachandran: Writing – review & editing, Writing – original draft, Visualization, Validation, Methodology, Investigation, Formal analysis, Data curation, Conceptualization. **Adersh Asok:** Writing – review & editing, Visualization, Validation, Supervision, Software, Resources, Project administration, Methodology, Investigation, Funding acquisition, Formal analysis, Data curation, Conceptualization.

Declaration of competing interest

The authors declare the following financial interests/personal relationships which may be considered as potential competing interests: Authors report financial support and administrative support were provided by Council of Scientific & Industrial Research. Authors has patent pending to Council of Scientific & Industrial Research. If there are other authors, they declare that they have no known competing financial interests or personal relationships that could have appeared to influence the work reported in this paper.

Data availability

Data will be made available on request.

Acknowledgments

The authors acknowledge the Council of Scientific & Industrial Research, Govt. of India for the financial support provided for the FTT project MLP-0080 under the Energy & Energy Devices theme.

Appendix A. Supplementary data

Supplementary data to this article can be found online at https://doi.org/10.1016/j.rineng.2024.102923.

References

[1] L. Mehigan, J.P. Deane, B.P.O. Gallachóir, V. Bertsch, A review of the role of distributed generation (DG) in future electricity systems, Energy 163 (2018) 822–836, https://doi.org/10.1016/J.ENERGY.2018.08.022.
[2] M.R. Animesh, P. Corti, A. Asok, P. Bonomo, Indian BIPV Report 2022: Status and Roadmap, 2022, pp. 1–79. https://solarchitecture.ch/wp-content/uploads/2022/08/BIPV-Report-India_v01.pdf.
[3] Evolution of solar PV module cost by data source, 1970-2020 – charts – Data & Statistics - IEA, n.d. https://www.iea.org/data-and-statistics/charts/evolution-of-solar-pv-module-cost-by-data-source-1970-2020. (Accessed 7 May 2024).
[4] V. Benda, Photovoltaics, including new technologies (thin film) and a discussion on module efficiency, futur, Energy Improv. Sustain. Clean Options Our Planet. (2020) 375–412, https://doi.org/10.1016/B978-0-08-102886-5.00018-9.
[5] H.F. Yu, M. Hasanuzzaman, N.A. Rahim, N. Amin, N. Nor Adzman, Global challenges and prospects of photovoltaic materials disposal and recycling: a comprehensive review, Sustainability 14 (2022), https://doi.org/10.3390/su14148567.
[6] A. Ejaz, H. Babar, H.M. Ali, F. Jamil, M.M. Janjua, I.M.R. Fattah, Z. Said, C. Li, Concentrated photovoltaics as light harvesters: outlook, recent progress, and challenges, Sustain. Energy Technol. Assessments 46 (2021) 101199, https://doi.org/10.1016/J.SETA.2021.101199.
[7] E. Bellos, C. Tzivanidis, A review of concentrating solar thermal collectors with and without nanofluids, J. Therm. Anal. Calorim. 135 (2019) 763–786, https://doi.org/10.1007/s10973-018-7183-1.
[8] M. Ghodbane, D. Benmenine, A. Khechekhouche, B. Boumeddane, Brief on solar concentrators: differences and applications, Instrum, Mes. Metrol. 19 (2020) 371–378, https://doi.org/10.18280/I2M.190507.
[9] V. Panchenko, A. Izmailov, V. Kharchenko, Y. Lobachevskiy, Photovoltaic solar modules of different types and designs for energy supply, Int. J. Energy Optim. Eng. 9 (2020) 74–94, https://doi.org/10.4018/IJEOE.2020040106.
[10] A. Arabkoohsar, G. Xie, J. Wei, A. Asok, A. Behzadi, O. Mahian, Perspectives and review of photovoltaic-thermal panels in net-zero energy buildings, J. Therm. Anal. Calorim. 147 (2022) 8621–8630, https://doi.org/10.1007/S10973-021-11191-6.
[11] S. Castelletto, A. Boretti, Luminescence solar concentrators: a technology update, Nano Energy 109 (2023) 108269, https://doi.org/10.1016/J.NANOEN.2023.108269.
[12] M.A. Ferrara, F. Borbone, G. Coppola, Holographic optical lenses recorded on a glassy matrix-based photopolymer for solar concentrators, Photonics 8 (8) (2021) 585, https://doi.org/10.3390/PHOTONICS8120585, 2021) 585.
[13] W. Iqbal, I. Ullah, S. Shin, Optical developments in concentrator photovoltaic systems—a review, Sustainability 15 (2023), https://doi.org/10.3390/su151310554.
[14] M. Carlini, S.J. McCormack, S. Castellucci, A. Ortega, M. Rotondo, A. Mennuni, Modelling and numerical simulation for an innovative compound solar concentrator: thermal analysis by FEM approach, Energies 13 (2020), https://doi.org/10.3390/en13030548.
[15] F.L. Rashid, M.A. Al-Obaidi, A.J. Mahdi, A. Ameen, Advancements in Fresnel lens technology across diverse solar energy applications: a comprehensive review, Energies 17 (2024), https://doi.org/10.3390/en17030569.
[16] J.S. Price, X. Sheng, B.M. Meulblok, J.A. Rogers, N.C. Giebink, Wide-angle planar microtracking for quasi-static microcell concentrating photovoltaics, Nat. Commun. 6 (2015) 6223, https://doi.org/10.1038/ncomms7223.
[17] N. Chen, X. Zhang, Y. Bai, H. Zhang, Environmental friendly PV power plant, Energy Proc. 16 (2012) 32–37, https://doi.org/10.1016/J.EGYPRO.2012.01.007.
[18] Lumiduct | wellsun, n.d. https://www.wellsun.nl/lumiduct. (Accessed 2 September 2024).
[19] J.H. Karp, E.J. Tremblay, J.E. Ford, Planar micro-optic solar concentrator, Opt Express 18 (2010) 1122–1133, https://doi.org/10.1364/OE.18.001122.
[20] A.C. Wei, Z.R. Chen, J.R. Sze, Planar solar concentrator with a v-groove array for a side-absorption concentrated photovoltaic system, Optik 127 (2016) 10858–10867, https://doi.org/10.1016/J.IJLEO.2016.08.045.
[21] P. Xie, H. Lin, Y. Liu, B. Li, Total internal reflection-based planar waveguide solar concentrator with symmetric air prisms as couplers, Opt Express 22 (2014) A1389–A1398, https://doi.org/10.1364/OE.22.0A1389.
[22] M. Buljan, J. Mendes-Lopes, P. Benítez, J.C. Miñano, Recent trends in concentrated photovoltaics concentrators' architecture, J. Photonics Energy. 4 (2014) 40995, https://doi.org/10.1117/1.JPE.4.040995.
[23] S. Bouchard, S. Thibault, Planar waveguide concentrator used with a seasonal tracker, Appl Opt Vol 51 (28) (2012) 6848–6854, https://doi.org/10.1364/AO.51.006848, 51:6848–54.
[24] M.C. Chien, Y.L. Tung, C.H. Tien, Ultracompact backlight-reversed concentration optics, Appl Opt Vol 48 (21) (2009) 4142–4148, https://doi.org/10.1364/AO.48.004142, 48:4142–8.
[25] D. Moore, G. Schmidt, B. Unger, Concentrated photovoltaics stepped planar light guide. https://doi.org/10.1117/12.877725, 2010.
[26] J.R. Ong, H.S. Chu, C.E. Png, K. Ong, L.K. Bera, Planar micro-optic solar concentrator for natural daylighting systems in tropics. 2016 Asian Conf Energy, Power Transp Electrif ACEPT 2016, 2017, https://doi.org/10.1109/ACEPT.2016.7811514.
[27] N.H. Vu, T.T. Pham, S. Shin, Large scale spectral splitting concentrator photovoltaic system based on double flat waveguides, Energies 13 (2020) 2360, https://doi.org/10.3390/EN13092360, 2020;13:2360.
[28] V. Zagolla, D. Dominé, E. Tremblay, C. Moser, L.H. Slooff, E.E. Bende, et al., Self-tracking solar concentrator with an acceptance angle of 32, Opt Express 22 (S7) (2014) A1880–A1894, https://doi.org/10.1364/OE.22.0A1880, 22:A1880–94.
[29] J. Kim, J. Lee, R. Dhakal, Bio-inspired thin and flat solar concentrator for efficient, wide acceptance angle light collection, Appl Opt Vol 53 (2) (2014) 306–315, https://doi.org/10.1364/AO.53.000306, 53:306–15.
[30] C.-H. Kuo, T.-C. Teng, Y.-J. Li, Planar solar concentrator composed of stacked waveguides with arc-segment structures and movable receiving assemblies, Opt Express 28 (23) (2020) 34362–34377, https://doi.org/10.1364/OE.405909, 28: 34362–77.
[31] John Paul Morgan, Morgan Solar Inc, Light-guide Solar Panel and Method of Fabrication Thereof, US Patent 7873257B2, January 18, 2011.

[32] What we presented at CPV-7: the gen 3 sun simba optic | the unofficial morgan solar weblog, n.d. https://morgansolar.wordpress.com/2011/04/27/what-we-presented-at-cpv-7-the-gen-3-sun-simba-optic/. (Accessed 2 September 2024).
[33] A.M. Ramachandran, S.M. S, A.S. Thampi, M. Singh, A. Asok, A comprehensive review on optics and optical materials for planar waveguide-based compact concentrated solar photovoltaics, Results Eng 16 (2022) 100665, https://doi.org/10.1016/J.RINENG.2022.100665.
[34] T. Ta Ner, A.S. Dalkilic, A feasibility study of solar energy-techno economic analysis from aksaray city, Turkey, J. Therm. Eng. 3 (2017), https://doi.org/10.18186/JOURNAL-OF-THERMAL-ENGINEERING.331756, 1–1.

Results in Engineering 16 (2022) 100665

Contents lists available at ScienceDirect

Results in Engineering

journal homepage: www.sciencedirect.com/journal/results-in-engineering

A comprehensive review on optics and optical materials for planar waveguide-based compact concentrated solar photovoltaics

Animesh M. Ramachandran [a,b], Sangeetha M. S [a,b], Adhithya S. Thampi [a,b], Manjit Singh [a,b], Adersh Asok [a,b,*]

[a] Photosciences and Photonics, Chemical Sciences and Technology Division, CSIR-National Institute for Interdisciplinary Science and Technology (NIIST), Thiruvananthapuram, Kerala 695 019, India
[b] Academy of Scientific and Innovative Research (AcSIR), Ghaziabad 201002, India

ARTICLE INFO

Keywords:
Planar waveguide
Planar light concentrator
Solar concentrator
Geometric optics
Diffraction optics
Luminescent solar concentrators
Concentrated photovoltaics
Building integrated photovoltaics
Micro-optics

ABSTRACT

In recent years, the technology of waveguide-based planar solar concentrators has been getting more attention in the Concentrated Photovoltaics (CPV) sector due to its compact design and performance versatility and its extended potential applicability from large power plants to built environments, such as Building Integrated Photovoltaics (BIPV). Within the last two decades, geometric design-based Planar Light Concentrator (PLC) and diffraction grating-based PLC have been developed with versatile design architectures along with luminescent PLC, which relies primarily on the development of concerned luminescent optical materials. However, congregating and evaluating the technical advancement gained in the field seems challenging due to the segregated state-of-the-art approaches. Hence, this review attempted to organise the present state of waveguide-based PLC in the frame of reference of PLC optics and optical material design. A systematic comparison of optics and optical material design parameters and the merit of the different PLC systems have been explored within this review to serve as a ready reference for its adoption to develop compact planar waveguide-based CPV systems.

1. Introduction

Being the most abundant natural source of energy, solar energy is considered the future of the global renewable energy sector. However, unlike direct utilisation of solar energy (for example, daylighting applications), energy converted utilisation of solar energy is limited to the low energy density of input solar radiation for the required conversion, which can be either thermal or electrical [1]. With the global urbanisation expansion, the area utilisation of these solar power conversion systems and their environmental impacts is also becoming a major concern [2–4]. The most straightforward approach that can be adopted to address this issue is concentrating solar radiation on a finite area using techniques of optical light concentration [5–7].

Through the ages, the designs for solar light concentration evolved from imaging optics (mirrors and lenses) [6,8] to modern planar Fresnel optics [9,10]. However, the conventional optics systems suffer from bulkiness and cost-effectiveness due to the large optics elements and focal length of light concentration, which in turn increase the mounting cost. Later, planar optics-based lens and mirror systems were introduced, which reduced the system's volume and thereby offered a compact and slim design [9,11,12]. Reforming the designs further with multi-optical light concentrating elements largely reduced the system volume [13–16]. However, the collection of energy from multi-point became a major concern for the designs. Also, the system size is much larger than the optics size due to the concerns of focal length. In this regard, waveguide-based planar light concentrator (PLC) has evolved as the best solution, which enables a single point of energy collection, dispersed light collection from the waveguide, and reduced sizing of the whole light concentrating system [17,18].

Recently, the PLC technology has been well acknowledged globally, and many research efforts have been put forward to develop new designs and material solutions, indicating its prospect for CPV technology. Recognising its importance, the US Department of Energy acknowledged the potential of waveguide-based PLC through the Advanced Research Projects Agency-Energy (ARPA-E) project in 2016 [19]. Within the last two decades, the field of waveguide-based PLC evolved from geometric

* Corresponding author. Photosciences and Photonics, Chemical Sciences and Technology Division, CSIR-National Institute for Interdisciplinary Science and Technology (NIIST), Thiruvananthapuram, Kerala 695 019, India.
E-mail address: adersh.asok@niist.res.in (A. Asok).

https://doi.org/10.1016/j.rineng.2022.100665
Received 8 June 2022; Received in revised form 2 September 2022; Accepted 19 September 2022
Available online 4 October 2022

optics integration to optical material integration, such as luminescent solar concentrators (LSC [20,21]), and nano-design solutions for diffraction-based PLC [22]. The utilisation of waveguide-based PLC for CPV has huge applicability due to its lower cost per energy.

Different types of solar cells, including silicon, thin films, and multi-junction cells, were utilised for CPV systems. Recently CPV systems with multi-junction solar cells are gaining more attention due to its durability and superior performance at high temperatures [23]. SunSimba of Morgan Solar was one of the commercialised planar waveguide-based PLC that utilise geometric optics designs [24,25]. The unique design structure of waveguide-based PLC can be explored not only in large power plants, but also in the BIPV segments. Because of the compact flat design and aesthetically appealing structures, the adaptability of waveguide-based PLC has huge potential in the BIPV sector in developing energy-generating cladding, roof, glazing and shading elements. In 2017, SPOTlight Lumiduct (developed through the collaboration of Morgan Solar and Wellsun), a BIPV shading device (with waveguide based PLC act as both shading and CPV system) has been successfully demonstrated in commercial scale, clearly indicating the potential of such BIPV systems [26,27].

Replacement of existing BIPV products with CPV-based BIPV elements can greatly reduce the total cost by reducing the consumption of PV material, which is very prominent in existing BIPV systems. However, the low solar acceptance angle of such geometric optics-based systems creates the requirement of sun tracking, which in turn reduces its applicability in built environments. Rather than using an optics design system, a luminescent material-based waveguide LSC CPV system is a direct approach to the problem. Simple LSC-based CPV is now becoming a popular BIPV glazing solution, with more aesthetic diversity compared to existing systems and an additional prospectus of visible light selectivity and transmissivity [28–30]. The technological advancement of LSC was majorly focused on developing the key luminophore as the optical materials, which range from material distinctions of organic and inorganic materials to their hybrids [31–33]. Vigorous studies have been conducted in the area, however, the final system efficiency is the major concern when compared with other CPV technologies. Combined approaches are also explored in the field to enhance the output or provide additional functionalities [34].

However, extending CPV systems from large power plants to BIPV systems requires vigorous optics design and optics material innovations or in combination with appropriate systems engineering to cater to the elemental requirements without compromising the system efficiency. The indicated fact seems to be knotty without extracting the existing knowledge base and status. Conglomerating the state-of-the-art technologies and approaches exclusive to planar waveguide-based CPV technologies seems challenging but essential for the sector. Realising this, the present review discusses the different approaches that have been introduced in the field of waveguide-based PLC, focusing on drawing comparisons. The importance of optics and optical materials can be substantially perceived within the scope of this review. The review is expected to mark its impact on the future of renewable energy with a perspective of efficient energy utilisation, both for large solar power plants and its adaptability in built environments.

2. Waveguide-based planar light concentrator

Waveguide-based PLC essentially consists of a planar (shape can be extended from flat plate to circular, etc., with regular or irregular cross-section) light guiding element, enabling light transport through reflection at surfaces through total internal reflection (TIR) or mirror reflection. The condition of light transport is determined by the primary optics, which enables the amount and nature (spectral selection) of light output, which is collected from the lateral face. The general schematic of waveguide-based PLC is shown in Fig. 1. Depending on the primary

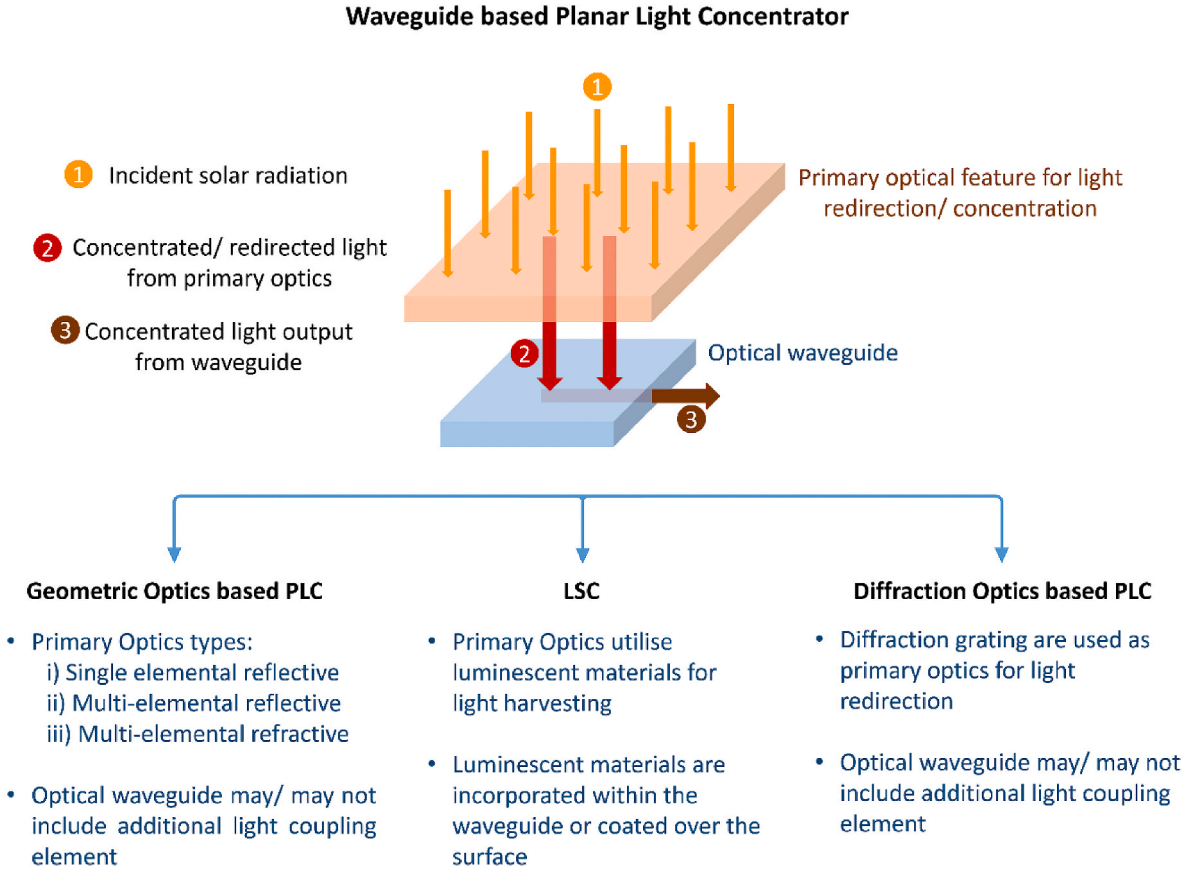

Fig. 1. Representative scheme of waveguide-based planar light concentrator with its classification.

optics, they are classified as geometric optics-based PLC (which utilises reflective and refractive elements for light concentration and is coupled to the waveguide), LSC (which utilises luminescent molecules for light concentration with spectral selectivity), and diffraction optics based PLC (which use diffraction gratings for light redirection and spectral selection).

The parameters defining the merit of waveguide-based PLC are:

1. Concentration ratio (or) geometric concentration (GC): This is a direct indication of the system's general design merit. It is the ratio of the inlet aperture of primary optics to the concentrated light area (output plane), or PV cell area.

$$GC = \frac{inlet\ aperture\ area}{output\ area}$$

2. Optical efficiency (OE): This is a merit value that determines how much light energy (for the concerned spectral range) is transported from the inlet aperture to the final output area. Optical efficiency encompasses the merits of different optical elements, optics material efficiency, and system fabrication efficiency. The product of GR and OE gives the final optics concentration factor.

$$OE = \frac{\int_{\lambda_{min}}^{\lambda_{max}} E_{out}(\lambda).d(\lambda)}{\int_{\lambda_{min}}^{\lambda_{max}} E_{in}(\lambda).d(\lambda)}$$

E_{out} (λ) measures the output energy of the photons that can be obtained from the output plane and E_{in} (λ) measures the input energy of the system. λ_{max} and λ_{min} denote the maximum and minimum wavelength of concerned spectral coverage.

3. Acceptance angle: This is a merit value that determines the performance of the CPV system with seasonal changes of solar angle. It is the angular span (about an axis) within which the system performs with a minimal percentage (usually taken as 90%) of the maximum optical efficiency.
4. Spectral selectivity: Unlike geometric optics-based PLC, LSC and diffraction grating-based PLC can provide spectral selectivity of the concentrated light, which is matched with the spectral range of the PV material. This prospectus can offer additional functionalities for the system like UV or NIR screening, visible light transmission, etc.
5. Spectral and spatial uniformity of concentrated light: Uniformity of the output radiation is also a major concern in CPV systems, as non-uniformity in the intensity and spectral coverage on PV can subside cell efficiency.

The review of the design and performance of different waveguide-based PLC has been conducted and presented below.

2.1. Geometric optics-based PLC

In geometric optics-based PLC, the primary optics can redirect and concentrate light in planes of specific size and number using multi-modes of reflection, refraction, and total internal reflection. The initially concentrated/directed light can be either directed directly to the waveguide or can be directed to specific optical features inside/outside the waveguide, for light redirection towards the plane of concentration. Planar light guiding element can be attached with the primary optics as a single unit, or can be separated with additional optical features of light transport. Guiding the light within the element can be achieved mostly with TIR, except for reflecting surfaces. The definitive optical design vouches for the geometric concentration factor, optical efficiency, and acceptance angle. Till now, many non-conventional geometric solar concentrators with planar light guiding have been designed and explored, especially in the last decade. The section provides an overall outline of the developments in geometric optics-based PLC, and the details are summarized in Table 1.

Based on the processes involved in the light concentration, geometric concentrators with planar light guiding can be classified mainly as 1) Single elemental reflective type, 2) Multi-elemental reflective type, 3) Multi-elemental refractive type, as explained below.

1) *Single elemental reflective type:* In this, reflective optics are incorporated within or outside the waveguide for light concentration/redirection to the waveguide. A reflective array of v-shaped grooves on a planar optical waveguide can be considered one of the most straightforward approaches for redirecting light to lateral directions. The reflection from the grooves can be either through reflective coatings or by TIR. An-Chi Wei et al. proposed a planar solar concentrator with reflective arrays of v-grooves placed at the bottom of an optical slab, and, in which, solar cells are positioned at edges, making a single element compact configuration [35]. The system (scheme as shown in Fig. 2a) essentially consists of an optically transparent material with a planar surface at the top and metal-coated reflective v-grooves at the bottom. Incident light falling on the system is reflected by the grooves and directed to the solar cells placed at the top portion of the lateral side of the concentrator, as shown in Fig. 2a.

A complete geometrical design for the specific PLC can be described based on the equations described below;

$$\theta_i = \frac{1}{2}\tan^{-1}\left(\frac{Q_i}{f - d/2}\right) \quad (1)$$

$$w_1 = 2d \sin\theta_i \quad (2)$$

$$s_{i+1} = \frac{(Q_i + w_i \cos\theta_i) w_i \sin\theta_i}{f - d/2 - w_i \sin\theta_i} \quad (3)$$

Where, the major design parameters are shown in Fig. 2c, and the design parameters concerned with the design for i^{th} groove are groove angle (θ_i), groove width (w_i), the vertical distance between the concentrator bottom and center of the solar cell (f), distance between the solar cell and the groove ridge (Q_i), and inter-groove distance between i^{th} and $(i+1)^{th}$ groove (s_{i+1}) for eliminating the subsequent refection of light from adjacent grooves. The concentrator is designed and fabricated (as shown in Fig. 2c) with PMMA (refractive index 1.507 ~ 1.483 in the range of wavelength 400 nm–1000 nm) as the transparent matrix and Aluminium and Silicon dioxide as reflective coatings with theoretical reflectance of 83.9%. The simulated ray tracing conducted for the fabricated design is as shown in Fig. 2d, using LightTools ray tracing software. The major design parametric limitation of v-groove PLC is the concentrator's aspect ratio, as there are no multiple reflections for guiding the light rays through the optical slab. Subsequently, this may yield a very high optical material requirement due to the higher width compared to the length of the system. The fabricated design shown in Fig. 2c has an incident aperture size of 30 mm × 30 mm and solar cell size of 30 mm × 5 mm, yielding a geometric concentration ratio of 5. The optical efficiency was expected to be 67.7% from the ray-tracing simulation, considering the reflection efficiency of the coating and Fresnel losses. However, the fabricated system showed a 50% optical efficiency when experimentally measured. This optical loss was attributed to fabrication inaccuracies like distorted valleys of grooves, the surface roughness of the optical materials used for optics matrix, other discrepancies such as light collimation of solar simulator, etc., as discussed in the article. Also, the acceptance angle for the desired

Table 1
Summary of review on different design configurations (optics and optics materials) of geometric optics-based PLC (in chronological order).

Reference, year	Research method E: Experimental S: Simulated	Optical material data	Structure form	Dimensions	Optical performance (OE/PCE (%)), GC	Acceptance angle (°)
Geometric Optics-based PLC P: Primary Optics; W: Waveguide; C: Light coupler						
[11,37,38], 2007	E	P: Acrylic W: Acrylic + Centre piece for light collection: Glass	P: Total internal reflecting surface (parabolic/cubic/ hyperbolic/flat) W: Wedge shaped	200 mm × 200 mm square (Generation 2) 200 mm hexagonal (Generation 3)	GC claimed: ~ 1000 X	±0.75 ±0.9
[39], 2010	E and S	P: BK7 glass W: F2 glass P: F/1.1 lens array W: BK7	P: Hexagonal lens array W: Slab waveguide C: Air prism	P: 2.3 mm diameter F/1.1 hexagonal lens array W: 75 mm long by 1 mm thick	OE: 81.9 GC: 300 X OE: 32.4 GC: 37.5 X	±1
[43], 2010	S	P, W: Refractive Index 1.51 Low index layer Refractive Index 1.38	P: Staggered microlens array W: Stepped guide layer + Low index layer	P: Lens aperture of 3 mm × 1.5 mm W: Thickness of 2.42 mm	GC: 112.5 X	±1
[41], 2012	S	P: f/1.2 lens array W: Refractive Index 1.7	P: Cylindrical lens array W: Planar waveguide C: Air prism	P: Lens pitch 2.6 mm W: 10.4 mm × 30 mm, core thickness of 1 mm C: width of 1.5 mm	OE: 80	North-South axis: ± 9 East-West axis: ±54
[42], 2014	S	P: BK7 glass W: F2 glass	P: Array of cylindrical lens W: Planar waveguide C: Air prism	P: Lens pitch - 5 mm Lens F/#: 1.81 Air-gap thickness of 0.2 mm W: Thickness of 1 mm C: Width of 90 μm	OE: 70 GC: 50 X	±7.5
[46], 2014	E and S	P: Plastic W: Fused Silica Actuator: Paraffin wax	P: Aspheric lens pair W: Planar waveguide + dichroic membrane + actuation element	53 × 53 mm^2	OE: 2.8 GC: 8 X (Simulated) GC: 3.5 X (Experimental)	±16 (Experimental)
[47], 2014	S	P: Polymer W: Polymer	P: Cylindrical microlens W: Curved light guide	20 cm long, 1.1 cm thick	GC: 39 PCE: 20% (module efficiency) (Si based solar cells)	±15
[36], 2015	E	P: Glass coated with silver W: Caged air	P: Reflector (square, hexagonal, circular) W: Cage waveguide	–	Hexagonal reflector showed better light transmission to waveguide (used GC: 6 X)	±1
[35], 2016	E and S	P, W: PMMA C: Al and SiO_2 coated reflective grooves	V grooved single elemental	30 × 30 mm^2 with solar cell size of 30 × 3 mm^2	GC: 5 X PCE: 24.8 and 25.1 at the two ends of concentration (used Single-junction GaAs solar cells)	2
[44], 2017	Trigonometric analysis and simulation	P: PMMA W: PMMA	P: Square lens array W: Planar waveguide C: Air prism + fibre optic ribbon for daylighting	P: Lens array period of 2 mm W: Thickness of 2 mm C: Prism base width of 80 μm	OE: changed from 1 to 0.1 with incident angle direction of 0° to 40° GC: Study conducted for varied concentrator length	0.38 (trigonometric analysis)
[18], 2020	S	P, C, W, Compound parabolic collector (CPC): PMMA P, CPC: PMMA C, W: NBK7 glass	P: Sheet collector with arc-segment lens structures W: Concentric light guide channel with additional CPC C: Embedded prism	Optimised mode with Length: 413.7 mm Width: 300 mm Height: 25 mm Length of CPC: 21.2 mm	OE: 87.6 GC: 739 OE: 87.5 GC: 738	0.35 to −1.65 −12 to 12 In two directional axis

maximum range of optical efficiency is analysed with ray tracing, showing a low acceptance angle of 2°, indicating the limitation of v-groove designs. The major advantage of these types of design is that the whole system is single elemental, eliminating the need for elemental inter-alignment.

Another approach to fabricate a single elemental reflecting waveguide-based PLC is by creating a light-trapping layer embedded with solar cells. Lourens van Dijka et al. utilised a concentrator array as an external light trapping unit with solar cells [36]. The concentrator is a regular shaped reflecting surface with a metallic coating, that concentrates and directs light to the solar cells. The rays that are reflected from the solar cells are reflected back to it from the bottom of the concentrator, making a cage for light trapping. A schematic of the design with a parabolic reflector as concentrating element is shown in Fig. 3a. The analysis was carried out with different concentrator geometries of square, hexagonal, circular, and parabolic, with the same geometric concentration factor of 6X (photographs of the prototype are shown in Fig. 3b), which was fabricated through 3D printing. The printed parts are chemically polished and coated with silver to yield the reflecting surface. The theoretical analysis shows that circular concentrators in the hexagonal array have better optical performance, i.e. light transmissivity towards the solar cell, especially at higher concentration ratios.

The critical parameters for the external light trapping are the transmittance of the concentrator, the number of reflections that can occur, the reflectivity of a solar cell, and the reflectivity of the cage surface. The performance of the optical light trap is represented as absorptance of the solar cell (A_T),

$$A_T = T_C \cdot \frac{A_{SC}}{1 - R_{SC}\left(1 - C^{-1}\right)R_{cage}} \quad (4)$$

where T_C is the concentrator transmittance, A_{SC} is the absorbance of the

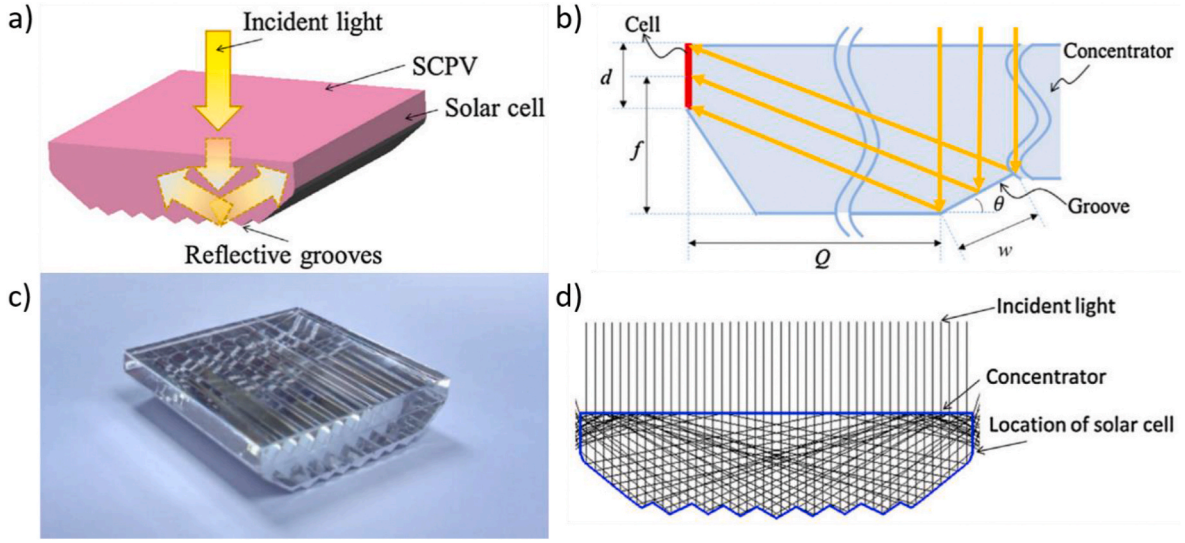

Fig. 2. a) Schematic of the v-groove PLC; b) Schematic of ray trajectories of light rays incident on the v-groove surface; c) Photograph of fabricated v-groove; d) Ray tracing conducted on the designed v-groove PLC using LightTools ray tracing tool. Source: Reproduced with permission from Ref. [35]. Copyright © 2016, Elsevier.

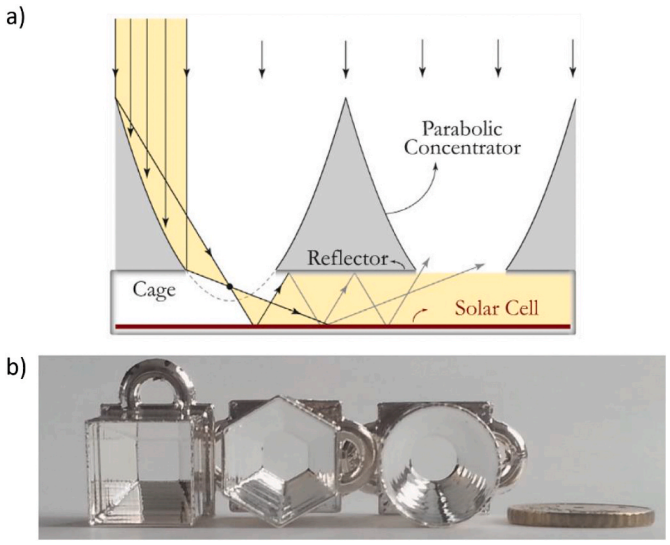

Fig. 3. a) Schematic of the reflective and cage type PLC with a parabolic surface as the reflector; b) Fabricated square, hexagonal and circular reflector, with a silver coating (10 euro cent coin placed at right for size comparison). Source: Reproduced with permission from Ref. [36]. Copyright © 2015, The authors, Published by Elsevier.

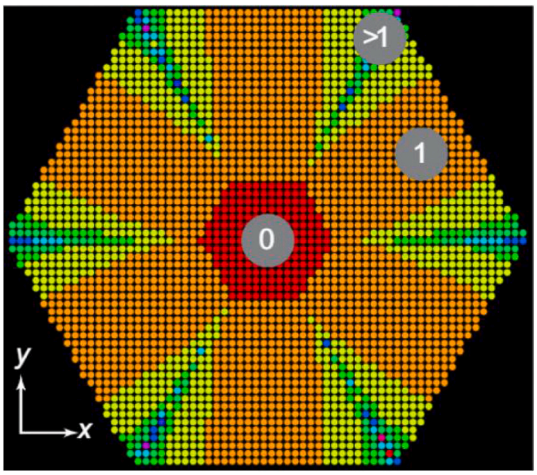

Fig. 4. The number of reflections occurred per ray for 3000 rays in a hexagonal light concentrator. The position of rays is considered as before the ray release; the range of reflections is 0–13 represented as the hue of the dots. Reproduced with permission from Ref. [36]. Copyright © 2015, The authors, Elsevier.

solar cell, R_{SC} and R_{cage} are the reflectance of the solar cell and cage, respectively.

The design, optical finish, and reflectivity of the concentrator surface determine the concentrator's optical efficiency, i.e. the transmissivity towards the solar cell. Fig. 4 represents the number of reflections that occurred by rays that are transmitted through a hexagonal concentrator of 15X concentration, where the hue of the colour code representation ranges from 0 to 13 times of reflection.

Experimentally, the utilisation of the external light trapping mechanism showed a path length enhancement of more than twice, yielding an improvement of up to 69% for the external quantum efficiency in an organic solar cell, with an increase of 13% in short circuit current.

Sun Simba concentrator of Morgan Solar is one of the commercially extended single elemental reflective PLCs [37]. This light concentrating and guiding system is made with an optically transparent material like acrylic, consisting of two layers, as shown in Fig. 5 (Fig. 5a shows the photographs of the Sun Simba concentrator, and Fig. 5b shows the typical design structure of the concept and the ray tracing of it) [11,37]. However, the system can be considered as a single reflecting PLC entity, as the layers are embedded together. The first layer is a light-insertion layer, where light is reflected and concentrated as an output to the second stage of the light-guiding layer. The light output aperture from the first layer can be modified with different geometric features of reflecting layer like parabolic, cubic, hyperbolic, flat, etc. The light guiding layer can be flat or wedge shaped to collect the light rays and transport it to the centre of the system, where the solar cell is attached. In wedge-shaped guiding layers, the thickness of the light guide increases near the centre, which allows light to more efficiently couple towards the center without interacting with injection faces closer to the center. The whole design is structured as concentric circles towards the centre. As it is a single elemental reflective PLC design with centre point light concentration, it faces a low solar acceptance angle, and hence requires a precise 2-axis tracking system. However, this limitation can be compensated with a very high light concentration ratio and cheaper manufacturing techniques employed. Morgan Solar claims an

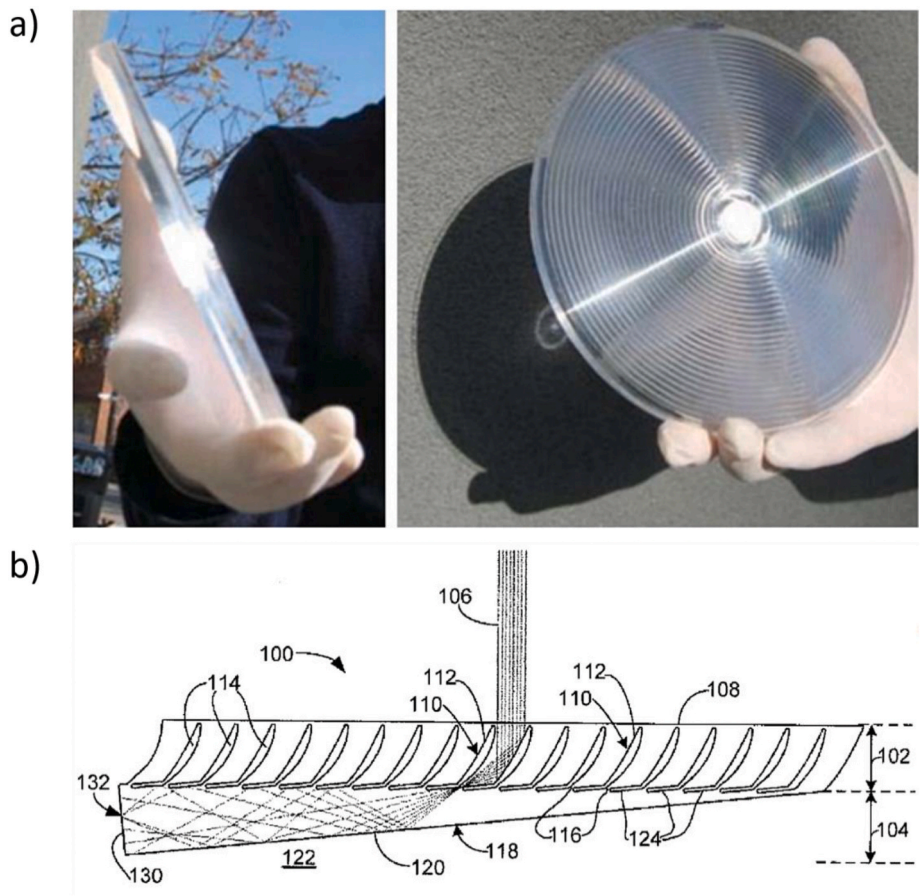

Fig. 5. a) Photographs showing solar concentration in Sun Simba concentrator of Morgan Solar. Source: Reproduced with permission from Ref. [11]. Copyright © 2014, © The Authors. Published by SPIE; b) Ray tracing in a typical single elemental reflective type PLC design by Morgan Solar showing the concentration of light to the lateral direction. Source: [37].

acceptance angle of ±0.9° and a concentration of 1000 suns with combined acrylic and glass optical structure [38].

2) *Multi-elemental reflective type*: In this type, reflective surfaces are used for light redirection/concentration, which is optically distant from the waveguide, making a multi-elemental waveguide-based PLC. Much similar to the Sun Simba concentrator, a two-staged planar solar concentrator was presented by Kuo et al., which consists of transparent waveguide sheets stacked with an array of arc segment structures (i.e., a sheet collector with arc-segment structures (SCAS)), as shown in Fig. 6a [18]. An appreciable coupling efficiency with high concentration ratios and wide angular tolerance is obtained by the arc segment structures, which are carried by the stacked waveguide sheets as TIR collectors in the first stage. When light enters arc segment structures, it undergoes reflection and concentrates the light to the sheet waveguide below, where the light undergoes more of a skewed propagation. The second stage (movable) of the system is to collect the concentrated light through light guiding channels (LGC) and subsequently focusing it on the solar cell placed at the end using a compound parabolic collector (CPC) (shown in Fig. 6b).

Additionally, embedded prisms of higher refractive index (taken as 1.77) are also used to reduce the skewness of the incoming light for better optical efficiency and reduced losses. The whole design is structured as a concentric circle towards the center. The incident angle has been varied from 0° to 12° to attain the angle distribution of light within ±15° for uniform light distribution to the solar cells. Average optical efficiency of 0.87 and 738X concentration ratio was obtained from the simulation results of the designed system.

3) *Multi-elemental refractive type:* Generally, multi-elemental refractive type PLC systems consist of an array of convergent lenses (micro lenses), the output light rays from the lenses are connected optically with a light dispersive/coupling element (gratings, prisms, or scattering surfaces) in a light-guiding layer. The multiple light dispersive elements (usually air prisms) in the light-guiding layer, positioned in line with the incoming concentrated light, disperse the light and are guided by the guiding layer to the solar cell attached to the lateral face. By using planar slab waveguides, the length of the concentrator can be extended unlimited, but the system suffers from decoupling losses that can occur at the subsequent coupling elements (as shown in Fig. 7b) [39]. The decoupling loss is directly correlated to the coverage area of the coupling element. In order to eliminate the decoupling losses, the guiding layer can be converted to wedge-shaped, eliminating the process of multiple TIR within the guiding layer (Fig. 7a) [39,40]. However, the aspect ratio of wedge-shaped guiding layer limits its usage for longer-length concentrators.

Fig. 8 shows the typical geometrical features of a micro lens-based PLC (with planar light wave guiding) system, where H and L are the width and length of the waveguide, P denotes the position of the lens, 2r is the lens diameter, φ is the ray propagation angle.

To calculate the total efficiency, equation (7) denotes the optical efficiency from input position P, which includes the back surface interactions, where C_{lens} is the concentration of the primary lens. Equation (6) includes the efficiency factor with Fresnel reflection loss (R) and

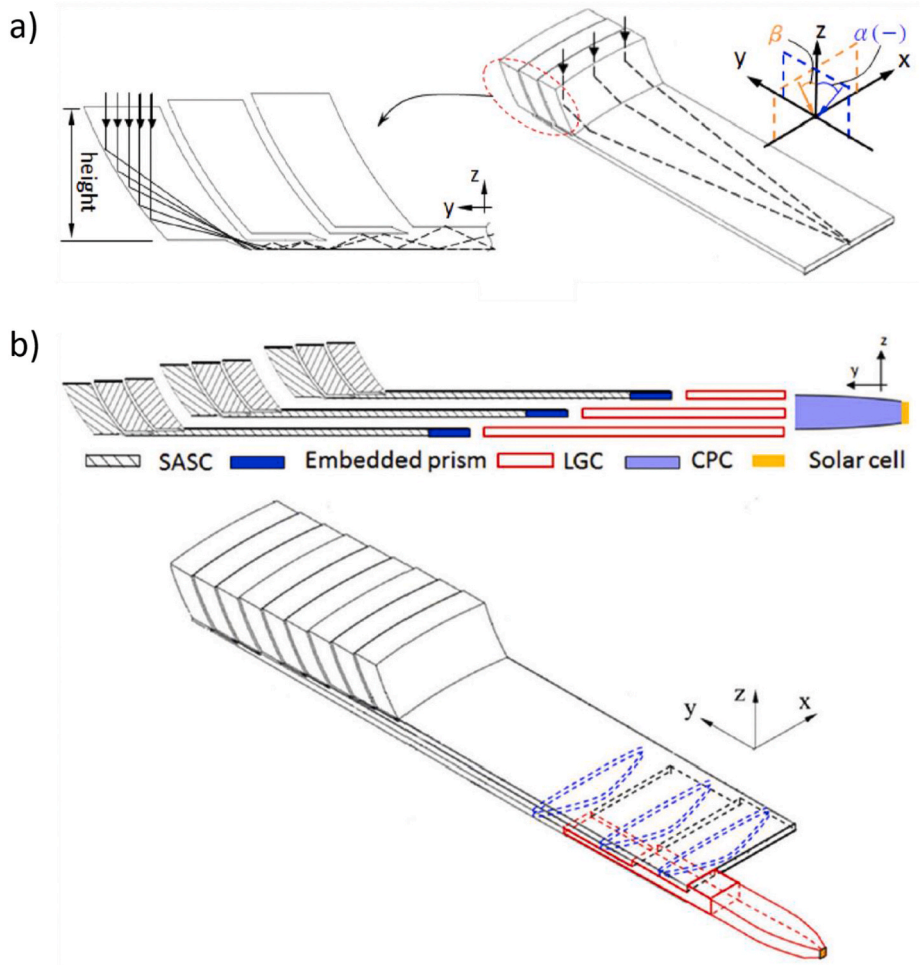

Fig. 6. a) 2D and 3D representative ray tracing in the PLC of sheet collector with arc-segment structures; b) Side view and perspective view of complete stacked up assembly of PLC with arc-segment structures (SASC), embedded prisms, light guide channels (LGC), compound parabolic collector (CPC), assembled with a solar cell. Source: Reproduced with permission from Ref. [18]. Copyright © 2020, Optical Society of America.

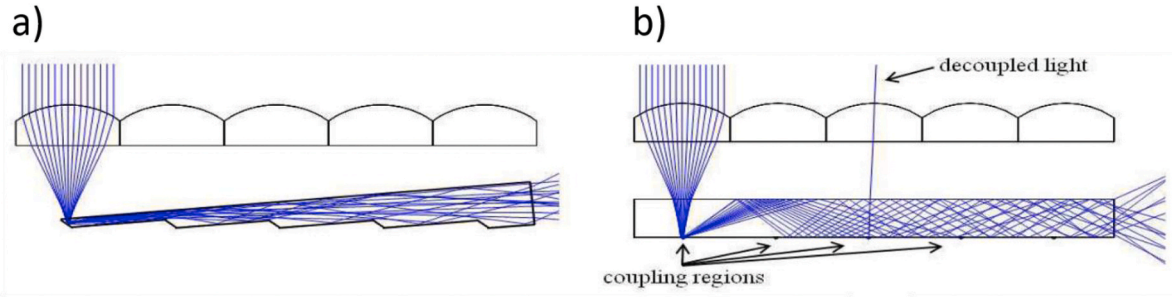

Fig. 7. Ray tracing in a refractive type PLC with a) wedge-shaped light guiding layer to avoid decoupling loss and (b) uniform planar light guiding layer showing decoupling loss. Source: Reproduced with permission from Ref. [39]. Copyright © 2010, OSA.

material absorption, where α is the absorption coefficient of the matrix material. Equation (5) denotes the total efficiency, integrated over all coupled ray angles confined within the waveguide. The equation denotes that the efficiency has a direct correlation with the width and length of the concentrator, i.e., a combination of higher length and width yields higher efficiencies.

$$\eta_{\text{decouple}}(\mathrm{P},\varphi) = \left(1 - \frac{1}{\mathrm{C}_{\text{lens}}}\right)^{\frac{\mathrm{P}\tan\varphi}{2\mathrm{H}}} \tag{5}$$

$$\eta_{\text{position}}(\mathrm{P},\varphi) = (1-\mathrm{R})\,\eta_{\text{decouple}}(\mathrm{P},\varphi)\exp\left(-\alpha \mathrm{P}\cos\varphi\right) \tag{6}$$

$$\eta_{\text{total}} = \frac{\sum_{\mathrm{P},\varphi}\int \eta_{\text{position}}(\mathrm{P},\varphi)}{(\mathrm{L}-\mathrm{r})/2\mathrm{r}},\ \mathrm{P} = \mathrm{r}, 3\mathrm{r}, 5\mathrm{r}, \ldots, (\mathrm{L}-\mathrm{r}) \Big/ 2\mathrm{r} \tag{7}$$

Eric J. Tremblay et al. fabricated 120° apex symmetric prisms to collect the rays coming out at 60° to the horizontal, making no shadowing effect with adjacent prisms [39]. Also, certain parts of rays deviating more from the primary lens optics undergo TIR and travel to the lateral face (Fig. 9a). For aligning the two optics, self-aligned fabrication technique was used, which utilises UV light that focuses

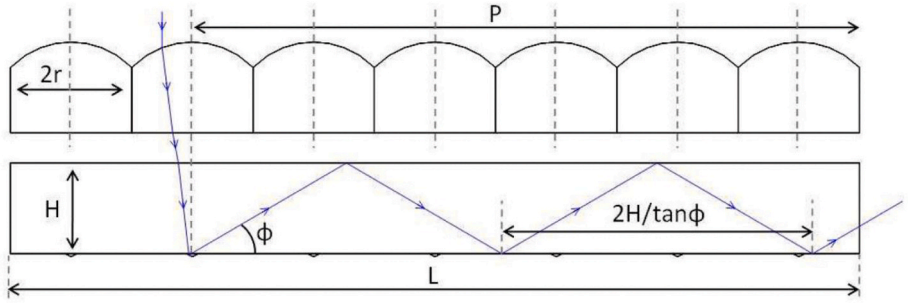

Fig. 8. Geometric features in a lens-based refractive type PLC. Source: Reproduced with permission from Ref. [39]. Copyright © 2010, OSA.

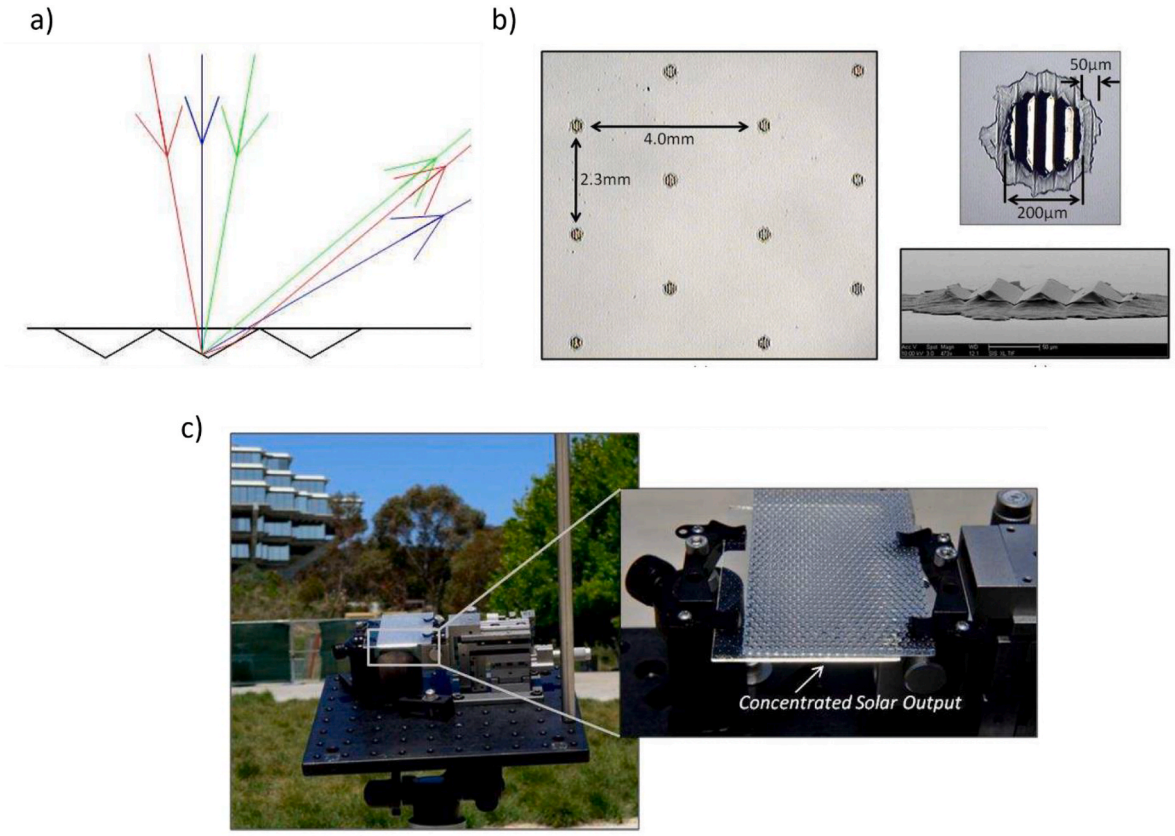

Fig. 9. a) Possible ray pathways in a 120° apex symmetric prisms showing maximum transport of light rays to lateral side; b) Optical and SEM images of 120° apex symmetric prisms fabricated through self-aligned fabrication technique (irregularities of 50 μm is shown, causing the optical losses); c) Photographs of prototyped refractive type PLC in outdoor settings showing light concentration when aligned properly at 90° to the sun. Source: Reproduced with permission from Ref. [39]. Copyright © 2010, OSA.

light from the primary spherical lens to cure the polymer prism, which is already embossed with the pattern. Thus the need for optical alignment is eliminated with the whole fabrication process. The fabricated prism is shown in Fig. 9b. Optimised designs showed a theoretical light concentration of 300X with an optical efficiency of 81.9%. Fig. 9c shows the prototype demonstration of a whole concentrator system having a light concentration of 37.5X and 32.4% optical efficiency, the observed low optical efficiency can be attributed to manufacturing defects resulting in optical defects and faults in the lens array. Since the whole system relies on the positioning of the lens prism alignment (requires <20 μm lateral alignment and <0.01° rotational accuracy for the designed 300X concentration), the design tends to make a low acceptance angle and requires precise 2-axis tracking.The requirement of precise alignment for such systems limits its applicability in large area optical concentrating systems and also for BIPV.

S. Bouchard et al. substituted the conventional spherical lens with a cylindrical lens, resulting in the reduction of the concentrator's cost of tracking by improving the acceptance angle in a single axis [41]. This also reduced the final geometrical concentration value. This design produces a compact, lightweight, and efficient concentrated photovoltaic system with uniform distribution of flux and shows the possibility of low-cost roll-to-roll production. The model showed a peak concentration level of 8.1X with an optical efficiency of 80%, by conducting ray tracing using LightTools, during the daytime from 8:30 a.m. to 4:30 p.m. The proposed concentrator shows an acceptance angle of ±9° on the North-South axis and ±54° on the East-West axis.

Peng Xie et al. also evaluated their cylindrical lens-based PLC design using the Zemax ray tracing tool [42]. The design of the concentrator is as shown in Fig. 10, in which the light guiding layer is embedded with an air prism at the top surface as the light coupling element, and it is separated from the lens array with an air gap. At a geometrical concentration ratio of 50, the suggested concentrator system achieved 70%

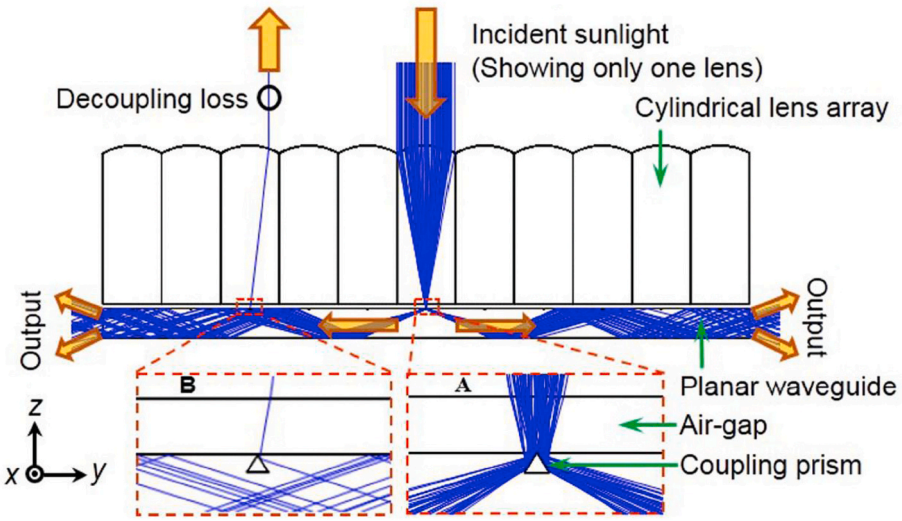

Fig. 10. Cross-section view of the planar waveguide solar concentrator with the cylindrical microlens as primary concentrator and air prism as a coupling element, showing the ray tracing of incoming rays in a lenslet. Insets show the light coupling in the air prism (right) and the decoupling effect occurring due to TIR from the subsequent air prism (left). Source: Reproduced with permission from Ref. [42]. Copyright © 2014, OSA.

optical efficiency and a 35X flux concentration ratio using the TIR-based air prism optical couplers. Further, an acceptance of 7.5° was obtained with the utilisation of a cylindrical lens as the primary concentrator.

Moore et al. presented a "stepped-shape" of injection facets (plane of couplers) based planar solar concentrator design with a major advantage of diminishing ray leakages from the waveguide, as shown in Fig. 11 (shows two subsequent layers) [43]. The simulated design was able to transport 90% of light to reach the PV cells without undergoing any loss and achieved a geometrical concentration of 112.5X.

Apart from CPV application, the appropriateness of usage of planar solar concentrators for the application in the natural daylighting system was investigated by Jun Rong Ong et al. [44]. The designed micro-optics solar concentrator is built up using a module of lens arrays and a waveguide of planar slab structure with a uniform cross-section (Fig. 12). The lens array concentrates light to the light couplers which are embedded on the waveguide's bottom surface, which subsequently redirects it to the optical fibres. Total internal reflection (TIR) is used to route the collected light into the planar waveguide, which is achieved by incorporating a layer between an array of lenses and a waveguide with a low index or air space. Roll-to-roll printing methods are compatible with the periodic array of lens and constant waveguide cross-sections. The major consideration in the design of a uniform concentrator cross section is the injection of light that is focused, which should have high efficiency with minimal decoupling losses when it propagates through the length. Plain void structures are adopted in the proposed design to avoid decoupling losses caused by coupling features when redirecting light.

A simple concentrating photovoltaic system with a Fresnel lens array and double waveguide was proposed by Ngoc Hai vu et al. [45]. The coupler prisms are coated with dichroic mirror coating for the reflection

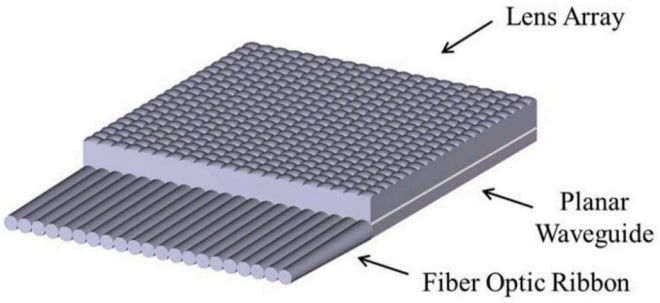

Fig. 12. Schematic of refractive type concentrator-based solar collector with lens array, planar waveguide, and fiber optic ribbon. Source: Reproduced with permission from Ref. [44]. Copyright © 2016, IEEE.

of light with varied energy bands. The array of Fresnel lens focuses the sunlight and reaches redirecting prisms through the upper waveguide which have the property of reflecting the middle band of the solar spectrum, which then propagates within the first waveguide and is transported to the solar cell (GaInP/GaAs dual junction solar cell). Subsequently, the transmitting lower energy band enters the second waveguide and is reflected by the dichroic mirror-coated prism at the second waveguide to redirect to the solar cell (GaInAsP/GaInAs dual junction solar cell) of different absorption ranges. The simulation result shows that the system design has an optical efficiency of 84.02% for the middle energy band of the solar spectrum and 80.01% for the low energy band. The system has an acceptance angle of ±0.5°.

Volker Zagolla et al. further improved the concept of refractive type PLC with the introduction of self-tracking within the system [46]. The

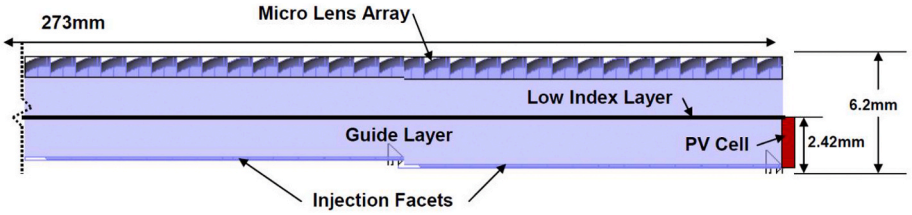

Fig. 11. Subsequent layers of stepped planar light guides, showing the offset of injection facets. Source: Reproduced with permission from Ref. [43]. Copyright © 2010, SPIE.

design has a dichroic membrane layer that separates the solar spectrum (the visible region is reflected, and NIR (>750 nm) is transmitted). The active component of the concentrator is the actuator, which has a metal array of holes filled with black paraffin wax, the dichroic membrane layer. The paraffin wax absorbs the transmitted IR part and expands when a phase change occurs, which contributes to the actuation. Upon melting of the paraffin wax, its expansion in an upward direction occurs thereby filling the air gap between the dichroic membrane and waveguide and converting it into a light coupler element The direction of the expansion is constrained only in one direction by the metal holes. The formed light couplers redirect the light into the planar waveguide and propagate via TIR and reach PV cells attached at its edge. The scheme of the design and different stages of the mechanism is as shown in Fig. 13. The demonstrated system shows an effective light concentration of 3.5X over 80% of the desired acceptance angle of ±16°.

For eliminating the need for positioning the primary lens optics and coupler, Jaeyoun Kim et al. proposed a curved light guiding layer connected optically with the multi-lens system through an optical funnel, as inspired from the ommatidium in the eye of insects [47]. The optimised design of the concentrator as shown in Fig. 14a can achieve a light concentration factor up to 39 with an acceptance angle of ±15° (the concentrator design considered was about 20 cm in length and thickness under 1.1 cm). Fig. 14b shows the light propagation with a normal and oblique angle of 40° in the designed concentrator. It has proven difficult to enhance both the angle of acceptance and the concentration factor in traditional flat concentrators. This challenge is overcome by this bio-inspired concentrator. The architecture and optical behaviour of ommatidium which is in the insect's compound eye led them to create a unique flat solar concentrator, where micro lenses act as a light-gathering element. Ommatidium of insects has a transparent cornea which acts as a lens, and a rod-like transparent cylindrical structure, which is the rhabdom. Collection of light along with focusing is done by lens and rhabdom act as a waveguide.

2.2. Luminescent solar concentrator (LSC)

A Luminescent Solar Concentrator (LSC) is a device that harvests light using a linear down-conversion/non-linear up-conversion process that uses luminophore materials that are either dispersed within or coated (with/without additional host material) over a transparent waveguide matrix. However, in practice, down-conversion-based LSC is primarily adopted to develop high-efficiency LSC-based CPV devices. The concept of utilising down conversion for LSC was first put forward by Weber and Lambe in the 1970s, and within the last two decades, further developments have been encountered with the new classes of luminescent and transparent host matrix materials [48,49]. In LSC, the transparent matrix serves as an optical waveguide for redirecting and concentrating solar radiation to the lateral face where a solar cell is attached. The approach of LSC-based PLC is mostly used for developing BIPV glazing elements. Since fluorescence is the major optical down conversion phenomenon utilised in LSC, in which highly emissive fluorophores are incorporated in the host matrix, it is also commonly termed as fluorescent concentrator. For an ideal case to attain near-unity conversion efficiency, the energy of emitted photons with high quantum efficiency should be slightly greater than the bandgap of the edge-located solar cell. During the course, LSC has gained significant attention as a key driver in the research and development of photovoltaic systems, owing to their improved spectral response, economical approach, and potential to offer enhanced power conversion efficiency (PCE) of solar cells [31,48–50].

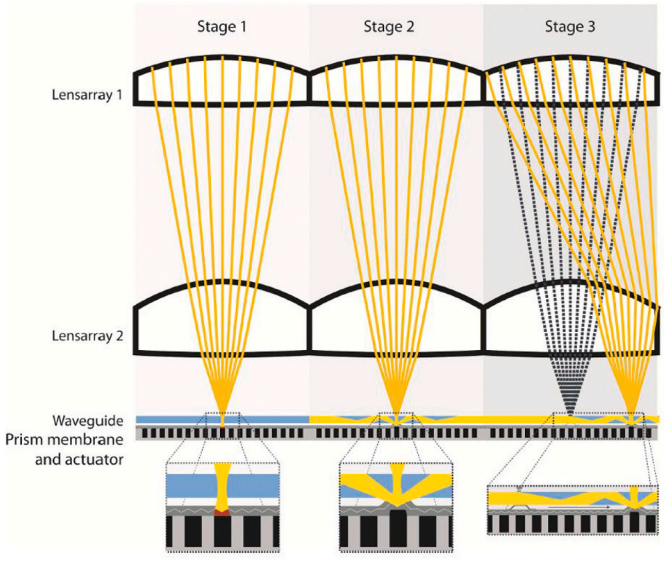

Fig. 13. Representation of the stages in self-tracking planar solar concentrator showing the mechanism. Stage 1: Splitting of rays by a dichroic mirror, paraffin wax absorbs transmitted light (>750 nm), Stage 2: At the melting point of the wax, it melts and expands, converting it into a coupler to the incoming light, Stage 3: Actuation mechanism happening at the different position according to the sun's position. Source: Reproduced with permission from Ref. [46]. Copyright © 2014, OSA.

In comparison with the non-concentrating PV systems, LSC eliminates the complexity of the adoption of efficiency boosting techniques such as optics and tracker systems and difficulties associated with the module assembly. This becomes possible due to the flexibility offered by the LSC, as it works under every solar angle and also collects diffuse light, thereby acting as an enabler for developing innovative technologies for building integrated applications. Further, the expensive PV material area can be reduced by increasing the concentration of luminophore or size of LSC, which should be optimised. In recent years, LSC acquired a unique position in the BIPV sector as a viable, promising solar technology for glazing elements, due to its lower cost and improved aesthetic values compared with existing glazing solutions [33]. The relatively low-cost transparent plastic matrix materials (like PMMA) can considerably reduce the area cost of the existing BIPV glazing solutions, offering a low cost per energy generation [49]. Hence, the LSCs evince as a revolutionary solar energy technology in the building architecture by facilitating semi-transparent, electrodeless PV glazing systems without diminishing the aesthetic value of the buildings and the standard of life of the indwellers. Large-scale applications, such as windows with coloured as well as transparent LSCs can be easily accommodated to add visual comfort or daylight inside the buildings accordingly. Accounting for these benefits and ease of 'invisible' integration of PV into urban structures to generate electricity and preserving the aesthetic and functional aspects, LSC can get wide public acceptance in the near future [32].

Working mechanism: The working mechanism of a typical LSC structure is shown in Fig. 15. The optical concentration of solar rays, both direct (R_1) and diffuse (R_2) light, falling on the LSC penetrates into the matrix and is captured by the luminophores. The excited luminophore isotropically re-emits radiation at a longer narrow band wavelength (down conversion). A part of the emitted rays is guided via TIR through the waveguide and concentrates into the edge-mounted PV cell through the optical coupling for electricity conversion (represented as G).

Efficiency parameters: Theoretical evaluation of LSC operations can be done by the following parameters [31]:

i. Geometric Gain (G_g): Gives the ratio of the top surface aperture area (A_{Apr}) to the total edge area of LSC enclosed by PV solar cell (A_{Edge}).

$$G_g = \frac{A_{Apr}}{A_{Edge}} \tag{8}$$

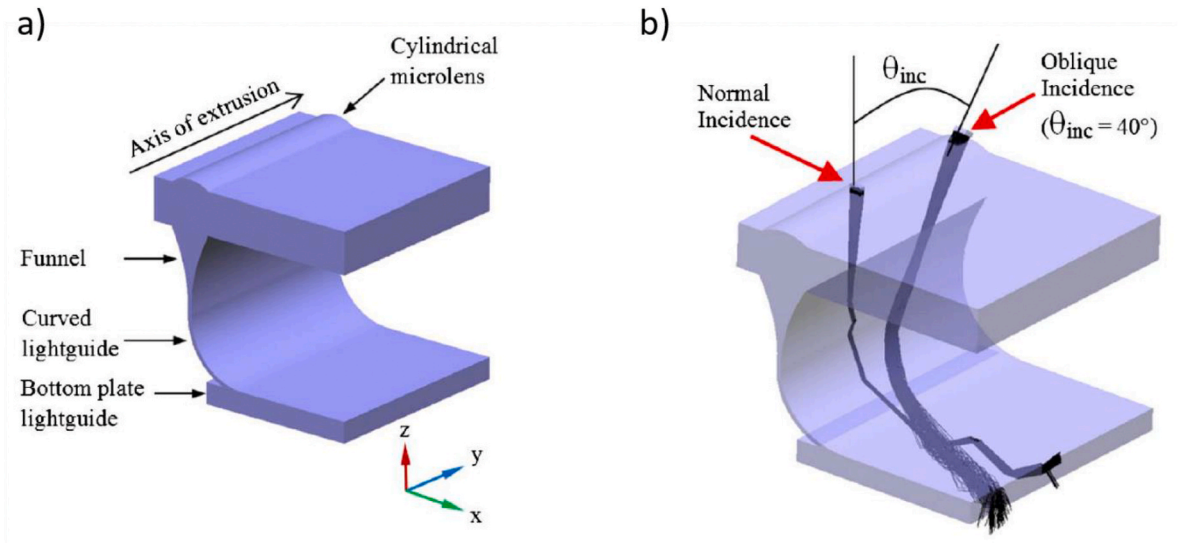

Fig. 14. a) Schematic representation of cylindrical micro lens and curved light wave guide based refractive type solar concentrator; b) Ray tracing showing high angular tolerance of 40° in the y-z plane for light concentration. Source: Reproduced with permission from Ref. [47]. Copyright © 2014, Optical Society of America.

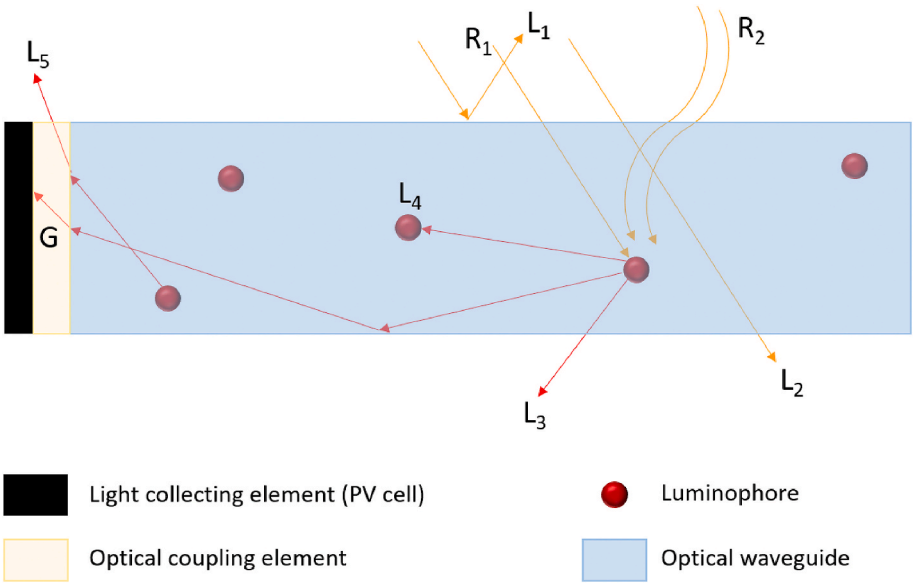

Fig. 15. Schematic representation of optical concentration mechanism and optical losses in a typical Luminescent solar concentrator, where R1, and R2 represent direct and diffuse irradiation respectively; G represents the pathway of optical gain from the radiation emission from the luminophore; L1 represents the Fresnel loss occurring at the waveguide air interface; L2 represents the unabsorbed radiation loss; L3 represents the escape cone loss; L4 represents the reabsorption loss occurring in the LSC; L5 represents the radiation loss occurring in the optical coupling element between the waveguide and PV cell.

ii. Optical Efficiency (OE): Gives the ratio of the output energy to input energy in the desired wavelength range (λ_{min} to λ_{max}).

$$OE = \frac{\int_{\lambda\ min}^{\lambda\ max} E_{POUT}(\lambda).d(\lambda)}{\int_{\lambda\ min}^{\lambda\ max} E_{PIN}(\lambda).d(\lambda)} \quad (9)$$

E_{POUT} (λ) measures the output energy of the photons that can be obtained from the detector plane and E_{PIN} (λ) measures the input energy of the system.

iii. Photon concentration ratio (CP): can be given as;

$$C_p = G_g \times OE \quad (10)$$

iv. Total solar concentration ratio (C): can be given as;

$$C = G_g \frac{\int_{\lambda\ min}^{\lambda\ max} N_{POUT}(\lambda).\ EQE(\lambda).d(\lambda)}{\int_{\lambda\ min}^{\lambda\ max} N_{PIN}(\lambda).\ EQE(\lambda).d(\lambda)} \quad (11)$$

where EQE (λ) measures the external quantum efficiency of PV solar cell, $N_{P_{OUT}}(\lambda)$ and $N_{P_{IN}}(\lambda)$ measure the number of output and input photons at a specific wavelength respectively.

v. Power Conversion Efficiency (PCE): PCE of the LSC can be derived from the output electrical parameters of the solar cell;

$$PCE\ (\eta_{LSC}) = \frac{V_{oc}.J_{sc}.FF}{P_{in}} = \frac{V_{oc}.I_{sc}.FF}{P_{in} \times A_{Edge}} \quad (12)$$

where J_{sc} measures the short-circuit current density of PV cell ($A.m^{-2}.nm^{-1}$), V_{oc} measures the open-circuit voltage, I_{sc} measures the short-circuit current (Ampere), FF measures fill factor and P_{in} is total flux (power) density of the incident solar radiation.

Also, the percentage increase in efficiency

$$\Delta\eta(\%) = \frac{\eta_{LSC} - \eta_{cell}}{\eta_{cell}} X\ 100\ \% \quad (13)$$

where η_{cell}denotes the solar cell efficiency

Optical losses in LSC: Various potential loss mechanisms occurring inside LSC during the process are also shown in Fig. 15, which significantly affect the solar concentration ratio, OE, and PCE. The concentration of luminophores and thickness of the system affect the percentage of the radiation absorbed by the luminophores. The Fresnel loss (L_1), occurs for the incident radiation, and the unabsorbed radiation (L_2) passing through the system denotes the system losses that occur before light absorption by luminophores. As said, the waveguiding mechanism in LSC is TIR, for which the critical solid angle is determined by the refractive index of the host matrix 'n', $\theta_c = \sin^{-1}(1/n)$. A fraction of emitted photons strikes at the waveguide/air interface with an incidence angle less than θ_c, circumventing through the bottom and other surfaces (escape cone loss, L_3). Mismatches in the refractive indices and imperfect optical coupling for the fraction of radiation striking the optical coupling element, cause them to deviate and leave the LSC (L_5).

Other loss processes depend either on the chromophores or transparent matrix material. For luminophores with small stokes-shift, re-absorption of luminescence by another luminescent molecule results in energy loss with an efficiency of $\eta_{RA(\lambda)}$ (L_4) [31]. The amount of re-absorbing photons exhibit an increasing trend with the increase in geometric gain. Further, the thermal drop of photons associated with non-unity quantum yield (FQY) of chromophore, attenuation, and scattering of the host material (with efficiency $\eta_{S(\lambda)}$) cannot be overlooked. It is observed that from the expression of trapping efficiency ($\eta_{TR(\lambda)} = \cos\theta_c = \sqrt{(1-1/n^2)}$), a polymeric host matrix having n = 1.5, incorporated with the chromophores showing isotropic emission could attain a maximum trapping efficiency of $\eta_{TR(\lambda)} = 0.745$, when there is no scattering loss of radiation. Anisotropic emission can maximize the trapping efficiency by promoting the in-plane emission. Optical absorption by the matrix material and scattering by the slab surfaces or bulk defects that come from the structural or large chromophore aggregates, also contribute to the increase in the escape cone losses [32]. Optical materials like fluorinated PMMA or N-BK7 glasses can improve the optical efficiency compared to common PMMA or soda lime glass [32]. The different chromophore and matrix-related loss processes are represented in Fig. 16. Considering these loss mechanisms, an expression for the optical efficiency can be given as:

$$\lambda_{LSC} = \int \left[(1 - R(\lambda))\left(1 - e^{-\alpha_C(\lambda)d}\right)\left(e^{-\alpha_{WG}(\lambda)L}\right)\eta_{TR}(\lambda)\varphi_{PL}(1 - \eta_{RA}(\lambda))(1 - \eta_s(\lambda))\right]d\lambda$$

where, the effectivity of waveguide, $R(\lambda) = [(n-1)/(n+1)]^2$, $\alpha_C(\lambda)$ is the absorption coefficient of the luminophore, $\alpha_{WG}(\lambda)$ is the absorption coefficient of the waveguide material and d and L are the thickness of the waveguide and its length.

As it is mentioned earlier, all kinds of significant loss processes have a considerable dependency on the enlarging size of LSC, which act as a barrier to its widespread large-scale applications in the BIPV systems. Therefore, recent investigations have focused on strategies to improve optical performance by reducing LSC loss mechanisms. In this context, various configurations of LSC and their performance with respect to the shape, geometric gain, host material, luminescent species, doping concentration, and PV solar cell type are reviewed and compared.

In this section, the discussion on the different design architectures and optimised material specifications adopted to fabricate the device systems of LSC in the field of photovoltaics in the last decade is carried out. The section provides an overall outline of the developments in LSC, classified by the luminophore materials (inorganic, organic, and hybrid), and the details are summarized in Table 2.

Inorganic luminophores: Recently, inorganic luminophores are the most widely explored materials for LSC because of their high photostability, ability to tune the absorption and emission wavelength range upon synthesis parameters, and yield better optical properties. In the work done by Inman et al., lead sulphide (PbS) QDs were employed as luminophores with varying doping concentrations (Fig. 17) [51]. The geometry of LSC was a cylinder with the dimensions of height and radius of 2.5 cm and 0.6 cm, respectively. By the comparative study on the performance of the solid cylindrical LSC and hollow cylindrical LSC having 0.38 cm hollow in the centre, the latter obtained 3.5% more OE for the edge-attached PV solar cells. This is realized by the fact that the increasing thickness of LSC is responsible for attenuation and scattering losses; hence the sold cylinder structure showed decreased LSC OE.

CdSe core/multi shell QDs having 45% fluorescence quantum yield have been studied for various dimensions of LSC which served the effect of geometric gain on LSC optical performance [52]. The as-fabricated device of 5 cm × 3.1 cm LSC has attained PCE = 2.81% and current density = 77.2 mA/cm2, which was the maximum. The contribution of thermal drop associated with the increased surface aperture of LSC causes a reduction in PCE. In a later study by Coropceanu et al., using CdSe/CdS QDs with a high value of FQY of 86%, lead to an increased concentration density of irradiance in a 2 cm × 2 cm × 0.2 cm LSC [53].

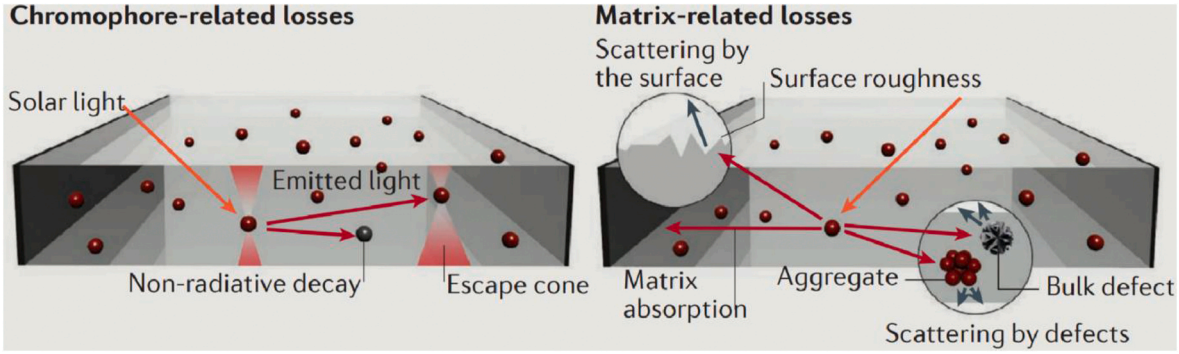

Fig. 16. Different loss processes (chromophore related and matrix related) in LSC with the functioning mechanisms. Source: Reproduced with permission from Ref. [32]. Copyright © 2017, Macmillan Publishers Limited, part of Springer Nature.

Table 2
Summary of review on different design configurations (optics and optics materials) of LSC-based PLC (in chronological order).

Reference, year	Research method E: Experimental S: Simulated	Optical material data	Structure form	Dimensions	Optical performance (OE/ PCE (%)), GC	Acceptance angle (°)
Luminescent Solar Concentrators						
L: Luminophore; HM: Host matrix; W: Waveguide; HMW: Host matrix waveguide (host matrix and waveguide are same)						
Luminophore coated on waveguide: (C); Luminophore dispersed in a waveguide: (D)						
[51], 2011	E	L: PbS QD HMW: PMMA	Solid cylindrical (D)	Radius: 0.6 cm Length: 2.5 cm	OE: 3	NA
			Hollow cylindrical (D)	Radius: 0.6 cm Length: 2.5 cm Hole radius: 0.38 cm	OE: 6.5	
[52], 2011	E	L: CdSe core/multi shell QDs HMW: LMA and EGDM	Rectangular (D)	$5 \times 3.1 \times 0.4$ cm^3 $4 \times 3.8 \times 0.4$ cm^3 $4.95 \times 3.1 \times 0.4$ cm^3 $3.2 \times 3.3 \times 0.4$ cm^3 $5 \times 3.8 \times 0.4$ cm^3	PCE: 2.81 (Si PV cell) PCE: 2.7 (c-Si PV cell) PCE: 1.3 (c-Si PV cell) PCE: 1.1 (c-Si PV cell) PCE: 0.79 (c-Si PV cell)	
[58], 2012	E	L: Ytterbium chelate OPyr–Yb–Phen HMW: PMMA	–	–	OE: 1	
[76], 2013	E	L: Coumarin dyes coupled with MNP (25 ppm) HM: PMMA W: Polycarbonate L: Coumarin dyes coupled with MNP (10 ppm) HM: PMMA W: Polycarbonate L: Coumarin dyes coupled with MNP (20 ppm) HM: PMMA W: Polycarbonate	Rectangular (C) Spin coated double layered LSC; Layer 1: HM/L Layer 2: PMMA/SiO_2 (for enhanced light trapping)	$20 \times 8 \times 0.3$ cm^3	Increase in PCE: 33.4 (mc-Si PV cell) Increase in PCE: 25.8 (c-Si PV cell) Increase in PCE: 53.2 (a-Si PV cell)	
[53], 2014	E	L: CdSe/CdS core/shell QD HMW: LMA and EGDM	Rectangular (D)	$2 \times 2 \times 0.2$ cm^3	OE: 48	
[70], 2014	E	L_1: DTB L_2: Lumogen F-Red 305 HMW: PMMA	Rectangular (D) Cascade LSC; Primary: HMW/L_1 Secondary: HMW/L_2	HMW/L_1: $11 \times 11 \times 0.6$ cm^3 HMW/L_2: $10.8 \times 0.6 \times 0.6$ cm^3	+56% Increase in PCE compared with traditional LSC structure	
[59], 2015	E	L: ZnS-coated CISeS QD HMW: Cross-linked Poly(lauryl methacrylate)	Rectangular (D)	$12 \times 12 \times 0.3$ cm^3	OE: 3.27	
[60], 2015	E	L: CulnS/ZnS 2 QD HMW: PMMA	Rectangular (D)	$2.2 \times 2.2 \times 0.3$ cm^3	PCE: 8.71 (c-Si PV cell)	
[62], 2015	E	CdSe/CdS QDs (with trench reflector) HMW: PLMA	Rectangular (D) (with trench reflector and photonic mirror)	(3.9×3.9 cm^2) $\times$ 30 μm	Concentration ratio: 30.3 (for blue photons) Waveguide efficiency: 82%	
[71], 2015	E	L: Red-305/Yellow-083 HM: EVA W: Glass	Rectangular sandwich structure; Edge mounted PV cell without reflector	$7.8 \times 7.8 \times 0.3$ cm^3 $15.6 \times 15.6 \times 0.3$ cm^3 $31.2 \times 31.2 \times 0.3$ cm^3 $61 \times 122 \times 0.3$ cm^3	PCE: 2.8 (mc-Si × 4) PCE: 1.81 (mc-Si × 4) PCE: 0.98 (mc-Si × 8) PCE: 0.33 (mc-Si × 20)	
			Rectangular sandwich structure; Bottom mounted PV cell with reflector	$61 \times 122 \times 0.3$ cm^3	PCE: 2.28 ((mc-Si with size: 15.6) × 2)	
[72], 2015	E	L: DTB and DPA HMW: PMMA	Rectangular (D)	$100 \times 150 \times 0.6$ cm^3	PCE: 1.26 (c-Si PV cell)	
[77], 2016	E	L: Organic-inorganic hybrid perovskite W: Glass	Rectangular (C)	$1.5 \times 1.5 \times 0.1$ cm^3	OE: 29	
[63], 2016	E	L: Lumogen F Red-305 HM: PAE W: PMMA	Rectangular (C)	$1.75 \times 1.75 \times 0.15$ cm^3	OE: 40	
[64], 2016	E	L: PbS/CdS HMW: Polymer	Rectangular (D)	$10 \times 2 \times 0.2$ cm^3	OE: 6.1	
[66], 2016	E	L: Giant core/alloyed-shell QD ($CdSe/Cd_x Pb_{1-x}S$ core/shell) HMW: PMMA	Rectangular (D)	$7 \times 1.5 \times 0.3$ cm^3	PCE: 1.15 (Si PV cell)	

(continued on next page)

Table 2 (*continued*)

Reference, year	Research method E: Experimental S: Simulated	Optical material data	Structure form	Dimensions	Optical performance (OE/ PCE (%)), GC	Acceptance angle (°)
[67], 2016	E	L: Giant CdSe/CdS QDs W: Glass	Rectangular (C) L encapsulated by silica shells and dispersed in polar solvents (Water/ Ethanol), and deposited on W	413 cm^2	OE: 17 (single λ)	
[78], 2017	E	L: Conjugated QD 545 and AF dye HM: DI water W: DI water + Glass	Rectangular (D) L dispersed DI water collected inside glass cell	2 × 2 × 0.3 cm^3	PCE: 2.87 (p-Si PV cell)	
[79], 2018	E	L: BPEA and PdTPBP HMW: Polyurethane	Rectangular (D)	5 × 1 × 0.1 cm^3	PCE: 6.1 (DSSC)	
[80], 2018	E	L_1: $CuInSe_2$/ZnS QD L_2: Mn^{2+} doped $Cd_xZn_{1-x}S$/ ZnS QDs HM: PVP W: Borosilicate glass	Rectangular (C) Double layered tandem LSC Bottom layer: HM/L_1 Top layer: HM/L_2	15.24 × 15.24 cm^2	PCE: 3.1 (GaAs PV cell) OE: 6.4	
[68], 2019	E	L: 0D Cs_4PbBr_6 perovskite NCs HM: PS W: Glass	Rectangular (C)	0.4 × 10 × 10 cm^3	OE: 2.4 PCE: 1.8	
[73], 2020	E	L: perylene-based chromophore H: DA polymer W: Glass	Rectangular (C)	–	OE: 4.9	
[74], 2020	E	L_1: carbon-dot (blue) L_2: carbon-dot (green) L_3: carbon-dot (red) HM: PVA W: Glass	Rectangular (C) Triple layered tandem LSC Top layer: HM/L_1 Middle layer: HM/L_2 Bottom layer: HM/L_3	8 × 8 cm^2	OE: 2.3 (external), 23.6 (internal)	
[50], 2021	E and S	L: Bi-doped $Cs_2Ag_{0.4}Na_{0.6}InCl_6$ double perovskites HMW: PMMA	Rectangular (D)	10 × 10 cm^2	OE: 39.4 (simulated), 21.2 (internal, prototyped)	
[75], 2021	E	L_1: BBT 2 L_2: BBT 3 L_3: BBT 4 HM: PMMA, PCMA W: Glass	Rectangular (C)	5 × 5 × 0.3 cm^3	OE: 5.8 (PMMA/L_1), 6.5 (PMMA/L_2), 9.0 (PCMA/L_3)	
[69], 2022	E	L: Gd_2O_2S: Er, Yb HMW: PMMA	Rectangular (D)	5 × 5 cm^2	PCE: 6.93 OE: 8.57	
[81], 2022	E	L: Si doped carbon dots HM: PVP W: Glass	Rectangular	5 × 5 × 0.2 cm^3 15 × 15 cm^2	PCE: 4.36 PCE: 2.06	

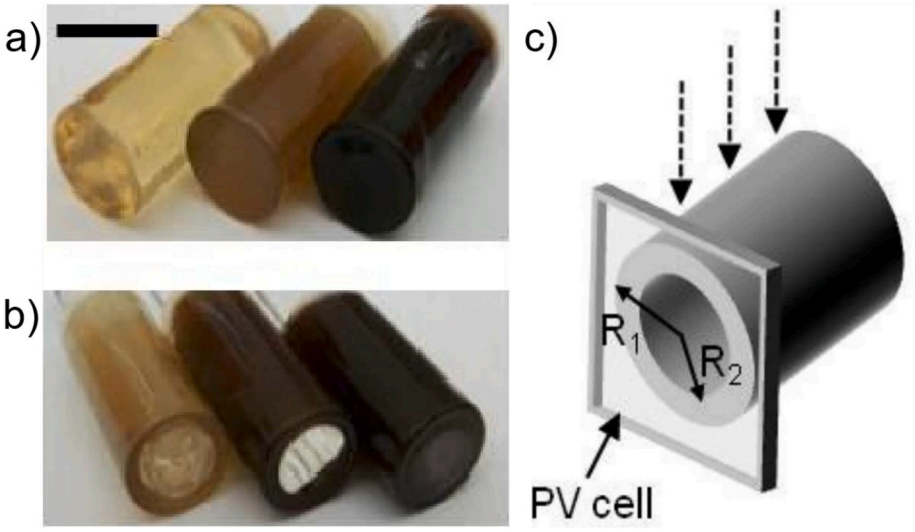

Fig. 17. Photograph of cylindrical structured LSCs with a) solid and b) hollow configuration with varying doping concentrations (The black scale bar represents 1.0 cm) (c) Schematic illustration of hollow LSC attached to PV cells. Source: Reproduced with permission from Ref. [51]. Copyright © 2011, Optical Society of America.

It showed a 48% improvement in OE for the device integrated with crystalline silicon (c-Si) PV solar cells.

Many research efforts have been directed in the field of LSC that revealed the effect of plasmonic coupling between luminophores with noble metal nanoparticles (MNPs) [54,55]. For example, Chandra et al. fabricated LSC with CdSe/ZnS core-shell QD coupled with gold-NP [56]. The as-fabricated LSC achieved an OE enhancement of ~20%–50% for different doping concentrations of QD and MNP. As the MNPs promote the absorption and luminescence rate, consequently it is reflected in the device performance. Similar investigations using 60 nm silver-NP and 100 nm gold-NP have been done by El-Bashir et al., which showed 2.4-fold and 4.75- fold enhancement in the fluorescence, respectively [57].

PV glazing systems build a key element in the BIPV applications owing to their light adaptability. In light of the applicability of transparent LSCs, colourless single layer LSC incorporated with ytterbium chelates having emission in the near-infrared (NIR) spectrum has been proposed in 2012 [58]. For the same purpose, Meinardi et al., explored a study on 12 cm × 12 cm × 0.3 cm LSC using heavy-metal-free colloidal ZnS-coated CISeS QDs on a large scale without the aid of a back reflector [59]. Being more proficient in the visible and NIR region, PCE of transparent LSCs (3.27% OE) for which the absorption and luminescence spectra belong to UV-band coupled to PV exhibit less value. A similar work done by Li et al., employed heavy-metal-free CuInS/ZnS_2 QDs, having high FQY (~81%) and large Stokes shift (>150 nm) embedded in a PMMA host material to fabricate a colourless LSC (2.2 cm × 2.2 cm × 0.3 cm) (Fig. 18) [60]. From the results, the effect of the optical properties of the QDs on the LSC performance was obvious and it achieved a maximum OE of ~26%. Besides, the appreciable change in the current density from 0.72 mA/cm^2 to 14.8 mA/cm^2, LSC with reference to the blank PMMA leads to a PCE of 8.71%. The very small spectral overlap between the absorption and emission and high FQY minimized the re-absorption losses while enhancing the intensity of edge-detected light of the LSC. With integration to a black background, the LSC (10 cm × 10 cm) has achieved 8.1% OE and 2.18% PCE using CuInS/ZnS_2 as luminescent material coupled with a c-Si PV solar cell [61]. Further, by replacing the black background with a reflective substrate, PCE was improved to 2.94%.

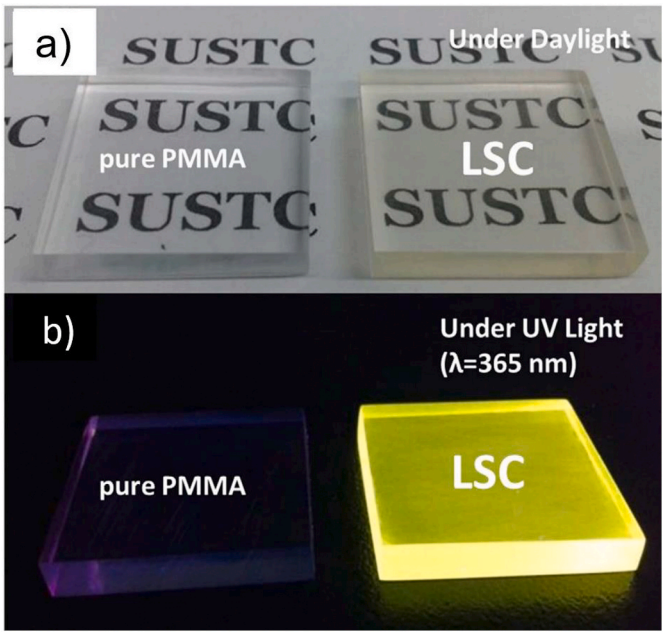

Fig. 18. Photograph comparing the a) transparency of fabricated CuInS/ZnS_2 QDs based transparent LSCs with pure PMMA on natural light and b) emission of same under UV light. Source: Reproduced with permission from Ref. [60]. Copyright © 2013, The authors, published by Springer Nature Limited.

Cavity adopted design by sandwiching PLMA/QD composite (30 μm) between two thin glass films have been investigated by Bronstein et al. for LSC, where giant CdSe/CdS QDs taken as luminophores (Fig. 19), and LSC is attached to mc-Si solar cell (0.15 mm^2) [62]. The concentration factor attained is 30-fold (for blue photons) and the boosted waveguide efficiency of ~82% has been reached by diminishing the escape cone and scattering losses by employing a photonic mirror and placed inside a trench diffuse reflector, thereby creating an optical cavity.

In the work by Gutierrez et al., the effect of a transparent host matrix can be realized with the comparative study of two different π-conjugated polymers of poly (arylene ethynylene) (PAE) having different gap energies such as E_1 and E_2 for the as-fabricated LSC [63]. The polymer matrix with energy gap E_1 showed low attenuation and scattering coefficients; thereby, thermal losses were minimized, and the device achieved improved OE (~40%). Emissive material in the NIR region is advantageous for their utility as semi-transparent facades and windows. Owing to their appreciable FQY (~40–50%) and high photo stability with respect to the bare QDs, PbS/CdS QDs incorporated LSC (10 × 2 × 0.2 cm) exhibited an improved optical performance of 6.1% OE [64,65]. In this study, it is observed that the fraction of solar absorption by QDs can be increased by using a giant core/alloyed-shell QD structure where the luminescent material taken was CdSe/$Cd_xPb_{1-x}S$ having a FQY of 40% doped into PMMA matrix [66]. The fabricated device was highly transparent (7 × 1.5 × 0.3 cm) and achieved a PCE of ~1.15%.

It is very important to check the photostability of the species which absorb solar radiation to ensure the long lifetime of the fabricated LSC system. Li et al., studied the stability of polymer/giant CdSe/CdS QDs composite for large-scale LSCs [67]. The giant QDs having a high FQY of 70% were encased by silica shells and observed an increased photostability under ambient(actual) conditions. For a monochromatic wavelength band, the LSC system (413 cm^2) exhibited an OE of ~17%, which found application as window glass owing to its semi-transparency.

The advantages associated with zero-dimensional (0D) perovskites such as high Stokes shift (1.5 eV), FQL, stability owing to large exciton binding energy, and easy manufacturing make them more efficient candidates than 3D NCs. Zhao, H. et al. conducted a study on colloidal 0D Cs_4PbBr_6 perovskite NCs (FQL≈58%) having small spectral overlap between absorption/emission profiles, and coupled with semi-transparent thin-film LSCs (100 cm^2) [68]. The LSC showed an OE of 2.4% when exposed to one sun illumination (100 $mWcm^{-2}$) and a PCE of 1.8% on natural sun illumination (30 $mWcm^{-2}$).

The emerging nano fluorophore-based LSC technology presents high photostability and capability of custom tailoring in the spectral range, making them an ideal class for the application as LSC integrated transparent solar window. In a recent work, Kataria et al. fabricated LSC with Gadolinium oxysulphide (Gd_2O_2S: Er,Yb) nano fluorophore incorporated in PMMA matrix [69]. The LSC shows a sufficiently high OE (~8.57%) and PCE (~6.93%). This enhanced efficiency is due to the possibility of multi-wavelength excitation offered by the nanocrystals in a broad range of the solar spectrum (from UV to NIR) and large Stoke's shift due to the visible range emission. In comparison with the traditional organic dye-based LSC, the use of Gd_2O_2S: Er,Yb nano fluorophore significantly avoid losses related to reabsorption. Further, the non-toxic nature, unit values of optical flux gain, and cost reduction factor altogether widens their practical applicability.

The major limiting factor of perovskite nanocrystals (PNCs) is their toxicity due to the presence of lead. For the increased eco-friendly applicability of perovskite-based LSCs, lead-free PNCs are needed without compromising the efficiency values. Zdražil et al., investigated the ability of self-trapped exciton emission (STE) shown by Bi-doped $Cs_2Ag_{0.4}Na_{0.6}InCl_6$ double perovskites to fabricate LSC (100 cm^2) and realized that the device achieved high visible transparency (average transmittance of 94.6%) and negligible reabsorption losses (Fig. 20)

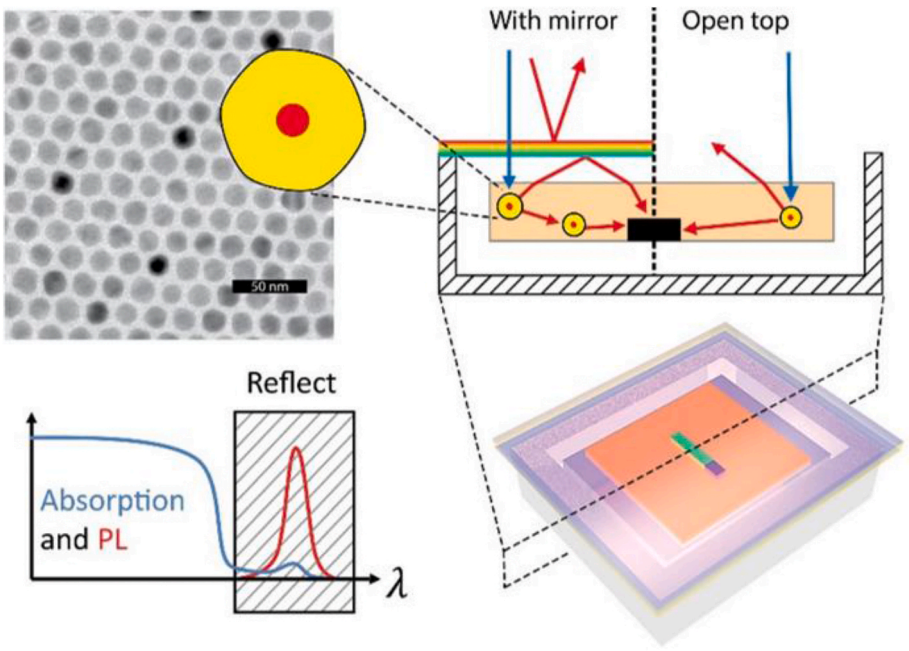

Fig. 19. Illustration of PLMA/QD composite-based LSC device (right bottom), cross-sectional view of the same showing the device design of trench reflector with/without a photonic mirror (right-top), TEM image of PLMA/QD (left top), and absorption and PL spectra of CdSe/CdS QDs (luminophore) showing large Stokes shift. Source: Reproduced with permission from Ref. [62]. Copyright © 2015, American Chemical Society.

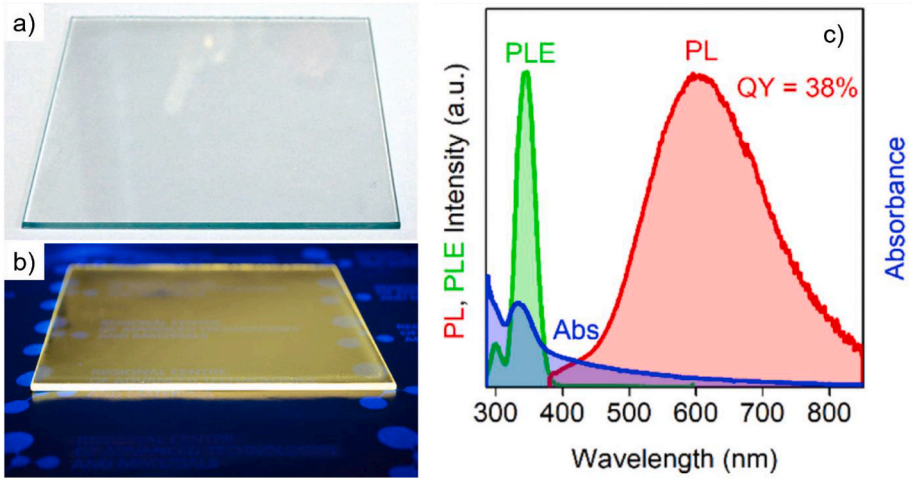

Fig. 20. Photograph of lead-free perovskite-based LSC (100 cm^2) showing a) high visible transparency (average transmittance of 94.6%) under day light, b) luminescent light concentration under UV light and c) absorbance and emission spectral profile of Bi-doped $Cs_2Ag_{0.4}Na_{0.6}InCl_6$ double perovskites showing large Stokes shift (Absorption (blue curve), normalized PL excitation (green curve, excitation maxima at 347 nm), and PL emission (red curve, emission maxima at 605 nm) spectra). Source: Reproduced with permission from Ref. [50]. Copyright © 2021, American Chemical Society.

[50]. The device resulted in an internal OE of 21.2% with an internal concentration factor of 2.7. Further, from the Monte Carlo (MC) ray-tracing simulations it is evaluated that the non-unity FQL is the major reason for the efficiency reduction. From the simulation results for LSCs of size 2500 cm^2, taking a unit value of FQL, the calculated efficiency is 39.4%.

Organic luminophores: Organic luminophores-based LSC is the earliest developed LSC system that utilises organic dyes infused/coated to the transparent matrix material. As a new-fangled fabrication from conventional LSC, Daorta et al., provided the concept of a cascade LSC using organic chromophores doped PMMA matrix [70]. The improved PCE of cascade LSC by ~56% is realized by the innovative design comprised of a primary LSC (11 cm × 11 cm × 0.6 cm) and four secondary LSCs (10.8 cm × 0.6 cm × 0.6 cm) doped with DTB and Lumogen F-Red 305 respectively. The coincidence of the absorption and emission spectrum of secondary LSC with that of primary LSC made the device to get increased PCE.

In the work of Zhang et al., taking the mixture of luminophores (Lumogen Red-305 and Yellow-083), glass-laminated LSCs with various geometric parameters (7.8 × 7.8 cm, 15.6 × 15.6 cm, 31.2 × 31.2 cm and 61 × 122 cm) have been fabricated and attached to mc-Si solar [71]. Even though the number of edge-detected photons is intensified by augmenting the LSC size, a reduction in the PCE (from 2.8% to 0.33%) has been observed due to the thermal drop associated with the geometric gain increase. An approach of bottom-mounted-PV LSCs was tried for varying sizes of PV solar cells, where reduced path length of luminescent radiation favoured the enhancement of PCE than that of the edge structure. The highest value of PCE (2.28%) was optimised for the dimensions of 61 × 122 × 0.3 cm and 15.6 cm for LSC coupled to edge-reflectors and bottom-mounted PV solar cells, respectively. The concept of using a luminescent mixture of dyes such as DTB (di-benzo-thiadiazole) and DPA (diphenylanthracene) was put forward by Aste et al., and implemented in a large-scale planar LSC [72]. By this approach, the absorbance band of the LSC (300–500 nm) has broadened,

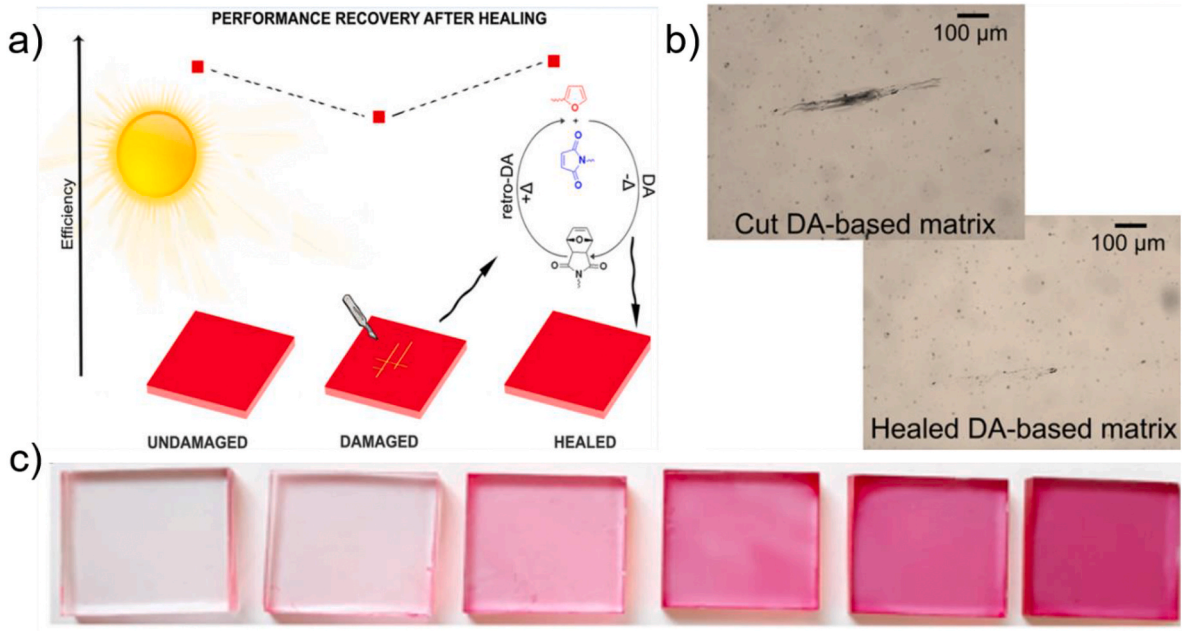

Fig. 21. a) Self-healing mechanism of as fabricated thermo-responsive LSC incorporated with DA-based transparent polymer matrix b) Photograph of DA-based matrix for mechanically induced damage and after healing, obtained from optical microscopy c) Photographs of thermos responsive LSCs at ascending concentrations of luminophore under natural solar radiation. Source: Reproduced with permission from Ref. [73]. Copyright © 2019, American Chemical Society.

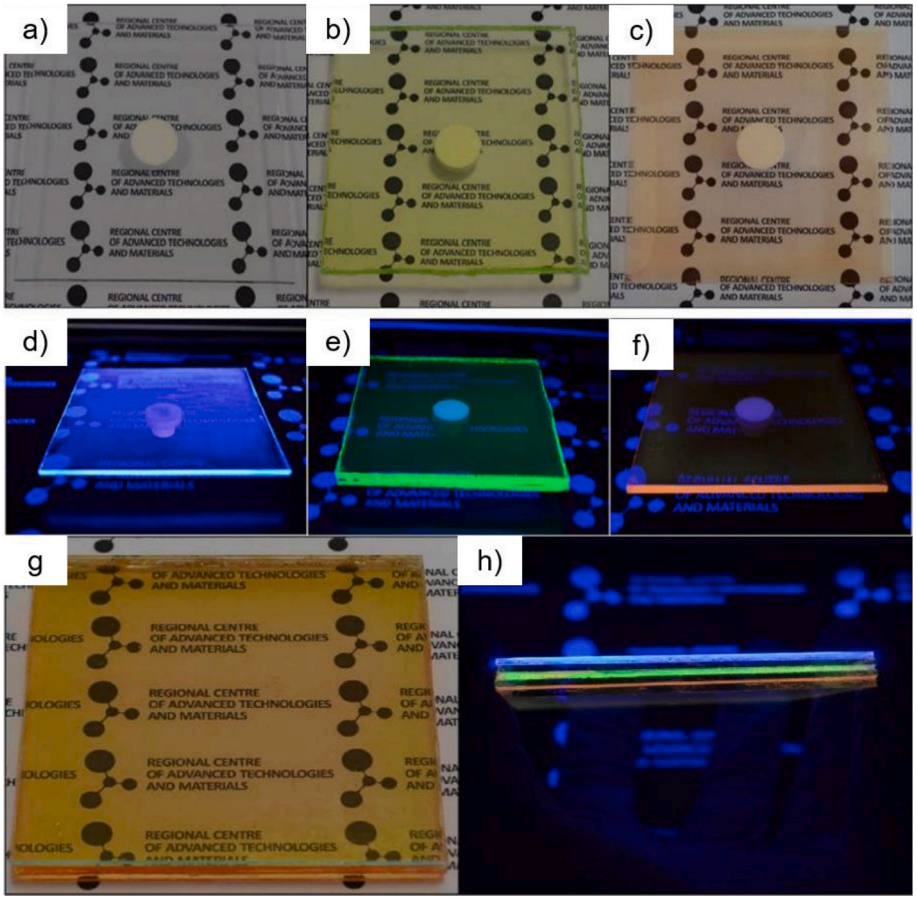

Fig. 22. Images of individual carbon dot-based LSCs (showing emission at blue, green, and red bands) under a)-c) natural illumination d)-f) UV illumination; tandem LSC under g) natural illumination h) UV illumination. Source: Reproduced with permission from Ref. [74]. Copyright © 2020, Royal Society of Chemistry.

and the luminescence band got peaks at the visible spectrum. The whole device with a c-Si solar cell demonstrated high EQE (~90–95%) and ~10% higher PCE (1.26%) compared to reference modules.

The development of smart materials as host matrix unfolds a new chapter in the fabrication of LSC for generating responsive smart LSC devices. Tatsi, E et al., synthesized thermally reversible, transparent polymer via Diels–Alder (DA) reaction between a furan-functionalized acrylic copolymer and an aliphatic bismaleimide; the resulting cross-linked structure enabled high thermal stability [73]. To this efficient host matrix, perylene-based chromophore was embedded with optimised concentration, resulting in an LSC system having a high OE of 4.9%. Besides, the self-healing property of the matrix material regained the mechanical structure from damage without compromising device efficiency (Fig. 21).

In 2020, the best alternative for the conventional semiconductor and perovskite quantum dots, carbon-dot (CD) based LSCs was fabricated by L Zdražil et al., with additional qualities that qualify for a low-cost, resource-efficient, and accessible system [74]. In this, a thin-film tandem LSC (64 cm^2) has been fabricated where the CDs were dopped in polymer matrices (Fig. 22). Owing to the high transparency (83.4% transmittance) in the visible band, the LSC integrated with CD (emission at the blue, green, and red bands) (Fig. 22) attained an external OQE of 2.3% with an internal OQE of 23.6%.

Novel chemical synthetic routes have been used to develop promising fluorophores by Pappucci et al., such as BBT2-4, which benzo [1,2-d:4,5-d′] bisthiazole (BBT) part (acceptor core (A)) is modified by introducing various donor groups (D) generating D-A-D structure [75]. The strong dependency of FQYs of fluorophores on the ambient polarity is revealed by Transient absorption spectroscopy (TAS). The as synthesized fluorophores showed a gradual increase of FQYs with respect to the solvents such as 10–52% (in PMMA), 18–73% (in Toluene), 52.6% (in PBzMA), and 65.6% (in PCMA). The toluene and PMMA-based LSCs show OE in the range of 5.8–7.5%, whereas PCMA/BBT4-based LSCs achieved higher OE of 9.0% owing to the low polarity. Also, the fluorophores were efficient in showing minimal spectral overlap.

Hybrid luminophores: Hybrid luminophores are developed and used in LSC systems to mitigate the limitations and improve the optical performance of singular organic and inorganic luminophore-based LSC systems. In 2014, a new strategical innovation has been developed as double-layered plasmonically enhanced LSCs (pLSC) (Fig. 23) [76]. In this, the pLSC (20 × 8 × 0.3 cm) made of the spin-coated polycarbonate substrate (50 μm PMMA) embedded with coumarin dye which is coupled to gold and silver-NPs where a coating approach was adopted on the top surface using SiO_2 doped (20 μm) PMMA for enhancing the trapping efficiency. On a comparative analysis using amorphous silicon (a-Si), mc-Si, and c-Si PV solar cells, PCE increase of 53.2% was achieved for a-Si PV solar cell with a doping concentration of 20 ppm MNP. Further, the significant hike of PCE from 15.14% to 25.80% on a slight change in the MNP concentration (from 5 ppm to 10 ppm) emphasizes the potential dependency of pLSC optical performance on MNP doping concentration. The increasing level of MNP concentration has been limited because of their non-radiative decay and fluorescence quenching, thereby reducing FQY.

The impact of high FQY (80%) and large Stokes shift shown by organic-inorganic hybrid perovskite luminescent material embedded in glass matrix thin film planar LSC (1.5 × 1.5 × 0.1 cm), coupled to edge-located 1.5 × 0.1 cm c-Si solar cell was studied by Nikolaidou et al. [77]. The comparable spectral characteristics of perovskite with c-Si solar cells improved the efficiency parameters, OE (29%), and PCE (~13%).

An innovative approach to the introduction of a QD/dye-conjugated luminophore system showing Förster resonance energy transfer (FRET) mechanism from QD to dye was used by Tummeltshammer et al. [78]. The broad adsorption band of QD 545 and higher FQY of Alexa Fluor 546 (AF) dye were advantageous in mitigating the optical losses associated with re-absorption and non-unity FQY (Fig. 24). From the comparative analysis of conjugated and unconjugated LSCs (2 cm × 2 cm × 0.3 cm), it is observed that the latter unconjugated LSCs were less efficient than the conjugated LSCs (PCE = 2.87%).

Incorporating the idea of combined down and up shifting of incident light by luminophores to enhance the trapping efficiency of LSC (5 cm × 1 cm × 0.1 cm) was introduced by Ha et al. [79]. In this structure, polyurethane doped with an organic fluorophore served as a down-shifting LSC, and PdTPBP/BPEA composite served as up-conversion LSC. This leads to a dual-band for absorption, such as in UV (300–450 nm) and in red (~650 nm); also, the emission belongs to the green band (~530 nm). The fabricated LSC, when attached to a dye-sensitized solar cell (DSSC) showed a PCE of ~6.1%. Benefitted from the large Stokes shift, a double-layered tandem LSC (15.24 × 15.24 cm^2) was fabricated by Wu et al., with $CuInSe_2$/ZnS QD (FQY = 65–75%) and Mn^{2+}doped $Cd_xZn_{1-x}S$/ZnS QDs (FQY = 78%) as down and top layers, respectively (Fig. 25) [80]. Under AM1.5G solar spectrum, LSC achieved 6.4% OE and 3.1% PCE.

In the latest work, the necessity for a luminophore to get maximum device performance was fulfilled by the carbon nanodot incorporation into silicon (Si-CDs) [81]. Having an ultrahigh FQY (up to 92.3%) and simple fabrication method (hydrothermal method), Si-CDs dispersed in polyvinyl pyrrolidone (PVP) matrix integrated to thin-film LSCs (5 × 5 × 0.2 cm^3) (Fig. 26) acquired a PCE of 4.36% (2.5-fold of Si- undoped CDs). Further, the work was extended to develop a large-area LSC (15 × 15 cm^2), on which natural sunlight irradiation (35 mW cm^{-2}) showed a PCE of 2.06%.

2.3. Diffraction based solar concentrators

Diffraction is a phenomenon based on the wave theory of light, which splits the different wavelengths of light present in a polychromatic light source. While discussing the waveguide-based solar concentrators, a number of PLCs have been designed based on the diffraction and light interference principle. Diffraction-based concentrators are dominantly dependent upon the brightness theorem, which

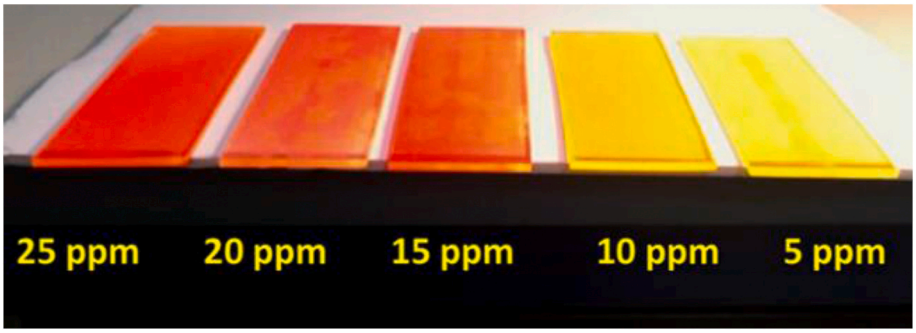

Fig. 23. Photograph of double layered pLSC spin-coated with SiO_2 doped PMMA, with the varying concentration of gold NPs in Coumarin dyes as luminophore. Source: Reproduced with permission from Ref. [76]. Copyright © 2013, Elsevier.

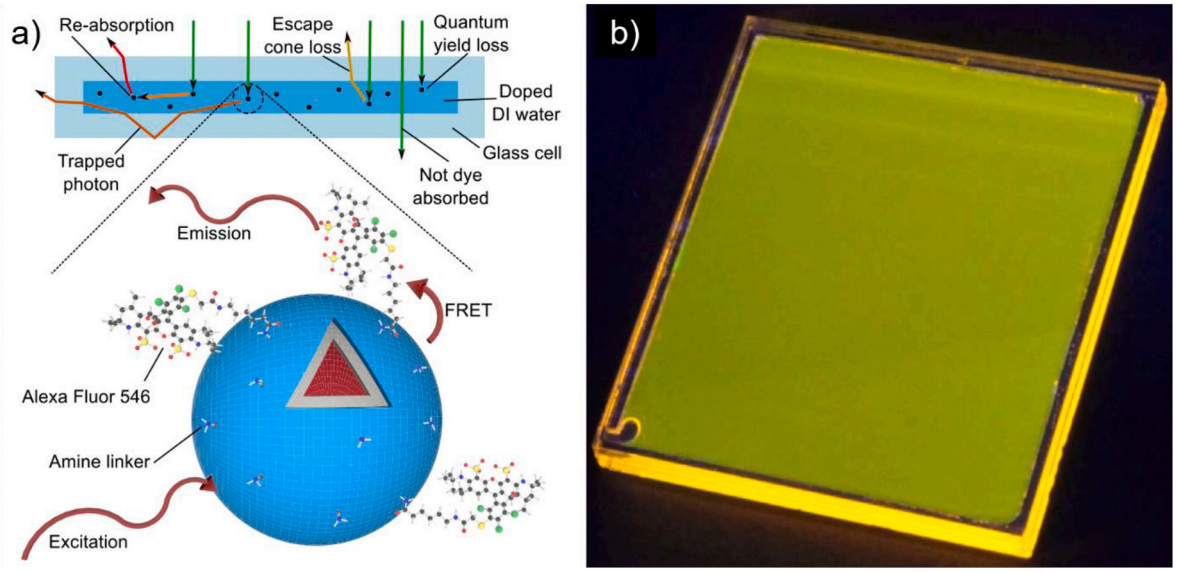

Fig. 24. a) Schematic representation of large-scale LSC embedded with QD/dye-conjugated luminophore with increased photostability and minimized optical losses (due to re-absorption and non-unity FQY) by FRET mechanism b) photograph of conjugated LSC under UV light. Source: Reproduced with permission from Ref. [78]. Copyright © 2016, Elsevier.

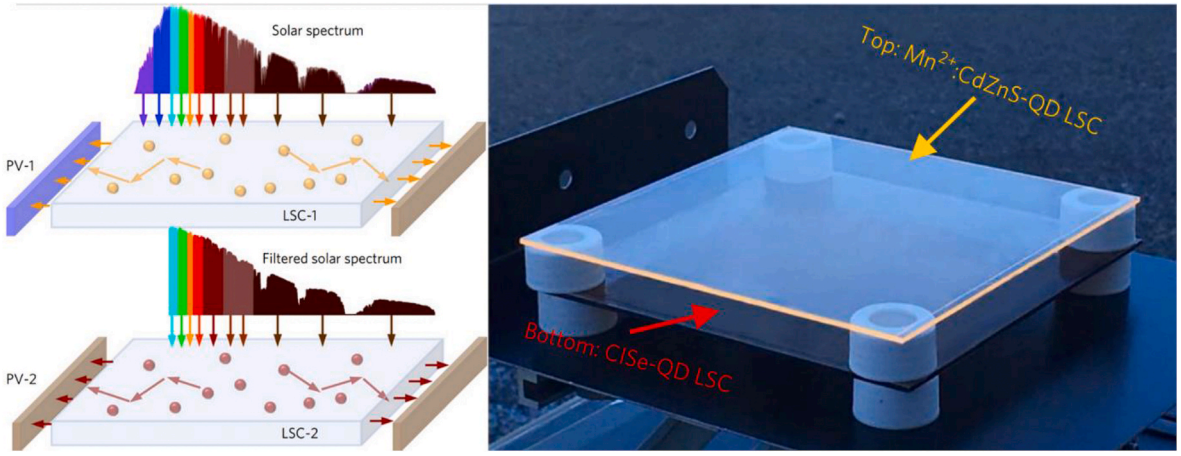

Fig. 25. Illustration and photograph (under AM1.5G solar spectrum) showing double layered tandem LSC. Source: Reproduced with permission from Ref. [80]. Copyright © 2018, Macmillan Publishers Limited, part of Springer Nature.

governs the order of diffraction and diffraction efficiency [82,83]. The holographic technique is the most commonly used fabrication technique for diffraction grating in bulk of planar materials. Planar waveguide-based diffraction solar concentrators use holograms or diffraction gratings alone or in combination with Fresnel lenses or conventional lenses for redirecting and focusing the light to the waveguide, in order to concentrate light to the lateral face. One of the key selling points of the diffraction-based planar concentrator is its ability to concentrate the light with spectral selectiveness, utilising the varied diffraction angle for different wavelengths. The basic working element of a diffraction-based PLC includes a diffraction grating that diffracts light with respect to the wavelength at an angle (diffraction angle), which can be altered by making a variation in the grating period, and grating thickness. Unlike any other PLC, diffraction grating-based PLC can be developed as an ultra-thin element with less bulky systems, adding to its advantage of low weight and cost. The section provides an overall outline of the developments in diffraction optics-based PLC, and the details are summarized in Table 3.

The simple design of a diffraction grating-based PLC is as shown in Fig. 27, proposed by Ties M. de Jong et al. (in which θ is the angle of incident, d is the grating thickness and Λ is the grating period) [84]. The diffraction grating is directly coupled with the waveguide for collecting and concentrating the light to the edges by TIR. The spectrum of rays to satisfy the TIR depends on the angle of diffraction, which is dependent on the order of diffraction. 0^{th} order will pass through without any deviation. For higher orders, if the angle exceeds the critical angle of the waveguide, it will be transported laterally.

They have considered the study on the two types of grating which are fabricated by holography. One is classical surface relief grating, and another is liquid crystal-based polarization grating. To utilise with better efficiency, the grating should have low sensitivity to the wavelength of light and to the incident angle of light. Surface relief isotropic grating can be classified as thick or thin grating [85]; thick gratings show the Bragg diffraction and thin grating shows the Raman-Nath diffraction. Thin and thick gratings can be defined by a parameter "Q" known as the Klein parameter [86].

$$Q = \frac{2\pi d\lambda}{n' \Lambda^2} \tag{14}$$

where n' is the average refractive index,

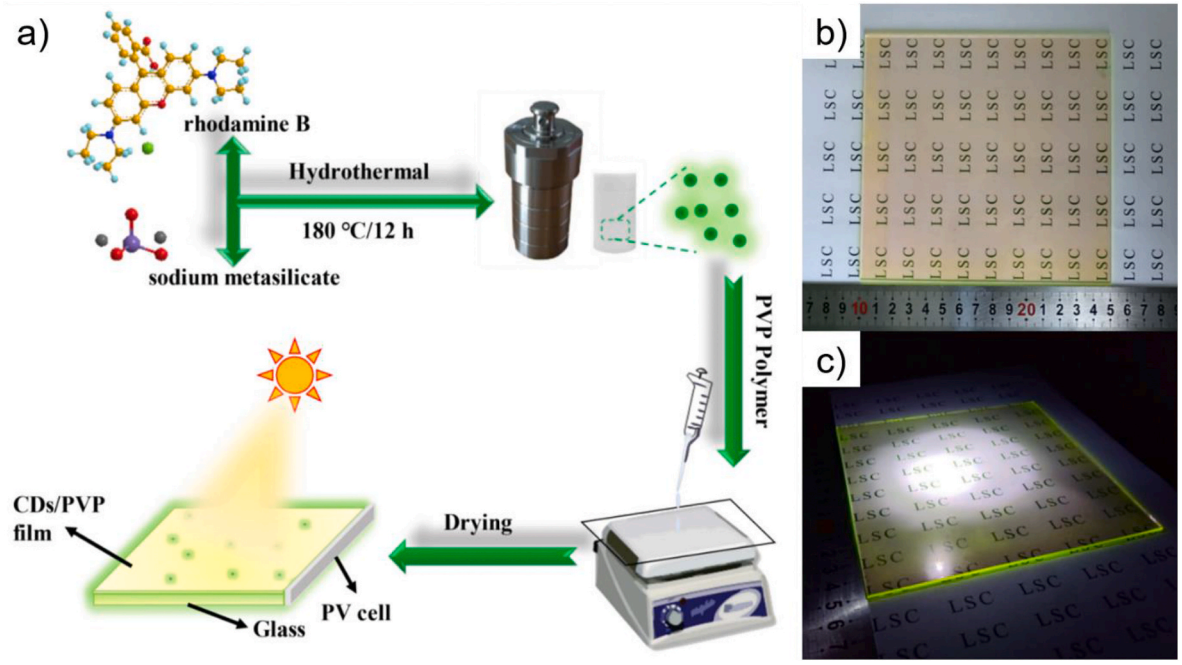

Fig. 26. Schematic representation of synthesis and fabrication of Si-CDs dispersed in polyvinyl pyrrolidone (PVP) matrix integrated to thin-film LSCs (5 cm × 5 cm × 0.2 cm); photographs of fabricated LSC under b) room light condition, c) solar spectrum. Source: Reproduced with permission from Ref. [81]. Copyright © 2022, Elsevier.

Table 3
Summary of review on different design configurations (optics and optics materials) of diffraction optics-based PLC (in chronological order).

Reference, year	Research method E: Experimental S: Simulated	Optical material data	Structure form	Dimensions	Optical performance (OE/ PCE (%)), GC	Acceptance angle (°)
Diffraction Optics-based PLC (For more details of grating optimisations, readers are advised to refer [17,34,84,87,90]) P: Primary optics; W: Waveguide, C: Light coupler						
[84], 2011	E and S	P: SU-8 (photoresist material of refractive index 1.59), Titanium dioxide (refractive index 2.49) (simulation) W: Refractive index 1.6	P: Diffraction gratings (Study was conducted on different diffraction grating types: sinusoidal and rectangular surface relief gratings, polarization grating) W: Planar waveguide	Study was conducted on a number of diffraction gratings	–	Study was conducted on a number of diffraction gratings with varying angles of incidence
[90], 2013	E	W: Fused silica	P: 2 Diffraction gratings (transmission and reflective) W: Wedge-shaped	Length to thickness ratio exceeds to 7	OE: 0.5375 GC: 3.77	±35 and ± 3 (for 90% of OE) ±53 and ± 9 (for 50% of OE) in the 2 planes of incidence
[34], 2016	E	P: Photoresist gratings + Epoxy luminophore composite layer (commercial materials are used) W: Glass	P: Diffraction grating for NIR concentration and LSC sandwich layer W: Planar waveguide + additional solar-control coating for NIR back reflection (commercial source)	10 × 10 cm^2 50 × 50 cm^2	PCE: 3.041 ($CuInSe_2$ PV cells) (outdoor condition) PCE: 2.08 ($CuInSe_2$ PV cells) (outdoor condition)	–
[17], 2017	E and S	P: PMMA W: PMMA C: Aluminum coated V-groove	P: Fresnel lens + Diffraction grating W: Planar waveguide with C C: Reflective V-groove (for spectral selective light concentration)	–	OE: 73 GC: 5 (theoretical)	–
[87], 2019	E	P: Silicon nitride W: Glass	P: Diffraction grating for NIR concentration W: Planar waveguide	5 × 5 mm^2 (prototype)	OE: 0.72 (NIR guiding) PCE: 0.65 and Visible light transmission: 64.9%	>100 (y-z plane) 27 (x-y plane)

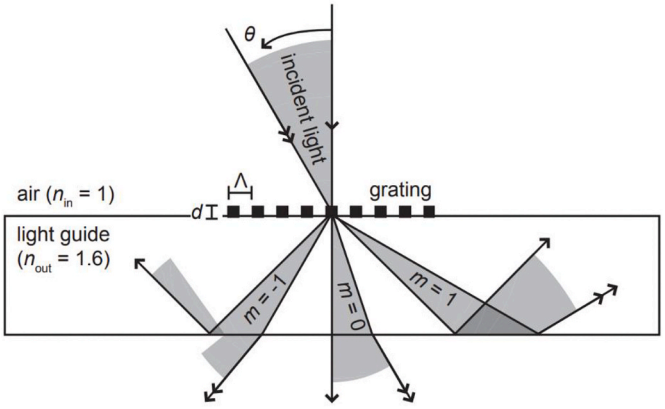

Fig. 27. Scheme of grating-based PLC. Here, for all angles of +1 order (m = 1) and a part of −1 order (m = −1) undergo TIR and is guided to the lateral direction. For all angles of 0 order (m = 0) and part of −1 order, the light is lost as it does not satisfy TIR. Source: Reproduced with permission from Ref. [84]. Copyright © 2011, OSA.

If Q < 1, then it is thin grating, and if Q > 10, it is thick grating.

The diffraction efficiency for sinusoidal surface relief grating in m^{th} diffraction order is

$$\eta_m = j_m^2\left(\frac{\Delta n \pi d}{\lambda}\right) \tag{15}$$

and for rectangular grating, it is

$$\eta_m = \cos^2\left(\frac{\Delta n \pi d}{\lambda}\right), m = 0 \tag{16}$$

$$\eta_m = \left(\frac{4}{(m\pi)^2}\right)\sin^2\left(\frac{\Delta n \pi d}{\lambda}\right), \text{m is an odd integer} \tag{17}$$

$$\eta_m = 0, \text{m is an even integer} \tag{18}$$

where Δn is the difference between the refractive index of grating and air, j_m is the ordinary Bessel function of the first kind. One can set the 1st order diffraction efficiency to 0^{th} by choosing a suitable d for a particular wavelength and period (large period surface relief grating) as shown in Fig. 28, and maximum light will diffract in +1 and −1 order.

Once the thickness d is defined (d = 821 nm for sinusoidal, 536 nm for rectangular) and λ = 633 nm, they observed the incident angle sensitivity to diffraction efficiency, as shown in Fig. 29.

It is found that the diffraction efficiency of 0^{th} order was less than 10% for incident angle 57° in sinusoidal and 47° in rectangular surface relief thin grating. The 1^{st} and higher order can be collected by the waveguide. Further, similar studies have been conducted for a number of gratings (small period surface relief grating, high Δn small period surface relief grating) and polarization gratings. In comparison, it was observed that polarization and surface relief grating show similar results when their thickness parameters are in the same regime. For the application of solar concentrators, the surface relief gratings are more suitable than polarization grating. Large period grating shows high diffraction efficiency for large incident angle variations.

Diffraction-based PLC with waveguide can also be used to concentrate the light with spectral selectivity and transmit the other spectral range, based on the application. Ameen Elikkotti et al., in 2018 fabricated a planer grating-based subwavelength broadband concentrator as a BIPV window element, to generate electricity and decrease the cooling load by reducing the solar heat gain [87]. They fabricated the grating in silicon nitride with a high refractive coating on top of the grating and the waveguide layer below it. The grating parameters and waveguide material have been chosen so that they can filter the infrared light from the solar spectra. The diffraction angle for visible light is less than the critical angle of the waveguide material making the visible region pass through. The diffraction angle is more than the critical angle for the infrared region, so it deviates towards the edge to generate electricity, as shown in Fig. 30. In Fig. 30, Λ is the grating period, a is grading width, t_g is grating thickness and t_1 is layer thickness and the glass is used as the waveguide.

The maximum concentration ratio is given by Ref. [88],

$$C_{max}(\lambda) \approx \frac{2r_d}{1 - r_{dt}}\tan(\Theta) \tag{19}$$

Where $C_{max}(\lambda)$ is maximum concentration ratio for the wavelength λ, r_d is diffraction efficiency of incident light in ± transmission mode, r_{dt} is the diffraction efficiency of + transmission order into - transmission order and vice versa, and θ is the diffraction angle. In their findings, the optical guiding efficiency obtained was 0.72%, the solar conversion efficiency was 0.65%, and visible light transmission was 64.9% on average.

In 2017, Céline Michel et al. proposed a design that uses the combination of lens, and diffraction grating, which couple the light into a waveguide, and it has v-groove light couplers in the focus plane, as

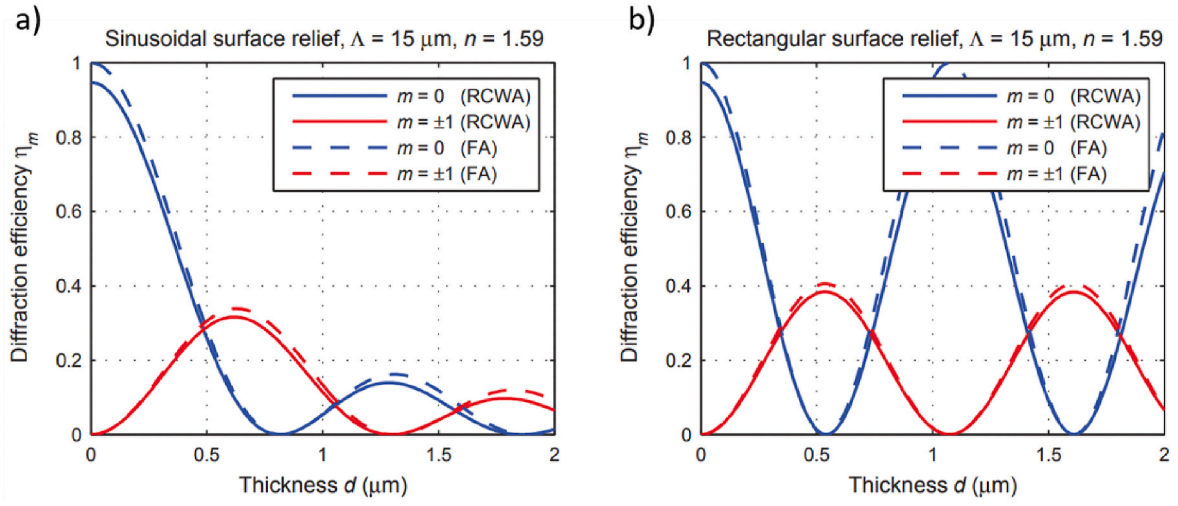

Fig. 28. Plot between diffraction efficiency as a function of d for sinusoidal and rectangular type grating, where n is the refractive index of grating material, FA is Fraunhofer approximation, and RCWA is rigorous coupled wave analysis wavelength λ = 633 nm. Source: Reproduced with permission from Ref. [84]. Copyright © 2011, OSA.

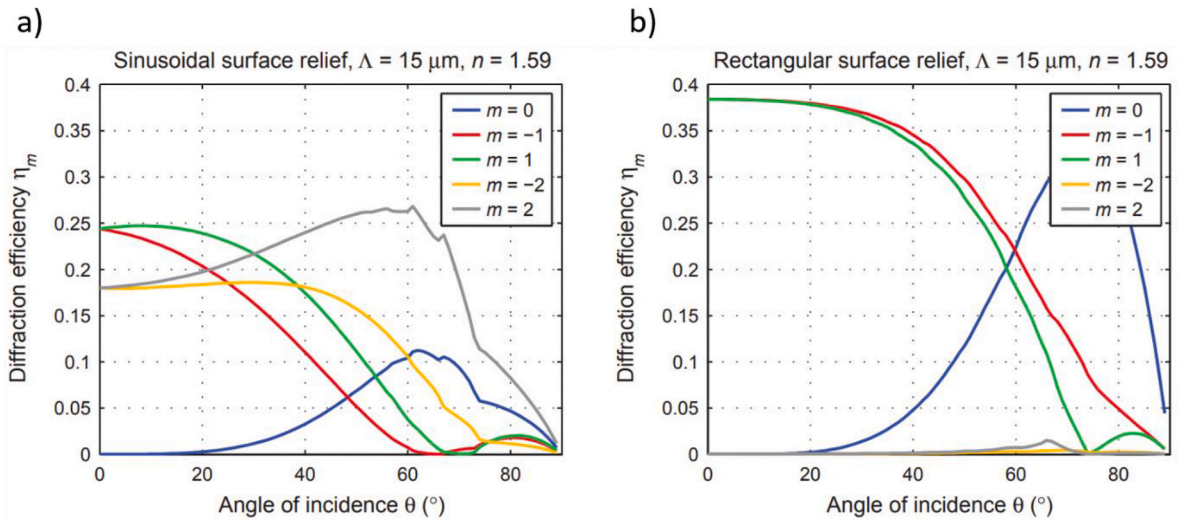

Fig. 29. Diffraction efficiency as a function of incident angle for thin surface grating of a) sinusoidal surface relief; b) rectangular surface relief. Source: Reproduced with permission from Ref. [84]. Copyright © 2011, OSA.

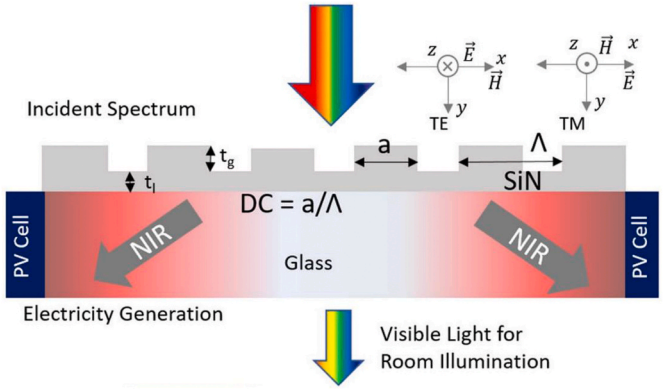

Fig. 30. Schematic illustrating the design of diffraction grating based PLC with spectral selectivity of light concentration (in the NIR region) and light transmissivity (in the visible region). Source: Reproduced with permission from Ref. [87]. Copyright © 2012, The Author(s), published by Springer Nature Limited.

shown in Fig. 31 [17]. There are two light focuses that fall on the two surfaces of reflective v-groove type microstructures on the bottom of the waveguide. Based on the wavelength, light splits and is redirected by total internal reflection towards edges. Two different types of DSSC with different absorption ranges in the visible region are placed on the two lateral edges to generate maximum electrical energy. Further, the infra-red range is eliminated in 0^{th} order diffraction, which only contributes to heat generation. The expected result was 73% optical efficiency and 5X concentration ratio and the experiment result agreed with the theory except for some optical losses incurred. A similar approach was also attempted by An-Chi Wei et al., using a micro-lens system and diffraction grating as a beam splitter [89].

A broad spectrum solar concentrator was designed by Tanant Waritanant et al., in 2012 [90]. As shown in Fig. 32, the concentrator design comprises two diffraction grating (blazed transmission and reflective grating). Transmission grating is on the top of the wedge prism-shaped waveguide, and reflective grating is on the bottom surface of the waveguide with some air gap to avoid decoupling of light. The system is designed so that the wavelength range does not undergo TIR in the wedge-shaped waveguide. Then, it is allowed to reflect at the reflective grating and return to the system for concentrating on the lateral side. Using equations of grating and critical angle, the wavelength that couples into the waveguide can be calculated as;

$$\Lambda_t\left(\cos\theta_w - \sqrt{n_w^2 - 1}.\sin\theta_w < \lambda_t < \Lambda_t\cos\theta_w n_w\right) \quad (20)$$

$$\Lambda_r\left(\cos\theta_w - \left(\sqrt{n_w^2 - 1} + n_w\right)\sin\theta_w < \lambda_r < \Lambda_r n_w\left(\cos\theta_w - \sin\theta_w\right)\right) \quad (21)$$

where, Λ_t and Λ_r are the grating period of transmission and reflective grating, λ_t , λ_r are the wavelength of light interacting with transmission and reflective grating. θ_w is wedge apex angle and n_w is the refractive index of the wedge prism. The transmission grating work for the shorter wavelength light (400 nm–600 nm) and reflection grating for longer wavelengths (600 nm–900 nm). The design achieved can have a collection efficiency of 53%, with a concentration ratio of 3.77. The angular tolerance achieved for 90% of collection efficiency was ±35° and ±3° in two planes of incidence, and for 50% it is ±53° and ±9° (if the length to thickness ratio is more than 7).

Yet another integrated approach to diffraction-based PLC was done by Mikhail Vasiliev et al., in 2016. They fabricated and conducted a study in a combination of the diffraction grating and LSC-based PLC, as a BIPV element for transparent window integration [34]. The design and principle of working are similar to common diffraction grating-based PLC, in which additional layers of epoxy-luminophore composite interlayer and high spectral selective solar-control coating (Viracon VNE2463) are also incorporated, as shown in Fig. 33a. The diffraction gratings provide higher diffraction angles in the NIR region, making it guide towards the solar cell placed at the lateral faces. Here the window glass is used as a waveguide on which diffraction grating is fabricated by a photolithography-assisted coating lift-off process. The light in the visible region is at lower angles (zero-order diffraction), making it pass through the whole window system (as shown in Fig. 33b). The additional solar-control coating back reflects the light in the NIR region from the rear end at all angles. The epoxy-luminophore composite interlayer provides additional energy harvest by down-converting the UV spectral region. The light transmission in the visible region of the system is high, as revealed in the photograph, Fig. 33c. Experimental outdoor test results show a maximum PCE of (3.041 ± 0.005) % in a 10 cm × 10 cm system aligned vertically in the sun's direction. Compared to normal LSC (flat plate glass structure with luminescent interlayer) of size 50 cm × 50 cm, which generates 2.43 W, the system with both diffraction grating and luminescent layer generated 3.64 W, with a power conversion efficiency of 2.08% (used $CuInSe_2$ solar cells, working at real operating temperature in excess of 40 °C).

Condensed review and research limitations: From the review, it is

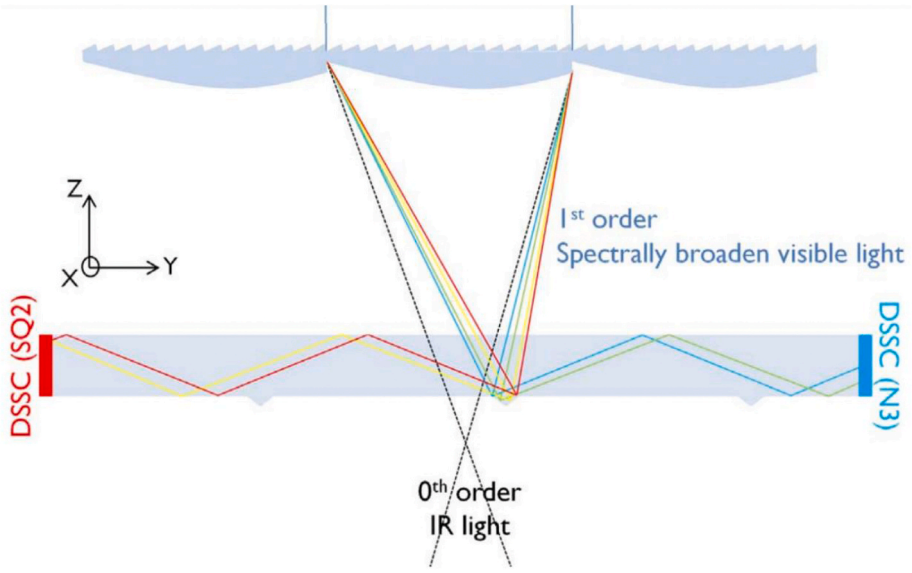

Fig. 31. Schematic of diffraction-based PLC with v-groove coupler waveguide, showing spectral splitting based light collection and concentration. Source: Reproduced with permission from Ref. [17]. Copyright © 2017, Elsevier.

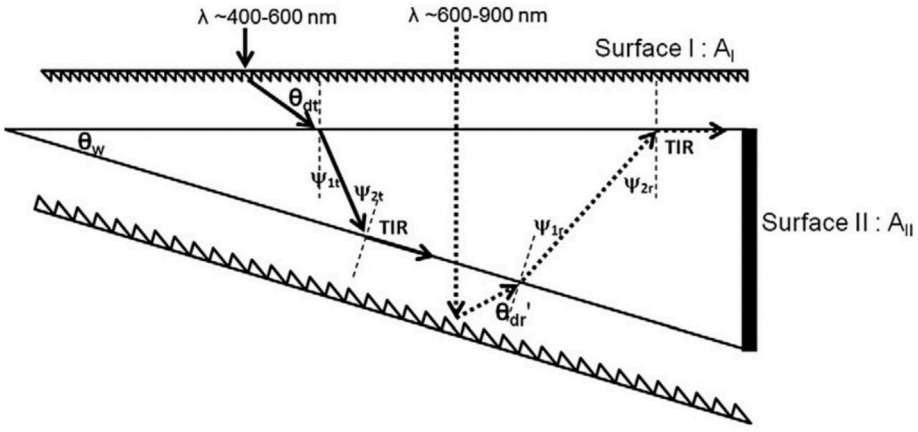

Fig. 32. Schematic showing double grating (transmission and reflection gratings) based PLC with wedge-shaped guiding layer. Source: Reproduced with permission from Ref. [90]. Copyright © 2012, Elsevier.

evident that the existing design innovations conducted on planar waveguide-based CPVs have more prominence for geometric optics-based designs. However, the primary design challenge is to achieve a scalable design solution without compromising on geometrical concentration, optical efficiency, and solar acceptance. More importantly, it is observed that very few design solutions are reported for larger optics areas (i.e., effective size greater than 10 cm). Even though designs with very high theoretical geometrical concentration (~1000X) ratios are reported, the translation to fabrication and assembly of flawless optics systems seem to be a major challenge. The reported geometrical concentration factor, optical efficiency, and design systems are well summarized and tabulated in the review for comparative analysis. The lower solar acceptance angle poses a severe drawback for geometric optics-based and diffraction-based PLCs, limiting their adaptability in built environments with limited room for solar tracking. Hence, it is observed that LSC-based PLCs are more explored for CPV systems for BIPV applications (glazing solutions) due to their simple architecture, unconditional solar acceptance, ability to collect diffuse radiations, and the possibility of aesthetic improvements. However, the reported power conversion efficiency and optical efficiency for LSC-based CPV systems seem to curb the enthusiasm. Hence, vigorous efforts on optical materials screening and development in hand with system design modulations are necessary for LSC-based CPV systems in the future. The involvement of multi-mode light collection approaches, for example, integrating LSC with geometrical/diffraction optics is a promising approach to improve the system efficiency. Further, it is observed that the current status of research is limited to lab-scale demonstrations, with very few successful on-field deployments. Hence, future research directions can be streamlined to cater to standard glazing size with required material stability, mechanical strength, and thermal characteristics to enable faster technology commercialization. When compared to geometric optics-based and LSC-based CPV systems, diffraction-based solar concentrators are less explored in the field. However, the additional prospectus of wavelength filtering and redirecting can be explored more in the future and can be aligned well with other PLC technologies.

Future Prospects, Practical impacts & Challenges: With a global trend of reduced cost of photovoltaic installations [91], the significance of CPV systems have shifted from large power plant installations to its applicability in built environments. To accomplish the targets of the Paris climate agreement [92] and the recent COP26 meeting [93], it is of utmost essential to meet the energy demand in industry, commercial and residential building spaces by adopting renewable energy technologies

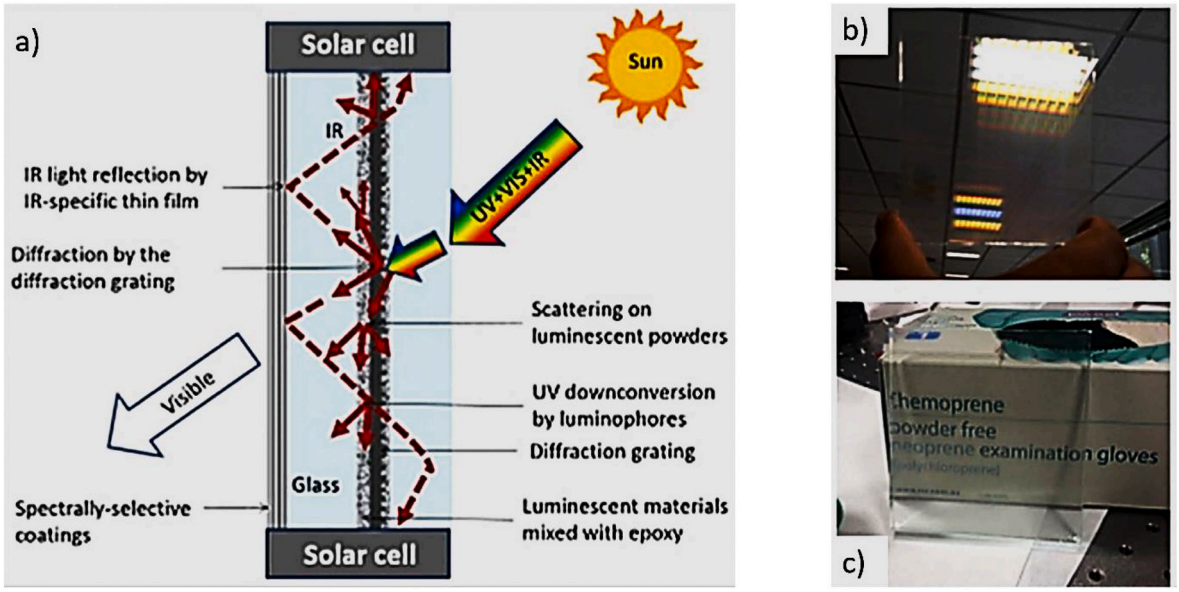

Fig. 33. a) Schematic representation of the design architecture in a diffraction-based hybrid energy-harvesting PLC, incorporating both diffraction based (by the diffraction grating layer) and luminescent-based (by the epoxy-luminophore composite layer) light concentration; b) Photograph of a 100 mm × 100 mm grating (1D, 20 μm-period diffraction grating); c) Photograph of the 100 mm × 100 mm grating (1D, 20 μm-period diffraction grating) embedded to glass with the epoxy-luminophore composite layer of thickness 0.5 mm, revealing its high visible light transmission. Source: Reproduced with permission from Ref. [34]. Copyright © 2016, The Authors(s), published by Springer Nature Limited.

for Decentralised Distributed Generation (DDG). Most of the initiatives to tackle this vast energy demand rely on the efficient utilisation of solar energy, where light energy management is an essential prerequisite. The role of PV in buildings [94–96], building-vehicle integration [97,98], and urban environments [99,100] for city planning have been indicated extensively for the past five years globally. Compact CPV systems for BIPV, solar urban planning and developments, and solar vehicles are some of the major focuses in this regard. In that, BIPV is considered the most promising approach to utilise built spaces for solar energy conversion, where conventional building elements are replaced with resembling PV products [101]. This can promote the widespread construction of energy efficient solar/green buildings, which are considered the backbone of DDG.

In this context, waveguide-based compact PLC systems play a pivotal role in developing efficient light trapping and guiding systems. Such systems are of utmost importance for sustainable light energy management and BIPV product development from the point of view of energy efficiency (through light concentration) and aesthetic appeal. Because of their compact design architecture, PV concealed architecture, aesthetic inclusions, and reduction in size and structural elements compared to conventional CPV technologies, waveguide-based planar CPV systems can exhibit superiority in BIPV systems. However, waveguide-based planar CPV systems are considered to be in their infant stage in the technological upfront of PV solutions. The requirement of complex R&D development and product-specific manufacturing automation is a major technical hindrance to product development. Also, the BIPV implementation challenges, the requirement of product multi-specifications, and vigorous technical planning for deployments such as building information modeling and solar-specific architectural innovations [102] create an ecosystem of both opportunity and challenges for the future.

3. Summary

Recently, waveguide-based planar solar concentrators have been influencing the research and development sector of Concentrated Photovoltaics (CPV) as a shaped-up technology due to its applicability in compact built environments. However, the sector is scattered with many methodological advancements, over the last two decades. In order to congregate and evaluate the technical specifications, advancement, limitations, and challenges for the applicability, the present review has been chronicled. The review is majorly focused on the present state of waveguide-based PLC in the frame of reference of PLC optics and optical material design, highlighting the existing types (based on geometric optics, LSC, and diffraction gratings). The systematic comparison of optics and optical material design parameters, the primary results, and the merit of different waveguide-based PLC systems have been explored within this review, which hopes to serve as a ready reference for its evaluation and adoption in CPV systems.

Credit author statement

Animesh M. Ramachandran conducted the detailed literature survey, analysed, organised and wrote the manuscript; Sangeetha M. S, Adhithya S. Thampi and Manjit Singh assisted the first author in conducting the required literature survey and supported manuscript preparation; Adersh Asok conceived the idea, and supervised the manuscript drafting.

Declaration of competing interest

The authors declare that they have no known competing financial interests or personal relationships that could have appeared to influence the work reported in this paper.

Data availability

Data will be made available on request.

Acknowledgments

Authors acknowledge the Department of Science and Technology, Govt. of India for the financial support under DST-INSPIRE faculty award scheme.

References

[1] B.E. Layton, A comparison of energy densities of prevalent energy sources in units of joules per cubic meter, Int. J. Green Energy 5 (6) (2008) 438–455, https://doi.org/10.1080/15435070802498036.

[2] R.R. Hernandez, M.K. Hoffacker, M.L. Murphy-Mariscal, G.C. Wu, M.F. Allen, Solar energy development impacts on land cover change and protected areas, Proc. Natl. Acad. Sci. U. S. A. 112 (2015) 13579–13584, https://doi.org/10.1073/PNAS.1517656112/SUPPL_FILE/PNAS.1517656112.ST05.DOCX.

[3] D.J. van de Ven, I. Capellan-Peréz, I. Arto, I. Cazcarro, C. de Castro, P. Patel, M. Gonzalez-Eguino, The potential land requirements and related land use change emissions of solar energy, Sci. Rep. 11 (2021) 1–12, https://doi.org/10.1038/s41598-021-82042-5.

[4] D. Turney, V. Fthenakis, Environmental impacts from the installation and operation of large-scale solar power plants, Renew. Sustain. Energy Rev. 15 (2011) 3261–3270, https://doi.org/10.1016/J.RSER.2011.04.023.

[5] PV FAQs: what's new in concentrating PV? (Miscellaneous) | OSTI.GOV. https://www.osti.gov/biblio/15015121. (Accessed 1 September 2022).

[6] K. Shanks, S. Senthilarasu, T.K. Mallick, Optics for concentrating photovoltaics: trends, limits and opportunities for materials and design, Renew. Sustain. Energy Rev. 60 (2016) 394–407, https://doi.org/10.1016/J.RSER.2016.01.089.

[7] V.K. Sharma, R. Singh, A. Gehlot, D. Buddhi, S. Braccio, N. Priyadarshi, et al., Imperative role of photovoltaic and concentrating solar power technologies towards renewable energy generation, Int. J. Photoenergy (2022) 1–13, https://doi.org/10.1155/2022/3852484, 3852484.

[8] X. Ma, H. Zheng, S. Liu, A review on solar concentrators with multi-surface and multielement combinations, J. Daylighting 6 (2019) 80–96, https://doi.org/10.15627/JD.2019.9.

[9] W.T. Xie, Y.J. Dai, R.Z. Wang, K. Sumathy, Concentrated solar energy applications using Fresnel lenses: a review, Renew. Sustain. Energy Rev. 15 (2011) 2588–2606, https://doi.org/10.1016/J.RSER.2011.03.031.

[10] M. Khamooshi, H. Salati, F. Egelioglu, A. Hooshyar Faghiri, J. Tarabishi, S. Babadi, A review of solar photovoltaic concentrators, Int. J. Photoenergy 958521 (2014) 1–17, https://doi.org/10.1155/2014/958521.

[11] M. Buljan, J. Mendes-Lopes, P. Benítez, J.C. Miñano, Recent trends in concentrated photovoltaics concentrators' architecture, J. Photon. Energy 4 (2014), 040995, https://doi.org/10.1117/1.JPE.4.040995.

[12] S. El Himer, S. El Ayane, S. El Yahyaoui, J.P. Salvestrini, A. Ahaitouf, Photovoltaic concentration: research and development, Energies 13 (2020) 5721, https://doi.org/10.3390/EN13215721.

[13] N.X. Tien, S. Shin, A novel concentrator photovoltaic (CPV) system with the improvement of irradiance uniformity and the capturing of diffuse solar radiation, Appl. Sci. 6 (2016) 251, https://doi.org/10.3390/APP6090251.

[14] L. Wang, Z. Yuan, Y. Zhao, Z. Guo, Review on development of small point-focusing solar concentrators, J. Therm. Sci. 28 (2019) 929–947, https://doi.org/10.1007/S11630-019-1134-4.

[15] K.T. Lee, Y. Yao, J. He, B. Fisher, X. Sheng, M. Lumb, et al., Concentrator photovoltaic module architectures with capabilities for capture and conversion of full global solar radiation, Proc. Natl. Acad. Sci. U. S. A. 113 (2016), https://doi.org/10.1073/PNAS.1617391113. E8210–8.

[16] M. Alves, A. Pérez-Rodríguez, P.J. Dale, C. Domínguez, S. Sadewasser, Thin-film micro-concentrator solar cells, J Phys Energy 2 (2019), 012001, https://doi.org/10.1088/2515-7655/AB4289.

[17] C. Michel, P. Blain, L. Clermont, F. Languy, C. Lenaerts, K. Fleury-Frenette, et al., Waveguide solar concentrator design with spectrally separated light, Sol. Energy 157 (2017) 1005–1016, https://doi.org/10.1016/J.SOLENER.2017.09.015.

[18] C.-H. Kuo, T.-C. Teng, Y.-J. Li, Planar solar concentrator composed of stacked waveguides with arc-segment structures and movable receiving assemblies, Opt Express 28 (2020) 34362–34377, https://doi.org/10.1364/OE.405909.

[19] University of Rochester | arpa-e.energy.gov. https://arpa-e.energy.gov/technologies/projects/planar-light-guide-concentrated-photovoltaics accessed June 6, 2022.

[20] P. Moraitis, R.E.I. Schropp, W.G.J.H.M. van Sark, Nanoparticles for luminescent solar concentrators - a review, Opt. Mater. (Amst) 84 (2018) 636–645, https://doi.org/10.1016/J.OPTMAT.2018.07.034.

[21] A. Kim, A. Hosseinmardi, P.K. Annamalai, P. Kumar, R. Patel, Review on colloidal quantum dots luminescent solar concentrators, ChemistrySelect 6 (2021) 4948–4967, https://doi.org/10.1002/SLCT.202100674.

[22] A. Elikkottil, A. Elikkottil, M.H. Tahersima, S. Gupta, S. Gupta, V.J. Sorger, et al., Silicon nitride grating based planar spectral splitting concentrator for NIR light harvesting, Opt Express 28 (2020) 21474–21480, https://doi.org/10.1364/OE.390666.

[23] H. Baig, K.C. Heasman, T.K. Mallick, Non-uniform illumination in concentrating solar cells, Renew. Sustain. Energy Rev. 16 (2012) 5890–5909, https://doi.org/10.1016/J.RSER.2012.06.020.

[24] Morgan solar closes $16.5 million in first tranche of series B funding – news. https://eepower.com/news/morgan-solar-closes-16-5-million-in-first-tranche-of-series-b-funding/# accessed June 6, 2022.

[25] A.J. Labelle, N. Coish, M. Sinclair, J. Slonetsky, S. Myrskog, J.P. Morgan, Anti-soiling coatings for Sun Simba concentrated photovoltaic (CPV) modules, AIP Conf. Proc. 1766 (2016), 040003, https://doi.org/10.1063/1.4962080.

[26] Timeline — morgan solar. https://morgansolar.com/timeline accessed June 5, 2022.

[27] Lumiduct | Wellsun. https://www.wellsun.nl/lumiduct accessed June 5, 2022.

[28] Smart window. https://www.eni.com/en-IT/smart-home/smart-window-eni.html accessed June 5, 2022.

[29] The holy grail: full transparent window and solar panel at the same time – Science for Society. https://hermanvandenbosch.com/2019/04/03/the-holy-grail-full-transparent-window-and-solar-panel-at-the-same-time/ accessed June 6, 2022.

[30] J.W.E. Wiegman, E. Van Der Kolk, Building integrated thin film luminescent solar concentrators: detailed efficiency characterization and light transport modelling, Sol. Energy Mater. Sol. Cells 103 (2012) 41–47, https://doi.org/10.1016/J.SOLMAT.2012.04.016.

[31] M. Rafiee, S. Chandra, H. Ahmed, S.J. McCormack, An overview of various configurations of Luminescent Solar Concentrators for photovoltaic applications, Opt. Mater. (Amst) 91 (2019) 212–227, https://doi.org/10.1016/J.OPTMAT.2019.01.007.

[32] F. Meinardi, F. Bruni, S. Brovelli, Luminescent solar concentrators for building-integrated photovoltaics, Nat. Rev. Mater. 2 (2017 212 2017) 1–9, https://doi.org/10.1038/natrevmats.2017.72.

[33] G. Griffini, Host matrix materials for luminescent solar concentrators: recent achievements and forthcoming challenges, Front Mater. 6 (2019) 29, https://doi.org/10.3389/FMATS.2019.00029/BIBTEX.

[34] M. Vasiliev, R. Alghamedi, M. Nur-E-Alam, K. Alameh, Photonic microstructures for energy-generating clear glass and net-zero energy buildings, Sci. Rep. 6 (2016) 1–14, https://doi.org/10.1038/srep31831.

[35] A.C. Wei, Z.R. Chen, J.R. Sze, Planar solar concentrator with a v-groove array for a side-absorption concentrated photovoltaic system, Optik (Stuttg) 127 (2016) 10858–10867, https://doi.org/10.1016/J.IJLEO.2016.08.045.

[36] L. Van Dijk, E.A.P. Marcus, A.J. Oostra, R.E.I. Schropp, M. Di Vece, 3D-printed concentrator arrays for external light trapping on thin film solar cells, Sol. Energy Mater. Sol. Cells 139 (2015) 19–26, https://doi.org/10.1016/J.SOLMAT.2015.03.002.

[37] J.P. Morgan, Application Data Provisional Application No. 60/915, vol. 207, 2007, p. 901.

[38] What we presented at CPV-7: the gen 3 sun Simba optic | the unofficial morgan solar weblog. https://morgansolar.wordpress.com/2011/04/27/what-we-presented-at-cpv-7-the-gen-3-sun-simba-optic/ accessed May 26, 2022.

[39] E.J. Tremblay, J.H. Karp, J.E. Ford, Planar micro-optic solar concentrator, Opt. Express 18 (2010) 1122–1133, https://doi.org/10.1364/OE.18.001122.

[40] M.C. Chien, Y.L. Tung, C.H. Tien, Ultracompact backlight-reversed concentration optics, Appl. Opt. 48 (2009) 4142–4148, https://doi.org/10.1364/AO.48.004142.

[41] S. Bouchard, S. Thibault, Planar waveguide concentrator used with a seasonal tracker, Appl. Opt. 51 (2012) 6848–6854, https://doi.org/10.1364/AO.51.006848.

[42] B. Li, H. Lin, P. Xie, Y. Liu, Total internal reflection-based planar waveguide solar concentrator with symmetric air prisms as couplers, Opt Express 22 (2014) A1389–A1398, https://doi.org/10.1364/OE.22.0A1389.

[43] D. Moore, G. Schmidt, B. Unger, Concentrated photovoltaics stepped planar light guide, Proc. SPIE-Int. Soc. Opt. Eng. 7652 (2010) 382–387, https://doi.org/10.1117/12.877725.

[44] J.R. Ong, H.S. Chu, C.E. Png, K. Ong, L.K. Bera, Planar micro-optic solar concentrator for natural daylighting systems in tropics, in: 2016 Asian Conf Energy, Power Transp Electrif ACEPT, 2016, pp. 1–5, https://doi.org/10.1109/ACEPT.2016.7811514.

[45] N.H. Vu, T.T. Pham, S. Shin, Large scale spectral splitting concentrator photovoltaic system based on double flat waveguides, Energies 13 (2020) 2360, https://doi.org/10.3390/EN13092360.

[46] V. Zagolla, D. Dominé, E. Tremblay, C. Moser, L.H. Slooff, E.E. Bende, et al., Self-tracking solar concentrator with an acceptance angle of 32°, Opt. Express 22 (2014) A1880–A1894, https://doi.org/10.1364/OE.22.0A1880.

[47] J. Kim, J. Lee, R. Dhakal, Bio-inspired thin and flat solar concentrator for efficient, wide acceptance angle light collection, Appl. Opt. 53 (2014) 306–315, https://doi.org/10.1364/AO.53.000306.

[48] I. Parola, D. Zaremba, R. Evert, J. Kielhorn, F. Jakobs, M.A. Illarramendi, et al., High performance fluorescent fiber solar concentrators employing double–doped polymer optical fibers, Sol. Energy Mater. Sol. Cells 178 (2018) 20–28, https://doi.org/10.1016/J.SOLMAT.2018.01.013.

[49] W. GJHM van Sark, K.W. Barnham, L.H. Slooff, A.J. Chatten, A. Büchtemann, A. Meyer, et al., Luminescent Solar Concentrators - a review of recent results, Opt. Express 16 (2008) 21773–21792, https://doi.org/10.1364/OE.16.021773.

[50] L. Zdražil, S. Kalytchuk, M. Langer, R. Ahmad, J. Pospíšil, O. Zmeškal, et al., Transparent and low-loss luminescent solar concentrators based on self-trapped exciton emission in lead-free double perovskite nanocrystals, ACS Appl. Energy Mater. 4 (2021) 6445–6453, https://doi.org/10.1021/ACSAEM.1C00360/SUPPL_FILE/AE1C00360_SI_001.PDF.

[51] R.H. Inman, G.V. Shcherbatyuk, D. Medvedko, A. Gopinathan, S. Ghosh, W. H. Weber, et al., Cylindrical luminescent solar concentrators with near-infrared quantum dots, Opt. Express 19 (2011) 24308–24313, https://doi.org/10.1364/OE.19.024308.

[52] J. Bomm, A. Büchtemann, A.J. Chatten, R. Bose, D.J. Farrell, N.L.A. Chan, et al., Fabrication and full characterization of state-of-the-art quantum dot luminescent solar concentrators, Sol. Energy Mater. Sol. Cells 95 (2011) 2087–2094, https://doi.org/10.1016/J.SOLMAT.2011.02.027.

[53] I. Coropceanu, M.G. Bawendi, Core/shell quantum dot based luminescent solar concentrators with reduced reabsorption and enhanced efficiency, Nano Lett. 14 (2014) 4097–4101, https://doi.org/10.1021/NL501627E.

[54] P. Barik, M. Pradhan, Plasmonic luminescent solar concentrator, Sol. Energy 216 (2021) 61–74, https://doi.org/10.1016/J.SOLENER.2021.01.018.

[55] D. Dutta, S. Chowdhury, C.T. Yang, V.R. Bhethanabotla, B. Joseph, Controlling metal-enhanced fluorescence using bimetallic nanoparticles, Surf. Plasmon.

Enhanc. Coupl. Control Fluoresc. (2017) 73–89, https://doi.org/10.1002/9781119325161.CH4.
[56] S. Chandra, J. Doran, S.J. McCormack, M. Kennedy, A.J. Chatten, Enhanced quantum dot emission for luminescent solar concentrators using plasmonic interaction, Sol. Energy Mater. Sol. Cells 98 (2012) 385–390, https://doi.org/10.1016/J.SOLMAT.2011.11.030.
[57] S.M. El-Bashir, F.M. Barakat, M.S. Alsalhi, Metal-enhanced fluorescence of mixed coumarin dyes by silver and gold nanoparticles: towards plasmonic thin-film luminescent solar concentrator, J. Lumin. 143 (2013) 43–49, https://doi.org/10.1016/J.JLUMIN.2013.04.029.
[58] A. Sanguineti, A. Monguzzi, G. Vaccaro, F. Meinardi, E. Ronchi, M. Moret, et al., NIR emitting ytterbium chelates for colourless luminescent solar concentrators, Phys. Chem. Chem. Phys. 14 (2012) 6452–6455, https://doi.org/10.1039/C2CP40791D.
[59] F. Meinardi, H. McDaniel, F. Carulli, A. Colombo, K.A. Velizhanin, N.S. Makarov, et al., Highly efficient large-area colourless luminescent solar concentrators using heavy-metal-free colloidal quantum dots, Nat. Nanotechnol. 10 (2015) 878–885, https://doi.org/10.1038/nnano.2015.178.
[60] C. Li, W. Chen, D. Wu, D. Quan, Z. Zhou, J. Hao, et al., Large Stokes shift and high efficiency luminescent solar concentrator incorporated with CuInS2/ZnS quantum dots, Sci. Rep. 5 (2015) 1–9, https://doi.org/10.1038/srep17777.
[61] M.R. Bergren, N.S. Makarov, K. Ramasamy, A. Jackson, R. Guglielmetti, H. McDaniel, High-performance CuInS2 quantum dot laminated glass luminescent solar concentrators for windows, ACS Energy Lett. 3 (2018) 520–525, https://doi.org/10.1021/ACSENERGYLETT.7B01346/SUPPL_FILE/NZ7B01346_SI_001.PDF.
[62] N.D. Bronstein, Y. Yao, L. Xu, E. O'Brien, A.S. Powers, V.E. Ferry, et al., Quantum dot luminescent concentrator cavity exhibiting 30-fold concentration, ACS Photonics 2 (2015) 1576–1583, https://doi.org/10.1021/ACSPHOTONICS.5B00334/ASSET/IMAGES/PH-2015-00334Q_M004.GIF.
[63] G.D. Gutierrez, I. Coropceanu, M.G. Bawendi, T.M. Swager, A low reabsorbing luminescent solar concentrator employing π–conjugated polymers, Adv. Mater. 28 (2016) 497–501, https://doi.org/10.1002/ADMA.201504358.
[64] Y. Zhou, D. Benetti, Z. Fan, H. Zhao, D. Ma, A.O. Govorov, et al., Near infrared, highly efficient luminescent solar concentrators, Adv. Energy Mater. 6 (2016), 1501913, https://doi.org/10.1002/AENM.201501913.
[65] M. Vasiliev, K. Alameh, M.A. Badshah, S.M. Kim, M. Nur-E-Alam, Semi-transparent energy-harvesting solar concentrator windows employing infrared transmission-enhanced glass and large-area microstructured diffractive elements, Photonics 5 (2018) 25, https://doi.org/10.3390/PHOTONICS5030025.
[66] H. Zhao, D. Benetti, L. Jin, Y. Zhou, F. Rosei, A. Vomiero, Absorption enhancement in "giant" core/alloyed–shell quantum dots for luminescent solar concentrator, Small 12 (2016) 5354–5365, https://doi.org/10.1002/SMLL.201600945.
[67] H. Li, K. Wu, J. Lim, H.J. Song, V.I. Klimov, Doctor-blade deposition of quantum dots onto standard window glass for low-loss large-area luminescent solar concentrators, Nat. Energy 1 (2016), 16157, https://doi.org/10.1038/nenergy.2016.157.
[68] H. Zhao, R. Sun, Z. Wang, K. Fu, X. Hu, Y. Zhang, Zero-dimensional perovskite nanocrystals for efficient luminescent solar concentrators, Adv. Funct. Mater. 29 (2019), 1902262, https://doi.org/10.1002/ADFM.201902262.
[69] V. Kataria, D.S. Mehta, Multispectral harvesting rare-earth oxysulphide based highly efficient transparent luminescent solar concentrator, J. Rare Earths 40 (2022) 41–48, https://doi.org/10.1016/J.JRE.2020.09.021.
[70] S. Flores Daorta, A. Proto, R. Fusco, L. Claudio Andreani, M. Liscidini, Cascade luminescent solar concentrators, Appl. Phys. Lett. 104 (2014), 153901, https://doi.org/10.1063/1.4871481.
[71] J. Zhang, M. Wang, Y. Zhang, H. He, W. Xie, M. Yang, et al., Optimization of large-size glass laminated luminescent solar concentrators, Sol. Energy 117 (2015) 260–267, https://doi.org/10.1016/J.SOLENER.2015.05.004.
[72] N. Aste, L.C. Tagliabue, C. Del Pero, D. Testa, R. Fusco, Performance analysis of a large-area luminescent solar concentrator module, Renew. Energy 76 (2015) 330–337, https://doi.org/10.1016/J.RENENE.2014.11.026.
[73] E. Tatsi, G. Fortunato, B. Rigatelli, G. Lyu, S. Turri, R.C. Evans, et al., Thermoresponsive host polymer matrix for self-healing luminescent solar concentrators, ACS Appl. Energy Mater. 3 (2020) 1152–1160, https://doi.org/10.1021/ACSAEM.9B02196/SUPPL_FILE/AE9B02196_SI_001.PDF.
[74] L. Zdražil, S. Kalytchuk, K. Holá, M. Petr, O. Zmeškal, Š. Kment, et al., A carbon dot-based tandem luminescent solar concentrator, Nanoscale 12 (2020) 6664–6672, https://doi.org/10.1039/C9NR10029F.
[75] C. Papucci, A. Dessì, C. Coppola, A. Sinicropi, G. Santi, M. Di Donato, et al., Benzo [1,2-d:4,5-d′]bisthiazole fluorophores for luminescent solar concentrators: synthesis, optical properties and effect of the polymer matrix on the device performances, Dyes Pigments 188 (2021), 109207, https://doi.org/10.1016/J.DYEPIG.2021.109207.
[76] S.M. El-Bashir, F.M. Barakat, M.S. AlSalhi, Double layered plasmonic thin-film luminescent solar concentrators based on polycarbonate supports, Renew. Energy 63 (2014) 642–649, https://doi.org/10.1016/J.RENENE.2013.10.014.
[77] K. Nikolaidou, S. Sarang, C. Hoffman, B. Mendewala, H. Ishihara, J.Q. Lu, et al., Hybrid perovskite thin films as highly efficient luminescent solar concentrators, Adv. Opt. Mater. 4 (2016) 2126–2132, https://doi.org/10.1002/ADOM.201600634.
[78] C. Tummeltshammer, M. Portnoi, S.A. Mitchell, A.T. Lee, A.J. Kenyon, A. B. Tabor, et al., On the ability of Förster resonance energy transfer to enhance luminescent solar concentrator efficiency, Nano Energy 32 (2017) 263–270, https://doi.org/10.1016/J.NANOEN.2016.11.058.
[79] S.J. Ha, J.H. Kang, D.H. Choi, S.K. Nam, E. Reichmanis, J.H. Moon, Upconversion-assisted dual-band luminescent solar concentrator coupled for high power conversion efficiency photovoltaic systems, ACS Photonics 5 (2018) 3621–3627, https://doi.org/10.1021/ACSPHOTONICS.8B00498/SUPPL_FILE/PH8B00498_SI_001.PDF.
[80] K. Wu, H. Li, V.I. Klimov, Tandem luminescent solar concentrators based on engineered quantum dots, Nat. Photonics 12 (2018) 105–110, https://doi.org/10.1038/s41566-017-0070-7.
[81] X. Gong, S. Zheng, X. Zhao, A. Vomiero, Engineering high-emissive silicon-doped carbon nanodots towards efficient large-area luminescent solar concentrators, Nano Energy 101 (2022), 107617, https://doi.org/10.1016/J.NANOEN.2022.107617.
[82] R. Winston, W.T. Welford, Nonconventional optical systems and the brightness theorem, Appl. Opt. 21 (1982) 1531–1533, https://doi.org/10.1364/AO.21.001531.
[83] R. Winston, W.T. Welford, Efficiency of nonimaging concentrators in the physical-optics model, JOSA 72 (1982) 1564–1566, https://doi.org/10.1364/JOSA.72.001564.
[84] T.M. de Jong, D.K. G de Boer, C.W. M Bastiaansen, M. Xu, D.K. G de Boer, C. M. van Heesch, et al., Surface-relief and polarization gratings for solar concentrators, Opt. Express 19 (2011) 15127–15142, https://doi.org/10.1364/OE.19.015127.
[85] M.G. Moharam, T.K. Gaylord, Thin and thick gratings: terminology clarification, Appl. Opt. 20 (1981) 3271–3273, https://doi.org/10.1364/AO.20.003271.
[86] W.R. Klein, B.D. Cook, Unified approach to ultrasonic light diffraction, IEEE Trans. Son. Ultrason. 14 (1967) 123–134, https://doi.org/10.1109/T-SU.1967.29423.
[87] A. Elikkottil, M.H. Tahersima, M.V.N.S. Gupta, R. Maiti, V.J. Sorger, B. Pesala, A spectrally tunable dielectric subwavelength grating based broadband planar light concentrator, Sci. Rep. 9 (2019) 1–9, https://doi.org/10.1038/s41598-019-48025-3.
[88] B. Pesala, High-contrast grating based planar light concentrators, Proc. SPIE 8270 (2012) 132–138, https://doi.org/10.1117/12.924080, 8270, High Contrast Metastructures.
[89] A.C. Wei, W.J. Chang, J.R. Sze, A side-absorption concentrated module with a diffractive optical element as a spectral-beam-splitter for a hybrid-collecting solar system, Energies 13 (2020) 192, https://doi.org/10.3390/EN13010192.
[90] T. Waritanant, S. Boonruang, T.Y. Chung, High angular tolerance thin profile solar concentrators designed using a wedge prism and diffraction grating, Sol. Energy 87 (2013) 35–41, https://doi.org/10.1016/J.SOLENER.2012.10.009.
[91] Renewable power generation costs in 2021. https://irena.org/publications/2022/Jul/Renewable-Power-Generation-Costs-in-2021. (Accessed 2 September 2022).
[92] The Paris agreement | UNFCCC, in: https://unfccc.int/process-and-meetings/the-paris-agreement/the-paris-agreement. (Accessed 1 September 2022).
[93] COP26: together for our planet | united nations. https://www.un.org/en/climatechange/cop26. (Accessed 1 September 2022).
[94] Y.A. Sheikh, M.U. Maqbool, A.D. Butt, A.R. Bhatti, A.B. Awan, K.N. Paracha, et al., Impact of rooftop photovoltaic on energy demand of a building in a hot semi-arid climate, J. Renew. Sustain. Energy 13 (2021), 065101, https://doi.org/10.1063/5.0063044.
[95] A. Arabkoohsar, G. Xie, J. Wei, A. Asok, A. Behzadi, O. Mahian, Perspectives and review of photovoltaic-thermal panels in net-zero energy buildings, J. Therm. Anal. Calorim. 147 (2022) 8621–8630, https://doi.org/10.1007/S10973-021-11191-6.
[96] H. Gholami, H.N. Røstvik, D. Müller-Eie, Holistic economic analysis of building integrated photovoltaics (BIPV) system: case studies evaluation, Energy Build. 203 (2019), 109461, https://doi.org/10.1016/J.ENBUILD.2019.109461.
[97] H. Martin, R. Buffat, D. Bucher, J. Hamper, M. Raubal, Using rooftop photovoltaic generation to cover individual electric vehicle demand—a detailed case study, Renew. Sustain. Energy Rev. 157 (2022), 111969, https://doi.org/10.1016/J.RSER.2021.111969.
[98] Y. Zhou, S. Cao, R. Kosonen, M. Hamdy, Multi-objective optimisation of an interactive buildings-vehicles energy sharing network with high energy flexibility using the Pareto archive NSGA-II algorithm, Energy Convers. Manag. 218 (2020), 113017, https://doi.org/10.1016/J.ENCONMAN.2020.113017.
[99] M. Formolli, S. Croce, D. Vettorato, R. Paparella, A. Scognamiglio, A.G. Mainini, et al., Solar energy in urban planning: lesson learned and recommendations from six Italian case studies, Appl. Sci. 12 (2022) 2950, https://doi.org/10.3390/APP12062950.
[100] Y. He, Y. Zhou, J. Yuan, Z. Liu, Z. Wang, G. Zhang, Transformation towards a carbon-neutral residential community with hydrogen economy and advanced energy management strategies, Energy Convers. Manag. 249 (2021), 114834, https://doi.org/10.1016/J.ENCONMAN.2021.114834.
[101] T.E. Kuhn, C. Erban, M. Heinrich, J. Eisenlohr, F. Ensslen, D.H. Neuhaus, Review of technological design options for building integrated photovoltaics (BIPV), Energy Build. 231 (2021), 110381, https://doi.org/10.1016/J.ENBUILD.2020.110381.
[102] M.R. Animesh, P. Corti, A. Asok, P. Bonomo, Indian BIPV Report 2022: Status and Roadmap, 2022, pp. 1–79. https://solarchitecture.ch/wp-content/uploads/2022/08/BIPV-Report-India_v01.pdf.